Development of Xenon Level Instrumentation for the LZ Dark Matter Detector



FengTing Liao

Christ Church College

University of Oxford

A thesis submitted for the degree of

Doctor of Philosophy

Trinity 2017

for my family

Acknowledgements

Firstly, I would like to thank my supervisor - Professor Hans Kraus for all his advice and wisdom. I am really fortunate to have his support during my time as a graduate student. I highly admire his perseverance and his highest standard in performing research and wish I would become as knowledgeable as he is one day. I shall never forget the days trying out different ideas for electronics with him.

I then would like to extend my gratitude toward many coworkers. I would like to thank Paul Scovell for his humour, guidance for some of the tests in this thesis, and feedback on thesis chapters. I would like to thank Alfredo Thomas and Henrique Araujo for making the system test of the sensors at Imperial College a reality. I will always remember the many days and nights of operating the chamber with Alfredo. I would like to thank Tom Shutt, Kim Palladino, Dan Akerib, Will Waldron, TJ Whitis, Tomasz Biesiadzinski, Alden Fan, and many other past and present members of the SLAC system test team for their help in running the system test project and insights in the system test data. I would like to thank the past and present colleagues at Oxford - Xiaohe, Amy, Junsong, Kathryn, Cees, and Theresa. It has been delightful working with you and discuss exciting ideas in physics.

I would also like to acknowledge the Ministry of Education of the Taiwanese government, the Chengzhong Culture and Education Focus Foundation, the Leche Trust, the Christ Church College for supporting scholarships, awards, and grants for my study at Oxford.

Lastly, my family has been supporting and encouraging me to pursue my dreams and my love. Their love gives me the strength to complete this work. My Sisters and my Mom and Dad, thank you!

Abstract

Galactical and cosmological evidence show that a quarter of the energy budget of our universe is made of collisionless, non-relativistic, and non-baryonic dark matter. Its potential coupling to standard model particles, however, has not yet been understood. One of the leading candidates - Weakly Interacting Massive Particles (WIMP) - allows the production of a dark matter relic density as observed today and couples to standard model particles at or below the weak scale.

LUX-ZEPLIN (LZ) is a future tonne-scale two-phase xenon TPC aiming to detect WIMP recoils with xenon nuclei. The experiment will begin WIMP search data-taking in 2020 at the Sanford Underground Research Facility (SURF) in Lead, South Dakota and has a projected sensitivity of $3 \times 10^{-48}\,\mathrm{cm}^2$ or better in probing a $40\,\mathrm{GeV/c}^2$ WIMP. The main observables of particle interactions in LZ are the primary scintillation (S1) and secondary scintillation (S2). However, optimising and achieving a stable S2 signal in such a tonne-scale TPC is non-trivial. Effects from the structural design of the S2 production region (top-corner structure), TPC tilt, and the xenon circulation system requires precise monitoring of the liquid surface. Such monitoring is achieved by the capacitive liquid level sensors developed within this thesis. The sensors are strategically placed to ensure that non-uniformity of the S2 signal due to the effects can be understood and corrected.

In this thesis, the development of a monitoring system designed to optimise the quality of the S2 signal, based on the capacitive level sensors is discussed. A design of the electronics scheme based on a differential measurement allows femtofarad precision measurement of sensor's capacitance at picofarad level, even in the presence of cable capacitance at nanofarad level. A systematic study of the response of such a sensor to LXe and the application of the precision level sensors to two-phase TPC was carried out. Findings of intrinsic influences from LXe artefacts and LXe dielectric constant variation with its saturated temperature are identified; the result on the application of the sensors contributes to the designs of LZ circulation and the top-corner region. The final LZ level sensors show an artefact-free liquid level measurement and a $12\,\mu$m precision in measuring liquid nitrogen level (projection for LXe: $\sim 9\,\mu$m) over a 20 mm measurement range.

Contents

1 Introduction **1**

2 Dark Matter **5**
2.1 The ΛCDM Model . . . 6
2.2 Evidence of dark matter . . . 8
2.2.1 Galactic Scale . . . 9
2.2.2 Cosmological Scale . . . 12
2.3 Candidates . . . 15
2.4 WIMP Detection . . . 22
2.4.1 WIMP Interaction Rate . . . 23
2.4.2 Direct detection experiments . . . 30

3 Detection with Two-phase Xenon TPC **34**
3.1 Two-Phase Xenon TPC . . . 35
3.1.1 Why Xenon? . . . 35
3.1.2 Particle Interaction . . . 37
3.1.3 Energy Partitioning . . . 39
3.1.4 Primary Scintillation (S1) . . . 43
3.1.5 Electron Transportation . . . 45
3.1.6 Secondary Scintillation (S2) . . . 46
3.2 LUX-ZEPLIN (LZ) . . . 49
3.2.1 Time Projection Chamber (TPC) . . . 50
3.2.2 Cryogenic and Recirculation system . . . 55
3.2.3 Radioactive Background Veto . . . 57
3.2.4 Calibration . . . 59
3.3 Conclusion . . . 62

4 Level Sensors **64**
4.1 Motivation . . . 65
4.2 Placement of Level Sensors in LZ . . . 68
4.3 Liquid Level Measurement Technology . . . 71
4.3.1 Capacitive Sensors . . . 73
4.3.1.1 Parallel Wires . . . 73
4.3.1.2 Concentric Cylinders . . . 75
4.3.1.3 Parallel Plates . . . 76
4.3.2 Choice of Materials . . . 77
4.4 Requirements of the Sensor . . . 78
4.4.1 Radiopurity . . . 78

4.4.2 Xenon Cleanliness . . . 79
4.4.3 High Voltage Concerns . . . 79
4.4.4 Sensitivity . . . 80
4.5 Electronic Design . . . 81
4.6 General Geometrical Design Rules . . . 85
4.6.1 Parameterised Dimension . . . 85
4.6.2 Stray Capacitance . . . 86
4.7 Prototype Tests . . . 87
4.7.1 Mineral Oil Tests . . . 88
4.7.1.1 Horizontal Parallel Plate Sensor (HPPS) . . . 88
4.7.1.2 Vertical Parallel Rod Sensor (VPRS) . . . 92
4.7.1.3 Conclusion on HPPS and VPRS . . . 93
4.7.2 Medium Voltage Test . . . 93
4.8 Conclusion of Prototype Sensors . . . 99

5 R&D at LZ System Tests 101
5.1 System Test at Imperial College London . . . 102
5.1.1 Design of the Imperial System . . . 102
5.1.2 Sensors in Imperial Chamber . . . 105
5.1.3 Imperial System Operation in Run 5 . . . 108
5.2 Result of Imperial System Test . . . 111
5.2.1 Chamber Cool Down . . . 111
5.2.2 Liquid Xenon Filling . . . 112
5.2.3 Electron Lifetime . . . 119
5.3 System Test at SLAC . . . 121
5.3.1 Design of the SLAC Phase-I System . . . 121
5.3.2 Sensors in the SLAC System . . . 125
5.3.3 SLAC System Operation in Runs 3-6 . . . 128
5.4 Result from the SLAC system test . . . 130
5.4.1 Xenon Filling and Recovery of Sensors . . . 130
5.4.2 Liquid Surface Map Estimation . . . 135
5.4.3 Continuous Liquid Level Monitoring . . . 136
5.4.4 High voltage issues . . . 142
5.5 Systematic Effects . . . 145
5.6 Conclusion . . . 148

6 Final Design of LZ Level Sensor 150
6.1 Systematic Effects . . . 151
6.1.1 Liquid Artefacts . . . 151
6.1.1.1 Mock-up Test Setup . . . 151
6.1.1.2 Result of Mockup Tests . . . 153
6.1.2 Dielectric Constant Variations . . . 158
6.1.2.1 Theory of Dielectric Constant for Non-polar Material . . . 159
6.1.2.2 ε_{LXe} Measurement Method . . . 163
6.1.2.3 ε_{LXe} Result . . . 164
6.2 Design of LZ Level Sensors . . . 166
6.2.1 Technical Issues and Mitigation Strategies . . . 168

6.2.1.1 Material Expansion and its Mitigation 168
6.2.1.2 Fringe Field Interference and its Mitigation 169
6.2.1.3 Liquid Artefacts and their Mitigation 169
6.2.1.4 High Voltage and Mitigation 170
6.2.2 Final Design of a Forest-like Geometry 176
6.2.3 Performance of the Sensor 180
6.3 Conclusion 187

7 Conclusions **189**

A Level Sensors in the LZ Circulation System **192**
A.1 Design of the Sensors 192
A.2 Performance Tests 194

References **198**

List of Figures

2.1 Constraint on the matter density and the cosmological constant. . . 7
2.2 Rotational curve of spiral galaxy - NGC 6503. 8
2.3 The observation of merging clusters (Bullet Cluster). 10
2.4 The CMB map from Planck. 12
2.5 The CMB power spectrum measurement by Planck. 13
2.6 Summary of mass range of dark matter and mediator particle candidates, experimental anomalies, and search techniques. 17
2.7 Comoving number density of dark matter in the freeze-out process. 19
2.8 Possible detection channels for dark matter candidates. 22
2.9 Expected differential event rate of WIMP with different targets. . . 27
2.10 Experimental techniques in direct detection experiments. 30
2.11 The exclusion limits of some of the most sensitive direct detection experiments as of writing. 32

3.1 Xenon phase diagram. 36
3.2 The operation principle of a two-phase xenon TPC. 37
3.3 Micro-physics of the S1 and S2 production in xenon. 38
3.4 $\log_{10}(S2/S1)$ vs $S1$ parameter space for WIMP search. 42
3.5 Electron extraction efficiency in two-phase xenon TPC. 47
3.6 Variation of S2 gain and width with an electric field in GXe. . . . 49
3.7 Overview of the LZ system. 50
3.8 LZ TPC and top-corner region. 51
3.9 LZ cryogenic and recirculation system. 56
3.10 Nuclear recoil spectrum from each calibration sources. 61

4.1 Geometrical effect on S2 signal from TPC tilt and liquid level variation. 66
4.2 Flow diagram of the LZ detector and the integration of WPS with the TPC of SLAC system test. 70
4.3 A closer look of the xenon tower. 71
4.4 Applications of parallel structures in the liquid level measurement. . 74
4.5 The circuit diagram of the sensor's readout. 82
4.6 Effects of fringe fields. 86
4.7 Prototype level sensor sensors. 87
4.8 The configuration of tests to detect oil dropping and liquid filling. 89
4.9 Result of oil dropping test of HPPS. 91
4.10 Precision of HPPS. 92
4.11 Result of oil filling test of VPRS. 94
4.12 The circuit diagram with the implementation of blocking capacitors. 95

4.13 Preparation for a high voltage test experiment. 96
4.14 Reuslt of the medium voltage test of the prototype sensor. 97

5.1 Schematic of the two phase chamber at Imperial College. 103
5.2 Inner look of the Imperial chamber and level sensors on two towers. 106
5.3 CAD drawings of Imperial level sensors. 107
5.4 Slow control data of the chamber in the Run5 sensor test. 109
5.5 Electronics readout of sensors during the cool down process in Run5. 113
5.6 Data of the T2 IHLS. 114
5.7 Data of T1 IVLS. 115
5.8 Data of T2 IVLS. 116
5.9 Data of the ELM test after the run of the sensors. 119
5.10 Overview of the system test detector system. 122
5.11 SLAC Phase-I system test TPC 123
5.12 SLAC top-corner structure in Run 3-6 of the Phase-I system test. . 124
5.13 Assembly locations of the system test level sensors on the top-corner structure. 126
5.14 SLAC system test level sensors in Runs 3-6. 127
5.15 SLAC system test level sensors in Runs 3-6. 128
5.16 High voltage simulation of level sensors at the top-corner with QuickField. 129
5.17 LXe filling test of the sensors in Run 4 on 4th May. 131
5.18 LXe recovery test of the sensors in Run 4 on 25th May. 132
5.19 Correlations of TPC's liquid level and long-period oscillations with liquid flow rate. 136
5.20 Liquid level oscillations with a shorter period. 138
5.21 Fast Fourier transform the data of SHLS001 and SVLS. 139
5.22 Liquid level measurement in HV. 140
5.23 Example of correlation between signal and liquid level oscillation on 06/02/2017 in Run 6. 141
5.24 High voltage study with COMSOL of system test level sensors. . . . 143
5.25 Squeezing effect of fringe field that affects the field lines of the C_{ref} and C_{lvl}. 147
5.26 Readout dependence of the LX-filled SVLS with liquid temperature. 148

6.1 Experimental setup of the capillary effect study. 151
6.2 PCB drawings of mock-up sensors. 152
6.3 Data and illustration cartons show the PcbHLS measurements at the filling and emptying processes. 154
6.4 Images show occurrences of the features during liquid filling. 155
6.5 Images show occurrences of the features at emptying. 156
6.6 Data of PcbVLS mock-up tests. 157
6.7 Measured LXe density along the liquid/vapor coexistence line and expected dielectric constant change of LXe with temperature. . . . 161
6.8 Dependence of the LXe-filled C_{lvl} on chamber pressure changes. . . 165
6.9 Xenon dielectric constant changes with saturated temperature. . . 166
6.10 Frequency dependence of $\varepsilon_{LXe}(\omega)$ at a 170 K. 167
6.11 Drawing of the LZ top-corner design. 171

6.12 Field simulation of various distances between the sensor and the anode. 172
6.13 Field simulation of various distances between the sensor and the gate. 173
6.14 The result of electric field maps at the top corner region. 175
6.15 The level sensor with a set of vertically parallel plates. 177
6.16 COMSOL Simulation of fringe field of the final level sensor. 179
6.17 CAD drawing of the interface of the WPS with the top-corner region. 180
6.18 Separate tests of C_{lvl} and C_{ref} of all three WPS'. 183
6.19 The result of the combination test. 185

A.1 CAD drawings of MLS and LLS. The sensors are shielded inside a grounded guard tube (not shown here). Green: grounded supporting structures. Blue: V_{sense} plate. Pink: excitation plates of V_{ref} and V_{lvl}. Light beige: PEEK supporting structure. The parameters as follows correspond to the parameters in equation 4.5. (Top): Medium level sensor, with $L_{lvl} = 200\,\text{mm}$, $L_{ref} = 43\,\text{mm}$, $d_{lvl} = 2\,\text{mm}$, $d_{ref} = 1\,\text{mm}$, and $W_{lvl} = W_{ref} = 13\,\text{mm}$. (Bottom): Long level sensor, with $L_{lvl} = 800\,\text{mm}$, $L_{ref} = 175\,\text{mm}$, $d_{lvl} = 2\,\text{mm}$, $d_{ref} = 1\,\text{mm}$, and $W_{lvl} = W_{ref} = 13\,\text{mm}$. 193
A.2 C_{lvl}-only test result for MLS and LLS. The sensors were tested in two different buckets of liquid nitrogen. (Top): MLS. (Bottom): LLS. The rising of the reading of the liquid nitrogen evaporation is due to icing and water condensation on the warmer part of the electrodes of the sensor. 196
A.3 C_{ref}-only test result for MLS and LLS. The sensors were tested with the same bucket of liquid nitrogen. The LLS was installed upside down with MLS attached to its end. The cyan box in the data represents the period when liquid nitrogen was evaporating pass the C_{lvl} of MLS; the red box represents the time when effects of icing and water-condensation on the sensors were dominant. (Top): MLS. The reading decreasing after the red box is due to water-evaporation and sensor warm-up. (Bottom): LLS. The rise of the reading after the red box was due to sensor warm-up. The reading decreasing after 30 hours is due to a continuous evaporation of the water on the sensor. 197

List of Tables

3.1 Parameters of the LZ TPC. 53
3.2 Summary of baseline calibration for LZ. 59

4.1 Candidate material properties in room temperature. 77
4.2 Background of candidate materials. 78

5.1 Fitting parameters of the sensors. 118
5.2 The capacitance of the sensors at room temperature without any LXe filling. 118
5.3 Estimation of the relative liquid level height. 135
5.4 Expected and measured capacitance of SLAC level sensors at room temperature. 146

6.1 The measured and expected capacitance of the final level sensors. . 181

A.1 The measured and expected capacitance of the level sensors. We use the Agilent U1733C in 100 kHz mode to measure C_{aux}. Systematic errors were estimated based on results of liquid nitrogen evaporation tests shown in figure A.3 and A.2. The measured C_{lvl} of MLS is much higher than its expected value, owing to a closer distance between the sense plate and the excitation plate (the tolerance of the distance between plates is ± 0.5 mm). 194

Chapter 1

Introduction

Dark matter is a fundamental component of our universe and has not yet been discovered. Although it is non-relativistic, collisionless, and non-baryonic, one of its leading candidates - Weakly Interacting Massive Particle (WIMP) - can couple to a standard model particle and leave a traceable signal by imparting part of its energy on a nucleus in underground detectors. One such detector, LUX-ZEPLIN (LZ), is a tonne-scale two-phase xenon TPC under construction. LZ investigates potential WIMP interactions through two primary observables - primary scintillation (S1) and secondary scintillation (S2). Systematic effects on the S2 signal, however, can lead to misinterpretation of that observable and therefore need to be corrected. In this thesis, I discuss the development of a monitoring system based on capacitive level sensors to monitor potential effects on the signal.

Chapter 2 The chapter begins with introducing the standard model in cosmology that describes the information of the energy budget of the universe. The chapter then discusses the evidence of dark matter both at galactic and cosmolo-

gical scales and why WIMPs are a leading candidate for particle dark matter. The chapter concludes with a discussion on the search of WIMPs in direct detection experiments.

Chapter 3 The chapter describes how the technology of the two-phase xenon time projection chamber (TPC) can be used for WIMP searches. This includes the particle interactions which result in nuclear recoils (potential WIMP signal) and electronic recoils (background in WIMP search but potentioal signal in other dark matter searches). The chapter then describes the energy partition of the interactions that result in the observables (S1 and S2 signals). This is followed by explaining the microphysics of the observables - primary scintillation, electron transportation, and secondary scintillation and how they lead to the rejection of background recoils. After that, the chapter discusses the LZ experiment, a tonne-scale two-phase liquid xenon detector, and its various subsystems including the TPC, the circulation system, the veto system, and the calibration.

Chapter 4 The chapter begins with a discussion on the importance and challenges of achieving an optimised S2 production region described in Chapter 3. This necessitates a monitoring system of level sensors at various parts of the LZ system to complement the correction and optimisation of the detector signal. Following this, it describes how I led the development of the monitoring system from scratch. I first describe the general design principles of the sensors and a dedicated electronics scheme which is at the heart of the liquid level measurement. The electronics achieves a suppression of the contributions from the cable capacitance ($\sim$nF) to the systematic error while it measures the capacitance of the sensors

(∼pF) with excellent precision (∼fF). I show the application of the electronics to prototype level sensors in measuring the liquid level change induced by mineral oil with precision at μm level. I also show the result of a surface wave measurement of the sensor, independent of the influence in a medium electric field (up to 700 V/cm).

Chapter 5 The chapter discusses an R&D programme of the sensor in the LZ system tests at Imperial College London (Imperial) and SLAC National Acceelerator Laboratory (SLAC). The programs contributed to the understanding of the sensor's response to LXe and the application of the monitoring system in an LZ-like detector system. I led the program and constructed the R&D sensors to perform such systematic studies. The chapter starts with a discussion of tests in the Imperial system, including the design and the operation of the Imperial chamber and the test with the R&D sensors. Then, it describes the design and operation of the SLAC system and the monitoring system installed at the SLAC top-corner structure (near the S2 production region of the TPC). The results from these R&D sensors contributed considerably to our understanding of the choice of material, its capacitive response to the LXe, and the design of the LZ top-corner structure and the circulation system. Lastly, the chapter concludes with a detailed discussion of the systematic effects - LXe dielectric constant change, LXe artefacts, and electric field issues observed from these R&D sensors.

Chapter 6 Studies on the systematic effects shown in the R&D sensors of the LZ system tests paved the way for the final design of the LZ level sensors. The chapter starts with an investigation of the origin of two effects - LXe artefacts and

LXe dielectric constant changes. For understanding the LXe artefacts, mock-up tests with PCB level sensors were carried out. The tests show that the artefacts are caused by meniscus and capillary effects. Another investigation of the LXe dielectric constant change with xenon saturated temperature was performed with the R&D sensor at the system test chamber at Imperial. The measurement result of the constant allows a correction for the correlation between a measured liquid level and a given LXe temperature. Following these investigations, I review the mitigation strategies of the systematic effects and also present the simulation solution to the TPC high electric field concerns. The simulation result led to a design of the LZ top-corner structure which will be tested in a future run at the SLAC system test. Lastly, I present the final LZ level sensor with its design based on the results discussed in Chapter 4 and 5; I also present a test result of the sensor in liquid nitrogen which shows an artefact-free measurement of the liquid level.

Chapter 7 In this chapter, I briefly summarise the main findings in the development of the level sensor. I then conclude the chapter with a short discussion regarding how the sensor could be applied in understanding background events of future WIMP searches or the studies of the xenon microphysics.

Chapter 2

Dark Matter

Over the past 80 years, a wealth of evidence has suggested that baryonic matter contributes a fraction ($\sim$ 4.8 % by DES [1]) of the total composition of our universe. The measurements of rotational velocity curves of spiral galaxies [2], the observations of the Bullet Cluster [3], and the detection of Cosmic Microwave Background (CMB) [4] provide convincing evidence of the existence of dark matter. Although with all the evidence of dark matter's existence, its characteristics such as mass, spin, and possible interactions with Standard Model particles have yet to be understood.

In this chapter, we will first review the current status of the model and evidence of dark matter. The Weakly Interacting Massive Particles (WIMP) which could serve as one of the prominent answers to the dark matter search will then be discussed. Lastly, we will describe three major experimental searches and close with a discussion of direct direction detection.

2.1 The ΛCDM Model

The model for cold dark matter (CDM) and the inclusion of a cosmological constant (Λ) in it provides explanations to a wide variety of cosmological phenomena. The model entails the expansion (or collapse) of space mass density and the pressure in a homogeneous and isotropic universe. A detailed discussion on such model is best reserved for a textbook or a review [5–8]. Here, we briefly summarise the model which entails the energy budget of the universe.

The Friedman equation of the model, telling the cosmic expansion history, can be written as

$$\frac{H^2}{H_0^2} \equiv \frac{1}{H_0^2}(\frac{\dot{a}}{a})^2 = \Omega_m(\frac{a_0}{a})^3 + \Omega_k(\frac{a_0}{a})^2 + \Omega_\Lambda, \tag{2.1}$$

where H is the Hubble constant, a is the cosmic scale factor at time t, and H_0 and a_0 are present-day values of the Hubble constant and the scale factor, respectively. The $\Omega_{k,\ \Lambda,\ m}$ terms define the parameters for curvature, dark energy, and matter content of the universe. They are

$$\Omega_k = -\frac{1}{H_0^2 a_0^2 R^2}$$
$$\Omega_\Lambda = \frac{\Lambda}{3H_0^2}$$
$$\Omega_m = \frac{\rho_0}{\rho_c},$$

where Λ is the cosmological constant of vacuum energy density, R is the curvature, ρ_0 and $\rho_c = {}^{3H_0^2}/_{8\pi G}$ represent the matter density and the critical energy density, respectively, of the universe. For open, closed, and flat universes, the Ω_k is greater than, less than, and equal to zero, respectively. If $t = t_0$ (today), $a = a_0$ will lead

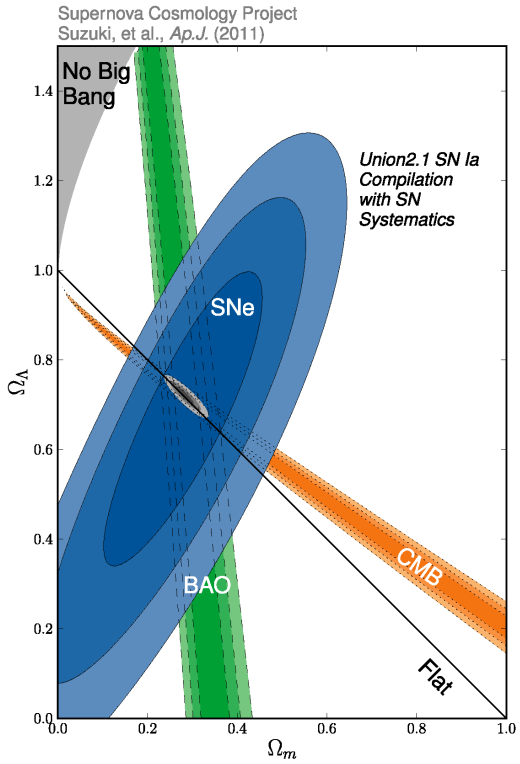


Figure 2.1: Constraint on the matter density Ω_m and the cosmological constant Ω_Λ with supernovae, cosmic microwave background, and baryon acoustic oscillation. Taken from [9].

to the relation that $\Omega_k + \Omega_\Lambda + \Omega_m = 1$.

The parameters $\Omega_{k,\ \Lambda,\ m}$ of the model have been well tested independently to understand the energy budget of our universe. This includes analysis of the luminosity distance as a function of redshift in Type Ia Supernovae, lensing studies of galaxy clusters, estimation of the Baryon Acoustic Oscillations, and the power spectrum of CMB [1, 4, 9, 10]. Analysis of the CMB power spectrum, for example, shows that $\Omega_k \approx 0.0008$ and implies a spatially flat geometry of our universe. The vacuum energy density term, also known as "dark energy", is measured to be $\Omega_\Lambda \approx 0.685$. The total matter density of the universe can be devided into two terms: $\Omega_m = \Omega_b + \Omega_c \approx 0.316$, where $\Omega_b \approx 0.049$ is the baryon energy density and $\Omega_c \approx 0.266$ is the cold dark matter energy density. (The values of these parameters are taken from Ref. [4].)

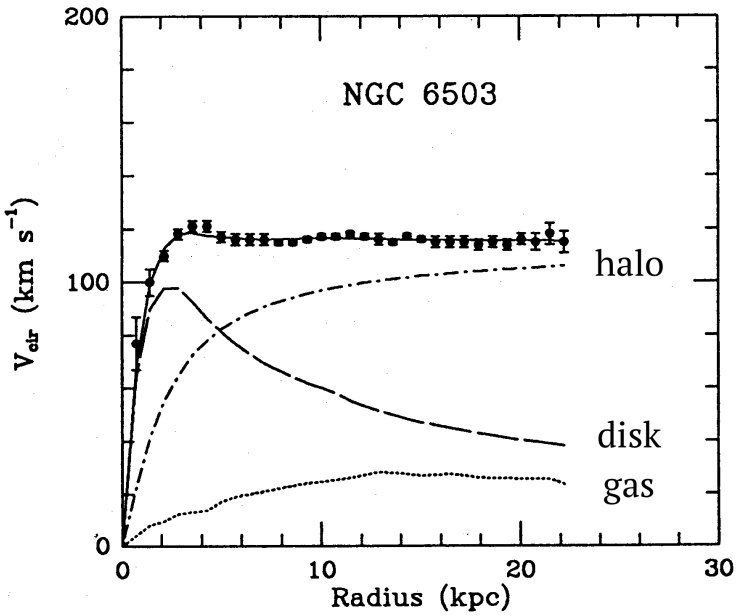


Figure 2.2: Rotational curve of spiral galaxy - NGC 6503. Taken from [15].

2.2 Evidence of dark matter

Studies of the mass-to-light ratio of galaxy clusters in the early 20th century suggested that an additional contribution to the matter density in the universe was necessary to account for the measured mass of galaxy clusters [11]. The ratio for the Coma cluster, first calculated by Fritz Zwicky in 1937 [12], using the virial theorem, and that for the Virgo cluster, obtained by Sinclair Smith around the same time [13], were shown to be surprisingly high. Although there is an error in these calculation, resulting an overestimated ratio of the hidden mass within the clusters, modern measurement using the virial theorem nevertheless reaches a similar result [14]. This early debate was not resolved until further evidence for dark matter at both galactic and cosmological scales. In the following sections, the evidence which supports the required missing mass is discussed.

2.2.1 Galactic Scale

At the beginning of 1970s, a study of rotation velocities of Andromeda galaxy with spectroscopic observation by Vera Rubin and Kent Ford began to shed light on the debate of the missing mass [16]. The bulge of a galaxy contains most of the luminous matter with its mass distribution $M(r)$ within a radius r expected to increase slowly with r away from the galactic centre. The mass distribution is an integral over the mass density profile $\rho(r)$ at different radii r: $M(r) = \int \rho(r) r^2 dr$. This gives the rotational velocity of a spiral galaxy as a function of the galactocentric radius r with a Newtonian dynamics framework:

$$v(r) = \sqrt{\frac{G \cdot M(r)}{r}}. \tag{2.2}$$

This equation predicts a decrease of the rotational velocity when the galactocentric radius increases. However, measurements find that the rotational velocity of outermost stars in a galaxy remains roughly constant [2, 17]. One of the explanations for such a phenomenon is the introduction of a dark matter halo to account for the missing mass which sustains the higher velocities at a larger galactic radius. Figure 2.2, for instance, shows a measurement of the rotational speed of a spiral galaxy - NGC-6503 [15]. If the luminous matter alone is the answer, $v(r)$ should fall because of the decrease of local luminous matter density. However, the data requires $M(r) \propto r$ at a radius of a few kpc, which could be obtained if an additional (non-luminous) mass component existed with a density profile approximated as $\rho(r) \propto r^{-2}$ to first order. Such studies of the curves are not only one of the convincing evidence of dark matter, but also one of the indications of dark matter



Figure 2.3: The observation of merging clusters or so-called Bullet Cluster. The pink area indicates the distribution of interstellar gas. The blue area shows the bulk of mass distribution in the lensing map. [Optical: NASA/STScI; Magellan/U.Arizona/D.Clowe et al.[3]; X-ray: NASA/CXC/CfA/M.Markevitch et al.[18]; Lensing Map: NASA/STScI; ESO WFI; Magellan/U.Arizona/D.Clowe et al.[19]]

halos that surround galaxies.

To probe the mass of dark matter within the clusters, Zwicky suggested the ultimate measurement could come from lensing [12]. The technique, called gravitational lensing, is based on an effect derived within General Relativity that sees the path of the light along the null geodesic in the space-time distorted in the presence of a massive body [20, 21]. This effect is applied to the observation of the light from galaxies which could be bent and focused, just as is the case with a lens, when it passed through a region occupied by non-luminous matter. There are two major flavours of gravitational lensing which observe such effects to the first order - strong lensing and weak lensing. The strong gravitational lensing requires a direct alignment between a background object, a foreground object, and the observer. Such alignment allows light from the background to take multiple paths to reach the observer who will detect multiple arc-shaped images of

the background galaxies [22]. As for the weak lensing, when the background object, the foreground object, and the observer are not closely aligned, images with shapes stretched tangentially around the foreground mass are formed. Because of the difficulties in differentiating effects due to the distorted galaxies far away from the foreground mass or the foreground mass being too small, the effects from weak lensing have to be studied statistically, averaging over many distorted images to map a systematic distribution of many galaxies along a direction [23]. These lensing techniques not only allow the study of the mass distribution of galaxy clusters [19] but also enable constraints on cosmological parameters using large statistical samples [1, 24, 25].

The smoking gun evidence of dark matter in the galactic scale comes from merging clusters (e.g. the Bullet Cluster) - 1E0657-558. Figure 2.3 shows the studies of the clusters in the visible by HST, the x-ray by Chandra, and the unseen matter by weak lensing [3, 18, 19]. As two galaxy clusters pass through each other, the baryonic matter in the clusters, which is predominantly in the form of hot gas, interacts electromagnetically. Such interaction slows down and concentrate the gas in the centre of the collision. The measurement of the interstellar gas by Chandra, using the observation of x-ray, shows the slowdown, a shock front, and a drag due to friction (pink area in figure 2.3) [18]. The mass distribution of the merger clusters, detected by the weak lensing, indicates that the clusters pass through each other without leaving the shock front or the drag as that of the gas. (blue area in figure 2.3) [19]. The phenomenon is difficult to explain with alternative theories, such as the Modified Newtonian Dynamics, but could be interpreted with the presence of collisionless particle dark matter.

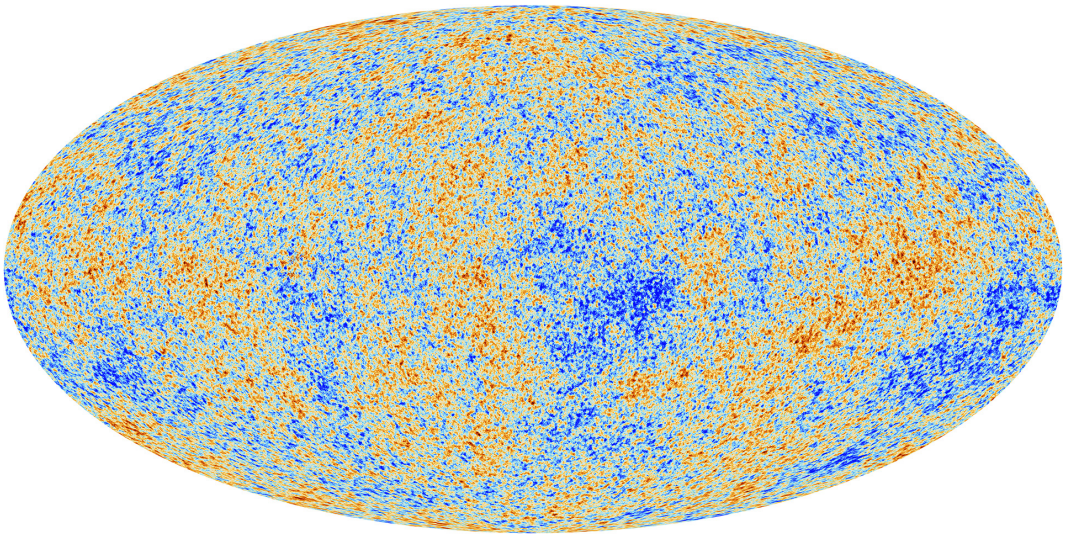


Figure 2.4: The CMB map from Planck shows the 10^{-5} anisotropies with high resolution. Taken from ESA.

2.2.2 Cosmological Scale

Studies at the cosmological scale necessitate a cold dark matter component in our universe. For example, the CMB map shown in figure 2.4 describes the left-over of electromagnetic radiation in an early stage of the universe. The early universe, before the formation of galaxies, was filled with hot and dense hydrogen plasma, which consists of electrons, protons, and photons in thermal equilibrium. As the universe expanded and its temperature fell below the binding energy of hydrogen, the electrons combined with protons to form hydrogen atoms which less readily absorb thermal radiation. Thus, as the electron-photon interaction rate fell below the Hubble constant rate, the photons decoupled from electrons made a final scatter and started to travel with the mean free path on the scale of the universe. The photons from the final scatter carry the information of temperature anisotropies due to non-uniformity of the matter density at that time. As a result, these photons can be used to probe the structure of the early universe.

The anisotropies are caused by a process called Baryonic Acoustic Oscillation

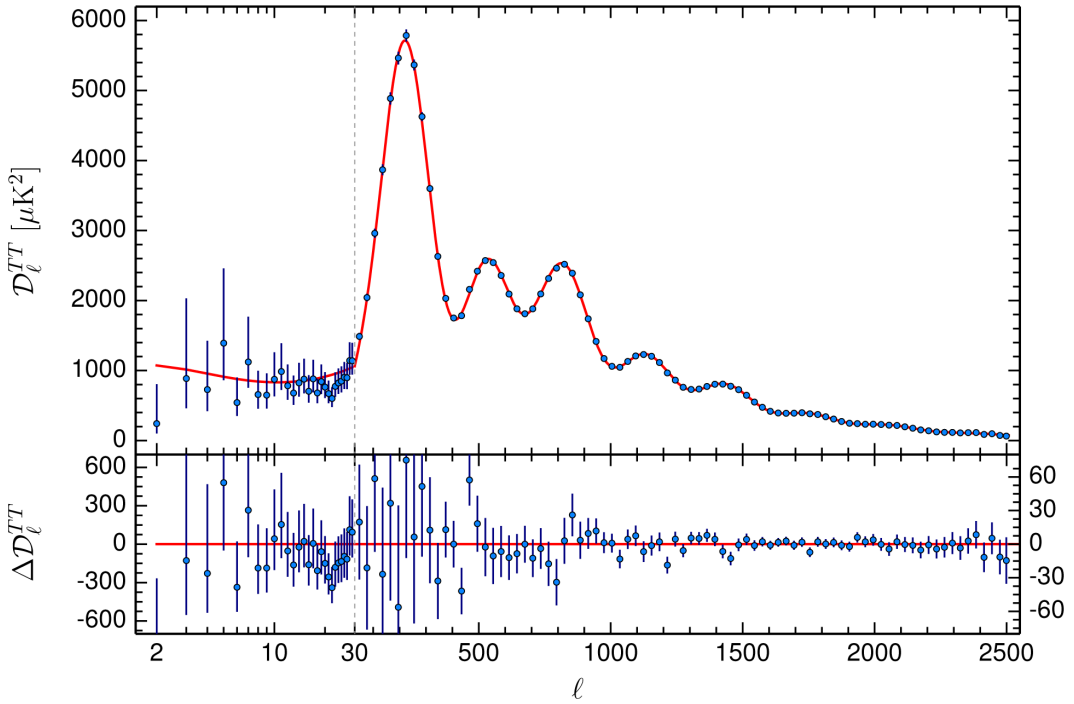


Figure 2.5: The CMB power spectrum measurement by Planck. The power of the temperature correlations at different angular separations in the CMB sky is parametrised with $D_l^{TT} = \frac{l(l+1)}{2\pi}C_l$, where TT indicates the temperature correlation, and l is the multipole number. The best-fit line (solid red) is made from the parameters in the ΛCDM model. Taken from [4].

(BAO) in the primordial plasma. The plasma in the early universe before recombination comprised regions with different densities due to primordial fluctuation. Over-dense regions attracted more baryons and dark matter gravitationally. As the attraction happened, heat, produced by photons scattering off electrons, increased the radiation pressure. The pressure, which affected baryons but not the dark matter, pushed baryons away from the dense regions (repulsion). The expansion of the regions decreased the radiation pressure and allowed the gravitational compression to restart (attraction). The competing processes between the repulsion and the attraction led to standing sound waves (acoustic oscillation), i.e. BAO. The radiation pressure reduced after the recombination, effectively ending the oscillations. The photons from the plasma then diffused through the baryonic matter and left behind a shell of over-dense baryonic matter at a fixed radius.

The relic of the oscillation can be observed in the CMB angular power spectrum shown in figure 2.5. The spectrum is obtained by expanding the CMB temperature map into Spherical Harmonics:

$$T_{fluct}(\theta, \phi) = \sum_{l=2}^{\infty} \sum_{m=-l}^{l} a_{lm} Y_{lm}(\theta, \phi), \tag{2.3}$$

where the multipole number l and the expansion coefficients a_{lm} can be seen respectively as the wave-number k and the amplitude of a given k in a Fourier transform. The l can also be understood as $l \sim 180°/\theta$, where the angle θ describes the separation of two points in the sky. The spectrum, measuring amplitude as a function of the mutipole l, can be defined as an average over m for every l:

$$C_l = \frac{1}{2l+1} \sum_{m=-l}^{l} |a_{lm}|^2 . \tag{2.4}$$

The peaks in the power spectrum contain information of our universe. In general, the odd peaks of the spectrum reveal information from the compression; the even peaks of the spectrum contain knowledge from the expansion. The amplitude of peaks driven by the force of gravity describes the overall matter content of the universe. The fitting result of the first peak suggests that the curvature of the universe is flat. If the curvature is positive or negative, the peak will appear at a lower or higher multipole which results in a magnified or diminished CMB. The second peak details the baryonic matter content. The amplitude of the peak is damped because the baryonic matter can absorb the radiation. The third peak describes the dark matter content. Because the dark matter does not interact electromagnetically with baryonic matter, it was unaffected by the increasing ra-

diation pressure. Thus, a higher density of dark matter, which corresponded to a larger gravitational potential well, attracted more baryons to fall into during the oscillation and amplified the odd-number peaks of the power spectrum. The peaks, estimated by the Planck observation, indicate the matter ratio of the universe of which 4.9 % is baryonic matter, 26.6 % is dark matter, and 68.5 % is dark energy [4].

Another evidence of dark matter in the large-scale structure of the universe comes from considering structure formation. N-body simulation of the structure, taking initial conditions from the ΛCDM model and the theory of cosmic inflation, predicts the structure growth. Such growth starts with an even distribution of particles from both baryonic matter and dark matter at some time (redshift). The distribution is perturbed through gravitational instability which creates overdense regions. The regions draw in surrounding matter, creating a positive feedback for density oscillation which eventually results in the growth of galaxies, galaxy cluster, and super clusters. The result of the simulation agrees remarkably well with experiments such as the CfA2 and the Sloan Digital Sky Survey [26]. Also, this type of study has shown that the structure formation requires dark matter, specifically non-relativistic dark matter since relativistic particles (e.g. neutrinos) tends to smooth the density fluctuation and leads to an increased physical size of clusters [27].

2.3 Candidates

Dark matter candidates will have to provide explanations for the astrophysical phenomena and survive conditions constrained by observations. One approach

to explain these observations is the Modified Newtonian Dynamics (MOND) that modifies GR to account for the observed properties of the galaxies. The MOND needs to explain current dark matter evidence, including rotation curves, gravitational lensing, the BAO, the structure formation in the universe, and the gravitational wave result (GW170817) from the merger of neutron stars. The explanation of the Bullet Cluster is challenging to be resolved by MOND without the presence of dark matter [28]. In addition, the constraint of the difference between the speed of gravitational waves and the speed of light by the GW170817 event disfavours MOND theories that treat the speed of light as a variable parameter [29].

Another approach is considering the particle behavior of the dark matter. It is natural to look at particles within the standard model (SM) for inspiration. For example, the Massive Compact Halo Objects (MACHO) consisting of baryonic matter that emits little radiation and moves through interstellar space or neutrinos that interact weakly were once considered as solutions for dark matter. The MACHO content can account for only 2.2 % of the total mass at maximum. The neutrinos, another alternative in the SM, although non-baryonic, also do not have enough mass to form the dark matter content and are relativistic which is incompatible with the structure formation. As a result, they were both disfavoured by the precision measurement of CMB and N-body simulations of structure formation [4, 26].

Since neither the MOND nor SM particles could provide a viable answer for dark matter, modern dark matter candidates (see figure 2.6) are based on theories beyond SM, including WIMPs, Hidden DM, Sterile Neutrino, Axions, and many others. Their properties are motivated by solving problems such as the gauge

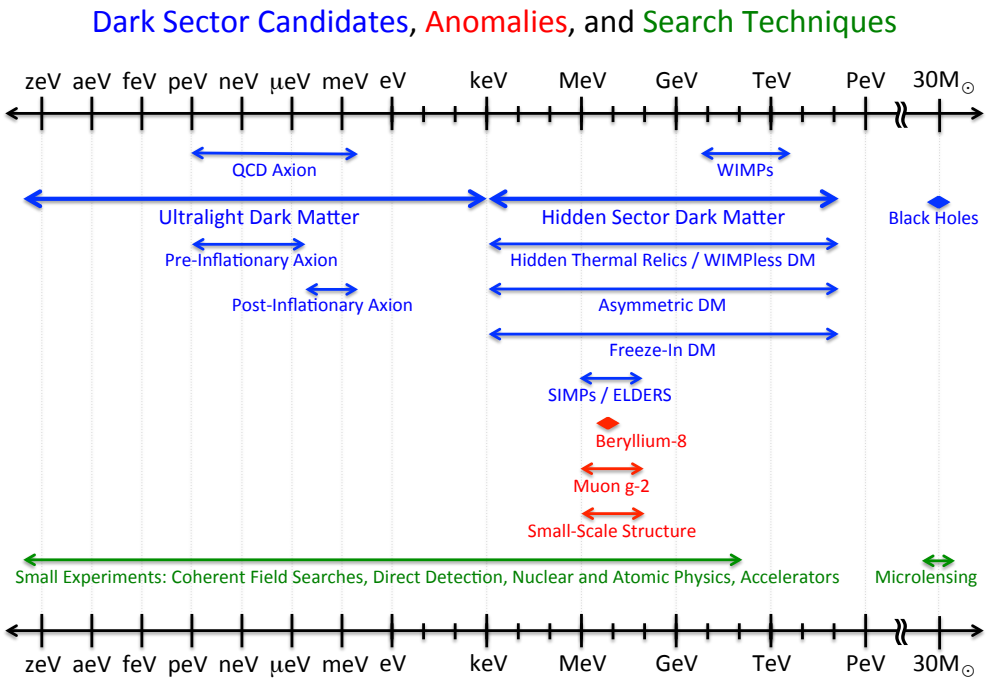


Figure 2.6: Summary of mass range of dark matter and mediator particle candidates, experimental anomalies, and search techniques. Taken from [30].

hierarchy, new physics flavour, neutrino mass, and strong CP [31]. Two of the well-motivated dark matter candidates in experimental searches are Axions and Weakly Interacting Massive Particles (WIMPs). These types of dark matter are neutral, collisionless, and non-baryonic and can produce the observed abundance of dark matter in the universe. In the following sections, their properties will be further discussed.

Axions The Axion arises from an additional $\mathrm{U}(1)_{\mathrm{PQ}}$ to the SM which was first introduced by Peccei and Quinn to resolve the absence of charge and parity violation in strong interactions [32]. It satisfies the generic conditions described above to make an attractive dark matter candidate [33]. Although the axion is quite light ($\sim \mu$eV to meV), it can be produced abundantly by the misalignment mechanism as a nonthermal relic in the early universe and fulfil the criteria necessary for cold dark matter [34, 35]. Regarding coupling with a SM particle, axions could

interact with photons through the Primakoff process ($a\gamma* \to \gamma$) which would allow a resonantly-enhanced conversion of axions to photons via scattering off a background magnetic field [36]. Such a process has been actively searched for by the Axion Dark Matter Experiment (ADMX). The experiment uses a radiofrequency receiver to detect the photons from a tuned cavity resonator and has set exclusion limits of the axion mass at $1.9 \sim 3.69\,\mu$eV [37, 38].

Weakly Interacting Massive Particle (WIMP) Another leading candidate for particle dark matter is the weakly interacting massive particle. The model of WIMPs is mainly motivated by the gauge hierarchy problem and naturally produces the observed relic abundance of dark matter in the universe [31]. WIMPs are stable, massive, and non-baryonic particles which interact with normal matter through gravity and couple to SM particles via the weak force. It is theorised that the mass and cross-section of the WIMPs are on the order of the weak scale, which favours some particles such as the neutralino in the supersymmetry theory (SUSY).

The production mechanism of the WIMP relic density in the early universe is as follows. Assuming a dark matter particle χ has a mass M_χ and an annihilation cross section σ_a as described in Ref. [39], the particle can couple to SM particles q through pair production and annihilation via the weak force, for which the relation is

$$\chi\bar{\chi} \rightleftharpoons q\bar{q}. \tag{2.5}$$

In the early universe, when $T \gg M_\chi$, the number density of WIMPs n_χ and other light SM particles were in thermal equilibrium. The universe broke the equilibrium

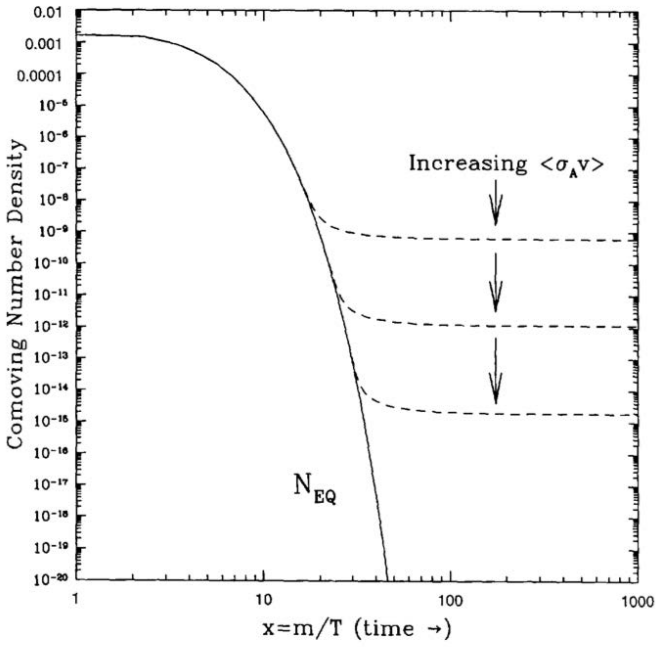


Figure 2.7: Comoving number density abundance of dark matter in the freeze-out process. The solid curve the equilibrium abundance. The dashed curves are the relic abundance with given $\langle \sigma_a v \rangle$. Taken from [39].

when $T < M_\chi$ and expoentially suppress the density of WIMPs. The density would not drop to zero because, in addition to universe cooling, the universe was expanding. The expansion diluteed the density and overcame the annihilation rate:

$$H(t) > n_\chi \langle \sigma_a v \rangle, \tag{2.6}$$

where $H(t)$ is the Hubble expansion rate, and $\langle \sigma_a v \rangle$ is the averaged thermal velocity of particles times annihilation cross-section. Such expansion eventually led to freezing n_χ into a relic density.

The described process is called "freeze-out" and can be quantified with the Boltzmann equation as follows:

$$\frac{\mathrm{d}n_\chi}{\mathrm{d}t} = -\langle \sigma_a v \rangle \left[\left(n_\chi\right)^2 - \left(n_\chi^{eq}\right)^2 \right] - 3H(t) n_\chi, \tag{2.7}$$

where n_χ^{eq} is the co-moving number density at thermal equilibrium. The first term on the R.H.S. of equation 2.7 illustrates that the rate of n_χ reaching n_χ^{eq} is determined by the average of particle flux times the annihilation cross section; the second term describes the decrease of n_χ owing to expansion $H(t)$. The result of equation 2.7 is shown in figure 2.7 which describes the process of the dark matter number density approaching its relic density.

The annihilation term in the equation suggests that the annihilation dominates at the beginning, but as the universe expands, the expansion term takes over the change of the number density. Eventually, the production of dark matter ceases when SM particles do not have enough energy to produce WIMPs; the annihilation process no longer happens effectively because the WIMPs become too sparse to interact. If the dark matter is stable, its relic density at the end of the freeze-out will still exist today.

The numerical solution for equation 2.7 has been obtained in Ref. [39] to estimate the relic density:

$$\Omega_\chi h^2 = \frac{3 \times 10^{-27}\,\mathrm{cm^3 s^{-1}}}{\langle \sigma_a v \rangle} \sim \frac{10^{-10}\,\mathrm{GeV^{-2}}}{\langle \sigma_a v \rangle}, \tag{2.8}$$

where $\langle \sigma_a v \rangle$ is the thermally averaged reaction cross-section times the velocity. The cross-section term can be constrained by the observed $\Omega_\chi h^2 \approx 0.1$ from CMB measurement. As a result, if

$$\langle \sigma_a v \rangle = \alpha_{weak}^2 \cdot M_\chi^{-2} \sim 10^{-9}\,\mathrm{GeV^{-2}}, \tag{2.9}$$

a dark matter particle with M_χ at GeV $\sim$ TeV coupling to SM particles at the weak

scale $\alpha_{weak} \sim 10^{-6}$ can naturally produce the required relic density of the universe today. The coincidence of agreement between equation 2.8 and the measurement of the extraordinary range of the energy scales involved gives the name of "WIMP miracle". The freeze-out scheme of the WIMP miracle not only connects the search for dark matter between astrophysics and particle physics but also provides a model-independent motivation for dark matter at the weak scale.

In fact, in particle physics, SUSY has long provided a stable particle, lightest supersymmetric particle (LSP), with properties of dark matter and mass scale at $10-100\,\mathrm{GeV/c^2}$. The SUSY suggests that every SM particle has a partner particle with the same quantum number and gauge interactions but a different spin by $1/2$. The theory introduces R-parity given as

$$R_p = (-1)^{L+3B+2S}, \tag{2.10}$$

where $R_p = +1$ for SM particles and $R_p = -1$ for their SUSY partners with L, B, and S being the lepton, baryon, and spin numbers respectively. The conservation of this parity implies that the LSP cannot decay and is a viable candidate for dark matter. The neutralino in LSP, in particular, is one of the well-motivated candidates and have a mixed state between the SUSY partners of the photon, Z, and Higgs bosons. It is worth noting that the neutralino has both scalar interaction and axial-vector interactions which could lead to spin-independent and spin-dependent elastic scatterings with a nucleus, respectively [39].

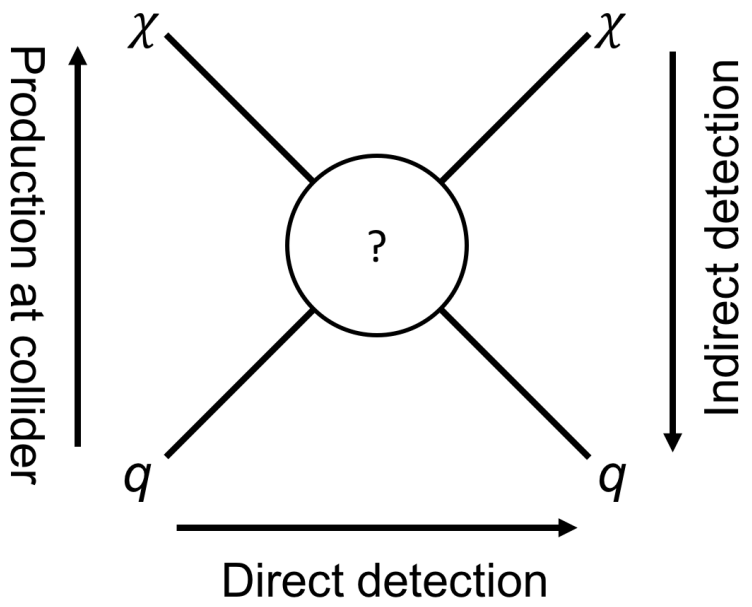


Figure 2.8: Possible detection channels for dark matter candidates.

2.4 WIMP Detection

The WIMP miracle, which provides a model-independent motivation, enables searches for the coupling between particle dark matter and SM particle in detectors. There are three major detection techniques in searching for WIMPs as shown in figure 2.8. They utilise the mechanism that WIMPs interact with normal matter via gravity, and couples to SM particles at the weak scale. Firstly, the pair production of WIMPs, $qq \rightarrow \chi\chi$, would allow colliders such as the LHC to probe the production cross-section of WIMPs in the early universe. A potential discovery of the particle from a collider experiment would be observing a clear missing transverse momentum event in the detector since WIMPs cannot be tagged by the calorimeter. Secondly, the annihilation of WIMPs, $\chi\chi \rightarrow qq$, could enable indirect searches such as Fermi-LAT, IceCube, and AMS-02 to investigate the annihilation

cross-section via spectral signatures. Lastly, the possibility of scattering between WIMPs and SM particles, $\chi q \to \chi q$, gives rise to direct detection experiments to probe WIMP-nucleus cross-sections in terrestrial detectors.

It is worth noting that three types of searches can provide different and complementary information about the nature of dark matter. The sensitivity to a dark matter candidate within different searches depends on the theory of WIMPs and is subject to various sources of systematics. Ideally, a discovery of WIMPs in one type of search would be confirmed by another and follow by independent studies of the WIMPs' properties, such as mass, spin, decay time, and potential new couplings to physics beyond the standard model.

In this section, we will focus on direct detection of WIMPs scattering off a target nucleus which could produce an observable recoil energy within a detector. The derivation and discussion of the detection follow closely from that in Ref. [39–41].

2.4.1 WIMP Interaction Rate

The canonical WIMP interaction in direct detection experiments is the elastic WIMP-nucleus scattering, producing a recoil spectrum of single scattering events in a target nucleus. If a dark matter particle with mass M_χ and velocity v elastically scatters off a nucleus with mass M_T isotropically, the velocity after the center-of-mass scattering is

$$\boldsymbol{v}_{CM} = \frac{M_\chi \boldsymbol{v}}{M_\chi + M_T}. \tag{2.11}$$

This gives the transfered momentum

$$\boldsymbol{q} = M_T \boldsymbol{v}_{CM} = \mu \boldsymbol{v}, \tag{2.12}$$

where $\mu = \frac{M_T M_\chi}{M_T + M_\chi}$ is the reduced mass. The recoil energy of the target nucleus due to q is

$$\begin{aligned} E_R &= \frac{q^2}{2M_T} \\ &= rE_i, \end{aligned} \tag{2.13}$$

where $E_i = \frac{1}{2} M_\chi v^2$, and $r = \frac{4M_\chi M_T}{(M_\chi + M_T)^2}$. As a result, for a WIMP with $M_\chi = 10 \sim 100\,\mathrm{GeV/c^2}$ and $v = 0.75 \times 10^{-3}\,\mathrm{c}$ [42], the the maximum energy it imparts on a xenon atom ($M_T \sim 123\,\mathrm{GeV/c^2}$) to produce a nuclear recoil is $E_R = 0.75 \sim 27.5\,\mathrm{keV}$.

Next, the observed event rate in a terrestrial detector with a given WIMP mass and recoil energy includes parameters from astrophysics, particle physics, and detector physics. This can be expressed as the number of observed events N_{obs} within a given time interval t on a detector with the number of target nuclei N_{Target} is

$$N_{obs} = \varepsilon(E_R) N_{Target} \sigma_\chi(q) \Phi_\chi(E_R, t) t, \tag{2.14}$$

where $\varepsilon(E_R)$ is the detection efficiency of a detector, $N_{Target} = N_A/A$ (N_A is the Avogadro number; A is the molecular weight), $\sigma_\chi(q)$ is the WIMP-nucleus scattering cross-section, and Φ_χ is the flux of WIMPs. Equation. 2.14 can be

written as the event rate per recoil energy interval,

$$\begin{aligned}\frac{\mathrm{d}R}{\mathrm{d}E_R} &= \varepsilon(E_R)\frac{N_{Target}}{rE_i}\sigma_\chi(q)\Phi_\chi(v) \\ &= \varepsilon(E_R)\cdot\frac{\sigma_\chi(q)}{2\mu^2}\cdot\frac{\Phi_\chi(v)}{v^2}.\end{aligned} \tag{2.15}$$

We first look at the contribution of the dark matter flux term from astrophysics in equation 2.15. The third term of the equation is

$$\frac{\Phi_\chi(v)}{v^2} = \frac{\frac{\rho_\chi}{M_\chi}\langle v\rangle}{v^2} = \frac{\rho_\chi}{M_\chi}\langle\frac{1}{v}\rangle, \tag{2.16}$$

where ρ_χ is the local dark matter density, $\langle\frac{1}{v}\rangle$ is the dark matter mean inverse speed. The estimation of local density is model dependent and varies in the literature [43, 44]. For comparison between experiments, the canonical value $\rho_\chi = 0.3\,{}^{GeV}/_{\mathrm{cm}^3}$ is used. The mean inverse speed is time dependent and is

$$\langle\frac{1}{v}\rangle = \int_{v_{min}}^{v_{esc}}\frac{f(v)}{v}\mathrm{d}^3v, \tag{2.17}$$

where $v_{min} = \sqrt{\frac{M_T E_R}{2\mu^2}}$ is the minimum WIMP velocity that can lead to a recoil energy E_R, v_{esc} is the velocity for WIMP to escape the Milky way, and $f(\boldsymbol{v},\mathrm{t})$ is the time-dependent distribution of WIMP velocity relative to the detector. The WIMP velocity distribution is expressed as the Maxwell-Boltzmann velocity distribution in the galactic rest frame by assuming that smooth and virialised components dominate the dark matter halo near the Sun (Standard Halo Model). This

is

$$f_{gal}(\boldsymbol{u}) = \begin{cases} \frac{1}{N_{esc}}(\frac{3}{2\pi\sigma_v^2})^{3/2}\exp(\frac{-3\boldsymbol{u}^2}{2\sigma_v^2}), & \text{for } \mid \boldsymbol{u} \mid < v_{esc} \\ 0, & \text{otherwise} \end{cases}, \tag{2.18}$$

where N_{esc} is a normalization factor, and $\sigma_v = \sqrt{3/2}v_c$ is the velocity dispersion related to the local circular speed, i.e. the speed of Sun to the galactic rest frame ($v_c = 220\,\mathrm{km/s}$). The distribution has to be in the detector reference frame for computing the event rate, which means

$$f(\boldsymbol{v}) = f_{gal}(\boldsymbol{v}_{obs} + \boldsymbol{v}), \tag{2.19}$$

with $\boldsymbol{v}_{obs}$ being the earth's velocity with respect to the Galaxy. The velocity is

$$\boldsymbol{v}_{obs}(t) \approx \boldsymbol{v}_{\odot} + b\boldsymbol{v}_{\oplus}\cos(\omega(t - t_c)),$$

where $v_{\odot} = 237.8\,\mathrm{km/s}$ is the motion of the Sun relative to the stationary halo, $v_{\oplus} = 29\,\mathrm{km/s}$ is the motion of the earth relative to the sun, $b = 0.49$ is a geometrical factor, and $t_c = 0.415\,\mathrm{year}$ (2nd June) is the characteristic time when v_{obs} is maximum [45].

The second term of equation 2.15 requires input from particle physics for the WIMP-nucleus scattering. The canonical WIMP candidate for the elastic scattering interaction in direct detection experiments is inspired by models of supersymmetric dark matter, in particular, the neutralino. The model assumes interactions are mediated by heavy particles such as Z bosons for axial-vector (spin-dependent) interaction and Higgs boson for scalar (spin-independent) interaction in the non-relativistic limit [39]. Thus, the scattering cross-section term can be expressed

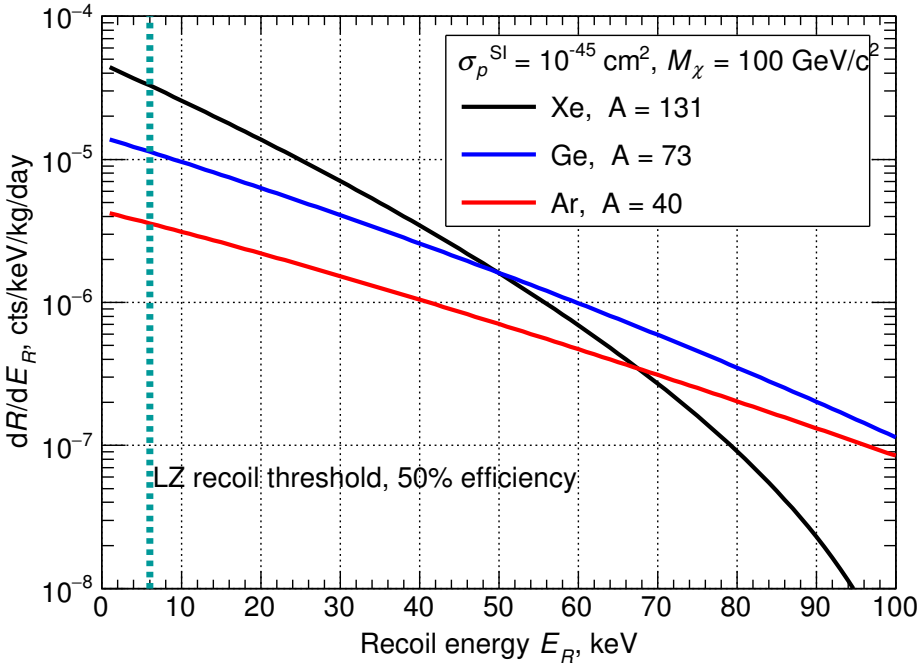


Figure 2.9: Expected differential event rate with different targets. We assume a 100 % detection efficiency and use the parameters of the Standard Halo Model in Ref. [45] to calculate the rate. The dashed cyan line is the projected LZ detector threshold of 6 keV$_{nr}$.

as

$$\frac{\sigma_\chi(q)}{2\mu^2} = \frac{1}{2\mu^2}[\sigma_0^{SD}F_{SD}^2(q) + \sigma_0^{SI}F_{SI}^2(q)], \tag{2.20}$$

which comprises cross-section $\sigma_0^{SD,\ SI}$ and form factor $F_{SD,\ SI}(q)$ terms from both spin-dependent (SD) and spin-independent (SI) scatters. In the case of SD scattering, the cross-section and the form factor terms are combined to be

$$\sigma^{SD} = \frac{32G_F\mu^2}{\pi}\frac{J+1}{J}[\langle S_n\rangle a_n + \langle S_p\rangle a_p]^2, \tag{2.21}$$

which G_F is the Fermi constant, J is the total spin of a target nucleus, $\langle S_{n,p}\rangle$ is the average spin contributions from the neutron or neutron groups, and $a_{n,p}$ is the coupling constant to neutrons or protons. As for the case of SI scatterings, the

cross-section contribution is

$$\sigma_0^{SI} = \sigma_p^{SI} A^2 (\frac{\mu}{\mu_p})^2, \tag{2.22}$$

where μ_p is the WIMP-proton reduced mass, and $\sigma_p^{SI} = \frac{4\mu_p^2}{\pi}(f_p)^2$ is the WIMP-proton cross section (f_p is the coupling of the WIMP with point-like protons). The σ_p^{SI} allows comparison with collider searches and between detection experiments using different target nuclei. The nuclear form factor F_{SI} comes from considering a scatter of a WIMP with a nucleus of a Gaussian softened solid sphere in Born approximation. This gives a Fourier transform of the mass distribution of the target nucleus. An accurate approximation of F_{SI} is the Helm form factor:

$$F_{SI}(q) = 3\exp(-q^2 s^2/2)\frac{\sin(qr) - qr\ \cos(qr)}{(qr)^3}, \tag{2.23}$$

where $s = 1\,\text{fm}$ is a measure of the nuclear skin thickness, and $r \sim A^{1/3}\,\text{fm}$ is the effective nuclear radius. In summary, the result of the cross-section terms suggests that nuclei with larger total spin J contribute more to the SD interaction cross-section; heavier nuclei, because of the A^2 enhancement, are more favourable for SI interaction searches. Although, the overall scattering rate for SD scattering as discussed in Ref. [39, 46] does not grow as rapidly as that for SI scattering, the SD scattering is a potential channel to understand the nature of dark matter. Studies on the SD channel can be found in Ref. [47, 48]. The rest of the discussion of this thesis will focus on the SI scattering.

Finally, by combining the ingredients from astrophysics and particle physics,

the differential event rate is

$$\frac{\mathrm{d}R}{\mathrm{d}E_R} = \varepsilon(E_R) \cdot \frac{\sigma_p^{SI}}{2\mu_p^2} A^2 F_{SI}^2(q) \cdot \frac{\rho_\chi}{M_\chi} \int_{v_{min}}^{v_{esc}} \frac{1}{N_{esc}} (\frac{3}{2\pi\sigma_v^2})^{3/2} \exp(\frac{-3(\boldsymbol{v}_{obs} + \boldsymbol{v})^2}{2\sigma_v^2}) \frac{1}{v} \mathrm{d}v^3, \tag{2.24}$$

which has been solved by many authors [40, 45]. The terms in equation 2.24 have different physical implications for direct detection experiments. Firstly, the A^2 suggests that experiments using heavier target nuclei can increase the rate considerably. Secondly, the nuclear form factor term $F_{SI}(q)$ suppresses the rate within a given WIMP mass. It is, however, more important for detecting heavier WIMPs because of their larger momentum transfer q. Thirdly, the v_{obs} parameter suggests that the differential rate can have an annual modulation signature, which is caused by the relative speed of the Earth to the Sun. This implies that the detected rate is higher in June and smaller in December. Fourthly, because of the exponential drop-off of the velocity distribution term, the recoil spectrum is forced to fall off exponentially. The drop also means that the largest contribution to the rate is at low recoil energies. An example of the differential event rate with different target nuclei is shown in 2.9. Because of the A^2 enhancement, xenon is the most sensitive detector target at low recoil energies for $M_\chi = 20 \sim 100\,\mathrm{GeV/c^2}$. It is, however, less sensitivity to lighter WIMPs, owing to the rapid decrease of transferred momentum q in $F_{SI}(q)$ that leads to larger suppression. Thus, for lighter WIMP direct detection searches, lighter target nuclei are more favourable.

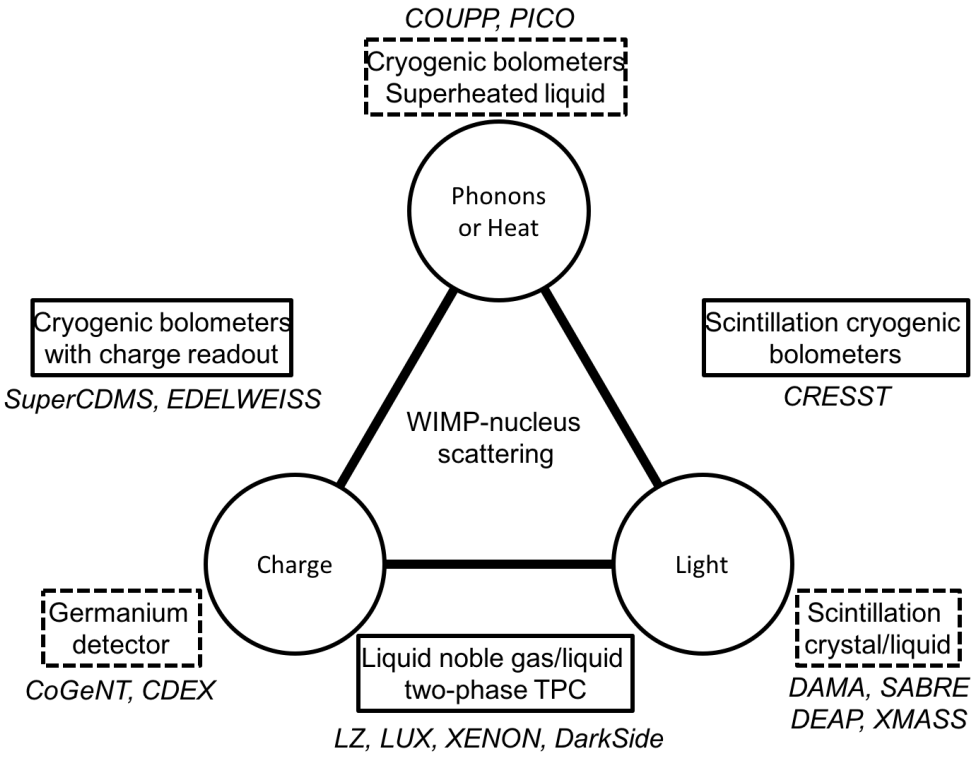


Figure 2.10: Experimental techniques in direct detection experiments. Dashed boxes indicate techniques using only one signal channel. Solid boxes suggest techniques using two signal channels. Words in italic are examples of experiments using the techniques in the rectangles near them.

2.4.2 Direct detection experiments

When direct detection experiments are built for detecting WIMP-nucleus elastic scattering signal, there are three general rules to consider. Firstly, because of the higher differential cross section at lower recoil energy, a detector needs to have a low energy threshold for small recoils at keV level. Secondly, because a background scattering event from neutrons (nuclear recoil, NR) or $\alpha/\beta/\gamma$ (electronic recoil, ER) could mimic a WIMP recoil event (NR like), a detector needs to be low background to increase its signal significance or have the ability to perform NR/ER discrimination. Thirdly, because the expected WIMP event rate is proportional to the exposure of a target medium, a detector needs to achieve a large detector mass and a stable performance over time scales of a few years.

These general rules lead to a wealth of detection techniques in the field. When a WIMP scatters off a detector nucleus, its energy deposition could result in three distinct channels: light, charge, and heat/phonon. Detection experiments utilising one or two of these channels for the search are summarised in figure 2.10.

The light channel refers to the detection of scintillation photons, emitted from a scintillator when recoil energy is deposited in it. For single channel detectors, a notable example is the DAMA experiment which uses ultra low-radioactive NaI (Tl) crystals. The experiment, although it cannot reject backgrounds via NR/ER discrimination, has reported a 1.33 ton$\times$y exposure and observed an annual modulated single-hit rate in the range of $2-6\,\mathrm{keV}$ with 9.3 significance over 14 annual cycles [49]. Its result, however, is in tension with other measurements which do not observe a similar modulated single-hit rate [50, 51].

The charge channel refers to detecting ionisation in a target medium which produces ions and electrons that can be collected with an applied electric field. For example, detectors, such as CoGeNT and CDEX, are using germanium crystals that contain such a channel with a low threshold down to $\sim 0.5\,\mathrm{keV}$ for searches of low-mass WIMPs at sub-GeV/c^2 level [52, 53]. The dead layer at the surface of the crystal gives different rise time between the surface signal (background like) and the bulk signal (WIMP-like). However, even though a background/bulk event separation is achieved, discrimination between ER and NR is not possible.

The heat or phonon channel is a result of an energy deposition in a target which leads to bubble formation in a superheated liquid through phase transition or athermal phonon production in a crystal at mK temperature. In the case of a superheated liquid detector, e.g. PICO, the bubbles from C_3F_8 can be detected

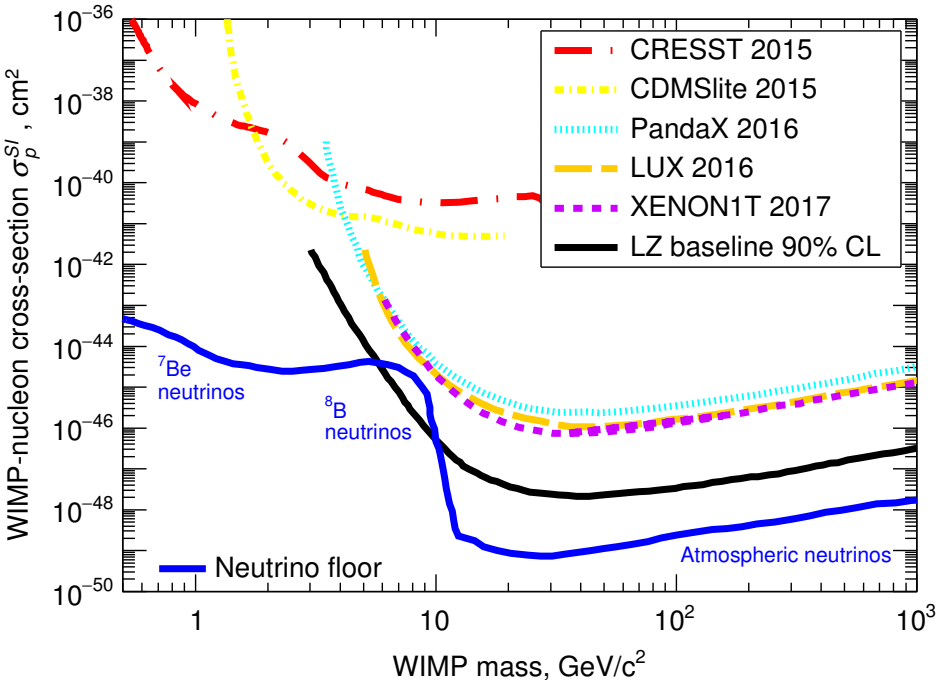


Figure 2.11: The exclusion limits of some of the most sensitive direct detection experiments as of writing. The experiments exclude the area above the limits of the dashed lines. The future tonne scale xenon TPC will reach a "neutrino floor" from solar neutrinos which will coherently scatter off a target nucleus and result in several background events.

with CMOS cameras and acoustic sensors. The PICO detector has excellent background rejection efficiency ($\sim 99.6\,\%$) because it's insensitive to most backgrounds from γ, e, and β and can reject α particles through the acoustic sensors (sound of the bubbles) [47]. The detector, although less sensitive to spin-independent scattering owing to low A^2 enhancement, is competitive in spin-dependent scattering searches because C_3F_8 has a larger contribution to the spin coupling than, for example, xenon. As for the case of cryogenic detectors using the phonon channel, they usually exploit an additional channel from either the scintillation or the charge signal to achieve NR/ER discrimination. For instance, the SuperCDMS and the EDELWEISS detectors have a similar approach in using germanium or silicon bolometers to readout ionisation signals with an applied electric field and

temperature signals with phonon sensors [54, 55]. Another example, the CRESST detector, uses a scintillation signal emitted by recoils in $CaWO_4$ crystals in addition to the phonon channel [56]. These detectors, although having crystals with limited sizes ($\sim$ 1 kg) and smaller atomic mass, achieve low energy threshold at sub-keV and are most sensitive in searching for low-mass WIMPs at sub-GeV level.

Lastly, the detectors using both charge and light channels, in particular, two-phase xenon time projection chambers (TPC), have been shown to be very sensitive in probing WIMP mass between $10 \sim 1000\,\mathrm{GeV/c^2}$ (see figure 2.11). The detectors offer advantages of low energy threshold at few keV, NR/ER rejection using a parameter space with both light/charge channels, and a homogeneous target with long exposure (ton $\times$ year). Experiments, e.g. LUX, XENON1T, and PandaX as of 2017, exploiting such technology have set some of the most stringent limits on the direct detection search of WIMP [57–59]. The physics behind this technology, which is applied to a multi-tonne scale detector - LUX-ZEPLIN (LZ), will be discussed in detail in Chapter 3.

Chapter 3

Detection with Two-phase Xenon TPC

A two-phase TPC with a massive liquid xenon (LXe) volume is one of the logical next steps in the direct detection of WIMPs with mass larger than 10 GeV/c^2 [60–62]. In this chapter, the motivation of using xenon as a target for dark matter detection will be addressed. The particle interactions, as well as their energy partitioning in the two-phase TPC, will be explained. The physics which results in the observed signals in a detector will be thoroughly described. Finally, the implementation of such a two-phase TPC system in the LUX-ZEPLIN (LZ) experiment will be discussed, in particular, its TPC, its circulation system, its veto system, and its calibration plan.

3.1 Two-Phase Xenon TPC

3.1.1 Why Xenon?

Liquid xenon (LXe) has been recognised as a very attractive detector medium for WIMP direct detection. The projected WIMP event rate in equation 2.15 depends on the amount of exposure (mass×time) and the threshold of the recoil energy (keV scale). LXe has shown to be both highly scalable and sensitive to small energy recoil (single photon and single electron detection). Therefore, it is used in many competitive experiments to search for WIMPs [57–59]. Here, key properties of xenon which make it an appealing target medium are summarised:

- Xenon has relatively high atomic mass ($M_{Xe} \approx 126\,\mathrm{GeV/c^2}$) which provides a good kinetic match to a WIMP mass of $\mathcal{O}(100\,\mathrm{GeV/c^2})$. The match suggests xenon could detect a large spin-independent scattering near the WIMP mass scale predicted by the freeze-out model. Furthermore, 50 % of the natural abundance of xenon isotopes are odd-neutron isotopes ^{131}Xe and ^{129}Xe. The abundance indicates that xenon is also sensitive to the spin-dependent interaction of WIMPs.

- The density of LXe is high ($\sim 3\,\mathrm{g/cm^3}$). This implies that background radiation such as gamma rays can be effectively shielded with LXe at the outer region of a detector which leaves the bulk volume of the liquid quiet (self-shielding) [63, 64]. Such a self-shielding property allows a larger volume of the detector to be used as fiducial volume and thus to increase the amount of exposure for WIMP search.

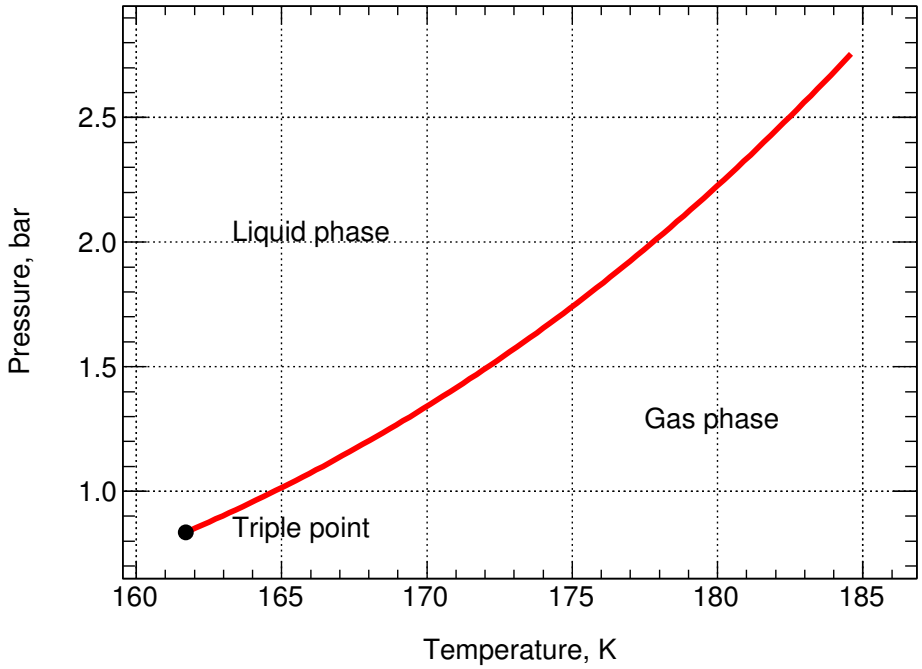


Figure 3.1: Xenon phase diagram. Data taken from NIST.

- Xenon, as a noble element with a low electronegativity, can be easily liquefied (see figure 3.1) and purified. The liquefication allows producing a large and homogeneous LXe volume to scale up the detector mass. The purification of xenon can be achieved with commercial heated getters to remove electronegative and light-absorbing impurities such as N_2 and O_2.

- Most of the naturally occurring isotopes of xenon are stable. As for radioactive isotopes of xenon, most of them are short-lived with a half-life less than a month. Thus, there is negligible internal background to overcome.

- The scintillation and ionisation of xenon provide two different channels for particle interaction discrimination. The scintillation generates photons at 178 nm wavelength which can be detected with PMTs without a wavelength shifter. The ionisation produces electrons which can be extracted and com-

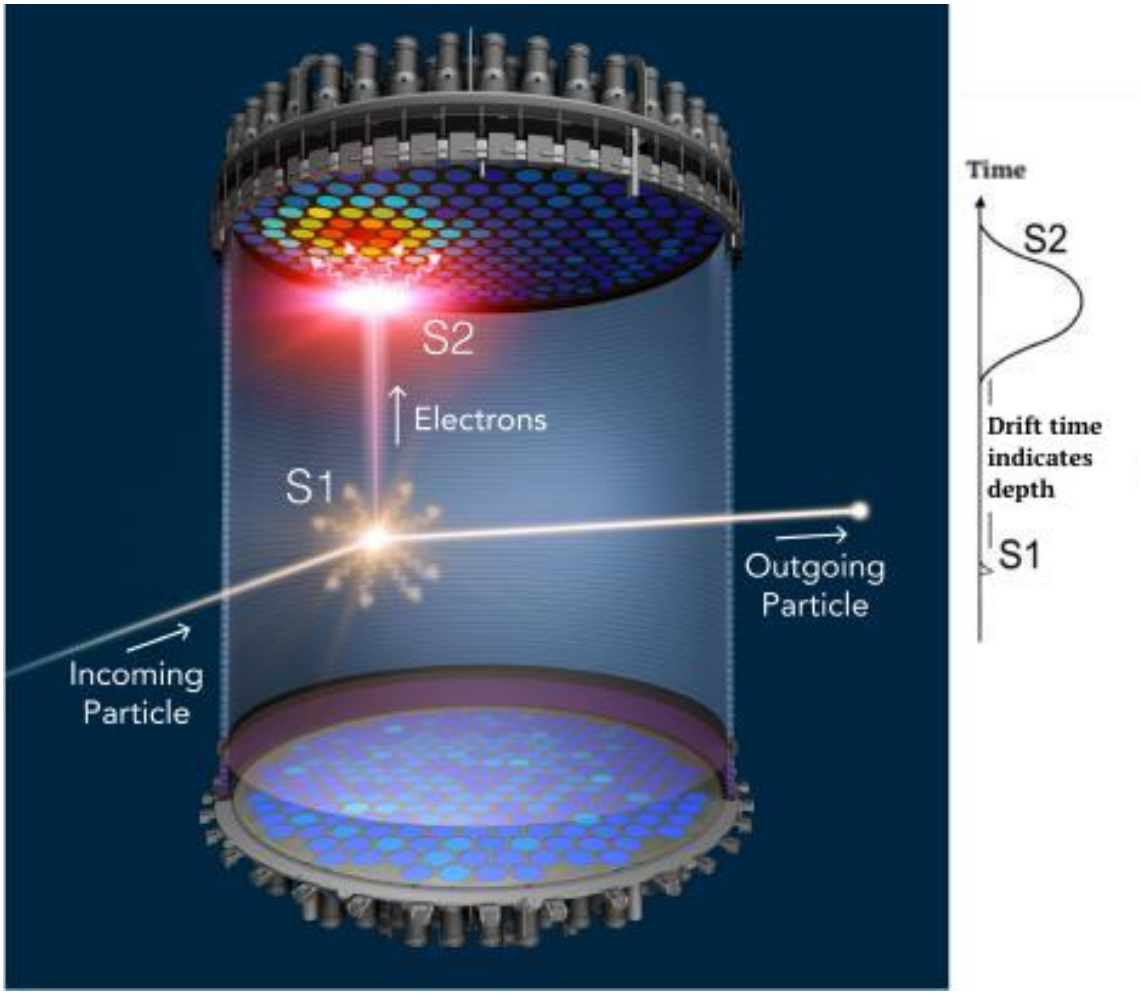


Figure 3.2: The operation principle of a two-phase xenon TPC. An incoming particle interacts with LXe (the WIMP target) and produces two signal channels: primary scintillation (S1) and ionisation via electroluminescence in the vapour phase (S2). The two channels enable event reconstruction and provide discrimination between NR and ER. Taken from [60].

pared to the scintillation channel for the discrimination of interactions.

3.1.2 Particle Interaction

Particles interacting with one of the xenon atoms can deposit a traceable amount of energy which results in electronic recoils (ER) or nuclear recoils (NR). The ER relates to interactions between xenon atoms and photons/electrons, for example, resulting from compton scatters, beta and conversion electrons, and atomic de-excitation of x-ray fluorescence and Auger electrons. The NR relates to interac-

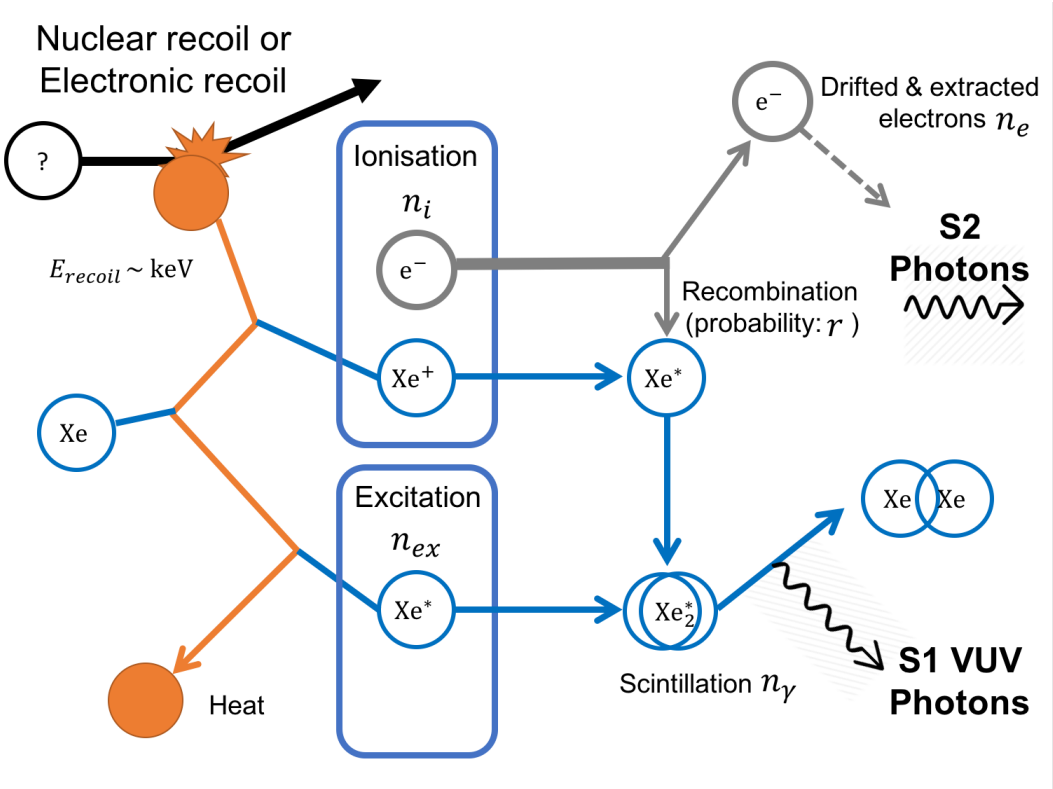


Figure 3.3: Micro-physics of the S1 and S2 production in xenon. The orange track represents a neutron from a nuclear recoil, or an electron ejected from a xenon nucleus from an electronic recoil. A scattering would produce excited or ionised atoms. The quanta of the ionisation and the excitation are denoted as n_i and n_{ex}. Part of the n_i will contribute to the S1 signal which gives the scintillation quantum, n_γ. The rest of the n_i will be extracted to produce S2 photons which give the electron quantum n_e.

tions of xenon atoms with neutral particles from processes such as WIMP-nucleus scattering, neutron scatters from elastic/inelastic scattering, and neutrino-nucleus coherent scatters.

A diagram explaining the microphysics of NR and ER interactions from a single scattering in a two-phase xenon experiment is shown in figure 3.2. Another diagram (figure 3.3) illustrates the associated micro-physics of light production in xenon.

Energy loss of xenon atoms in NR or ER could result in tracks with electrons, ions, and excited atoms. The relaxation of excited atoms and the recombination of

ionised atoms with electrons produce prompt scintillation that may propagate to PMTs (S1). Electrons, which are removed from the primary tracks because of an applied electric field (drifted field), drifts upward in the bulk LXe volume. As the drifted electrons reach the liquid surface of LXe, where an even stronger electric field (extraction field) is applied, the electrons are accelerated and extracted to the gas xenon (GXe). The extracted electrons, accelerated by the extraction field to sufficient energies, excite xenon atoms in the vapour phase. The excited gas atoms then relax and produce secondary light (S2) via the electroluminescence process (EL), which is detected by PMTs. The S2 signal will lead to a concentrated hit pattern on several PMTs around the location of the extraction electrons. The pattern can be used to reconstruct the X-Y position of the interaction in the horizontal plane of the TPC. The time difference between the S2 and the S1 signal corresponds to the drift time of the drifted electron and hence gives the depth of the interaction. Then, the three-dimensional vertex reconstruction by the S2 and S1 allows definition of the fiducial volumes of the TPC. The non-figucial volume mostly contains background interactions from radioactive materials; the fiducial volume mostly contains single scattering events for WIMP search. Such reconstruction methods also enable rejection of multiple scattering from neutrons and gamma rays.

3.1.3 Energy Partitioning

Energy depositions that result from the two interactions mechanism, as described in section 3.1.2, gives two distinct observed energy scales in a two-phase TPC,

keVee and keVnr, respectively. The deposition can be expressed as

$$\begin{aligned} E_{dep} &= \frac{\mathcal{W}}{\mathcal{L}} n_q \\ &= \frac{\mathcal{W}}{\mathcal{L}} (n_{ex} + n_i), \end{aligned} \tag{3.1}$$

where $n_q = n_{ex} + n_i$ is the total number of quanta produced in an interaction, $\mathcal{L}$ is the quenching factor depending on the type of interactions, and $\mathcal{W} = 13.7 \pm 0.2\,\mathrm{eV}$ is the average energy needed to produce excited or ionised atoms [65]. The total number of quanta is related to the actual energy deposition, an thus S1 and S2 are anti-correlated. Thus, the number of excitons n_{ex} and ions n_i produced can be translated to the number of photons n_γ and electrons n_e observed in a detector. They are written as

$$n_\gamma = (\frac{n_{ex}}{n_i} + r) n_i, \tag{3.2}$$

and

$$n_e = (1 - r) n_i \tag{3.3}$$

and where r is the probability of ions that recombine with electrons to form excitons. The electron and photon quanta directly relate to the S1 and S2 signals in a two-phase xenon TPC. Hence, the expression for energy reconstruction is

$$\begin{aligned} E_{dep} &= \frac{\mathcal{W}}{\mathcal{L}} (n_\gamma + n_e) \\ &= \frac{\mathcal{W}}{\mathcal{L}} (\frac{S1}{g1} + \frac{S2}{g2}), \end{aligned} \tag{3.4}$$

where $S1$ and $S2$ are in units of detected photons (phd), g_1 and g_2 are in units of detected photons per quantum. g_1 is the photon detection efficiency (PDE) α_1 in

liquid for $S1$ which is a product of the average PMT quantum efficiency and the average light collection efficiency of a TPC. g_2 is the electron detection efficiency for S2 which is a product of the PDE in gas α_2, the electron extraction efficiency κ, and the average single electron pulse size in phd. The g_1 and g_2 factors are detector dependent and would change if a detector's operation condition changes.

In the electronic recoil, the interaction track length is long ($\sim \mu$m) and about 5 % of the energy deposition is lost to heat [65–67]. Thus, the quenching factor $\mathcal{L}$ is negligible and treated as unity [68]. Also, the ratio of excitons and ions $n_{ex}/n_i = 0.2$ is constant and consistent within uncertainties of the most recent measurements [69].

As for the nuclear recoil, the interaction track length is shorter than that of ER at $\sim$ nm scale; a larger amount of the deposited energy is lost to heat which gives $\mathcal{L} \neq 1$ [65]. Thus, the energy deposition of NR is similar to ER but with the consideration of the quenching factor. The factor is traditionally given by the Lindhard model [70, 71]. It is described by

$$\mathcal{L} = \frac{kg(\epsilon)}{1 + kg(\epsilon)}, \tag{3.5}$$

where k is a proportionality constant between electronic stopping power and the velocity of the recoiling nucleus, $g(\epsilon)$ is proportional to the ratio of electronic stopping power to nuclear stooping power, and ϵ is the dimensionless quantity related to a recoil energy. The model, however, disagrees with measurements at energies $>$ 10 keVnr [72]. This is due to biexcitonic effects with two excitons (xenon excimers: Xe_2^*+Xe_2^*), instead of direct de-excitations to emit VUV photons (discussed in section 3.1.4), that can interact to produce only one photon, or one

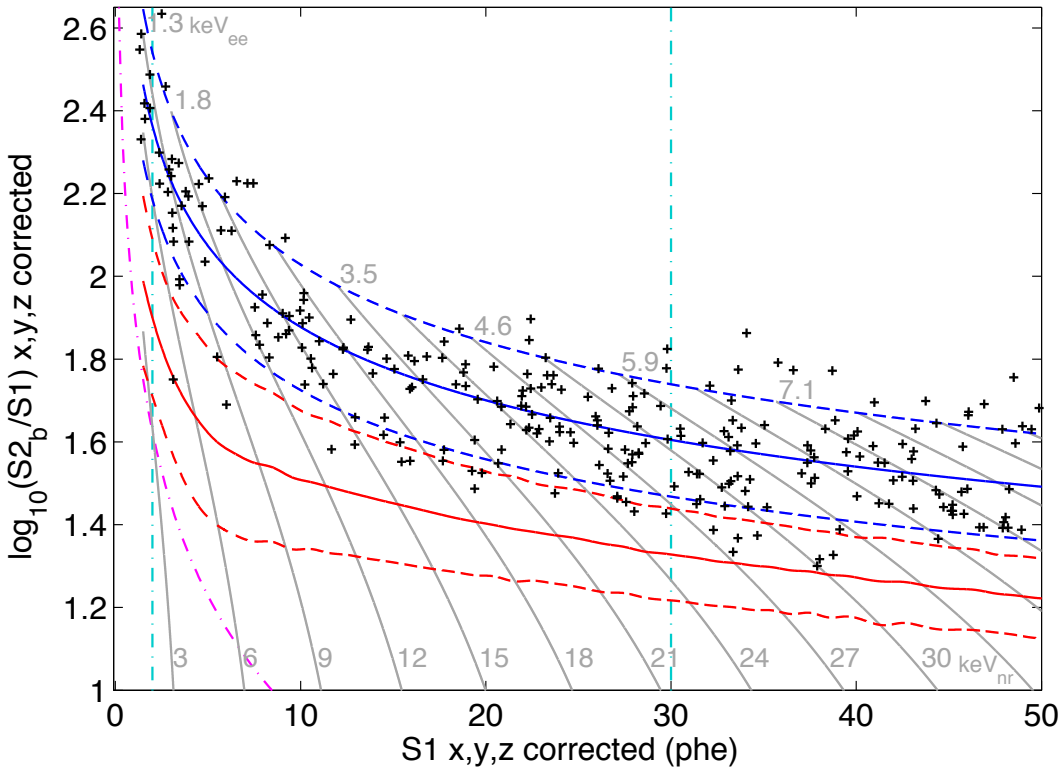


Figure 3.4: $\log_{10}(S2/S1)$ vs $S1$ parameter space for WIMP search. The red band is the expected NR band; the blue band is the expected ER band. Taken from [75].

photon and one electron [73, 74].

The distinct energy partition between ER and NR signals results in different $(S2/S1)$ ratios, with

$$(\frac{S2}{S1})_{\mathrm{NR}} < (\frac{S2}{S1})_{\mathrm{ER}}. \tag{3.6}$$

This leads to the use of a standard parameter space for plotting the discrimination between NR and ER events, $\log_{10}(S2/S1)$ vs $S1$ (see figure 3.4). The fraction of ER events that lie below the medium of NR band in such a plot can quantify the level of discrimination which a > 99.5 % rejection of ER interactions has been achieved [76, 77].

3.1.4 Primary Scintillation (S1)

The scintillation light from the S1 signal, induced by a particle interaction, consists of two channels of mechanism: excitation and ionisation. In general, both mechanisms end up producing xenon excimers Xe_2^* which result in the VUV emission of photons with a wavelength of $\lambda_{liq} \sim 178$ nm and a spectral width of $\Delta\lambda_{liq} \sim 14$ nm [78]. The excitation mechanism is as follows

$$\begin{aligned} e^- + \mathrm{Xe} &\rightarrow \mathrm{Xe}^* + e^- && \text{impact excitation} \\ \mathrm{Xe}^* + \mathrm{Xe} &\rightarrow \mathrm{Xe}_2^{*,\nu} && \text{excimer formation} \\ \mathrm{Xe}_2^{*,\nu} + \mathrm{Xe} &\rightarrow \mathrm{Xe}_2^* + \mathrm{Xe} && \text{relaxation} \\ \mathrm{Xe}_2^* &\rightarrow \mathrm{Xe} + \mathrm{Xe} + \mathrm{h}\nu && \text{VUV emmision.} \end{aligned} \tag{3.7}$$

The impact excitation generates excited xenon atoms Xe^* which further leads to the formation of a dimer $Xe_2^{*,\nu}$ with vibrational excitation. The relaxation of the dimer produces excimers Xe_2^* which, when returning to the ground state Xe atom, emits VUV photons. Also, the dimer $Xe_2^{*,\nu}$ comprises two lowest electronic states: one singlet and one triplet. The de-excitation of the states results in two decay time constants, $\tau_1 = 2.2\,\mathrm{ns}$ for the singlet state and $\tau_3 = 27\,\mathrm{ns}$ for triplet state [79].

The other mechanism, ionisation, is as follows

$$
\begin{aligned}
e^- + \mathrm{Xe} &\rightarrow \mathrm{X}e^+ + 2e^- && \text{impact ionisation} \\
\mathrm{X}e^+ + \mathrm{Xe} + \mathrm{Xe} &\rightarrow \mathrm{X}e_2^+ + \mathrm{Xe} && \\
\mathrm{e} + \mathrm{X}e_2^+ &\rightarrow \mathrm{X}e^{**} + \mathrm{Xe} && \text{recombination} \\
\mathrm{X}e^{**} + \mathrm{Xe} &\rightarrow \mathrm{X}e^* + \mathrm{Xe} + \mathrm{heat} && \\
\mathrm{X}e^* + \mathrm{Xe} + \mathrm{Xe} &\rightarrow \mathrm{X}e_2^* + \mathrm{Xe} + \mathrm{heat} && \text{excimer formation} \\
\mathrm{X}e_2^* &\rightarrow \mathrm{Xe} + \mathrm{Xe} + \mathrm{heat} && \text{VUV emission.}
\end{aligned} \tag{3.8}
$$

The impact ionisation produces xenon ions and electrons. After picoseconds of the ionisation, the recombination process occurs to combine dia-atomic xenon ions and neighbouring electrons. The de-excitation of the excimer, formed after recombination, is similar to the excitation channel and emits VUV photons. However, the relative population of singlet and triplet states in the ionisation channel is not necessarily the same as that in the excitation channel. Also, the recombination process can introduce a time delay to the excimer formation. Thus, the decay time constant $\tau_R \approx 45\,\mathrm{ns}$ of the channel is slightly longer than $\tau_{1,3}$ [80].

Both channels contribute to the observed primary scintillation (S1) in two-phase TPCs. The S1 shape is determined by the decay time constant. However, because all two-phase TPCs have applied electric fields for extracting electrons from the interaction, the recombination is suppressed and the decay time constant of S1 (τ_{S1}) tends to be smaller than τ_R but larger than τ_3 (for example, LUX observed $\tau_{S1} \approx 30\,\mathrm{ns}$ [81]). Furthermore, xenon is transparent to the propagation of its own scintillation light. This corresponds to the VUV photon energy which

is smaller than the threshold of the ionisation channel ($\sim 12.1\,\mathrm{eV}$). Although the photons can still be attenuated by impurities, such attenuation can be mitigated through LXe purification so that an absorption length λ_{obs} larger than the height and the diameter of a TPC can be achieved (e.g. LZ baseline $\lambda_{obs} = 30\,\mathrm{m}$) [60].

3.1.5 Electron Transportation

Once the ionisation electrons are extracted from an interaction site, they are drifted by an applied electric field E_d in the drift region. Such drifting delays the extraction of electrons at the liquid surface relative to the S1 signal at the microsecond level. For instance, if the $E_d = 310\,\mathrm{V/cm}$ in a TPC, with a drift length of $z_{TPC} = 1.456\,\mathrm{m}$, the expected LXe drift velocity $v_d = 1.8\,\mathrm{mm}/\mu\mathrm{s}$ leads to a maximum drift time t_d of $\sim 809\,\mu\mathrm{s}$ from the cathode.

The drifted ionisation electrons experience both transverse and longitudinal diffusion. The diffusion leads to an ellipsoidal electron cloud with its axis along the direction of the drift field. The width of diffusion can be characterised as

$$\begin{aligned} \sigma_{T,L} &= \sqrt{2D_{T,L}t_d} \\ &= \sqrt{2D_{T,L}z_{TPC}/v_d}, \end{aligned} \tag{3.9}$$

where D_T and D_L are the transverse and longitudinal diffusion coefficients, respectively. Measurement of the coefficients under an $E_d = 0.5 \sim 1.2\,\mathrm{kV/cm}$ give $D_T = 30 \pm 5\,\mathrm{cm^2/s}$ [82] and $D_L = 12 \pm 1\,\mathrm{cm^2/s}$ [83]. This suggest an ionisation point source is smeared by $\sim$ 1 mm over a 1 m drift length. However, the transverse diffusion has no first-order effects on the shape of the S2 width and is

smaller than the position resolution of a typical TPCs [84]. Interestingly, because the longitudinal diffusion elongates the electron cloud, although it is smaller than the transverse diffusion, it affects the S2 width [85] (see section 3.1.6).

In addition to the diffusion effects, the drifted electrons are affected by electronegative impurities such as O_2, H_2O, and N_2O. The impurities attenuate the number of electrons arriving at the liquid surface from an interaction site. Such effect can be parametrised as

$$N(t) = N_0 \exp(-t/\tau_e), \tag{3.10}$$

where N_0 is the number of electrons initially drifted at the interaction site, $N(t)$ is the number of surviving electrons after a drift time t, and τ_e is the electron lifetime. Thus, ideally, to have a minimum loss of electrons, the required electron life time should be larger than the maximum drift time of a TPC.

3.1.6 Secondary Scintillation (S2)

Drifted ionisation electrons from the LXe volume can overcome the potential barrier at the phase boundary of liquid surface and be extracted if an sufficiently high electric field is applied near the surface [88, 89]. Typically, free electrons confined by the Schottky barrier near the liquid surface are energetically more likely to stay in LXe when there is no electric field present. At a few tens of V/cm of applied electric field, thermal equilibrium between the electrons and the liquid is broken, and the mean electron energy starts to increase. The electric field not only increases mean electron energy but also reduces the potential barrier height at the liquid-gas interface ($\sim 1\,\mathrm{eV}$ in LXe) [88, 90]. However, many accelerated

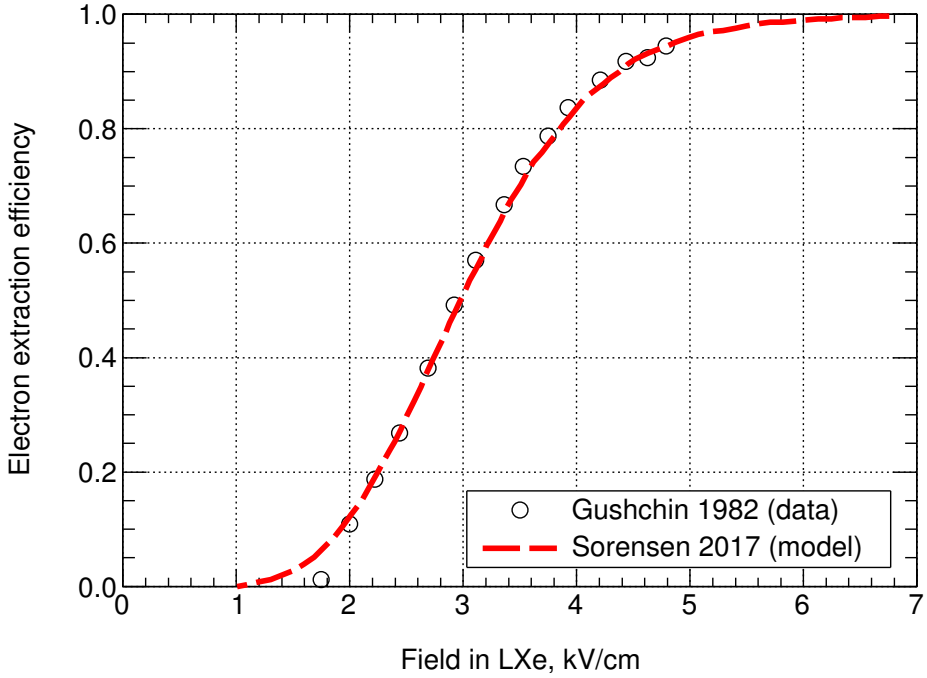


Figure 3.5: Electron extraction efficiency in two-phase xenon TPC. Absolute measurement data of the effeciency from [86]; model of equation 3.11 from [87].

electrons do not overcome the boundary in their initial attempt but reflect back to the bulk of the liquid. After a number of scatters, because of the applied field, they will return to the liquid surface and reattempt. This can be described by the cumulative probability of electron emission efficiency (EEE) relating to the extraction field in LXe E_e after n attempts shown in figure 3.5 as

$$\kappa_n(E_e) = 1 - (1 - \kappa(E_e))^n, \tag{3.11}$$

where $\kappa(E_e)$ is the probability of electron emission for a single attempt [87]. It is estimated that the mean number of reattempts of the electrons to cross the boundary is around 20 ± 4. The configuration of EEE in a TPC will effectively influence its electron detection efficiency $g2$ (discussed in section 3.1.3). Thus, it is natural to pursue a higher E_e to achieve a higher EEE, e.g. the LZ baseline

$E_e = 5.2\,\mathrm{kV/cm}$ in LXe gives EEE of 97.6 %.

The electrons extracted from the emission process described above will be further accelerated due to a higher E_e in GXe ($E_{e-liq} = E_{e-gas}/\varepsilon_{liq}$) and reach higher energies. The electrons have random walk trajectories which are slightly biased by the electric field E_{e-gas} and collide with xenon atoms to produce electroluminescence (EL) light (or commonly known as secondary scintillation (S2)). The scintillation through EL in GXe, arose from a similar mechanism described in section 3.1.4, has again a mix of the two lowest excitation states but with the excimer energy level slightly higher than that in LXe. This difference lead to the scintillation wavelength of $\lambda_{gas} \sim 171$ nm and the spectral width of $\Delta\lambda_{gas} \sim 12$ nm [91].

The S2 yield and width both highly depend on the electric field in gas. The correlation is shown in figure 3.6. The scintillation yield, which is proportional to the applied field E_{e-gas}, the TPC pressure P_{TPC}, and the gas gap x_{gap} between anode and gate of a TPC, can be expressed as

$$\frac{\mathrm{d}N_{ph}}{\mathrm{d}x_{gap}} = \alpha E_{e-gas}(x) - \beta P_{TPC} - \gamma \qquad [\mathrm{photons}\cdot e^{-1}\cdot\mathrm{cm}] \tag{3.12}$$

where $\alpha = 0.137\,\mathrm{V}^{-1}$, $\beta = 177\,\mathrm{bar}^{-1}\mathrm{cm}^{-1}$, and $\gamma = 45.7\,\mathrm{cm}^{-1}$ are empirical constants for xenon TPCs [90]. The equation suggests a threshold of the EL production at $E_{e-gas} \sim 4\,\mathrm{kV/cm}$ or $E_{e-liquid} \sim 2\,\mathrm{kV/cm}$. As for the S2 width, it depends on the electron drift velocity in GXe and the longitudinal diffusion of electrons in LXe. For a TPC operating with $E_{e-gas} = 5 \sim 12\,\mathrm{kV/cm}$ and $x_{gap} = 0.8\,\mathrm{cm}$, the drift velocity in gas $v_{d-gas} = 4 \sim 8\,\mathrm{mm}/\mu\mathrm{s}$ leads to S2 width at microsecond level [92]. However, the diffusion, due to the difference of electron arrival time at

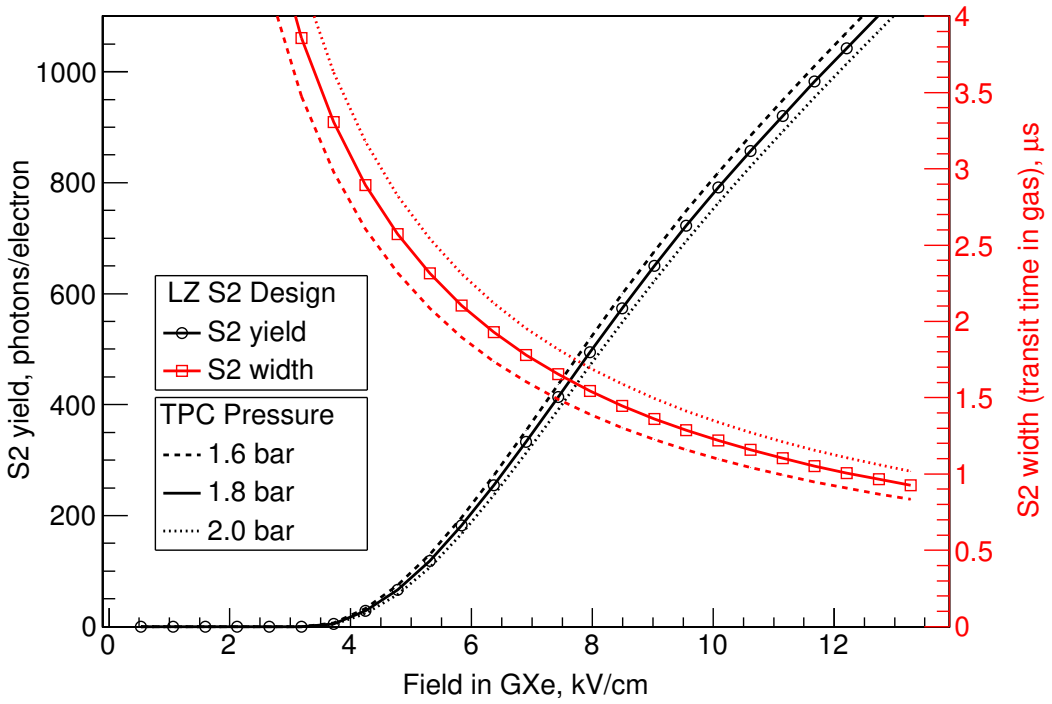


Figure 3.6: Variation of S2 gain and width with an electric field in GXe. The expected gain includes the effect from electron efficiency because it also depends on the variation of the GXe field. The S2 width only includes the effect from electron transit time in gas but not the delay time from the longitudinal diffusion in LXe. The values are calculated with LZ baseline parameters, which are $d_{anode-gate} = 1.3\,\text{cm}$ (distance between anode and gate), and $x_{gap} = 0.8\,\text{cm}$.

the liquid surface (discussed in section 3.1.5), smears the width and results in a Gaussian-shaped S2.

3.2 LUX-ZEPLIN (LZ)

The LZ detector is a two-phase LXe TPC with 7 tonnes of active LXe (5.6 tonnes of fiducial volume) which is currently under construction and will be operating at the 4,850-foot level of the Sanford Underground Facility (SURF) in Lead, South Dakota (USA) from 2020. It is a rare event experiment with a projected sensitivity of $3 \times 10^{-48}\,\text{cm}^2$ or better in probing a $40\,\text{GeV/c}^2$ WIMP under a minimum exposure of 5,600 tonne-days. An overview of the system is shown in figure 3.7.

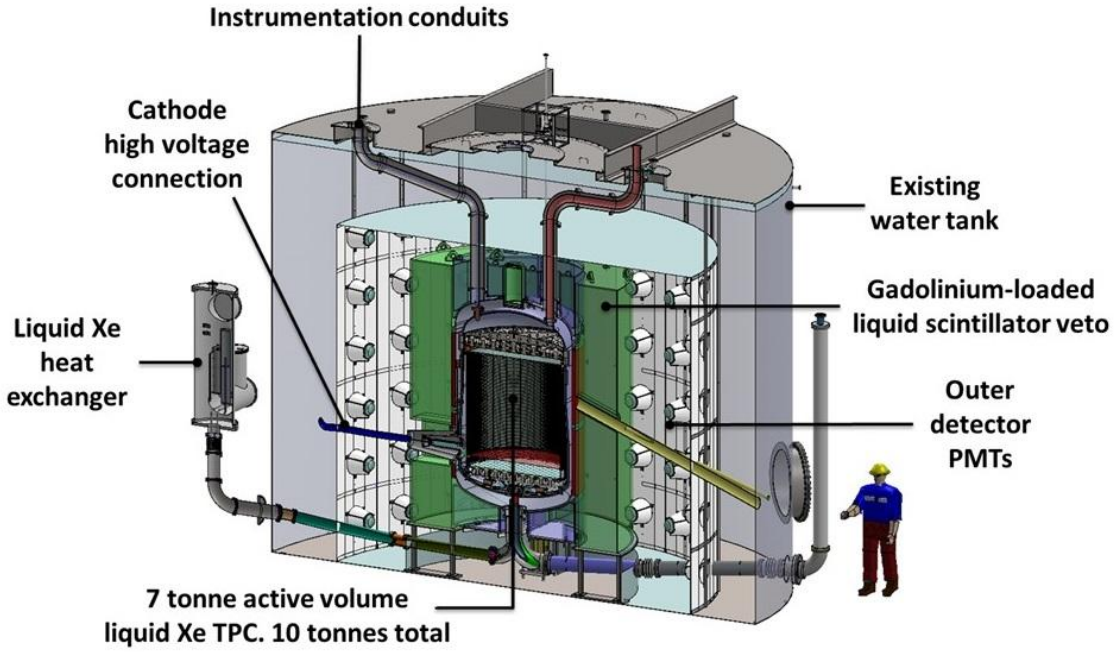


Figure 3.7: Overview of the LZ system. Taken from [60].

The main TPC, shown in the middle of the plot, is implemented with the technology discussed in section 3.1. The TPC will be connected to a recirculation system, which contains LXe heat exchangers and getters, for maintaining a high level of LXe purity. The TPC will be shielded within the outer detector, i.e. the existing water tank from LUX and a gadolinium-loaded liquid scintillator, to reduce the level of radioactive backgrounds such as neutron and gamma rays. In this section, we summarise the implementation of these detector components of the experiment. A full description of the detector system in greater detail can be found in Ref. [60].

3.2.1 Time Projection Chamber (TPC)

The LZ TPC will be housed in a cryostat, constructed from titanium and consisting of two vessels. The titanium of the vessels was selected from material, that was screened and showed the lowest radioactivity [93]. The structure of the TPC is

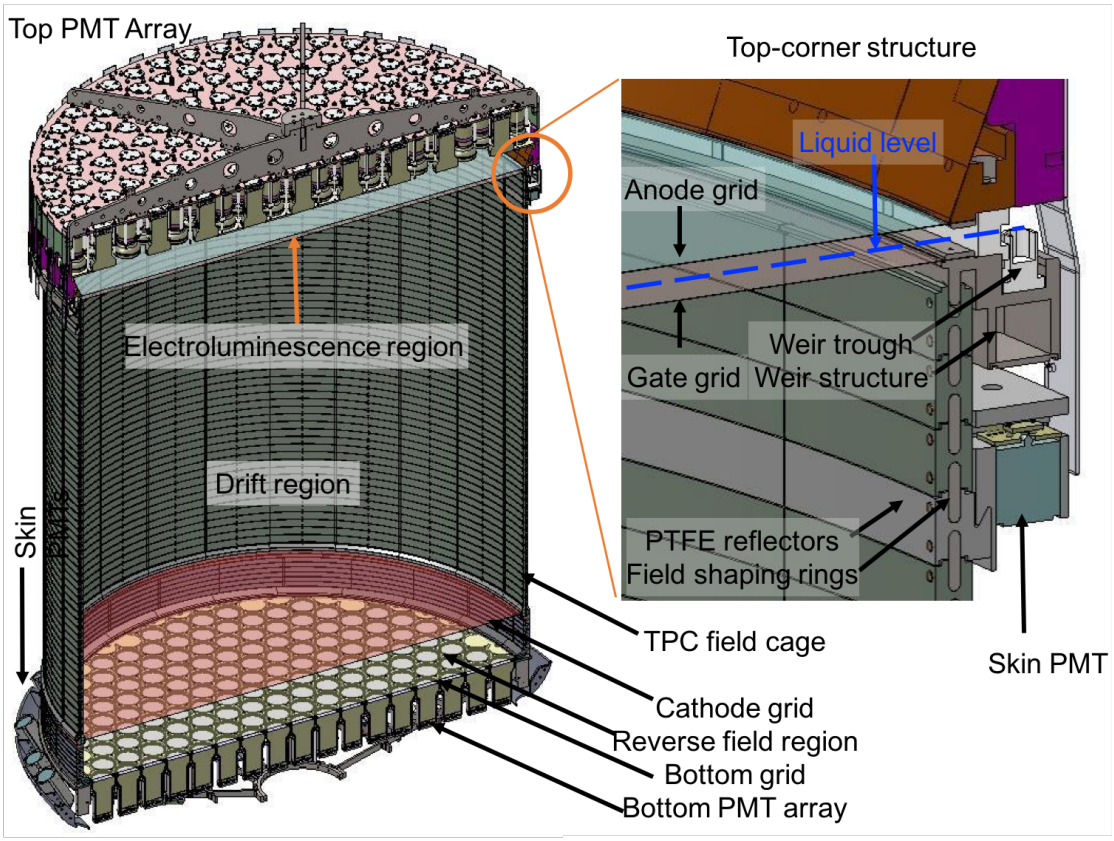


Figure 3.8: LZ TPC and top-corner region.

illustrated in figure 3.8. Two PMT arrays look at the EL region, the drift region, and the reverse field region (RFR). The design parameters of these regions are listed in table 3.1. There are also skin PMTs outside these regions to assist the veto system (discussed later in section 3.2.3) in rejecting background signals.

Drift region The drift region, with its height and inner diameter both 1456 mm, is the heart of the detector (WIMP target) where the S1 signals are produced. The region is constructed by the gate grid at the top, field shaping rings and PTFE reflector walls in the middle, and the cathode grid at the bottom. The grids are operated at ± 5.75 kV for the anode and gate and -50 kV for the cathode. The field rings are connected by pairs of 2 GΩ resistors to distribute the high voltage difference from the grids such that a drift field of 0.3 kV/cm can be formed. The

PTFE walls, which cover the resistors, have excellent reflectivity to VUV photons ($> 97\,\%$ [94]) for improving the light collection of S1 photons. The interface between the rings and the reflectors are designed such that the segmented reflectors will slide along the rings when the detector is cooled. Hence the configuration minimises the thermal contraction difference between the parts of the drift region, i.e. a reduction of the loss of LXe target volume. Because the region is crucial for S1 detection, the parts in the region, especially the reflectors and the opacity of grids, are optimised for achieving an 8.5 % of the S1 photon detection efficiency in the fiducial volume.

Extraction region The extraction region is located above the drift region and bounded by the grids of the anode and the gate. The grids with an applied voltage difference of 11.5 kV are 13 mm apart and straddle the liquid surface (5 mm above the gate). The region is responsible for the emission of drifted electrons into the vapour phase and the production of electroluminescence photons. The configuration of the region is supported by the top-corner structure (shown in figure 3.8), which is situated between the extraction region and the skin region. The structure not only supports the parallel geometry of the gate/anode grids but also handles the liquid surface level (detailed in Section 3.2.2). The variations of liquid level owing to the tilting of the TPC or the oscillation in the recirculation system are monitored precisely by precision level sensors (discussed in Chapter 4 and 6). In summary, it is challenging to design the region due to a constrained mechanical space and relatively high electric fields created by two different voltages from the gate and anode. The final design of the region regarding electric field configuration is discussed in Chapter 6.

	Baseline value	Comments
PMT		
Numbers at the top (bottom) array	253 (241)	
Average QE, %	25	
Extraction region		
Anode (Gate) voltage, kV	+5.75 (−5.75)	
Electric field in GXe (LXe), kV/cm	10.2 (5.2)	
Gate-Anode separation (and tolerance), mm	13.0 (±0.2)	
Gas gap (and tolerance), mm	8.0 (±0.2)	
Electron extraction efficiency, %	97.6	
S2 photon yield, photons/e	910	
S2 width FWHM, μs	1.0 to 2.0	Diffusion-broadend
S2 PDE (g_2), %	12	TPC centre interactions
Drift region		
Cathode voltage, kV	-50	
Drift field, kV/cm	0.31	Gate at -5.5 kV
Electrons drift velocity, mm/μs	1.8	
Maximum drift time, μs	806	Interactions at cathode
Electron longitudinal diffusion, μs	2.2	FWHM, cathode events
Electron transverse diffusion, mm	1.8	FWHM, cathode events
Photon absorption length in liquid, m	30	
S1 response, phe/keV	5.3	Zero field for ^{57}Co γ
S1 PDE (g_1), %	8.5	
Reverse field region		
Bottom grid voltage, kV	−1.5	
Field grading, kV/cm	2.9	

Table 3.1: Parameters of the LZ TPC.

Reverse field region The reverse field region, consisting of the bottom grid, field shaping rings, and the cathode grid, is located beneath the drift region for protecting the bottom PMT array. The region serves as a buffer zone to shield bottom PMTs from the high voltage cathode (nominally −50 kV). The field shaping rings in the region grade down the field at 2.9 kV/cm such that the PMTs can operate near ground potential.

PMT arrays The bottom and the top of the TPC are equipped with 3-inch-diameter PMTs (Hamamatsu R11410-22), which are commonly used in the field [95], to view the WIMP target region. The PMT has good spectral response to VUV photons at a quantum efficiency (QE) of around 30 %, low dark count, capability of operation at LXe temperature, and importantly ultra-low levels of radioactivity ($\sim$ mBq/unit in U/Th/^{60}Co/^{40}K) [60].

The bottom array is a close-packed hexagonal array which collects most of the S1 light (owing to the high probability of total internal reflection of photons at the liquid surface). The layout allows a 54 % coverage fraction of the photocathode surfaces on the plane of the bottom array. As for the top array, it is a closed-packed hybrid array with hexagonal arrangement near the centre of the TPC and circular arrangement near the perimeter of the top-corner structure. The array collects most of the S2 light and is crucial for reconstructing the x-y position of interactions, with, in particular, the wall events near the vertical cylindrical surface of the PTFE that defines the TPC. The events can come from a population of the radon progeny plated out on the PTFE walls. As a result, the outer few rows of the PMTs are circularly packed to minimise the leakage of these events.

3.2.2 Cryogenic and Recirculation system

The cryogenic and recirculation system is essential for achieving stable operation of the detector. An illustration of the system is shown in figure 3.9.

Cryogenic system The cryogenic system of the LZ system cools down the TPC and the liquid xenon tower to $\sim$ 175 K for LXe circulation. A central 750 litre LN_2 tank distributes gas and liquid nitrogen to different parts of the system such as the sub-cooler, the heat exchanger, and the cryo-cooler to facilitate xenon heat exchange. The Stirling cycle cryo-cooler operates at atmospheric pressure and liquefies cold vaporised gas nitrogen from a thermosyphon (TS) line in a closed-loop cycle. Several TS lines, connected between the cooler and the TPC vessel/LXe tower/cathode feedthrogh, act as heat sinks to remove heat from the xenon system. Such passive heat exchange cycles, which utilise the $\sim$ 100 K temperature difference between the nitrogen and xenon evaporation temperatures, provides the thermal control and temperature modulation of the LZ system.

Recirculation system The LXe is recirculated as shown in figure 3.9 continuously into the gas purification system through a hot zirconium getter. The recirculation is important not only for removing electronegative substances from the outgassing of PTFE reflectors and the plastics in PMT cables but also for avoiding dead regions which would serve as a source of diffusively-driven impurities. The overall circulation rate is 500 slpm in gas which is equivalent to 16 cm^3/s, or 2.8 kg/min, or 10 tonnes per 2.5 day of liquid xenon.

The recirculation starts with the filling of the detector. After the detector system is cooled to $\sim$ 175 K by the cryogenic system, the TPC can be filled with

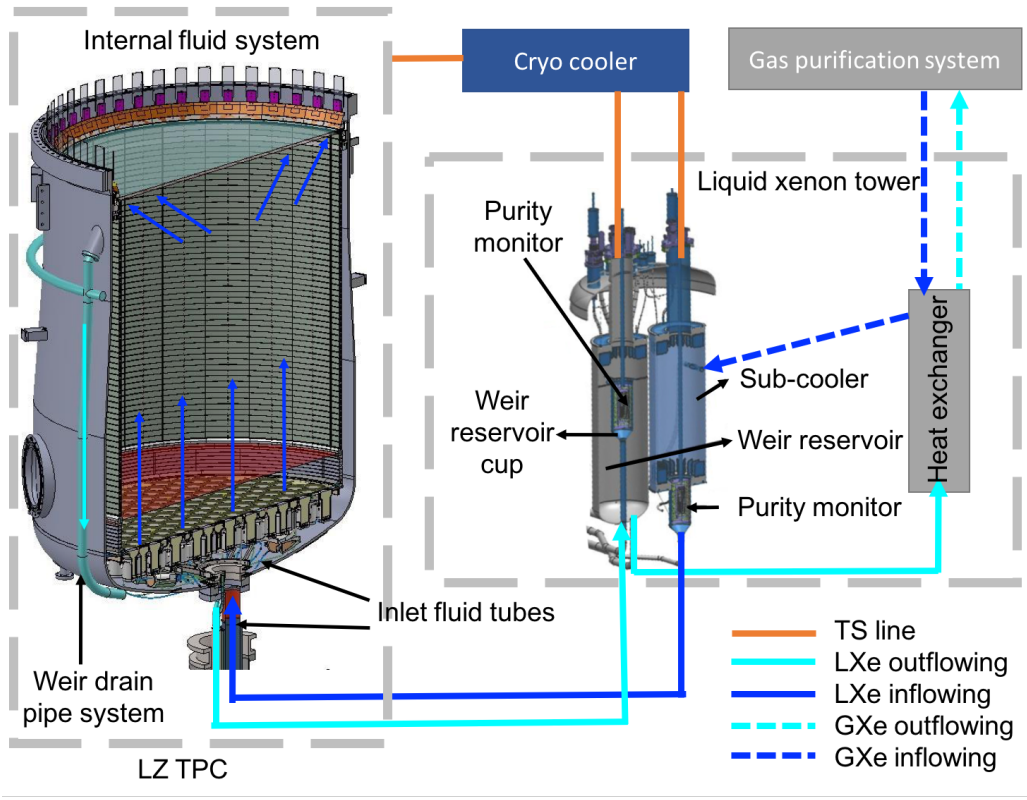


Figure 3.9: LZ cryogenic and recirculation system. The purity monitors in the LXe tower will provide online measurements of the electron lifetimes of the inflowing and outflowing LXe.

LXe for the science run. LXe enters from the bottom of the TPC vessel. As the LXe fills the TPC, it overspills into six evenly spaced weirs at the top-corner structure (shown in 3.8) which controls the liquid surface. The weir structure collects the LXe into weir drain pipes made of PTFE that return the liquid to the xenon transportation lines into the LXe tower. The tower counter flows the outflowing xenon of the TPC and the inflowing xenon from the purification system. The sub-cooler in the tower condenses the purified GXe and returns it to the TPC vessel.

As for the internal flow of the TPC, in general, the inflowing LXe is cooler than the outflowing LXe such that the heat load from the bottom PMTs ($\sim 8\,\mathrm{W}$) can be counterbalanced. The flow rate into the skin and the TPC are separately

controlled by inlet fluid tubes. The configuration creates an upward fluid flow and will flush out impurities in the TPC to the weir constantly. Also, the temperature of the LXe near the skin region is controlled by attaching six TS lines to the vessel at the level of the liquid surface. Thus, the skin LXe together with the inflow LXe can create a current to make the temperature of the LXe in the TPC uniform.

3.2.3 Radioactive Background Veto

In the WIMP search window, radioactive backgrounds from neutrons and gamma rays (mostly from PMTs and the titanium cryostat) needs to be vetoed. The neutrons could produce single scatters in the TPC and exit the detector without a secondary energy deposition. The gamma rays in a few-MeV range from components near the LXe volume can single scatter in the outer region of the TPC and deposit 0.5 keV to 6.5 keV of energy which corresponds to the WIMP signal region. The mitigation of the background other than the self-shielding of the xenon target relies on the veto system. The system consists of the skin region detector and the outer detector (OD). The system will not only veto the backgrounds with high efficiency but also help characterise and measure the background. Without the veto system, to achieve 5.6 tonnes of fiducial volume, the xenon volume in the TPC would have to be increased to 11 tonnes (originally 7 tonnes).

The xenon skin region detector, containing around 2 tonnes of LXe, is located between the TPC and the inner vessel as shown in figure 3.8. The side skin region is monitored by 94 1-inch R8520 PMTs at its top half side and 20 2-inches R8778 PMTs at its bottom half side. The bottom skin region is watched by 18 2-inches R8778 PMTs installed on the bottom PMT array. The detector has an energy

threshold of 100 keVee to observe ER events from gamma rays or neutron-capture background with > 95 % veto efficiency. The detector can also mitigate potential light leakage from this region to the xenon target.

As for the outer detector, it comprises the water tank and the gadolinium-loaded liquid scintillator (Gd-LS) as shown in figure 3.7. The water tank, filled with ultrapure water, is the existing tank from LUX for shielding backgrounds from outside the detector, in particular, the neutrons from cosmic‘ muon interactions in the underground rock. The Gd-LS is inside acrylic vessels and surrounds the TPC vessel. The scintillator is very efficient in capturing neutrons. Typical neutron capture occurring on the hydrogen atoms in the organic scintillator ($n + p \rightarrow d + \gamma$) has a cross-section of 0.33 b and emits 2.2 MeV gamma ray with a delay time of $200\,\mu$s. The neutron-capture cross-section for natural Gd, with major contributions from ^{155}Gd and ^{157}Gd, is high ($\sigma_{\mathrm{Gd}}(n,\gamma) = 49\,\mathrm{kb}$). A doping of 0.1 % Gd in the organic scintillator will be sufficient to dominate interactions from the neutron-capture over protons. The capture will lead to 8 MeV of energy in a cascade of $3-4$ γ rays. The time delay of the capture is also short ($\sim 30\,\mu$s) and hence reduces the dead time of the outer detector. The emitted gamma rays from the capture will be detected by 120 8-inch R5912 PMTs which are installed 84 cm radially from the acrylic vessels of the Gd-LS. The configuration gives an average light-collection efficiency of $\sim 7\,\%$ and a sensitivity of about 130 phe/MeV.

As a result, the veto system using both the skin region detector and the outer detector is effective in rejecting backgrounds. The system is projected to veto 90 % of neutrons escaping from the TPC and reject > 70 % of gamma rays with deposited energies in the WIMP signal range.

Source	What?	Purpose	Where?
Detector response			
^{83m}Kr	32.1 keV and 9.4 keV, β/γ	TPC (x, y, z)	Internal
^{131m}Xe	164 keV γ	TPC (x, y, z), Xe skin	Internal
^{220}Rn	various α's	Xe skin	Internal
^{57}Co	122 keV γ	Xe skin z dependence and threshold	CSD
^{228}Th	2.615 MeV γ, various others	Outer detector energy scale	CSD
^{22}Na	back-to-back 511 keV γ	TPC and outer detector sync	CSD
Electronic recoil			
Tritium	β decay, Q = 18.6 keV	ER band	Internal
Nuclear recoil			
AmLi	(α, n)	NR band	CSD
^{252}Cf	spontaneous fission	NR efficiency	CSD
DD	2450 keV and 272 keV neutrons	NR light and charge yields at 74 keVnr and 8.4 keVnr	External (Outside water tank)
Photoneutron	(γ, n) neutrons: ^{88}YBe (152 keV) ^{205}BiBe (88.5 keV) ^{206}BiBe (47 keV)	Low energy NR end-points: ^{88}YBe (4.6 keVnr) ^{205}BiBe (2.7 keVnr) ^{206}BiBe (1.4 keVnr)	External (TPC top)

Table 3.2: Summary of baseline calibration for LZ. Three calibration source deployment (CSD) tubes are located in the vacuum space of the TPC cryostat.

3.2.4 Calibration

For the direct detection of the hypothetical dark matter signal, the calibration of the detector is a prerequisite. The questions, which arise from non-WIMP interactions in the detector, such as the response of the detector and interactions of different particles that give different energy deposition must be understood. Table 3.2 summarises the baseline calibration plan of LZ.

The spatial correlation of the S1 and S2 signals with a given interaction position in the detector firstly needs to be calibrated. This includes correlations such as electron lifetime efficiency, electron extraction efficiency, electric field depend-

ence and position reconstruction efficiency. Such x-y-z dependence of the signals can be corrected through calibration sources - ^{83m}Kr and ^{131m}Xe. The ^{83m}Kr is a low-energy (41 keV) mono-energetic source with a half-life of 1.8 hours; the ^{131m}Xe source produces 164 keV gamma ray with a longer half-life of 11.9 day. The sources will be injected by xenon gas, flowing over a parent isotope that is emanating the calibration isotope (^{83}Rb for ^{83m}Kr and ^{131}I for ^{131m}Xe), to the xenon circulation system. The two sources provide complementary calibrations of the TPC. Because the time scale of liquid mixing in LZ may not allow ^{83m}Kr to become homogeneous given its short half-life, the ^{131m}Xe is a long-lived alternative for achieving homogeneity. On the other hand, its 164 keV gamma ray, compared with the 41 keV gamma ray of the ^{83m}Kr, may result in partial saturation of central PMTs in detecting S2 photons. Nevertheless, the saturation is expected to affect negligibly the unity of the x-y-z map making.

The veto system - the skin region detector and the outer detector - requires an energy threshold of 100 keVee and 200 keVee for achieving high veto efficiencies. The calibration sources for the skin detector other than the 164 keV gamma ray from ^{131m}Xe are ^{220}Rn and ^{57}Co. The ^{220}Rn will be introduced by its parent isotope - ^{228}Th through the gas system. The source emits 6.3 and 6.8 MeV alpha particles with a half-life of 150 ms and its daughter isotopes are expected to accumulate on surfaces before their decay. Hence, the source will not only provide a large light yield in the skin region but also information about the light/charge yield at xenon-surface interfaces. Furthermore, the ^{57}Co, producing 122 keV gamma ray, will be deployed through a calibration tube installed in the vacuum space of the cryostat vessel. The source will be lowered by a stepper motor such that the z

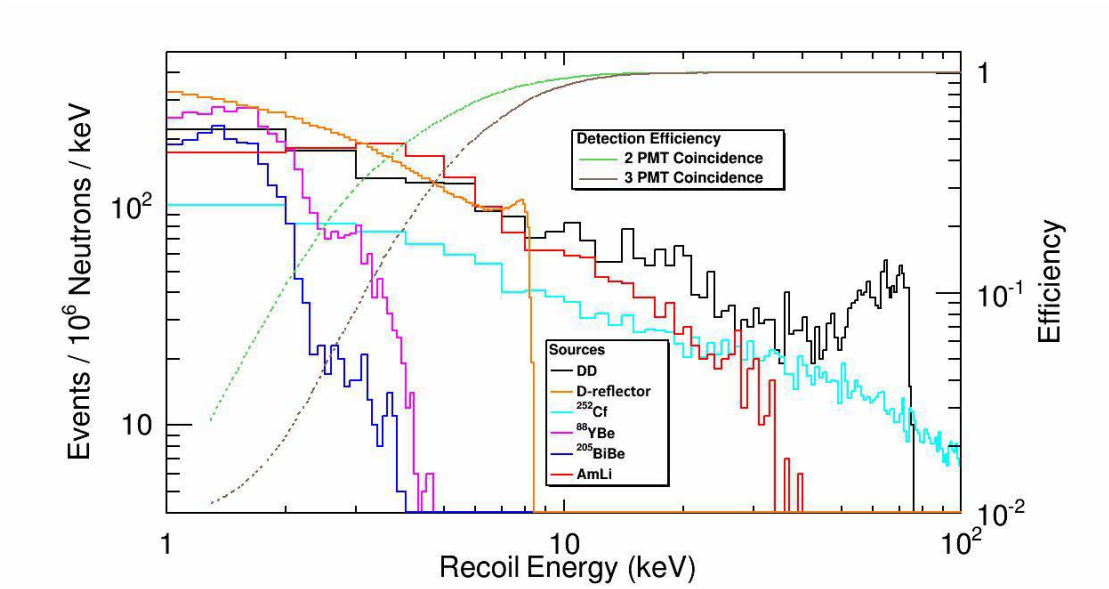


Figure 3.10: Nuclear recoil spectrum from each calibration sources. Black: DD; orange: DD back-scatter off deuterium; cyan: ^{252}Cf; red: YBe; blue: BiBe; magenta: AmLi. Taken from [60].

dependence of the side region of the skin detector can be calibrated. As for the OD, its energy scale will be calibrated by ^{228}Th and ^{22}Na sources. The ^{228}Th source produces 2.651 MeV gamma ray; the ^{22}Na releases back-to-back 511 keV gamma rays. The back-to-back gamma rays from ^{22}Na may also be usefully used to calibrate the timing synchronisation of the skin detector and the OD such that the timing resolution of the veto system can be optimised.

The low energy ER band of the combined S1 and S2 energy scale and the S2/S1 ratio is calibrated through mixing ^{3}H labelled CH_4 (tritium-labelled methane) with the xenon target volume. The tritium decays via beta decay and has an end point energy $Q = 18.6\,\text{keV}$. Momentum transfer onto a Xe nucleus results in a recoil energy that lies conveniently within energy threshold range of the WIMP search, i.e. $0.5 - 6.5\,\text{keVee}$. The source, although having a long 12.3-year half-life, cannot be absorbed effectively by the PTFE and can be removed efficiently through the getter in the gas purification system.

The NR band of the detector for the WIMP search (few keVnr to $\sim$ 50 keVnr) is calibrated by broadband sources in the recoil energy from 1.4 keVnr to $>$ 100 keVnr (see figure 3.10). Firstly, the NR detection efficiency is measured with ^{252}Cf source. The source produces neutrons through spontaneous fission and has a continuous NR spectrum which extends above 100 keVnr. Secondly, the NR band for WIMP search will be calibrated using the (α,n) reaction of the AmLi source. The source produces neutrons at a rate of 100 neutrons/s and has a broadband spectrum with a distinct energy end-point at 40 keV. Thirdly, for low energy recoils, the deuterium-deuterium (DD) neutron generator and DD-reflector are used. The generator and the reflector produce neutrons at 2450 keV and 272 keV, respectively. Such neutrons will result in end-points of 74 keVnr and 8.4 keVnr which are suitable for studying the NR scintillation/ionisation responses. Lastly, because LZ is projected to observe $\sim$ 7 background events from ^{8}B solar neutrino coherent scattering, it is important to understand the location of these events in the detector parameter space. Such background will be understood through calibrating the detector with low energy neutrons that result in $<$ 10 keVnr energy deposition. The photoneutron (γ,n) sources such as YBe and BiBe are used because their recoil spectrums conveniently overlap with that from the neutrino scattering in the S1/S2 parameter space.

3.3 Conclusion

In this chapter, we have described the technology of the two-phase xenon TPC. The technology is very competitive in WIMP search because of its scalability for increasing the target mass and the ability to discriminate the NR/ER events effect-

ively. We also discuss the LZ experiment that realises such technology to perform dark matter searches. The instrumentation of the TPC is crucial for producing the S1 and S2 signal. The circulation system is important for minimising systematic effects on the signals from impurities such as the electronegative substances or the left-over product from the calibration sources. The veto system and the calibration sources are essential to increase the fiducial volume of the detector and understand the population of events in the parameter space of the WIMP search. In summary, the intricacy of implementing a detector at tonne-scale for dark matter search requires a detailed understanding of different parts of the system. In the next chapters, issues regarding controlling the stability of the S2 signal in the detector will be discussed. We will describe a monitoring system which complements the correction of the signal in detail.

Chapter 4

Level Sensors

Management of a stable S2 signal in a tonne scale two phase liquid xenon chamber is a non-trivial task. Systematics of the S2 signal could be affected by the temperature, pressure, coefficient of thermal expansion (CTE) of different parts, geometrical alignment, and liquid xenon level of the LZ TPC. This is essential for interpreting the dark matter search data. For example, the WIMP-lepton scattering coupling provides a possible explanation to the DAMA/LIBRA annual modulation signal. Such a scenario is excluded with an analysis by XENON100 experiment [50]. One of the important steps in such an analysis is to rule out any potentially periodic correlation of the data with the detector operation parameters such as pressure, temperature, electron lifetime, and liquid xenon surface level . The liquid level, in particular, contributes to the variation of signals produced in the S2 region when other factors of the TPC remain stable. Therefore, to minimise the uncertainty of S2 signal, it is necessary to monitor the liquid level precisely. Such monitoring of the S2 signal stability in LZ is achieved through precision level sensors in the detector system.

In this chapter, the development of such level sensors is presented. The motivation for the installation of level sensors in LZ is first discussed. Then, primary driving factors of the design, such as sensitivity requirement, material selection, and geometrical parametrisation, are discussed. The design of the electronics, which enables precision measurement of the sensor without interference from considerable cable capacitance, is briefly summarised. Lastly, various tests of prototypes are presented to demonstrate the capability of sensors in level measurement.

4.1 Motivation

Geometrical Dependence of S2 Previous studies have shown that changes in the liquid level in the gate-anode region of the TPC affect the generation of secondary scintillation light (S2) (discussed in section 3.1.6) in a two-phase detector [81, 96]. Event reconstruction and discrimination depend strongly on the stability of the ionisation signal. A tilt of the gate-anode region, near the top of the TPC, to the gas/liquid surface (which remains horizontal) causes the S2 response to change from one side of the TPC to the other (see figure 4.1) [81]. The vertical position of the liquid level – hence the height of the gas region – has a strong influence on the S2 yield and width. The yield will be biased towards a thicker gas region which results in a non-uniform PMT hit pattern for the determination of the x-y position of the interaction. Hence, any uncertainty in the liquid level impacts the accuracy with which an interaction vertex can be localised. LZ performs the monitoring by installing a precision surface sensor at this region to measure the precise LXe surface level in the TPC.

As discussed in section 3.1.6, factors such as the TPC pressure, the applied

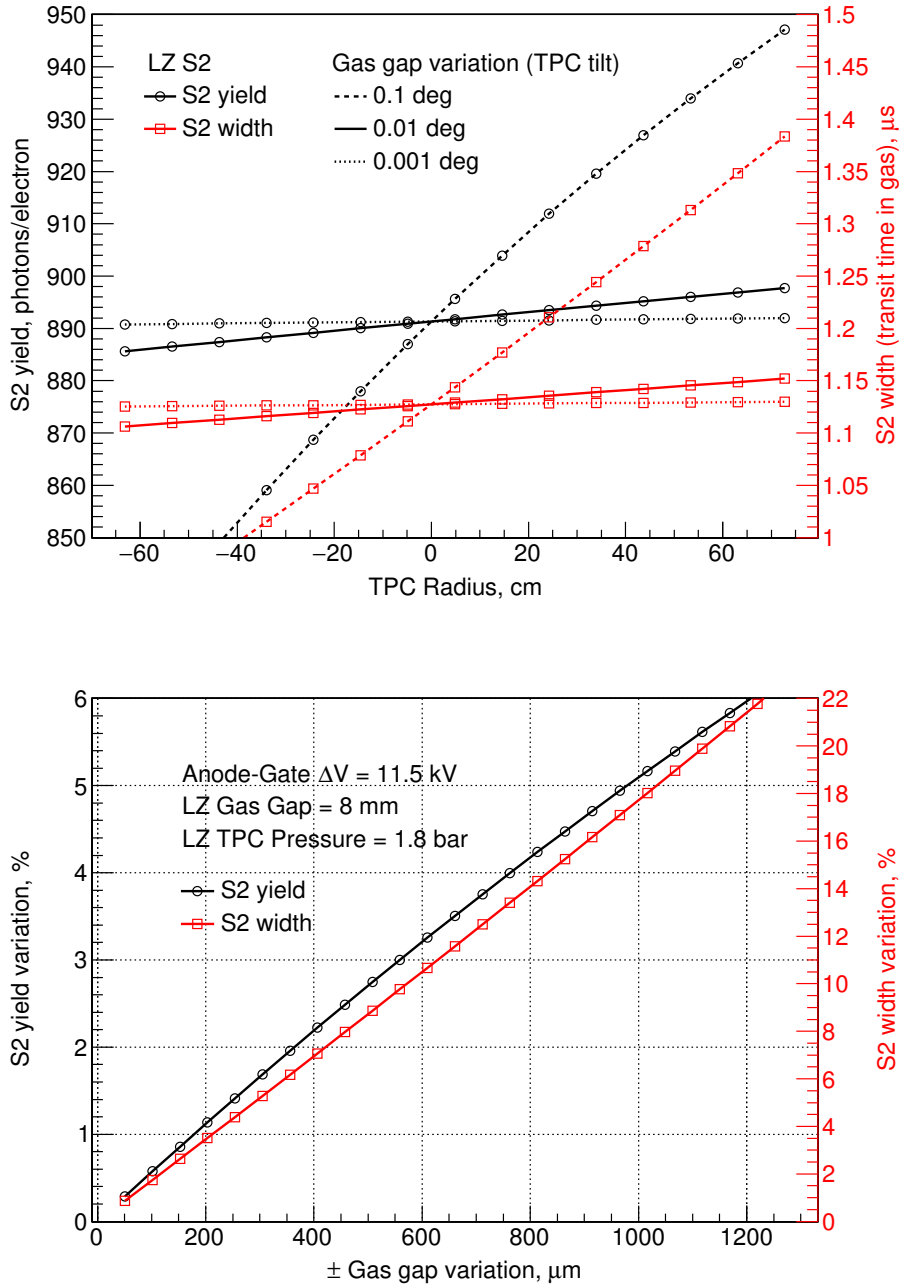


Figure 4.1: Geometrical effect on S2 signal from TPC tilt and liquid level variation. (Top): TPC tilted by 0.1 degree, i.e. $\sim$ 2 mm liquid level difference radially. (Bottom): Assuming an uniform liquid surface, oscillation of TPC liquid level results in significant changes in S2 width.

field, and the liquid level between gate and anode contribute to the variation of S2 yield. TPC pressure can be measured through a simple commercial pressure sensor. The applied voltage can be obtained from readings on power supply instrumentation. Variations in liquid level across the extraction region lead to variations of electric fields and thus a change in S2 gain and width. Such variations may come from geometrical effects of detector tilting or weir structure non-uniformity (LZ has developed strategies to mitigate them [60]).

The geometrical effect from non-uniform liquid level to the S2 signal can be estimated by combining equation 3.11 and 3.12 and expressing it as

$$N_{ph} = \kappa_n(E_{e-liquid}(x)) \cdot (\alpha E_{e-gas}(x) - \beta P_{TPC} - \gamma) x_{gas} \quad \text{[photons/e]}. \tag{4.1}$$

Equation 4.1 reveals two physical effects. First, any variation of the gas gap will affect the electric field E in gas and liquid, and thus the light yield produced. Secondly, because the equation allows interpretation of light yield at a given location in the S2 plane, a titled TPC or an oscillating liquid surface will lead to a non-uniform hit pattern of the light in the PMT array.

Examples of S2 signal changes due to geometrical effects are shown in figure 4.1. If the TPC tilts by 0.1 degree, the liquid level gradient will be ~ 2 mm and results in a variation of the S2 gain around $10 \sim 15\%$ and width around $30 \sim 35\%$ radially. Also, assuming a TPC with tilting corrected and a uniform gate-anode grid structure, oscillations in liquid level will contribute considerably to fluctuations in S2 gain and width. The effects will worsen the detector energy resolution and increase difficulties in calibrating S2 signal since the geometrical effects from liquid oscillation may be time-dependent. Therefore, the dependence necessitates

the instrumentation of level sensors for measuring liquid surface precisely at the EL region.

Influence from the Circulation System The LXe that overspills from the extraction region into the weir reservoir returns to return to the purification system; the purified LXe in the sub-cooler will flow back to the TPC. The purification, in particular, is achieved through circulation of xenon through the LXe tower shown in figure 4.3 to the hot getter. The tower vaporises and re-condenses xenon to form a recirculation loop between the TPC vessel and the purification system. Such a continuous process of recirculating the detector medium is essential to produce a large and uniform electron drift length [97]. However, any pressure build-up or thermal non-equilibrium along the recirculation loop, as found in the system test discussed in Chapter 5, could affect the stability of the liquid surface in the TPC. Thus, various places in the tower, such as the weir drain pipe, weir reservoir, and sub-cooler, require careful monitoring of the liquid level. The monitoring complements other control parameters, e.g. pressures, temperatures, and flow rates, to optimise the LXe recirculation system such that the best-quality LXe can be provided and the most stable liquid surface in the TPC can be achieved.

4.2 Placement of Level Sensors in LZ

The LZ experiment will have three kinds of level sensors installed [60, 98]. First, as shown in the blue circle of figure 4.2, Weir Precision Sensors (WPS) will be installed near the TPC's gate and anode to provide an accurate online measurement of the LXe level and will contribute further information to the event reconstruc-

tion. Another two types of level sensor - Medium Level Sensors (MLS) and Long level Sensors (LLS), are represented by the red triangles and the red squares in figure 4.2, respectively.

Six WPS sensors will be installed at 60-degree separation around the TPC and installed as a stand alone device in the weir region (see figure 4.2 (Bottom)). They will determine the precise height and uniformity of the LXe surface in the electroluminescence (EL) region. The WPS will also provide information about the systematic effect of any potential unevenness of the liquid surface such as surface waves and help with the optimisation of the S2 signal.

In total, two MLS and two LLS, which are driven by the design of WPS and have different measurement ranges (25 cm for MLS and 1 m for LLS), will be installed in different sub-systems: the bottom of the TPC, the weir reservoir, and the sub-cooler (see figure 4.2 and 4.3). The MLS mounted at the bottom of the TPC will serve as an indicator to inform the filling status of the TPC. One MLS installed in the cup of the weir reservoir will advise the level of returning liquid from the TPC weir drain pipe and also the liquid level in the purity monitor; another LLS installed next to the cup of the weir reservoir will measure the liquid which enters the two-phase heat exchanger. The other LLS in the sub-cooler will measure the liquid level of the xenon condensation for filling the detector and also the liquid level within another purity monitor. These sensors will show the performance of the circulation. Any oscillation of the liquid level in these sensors that correlates to the liquid level measured by WPS or pressure changes in the system should be minimised. As a result, such placement of the MLS and LLS will allow the fine-tunning of the detector so that a stable TPC liquid surface and

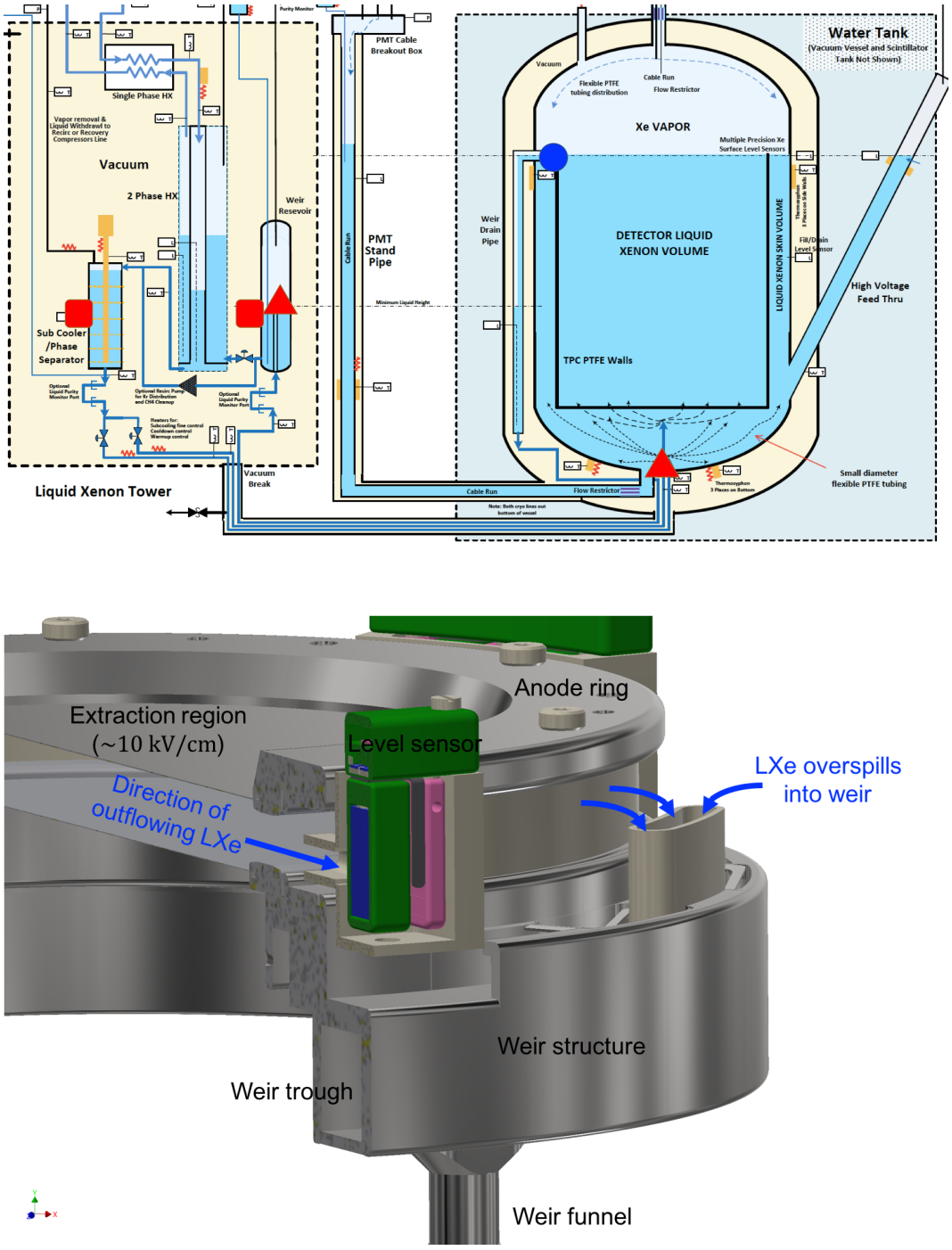


Figure 4.2: (Top): Flow diagram of the LZ detector. The WPS, MLS, and LLS are shown as blue circle, red squares, and red triangles, respectively. Taken from [60]. (Bottom): The integration of WPS in the weir region in Run 7 of the SLAC system test. As the LXe overflows the weir and enters the WPS, the liquid level will be measured. The weir trough collects excess LXe from the TPC and funnels it back to the circulation system.

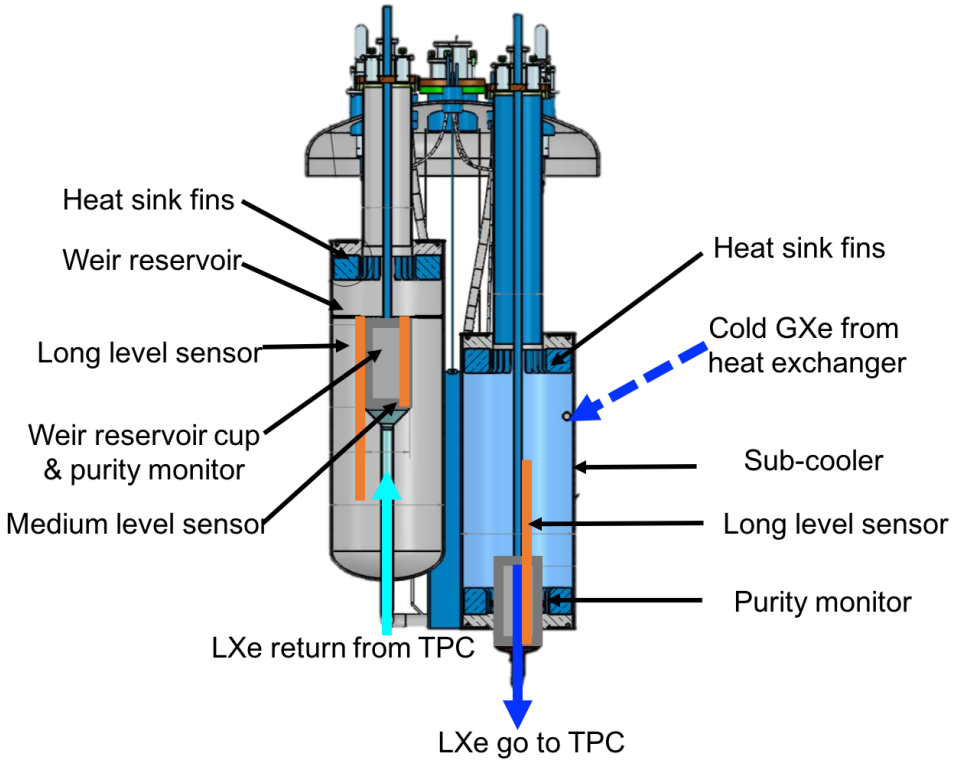


Figure 4.3: A closer look of the xenon tower in figure 3.9.

S2 signal can be achieved.

4.3 Liquid Level Measurement Technology

When the optimal technique for liquid level measurement is determined, the constraints from the environment within which the measurement is to be performed must be considered. The extraction and drift region of the LZ TPC is made of high voltage components such as gate and anode structures and field shaping rings. A sensor using mechanical floats for the liquid level measurement could obstruct a space in the extraction region and could short the voltage delivery for S2 signal production. Discrete measurements cannot fulfil the task because the continuous monitoring of the electroluminescence region is essential to correct systematics

in the S2 signal. Moreover, any measurement method generating dust or debris should be avoided. Dust and debris could drift to the S2 production region and obstruct the extraction of drifted electrons. Lastly, because of the requirement of low radioactive background and the use of PMTs in LZ, a sensor is expected to be radio-pure and non-luminous.

There are four methods by which a liquid level may be measured - mechanical, electromechanical, electronic contacting, and electronic non-contacting. Several candidate technologies were considered, but only the capacitive technique provides a viable solution.

The mechanical or electromechanical techniques make use of ruler engraved glass, floats, and discrete displacers like resistors. They are suitable for chambers which do not require the level of accuracy for measurements and the degree of mechanical stability as that in LZ. Another alternative, the electronic non-contacting method, such as a laser sensor, detection of radioactive substances, and ultrasonic wave emitter/receiver, provides a continuous measurement and a secure installation. However, they fail to use radiopure components and will result in undesirable light production and radioactive background in the detector [1]. After considerations, the electronic non-contacting method and, in particular, the capacitive measurement, is the optimal choice of technique. Such a sensor may utilise a minimum number of materials which allows a better control of its radiop-

[1]Frequency Scanning Interferometer (FSI) or electric-optical level sensors could be solutions for detector chambers which do not require the level of radiopurity that the LZ detector demands. Optical fibers in these systems are generally $50 \sim 100$ times more radioactive than PEEK or copper [99]. Also, these systems use lasers at far-infrared or infrared frequencies. At such frequencies, there are no data in the literature that discuss the LXe optical properties, e.g. refractive index or dispersive behavior at infrared photon energy ($\sim 1\,\mathrm{eV}$), and the response of PMTs (especially the Hamamatsu R11410). If a detector is not blind to electromagnetic waves at these frequencies, the sensors would be limited to provide intermittent measurements of liquid level.

urity. It is passive and does not emit photons actively, like for example the laser sensor would, which allows its placement near the electroluminescence region. Its passive characteristic also reduces the risk of generating debris or dust from any mechanical movement.

As a result, the LZ level sensors, i.e. WPS, LLS, and MLS, are based on simple capacitor physics, which will give considerable capacitance changes with small variation of liquid level, and fulfil the constraints discussed above. In the following sections, the pros and cons of the different geometrical configuration of sensors and the choice of material will be discussed.

4.3.1 Capacitive Sensors

There are three commonly used geometries of the capacitive level sensor - parallel wires, concentric cylinders, and parallel plates. Here, we discuss their common applications and constraints in liquid level measurement.

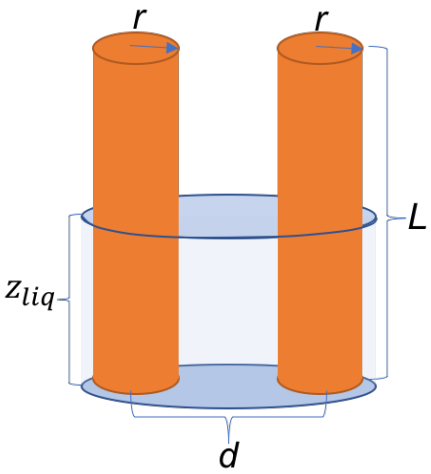
4.3.1.1 Parallel Wires

The parallel wire geometry usually consists of two parallel rods/wires as shown in figure 4.4a. This type of sensor could be scaled easily and was used in the LUX experiment to monitor the filling of TPC [100].

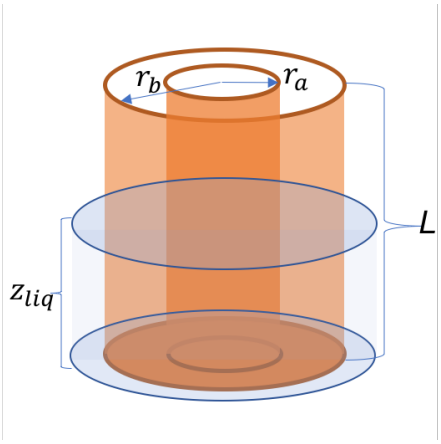
The capacitance change as function of liquid level variation is linear and can be expressed as

$$C_{Parallel\ Wires}(z_{liq}) = \frac{\pi\varepsilon_0(L + (\varepsilon_{liq} - 1)z_{liq})}{ln(\frac{d-r}{r})}, \tag{4.2}$$

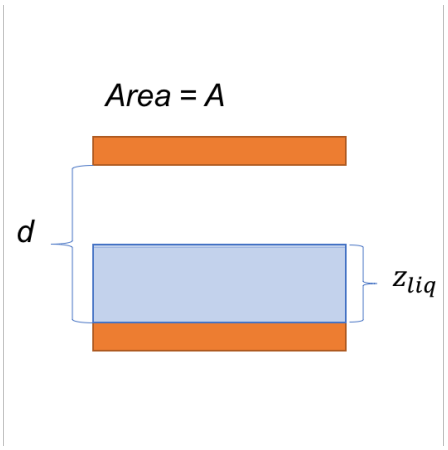
where ε_0 is vacuum permittivity, ε_{liq} is the relative permittivity of a liquid of



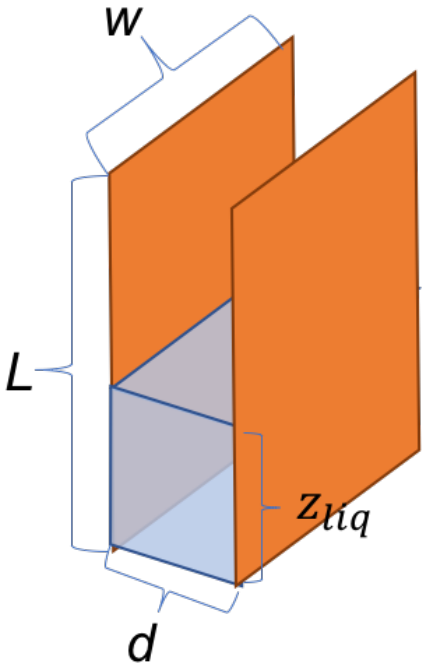
(a) Parallel rods



(b) Concentric cylinders



(c) Horizontally placed plates



(d) Vertically placed plates

Figure 4.4: Applications of parallel structures in the liquid level measurement.

interest between wires, d is the distance between two wires, r is the radius of the wires, L is the length of the wire pair, and z_{liq} is the liquid height [101]. The equation assumes no other materials surrounding the wire pair.

The open structure of a parallel wire sensor allows the LXe level or surface wave to enter the sensing region freely, which could enable the detection of ripples and waves around the EL region. But, in practice, having an open structure will allow coupling of the electric field between the electrodes with adjacent materials. Depending on the installation location of the capacitor, the adjacent material would be different. This uncertainty diminishes the stability of the capacitor. Thus, a proper shielding with an electrically grounded cage is necessary to ensure consistency of the sensor's calibration with data taken in LXe. The addition of the guard cage, however, removes the possibility for surface wave detection.

4.3.1.2 Concentric Cylinders

Another common technique for capacitive measurement is through the use of concentric cylinders (figure 4.4b). Such a technique is widely used in liquid nitrogen level measurement of cryogenic dewars. Also, experiments like PandaX use such a type of sensor to monitor the filling of TPCs [102]. The response of a concentric cylinder sensor to liquid level change is

$$C_{Concentric\ Cylinder}(z_{liq}) = \frac{2\pi\varepsilon_0(L + (\varepsilon_{liq} - 1)z_{liq})}{ln(r_b/r_a)}, \tag{4.3}$$

where $r_a$and r_b are the radii of inner and outer cylinders, respectively [103]. Similar to the parallel wire geometry, the concentric cylinder sensor can be scaled easily to a measurement length over one meter and has a linear response for liquid

measurement. Sensors with such geometry are usually less affected by fringe field effect. The advantage is due to the layering of the cylinders which confines the field between tubes and only allows the fringe effects to be more prominent at the two openings of its ends. The measurement of transient liquid surface waves is not possible with this technique. Surface waves are screened by the outer tube, and only the static liquid between the cylinders is measurable.

4.3.1.3 Parallel Plates

The last commonly known technique for capacitive level sensing is through the use of parallel plates. This geometry is frequently used in the production of commercial capacitors for electronics. Compared with other geometries, by placing multiple plates in parallel with their gaps filled with dielectric materials, capacitors with high capacitance and compact can be formed. There are two ways to apply this geometry in liquid level measurements as shown in figure 4.4c and 4.4d. The responses of the capacitor to level changes in horizontal and vertical setups are as follows:

$$C_{Horizontal\ parallel\ plates}(z_{liq}) = \frac{\varepsilon_0 \varepsilon_{liq} A}{d\varepsilon_{liq} - (\varepsilon_{liq} - 1)z_{liq}}, \tag{4.4}$$

and

$$C_{Vertical\ parallel\ plates}(z_{liq}) = \frac{\varepsilon_0 W(L + (\varepsilon_{liq} - 1)z_{liq})}{d}, \tag{4.5}$$

where d is the distance between plates, and $A = W \cdot L$ is the area of the plates with W being the width and L being the length of a plate.

Compared with other geometry arrangements, a parallel plate geometry is the most versatile. When placing plates horizontally to form a level sensor, it allows a large liquid surface between plates for surface wave detection. Moreover,

	PEEK	PTFE	Delrin	Copper
Tensile strength, MPa	98	27	72	300
Dielectric constant	3.1	2.1	3.4	-
Dielectric strength @ 2mm thickness, kV/mm	23	11	20	-
Coefficient of thermal expansion, ppm/K	55	75	120	14
Total mass loss, %	0.28	~ 0.43	~ 0.35	-
Thermal conductivity, $W \cdot m^{-1} \cdot K^{-1}$	0.32	0.25	0.37	401
Manufacture	VICTREX	DUPONT	DUPONT	-
Reference	[104]	[105]	[106]	[107]

Table 4.1: Candidate material properties in room temperature. The data regarding the outgassing (total mass loss) is taken from ESA database [108].

when the plates are placed vertically to create a level sensor, it provides the same linearity and scalability as found in the concentric tube and parallel wire technique. Although a bare pair of plates will suffer from fringe fields, the issue can be mitigated through the implementation of grounded shields. With the correct orientation of the sensors to the TPC and the implementation of guard electrodes, such geometrical arrangement could have the merits of the other two geometries, i.e. surface wave detection and shielding, for performing liquid surface monitoring around the LZ electroluminescence region.

4.3.2 Choice of Materials

There are four primary criteria in choosing materials to build the sensors: radiopurity, machinability, high voltage durability, and level of thermal expansion. LZ requires xenon friendly materials to mitigate any chance of contamination (discussed in section 4.4.2). Table 4.1 shows choices of different materials to construct the sensor. Mulitple experiments such as XENON, ZEPLIN, and LUX have used

Material	$^{238}U_e$	$^{238}U_l$	$^{232}Th_e$	$^{232}Th_l$	$^{60}C0$	^{40}K	^{210}Pb
Values in (mBq/kg)							
Copper	1.30	1.20	14.5	1.70	0.40	7.00	-
Stainless steel	1.20	0.27	0.33	0.49	1.60	33.1	-
PEEK	17.0	16.6	16.1	8.5	0.52	47.8	-
PTFE	0.02	0.02	0.03	0.03	-	0.12	-
Delrin	4.00	0.70	0.18	0.18	0.30	18.0	-

Table 4.2: Background of candidate materials. The subscripts - e and l - mean early and later in a decay chain. Taken from Ref. [60].

them for building the detectors for dark matter searches. Candidate plastics show low dielectric constant, good dielectric strength to withstand high voltage environment and high tensile strength for machining. PEEK, in particular, is suitable for our purpose. PEEK's higher tensile strength enables better stability during machining. The lower coefficient of thermal expansion of PEEK compared to that of PTFE and Delrin decreases potential systematics in the sensor induced by changes in temperature.

4.4 Requirements of the Sensor

The sensor must be designed to achieve high radiopurity, xenon compatibility, and maximum sensitivity. In this Section, the requirements that drive the design of the sensor are discussed.

4.4.1 Radiopurity

As in other rare event search experiments, the selection of materials with good radiopurity is essential. Section 4.3.2 describes several candidate materials, and their radioactivities are summarised in table 4.2. Because of the proven record of copper and PEEK regarding their radiopurity in other LXe experiments such

as XENON100 and EXO-200, they were chosen to form the bulk of the sensor. The candidate batch of the material for producing sensors was screened at Boulby with high-purity germanium detectors as described in Ref. [60]. The screening result shows that the sensors contribute to less than 0.01 ER counts, and less than 0.002 NR counts for 1000 live days of science data taking. Compared with the total LZ background of 6.83 counts, such contribution will give fewer than 0.00105 background counts after analysis cuts from a 99.5 % ER discrimination and a 50 % NR efficiency.

4.4.2 Xenon Cleanliness

Using materials that do not actively emit electronegative substances is crucial in achieving long electron lifetime and extracting electrons efficiently. Empirically, under the presence of acetone or weak acid solutions, dyed parts tend to leach out electronegative chemicals [109]. The chemical has a high probability of attracting electrons and hence diminishes the electron lifetime. Therefore, components proposed must be tested before their use in LZ. The candidate materials - PEEK and copper of R&D sensors described in Chapter 5 was tested in the system test chamber at Imperial College London to demonstrate their cleanliness.

4.4.3 High Voltage Concerns

The LZ R&D campaign, such as cathode wire emission, cathode HV delivery, and grids tests studied high voltage operation thoroughly to ensure an ideal HV environment for detector operation. The TPC relies on the drift region and extraction region to produce S1/S2 scintillations. As discussed in section 3.1.6, electrolumi-

nescence occurs in GXe for an applied electric field that is greater than 2.5 kV/cm. Any field above this value in the gas region of the TPC will generate light. Mitigation of extra light production outside the S2 region by lowering electric fields at various parts is vital. Also, electric sparks due to an abrupt electrical discharge may cause the breakdown of the gate/anode field and thus prevent the stable operation of the detector. Even though the onset of EL or charge multiplication in LXe is larger than 400 kV/cm, practical HV operation of a metal surface, e.g. cathode electrodes, in LXe TPCs has been limited to $40 \sim 65$ kV/cm. A conservative value, 50 kV/cm, is adopted to reduce the probability of high voltage sparks at local areas around detector components [110, 111]. Therefore, the electric field map of the level sensor in the perimeter of the TPC near the gate/anode region is studied to show the minimal impact of the above effects in the experiment. The mitigation will be discussed and shown in Chapter 6.

4.4.4 Sensitivity

LZ requires level sensors at the top-corner region, i.e. WPS, with excellent sensitivity, to aid the correction of the S2 signal or any geometrical effects. The stability of liquid surface level in the TPC depends on the circulation of the detector. Therefore, given a levelled TPC, the sensitivity is driven by the expected amount of surface excursion due to liquid circulation. In LUX, using the study of single electrons, the average excursion is less than ± 100 μm [81]. The experience from LUX and the calculation shown in figure 4.1 suggest that a sensor measuring 20 % of the excursion, i.e. 20 μm, will provide enough information of any subtle changes in liquid surface. As for the sensors in the circulation system, i.e. MLS

and LLS, the sensitivity requirement is less stringent and is set at 1 % of a sensor's measurement range, i.e. $\sim 0.25\,\mathrm{mm}$ for MLS and$\sim 1\,\mathrm{mm}$ for LLS. Rather than a precision measurement, it is more important to have these sensors covering a larger measuring range to inform the situation of the circulation. Therefore, because the design of MLS and LLS can be adapted from that of the WPS, the design of sensors is primarily driven by the required sensitivity of WPS.

4.5 Electronic Design

Reading capacitance changes of the level sensor inside the TPC from a long distance is challenging. The TPC, within the cryostat vessel, is surrounded by layers of shielding such as the Gd-doped liquid scintillator and a 200-tonne water tank. The distance between the sensor and the electronics outside the water tank will be around 10 m which then necessitates the use of long cables to read liquid level changes.

Long cables introduce considerable interference to capacitance measurements of sensors. Systematics of cable capacitance from temperature gradients between layers of the detector prohibit a simple correction factor. The expected capacitance change of the LZ cable is around 8 % as it cools from room temperature to 175 K [112]. Within such a temperature variation, we expect a $\sim 80\,\mathrm{pF}$ capacitance change for a 10 m long coaxial cable of around 1 nF capacitance. Furthermore, due to the limited space in the TPC, the capacitance of level sensors are at the picofarad level. The electronics measures the liquid level changes in the sensor at a femtofarad level under the influence of nanofarads of cable capacitance. Therefore, a customised differential readout scheme has been designed to suppress the

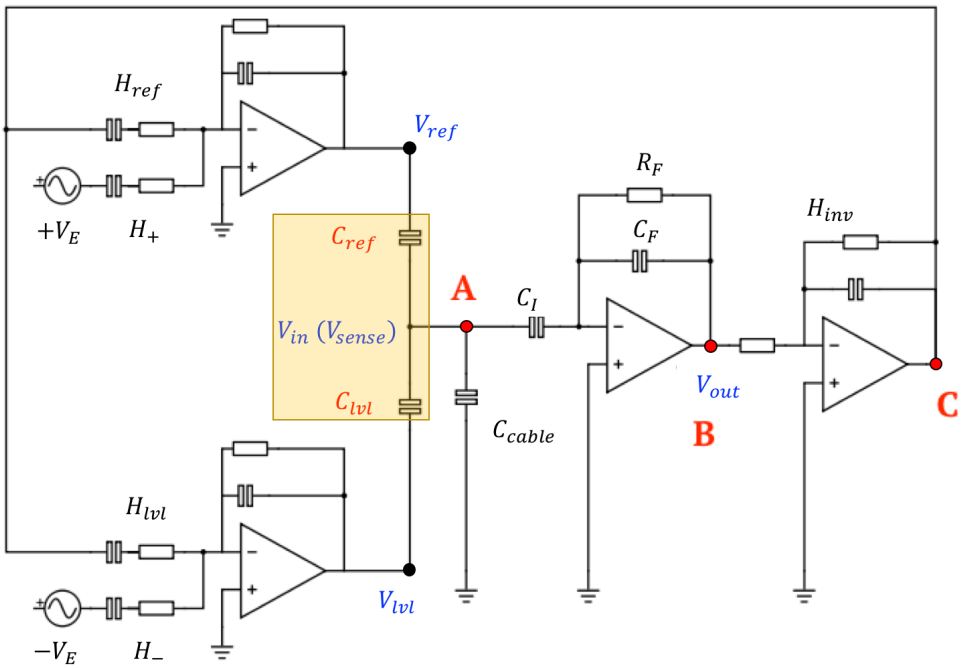


Figure 4.5: The circuit diagram of the sensor's readout. The yellow box represents the capacitive level sensor consisting of two capacitors - C_{ref} and C_{lvl}.

systematics from cable capacitance and to ensure variations in cable capacitance do not affect the liquid level measurement.

Eliminating the cable capacitance requires a careful consideration of the analogue circuit design. The suppression of the cable capacitance was achieved through three stages of amplifiers shown in figure 4.5. By monitoring two capacitances, C_{ref} and C_{lvl}, the electronics carries out a differential measurement. The level sensor holds the C_{ref} at a fixed reference capacitance and varies the C_{lvl} through the measurement of a liquid level.

The analysis of the circuit starts from node A in figure 4.5 with the measurement of sense voltage, V_{in}, of the sensor's sense plate. The output voltage is as follows:

$$V_{out} = -V_{in}\frac{G}{G+1}\frac{C_I}{C_F + \frac{C_I}{G+1}}\frac{i\omega\tau}{1+i\omega\tau}, \tag{4.6}$$

where G is the open loop gain of the op-amp, and $\tau = (C_F + \frac{C_I}{G+1})R_F$. With the electronics operating with a modulated signal at $\sim 200\,\text{kHz}$, the high pass filter part of the equation can be omitted, which gives:

$$V_{out} = -V_{in}\frac{1}{1+\frac{1}{G}}\frac{1}{\frac{C_F}{C_I}+\frac{1}{G+1}}. \tag{4.7}$$

At node B, V_{out} is passed to an inverter with gain H_{inv} and feeds $V_{adc} = -H_{inv}V_{out}$ to the ADC of the circuit. After node C, there are two summers adding the feedback signal from node B with positive or negative input excitations. The voltages on the excitation plates of the sensor's capacitors, C_{ref} and C_{lvl}, are

$$\begin{aligned} V_{ref} &= H_{inv}H_{ref}V_{out} - H_{+}V_E \\ V_{lvl} &= H_{inv}H_{lvl}V_{out} + H_{-}V_E, \end{aligned} \tag{4.8}$$

where $H_{ref,\ lvl,\ +,\ -}$ are the gains at the summers, and V_E is the modulated 200 kHz input signal. By combining equation 4.7 and equation 4.8 into the relation obtained with Kirchhoff's current law analysis at node A, the expression of the voltage which goes into the analog-to-digital convertor (ADC) of the electronic is obtained. It is

$$\begin{aligned} V_{ADC} =& (\frac{H_{-}}{H_{adc}}C_{lvl} - \frac{H_{+}}{H_{adc}}C_{ref})V_E/(\\ & (\frac{H_{lvl}}{H_{adc}}C_{lvl} + \frac{H_{ref}}{H_{adc}}C_{ref})+ \\ & (C_{lvl}+C_{ref})(\frac{C_F}{C_I}+\frac{1}{G})/(H_{inv}H_{adc})+ \\ & \frac{C_F}{H_{adc}H_{inv}} + \frac{C_{Cable}}{H_{inv}H_{adc}}(\frac{C_F}{C_I}+\frac{1}{G})), \end{aligned} \tag{4.9}$$

where C_{Cable} is the cable capacitance. If we let $C_I = 10\,\mu$F, $C_F = 10\,$pF, $G \approx 1600$, $R_F C_F > 100$, $H_{inv} = H_{adc} = H_{lvl} = H_{ref} = H_+ = H_- = 10$, and $C_{Cable} \approx 1$ nF, equation 4.9 for measuring C_{ref} and C_{lvl} at picofarad level can be simplified as

$$\frac{V_{ADC}}{V_E} \approx \frac{C_{lvl} - C_{ref}}{C_{lvl} + C_{ref}} \cdot \frac{1}{1 + \frac{1}{H}(\frac{C_F}{C_{ref}+C_{lvl}})(1 + \frac{C_{Cable}}{C_F G})} \tag{4.10}$$

$$\approx \frac{C_{lvl} - C_{ref}}{C_{lvl} + C_{ref}}. \tag{4.11}$$

The technique described above has several advantages. Firstly, via choosing high gain amplifiers and appropriate resistors to maximise the gain H in the feedback circuit, the suppression of the cable capacitance alleviates one of the difficulties in using long cables in the TPC. Secondly, the employment of modulated signals at 200 kHz enables the differential readout shown in equation 4.10 and decouples the sensors to any DC offset. Such a readout scheme allows the flexibility of installing sensors near high voltage components which operate at DC voltages. Moreover, the transient operation of the electronics at high frequency provides a better signal to noise ratio and reduces capacitors' impedances. This design effectively avoids the pickup of spurious charges and allows common mode cancellation. Lastly, by adjusting the gain H, the electronics can accommodate a broad range of measured capacitances, from a few hundreds of femtofarads to few hundreds of picofarads under the influence of nanofarads of cable capacitance. The technique and the development of the electronics are discussed in greater detail in Ref. [112].

4.6 General Geometrical Design Rules

The geometrical design of the sensors follows two general rules, namely the parameterised dimension and the consideration of fringe fields. The former entails the achievable precision; the latter increases the stability of the sensor's capacitance.

4.6.1 Parameterised Dimension

The sensor's dimension is parameterised with equation 4.11 for achieving a maximum precision of liquid level measurement. The readout differences between a liquid-filled and emptied sensor is

$$f(C_{ref}) = \frac{C_{ref} - C_{lvl}(Filled)}{C_{ref} - C_{lvl}(Filled)} - \frac{C_{ref} - C_{lvl}(Emptied)}{C_{ref} + C_{lvl}(Emptied)}. \tag{4.12}$$

where $C_{lvl}(Filled)$ and $C_{lvl}(Emptied)$ are the liquid filled and gas filled C_{lvl}, respectively. To optimize the choice of C_{ref} in equation 4.12, the choice of C_{ref} is motivated by a given C_{lvl}, i.e. the measurement range of the sensor. By solving $\frac{\mathrm{d}f}{\mathrm{d}C_{ref}} = 0$, the relation between C_{ref} and C_{lvl} is derived to be

$$C_{ref} = \sqrt{C_{lvl}(Filled) \cdot C_{lvl}(Emptied)}. \tag{4.13}$$

In general, the equation can be further generalised as

$$K_{ref} = K_{lvl} \cdot \frac{\sqrt{\varepsilon_{liq}}}{\varepsilon_{ref}}, \tag{4.14}$$

where ε_{liq} is the dielectric constant of the measurement liquid, ε_{ref} is the dielectric constant of the reference capacitor, and $K_{ref,\ lvl}$ are the constant terms of given

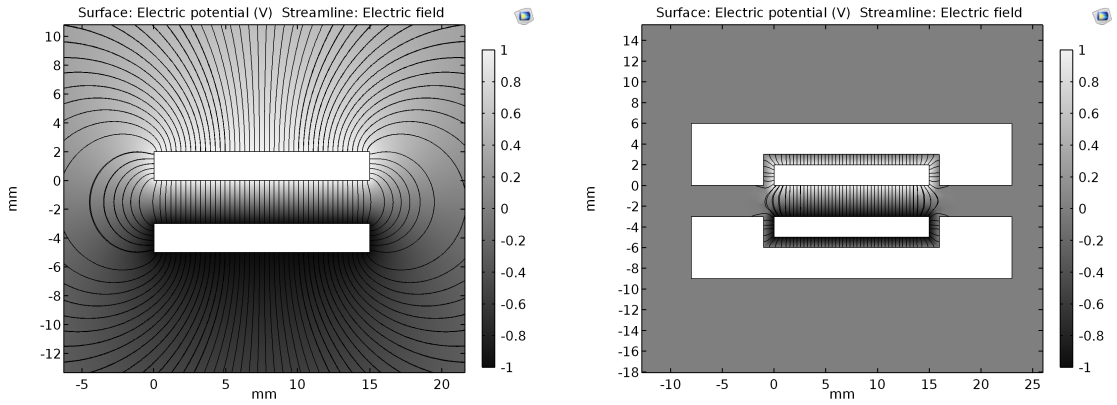


Figure 4.6: Effects of fringe fields. (Left): Parallel plate capacitor without guard electrodes. (Right): Parallel plate capacitor with guard electrodes. With the presence of a guard electrode, the field between excitation and sense electrode is more uniform and less stray couplings outside the gap between the two plates.

geometries. The advantage of such generalisation is that any systematic effects on the sensor are encapsulated into the K_{ref} and K_{lvl} and it gives a simple relation for the sensor's geometrical optimisation. In the case of a parallel plate capacitor, $K = A/d$ where A is the area of a plate, and d is the distance between plates.

4.6.2 Stray Capacitance

The level sensor should only measure capacitance changes induced by liquid level variation, but stray couplings with a sense electrode will affect the accuracy of the sensor. Figure 4.6 shows the difference of effects in implementing a guard electrode around the capacitor plates. Without the guard electrodes in figure 4.6 (Left), fringe field lines between the two plates may pick up changes in the adjacent environment introducing unexpected fluctuations in capacitances. This issue necessitates the presence of guard electrodes at ground potential around the electrodes as shown in figure 4.6 (Right). The configuration considerably improves the field uniformity and reduces spurious capacitive couplings. Hence, it ensures capacitive measurements only pick up the change of dielectric materials presented

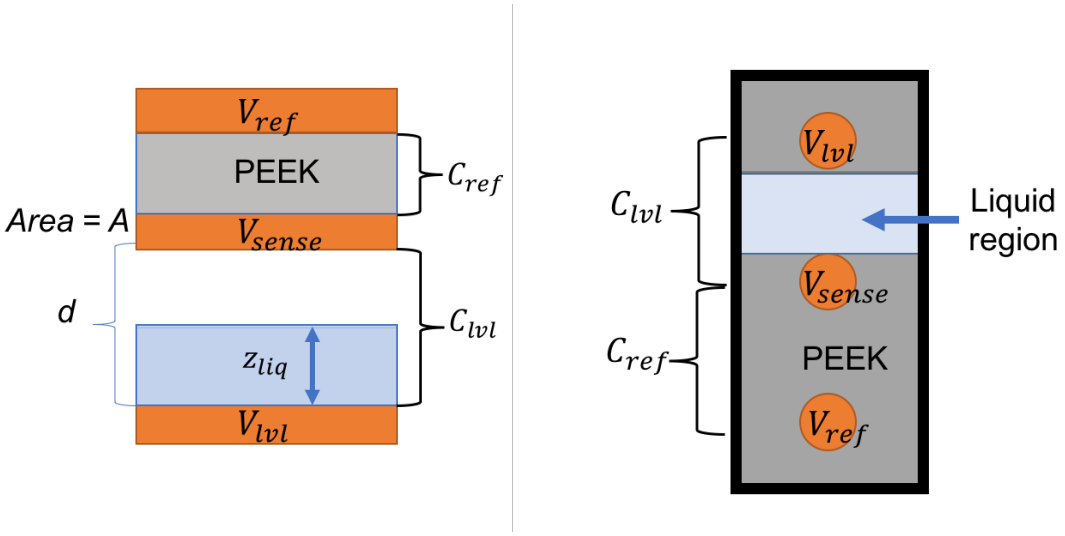


Figure 4.7: Prototype sensors. The V_{ref}, V_{lvl}, and V_{sense} correspond to the labels in the circuit diagram in figure 4.5. (Left): Horizontal parallel plate sensor (HPPS). (Right): Vertical Parallel Rod Sensor (VPRS).

between the electrodes.

4.7 Prototype Tests

The performance of prototype sensors with different geometry configurations was studied to explore their capability in liquid filling and surface wave measurements. Two types of geometrical design - vertical parallel rod sensor (VPRS) and horizontal parallel plate sensor (HPPS) (figure 4.7) were tested with mineral oil. The oil was used as the testing liquid because its dielectric constant is close to that of LXe and it has lower electrical conductivity than water and higher latent heat than liquid nitrogen (LN2) [2]. Moreover, the HPPS was tested in an applied electric field (up to 700 V/cm) to verify the capability of operating the sensor and the electronic in a medium voltage environment, as is the case in the LZ detector..

[2]Mineral oil is usually made of paraffinum liquidum consisting mostly N-alkane ($\varepsilon_{N-alkane} \sim 1.9$) and cycloalkanes ($\varepsilon_{Cycloalanes} \sim 2.0$) [113–115]. Generally the dielectric constant of the oil is around ~ 2.1 [116, 117]. We used the oil from Johnson's Baby Oil and Naissance British Pharmacopoeia Grade Mineral Oil for prototype tests.

4.7.1 Mineral Oil Tests

4.7.1.1 Horizontal Parallel Plate Sensor (HPPS)

Two oil test experiments - oil dropping and oil filling were performed to explore the capability of a horizontal level sensor with parallel plate geometry. Figure 4.7 (Left) illustrates the arrangement of plates and materials to form the sensor. The C_{ref} of the sensor comprises a top excitation plate, a PEEK spacer, and a sense plate in the middle. The C_{lvl} of the sensor separates the sense plate and a bottom excitation plate by a gap which is used for liquid level detection.

Figure 4.8 (Top) shows the setup for the tests. The setup consists of a set of 12 meters coaxial cables connecting the sensor and the electronics. As for the implementation of the mineral oil test, the HPPS was installed inside a beaker on a scale shown in figure 4.8 (Bottom Left). Above the sensor is a nozzle attached to a cup for introducing the oil into the beaker.

In the oil dropping experiment, oil droplets dripped periodically to fill the beaker. By counting the number of droplets during the filling process, the period between droplets ($T_{droplet} = T_{total}/N_{droplet}$) and the weight of each droplet ($W_{droplet} = W_{liquid}/N_{droplet}$) can be calculated. As for the oil filling experiment, the setup is the same as that of the oil dropping experiment except for the placement of the nozzle. The nozzle was pushed against the beaker's wall to allow oil flow down the beaker smoothly without generating any noticeable surface waves. Thus, by comparing the two experiments, we could determine the sensitivity and capability of the sensor.

During the oil-dropping experiment, 2332 ± 2 droplets dripped into the beaker within 557.9 ± 5.6 seconds. The average time interval between droplets is 0.24

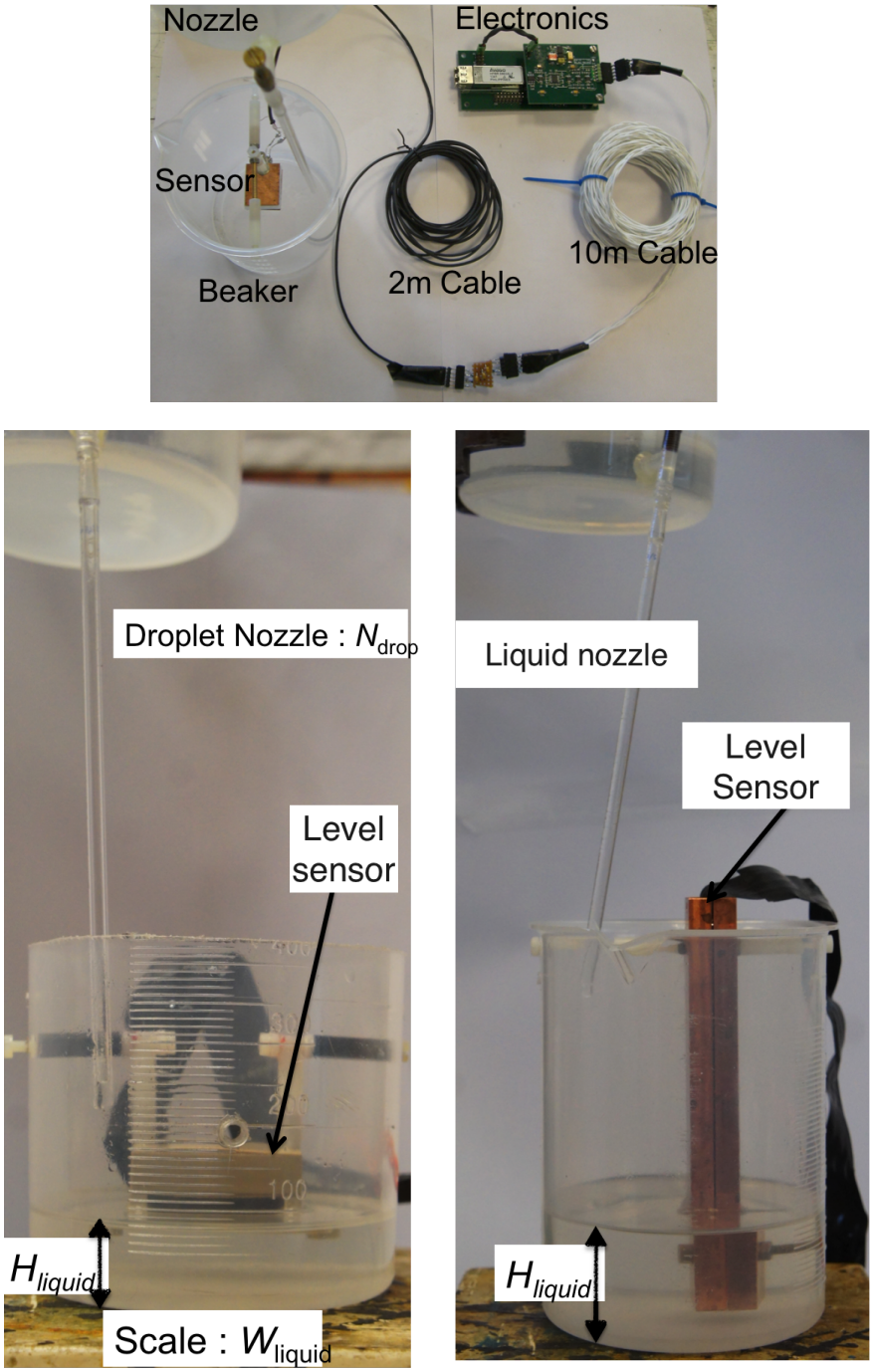


Figure 4.8: The configuration of tests to detect oil dropping and liquid filling. (Top): 12 meters coaxial cables, which is a length of cable expected in LZ, delivered the changes in capacitance of the sensor to the electronics. (Bottom Left): The HPPS was installed in a beaker placed on a scale. The nozzle can be freely adjusted to create surface wave measurement or liquid filling measurement. (Bottom Right): Configuration of VPRS test experiment to test its liquid filling capability.

seconds. On average, each droplet weights about $40.2 \pm 2\,\text{mg}$ and contributes an increase of $8.2 \pm 0.1\,\mu\text{m}$ in liquid level rise.

The HPPS is very responsive to liquid level changes (figure 4.9 (Top)) and demonstrates the capability to detect transient surface wave with excellent precision. In a chosen region of the data (figure 4.9 (Bottom)), the minimum voltage points of the periodic wave was calculated to obtain the average period of the surface wave and the voltage variation per droplet. The time difference between each wave trough was 0.2 ± 0.002 second. The moderate discrepancy between the wave periods of the data could be due to the interference between the previous droplet-generated surface wave and the new droplet-generated wave. Furthermore, each droplet corresponds to a $0.76 \pm 0.04\,\text{mV}$ voltage increase, indicating that the responsivity of the sensor is $92.9 \pm 5.2\,\text{mV/mm}$. Thus, the detected wave with the amplitude of $0.58 \pm 0.004\,\text{mV}$ equals to a $6.2 \pm 0.4\,\mu\text{m}$ variation in liquid level.

In the oil-filling experiment, the sensor did not detect any periodic structure in the data as it did in the oil-dropping experiment. The sensor's smooth response is expected as the oil flows down the sensor's beaker causing a gradual increase of the level (figure 4.10) without surface wave signature. A region of the data was selected to perform a straight line fit. The residual data is symmetrical around the mean of $0.00 \pm 0.16\,\mu\text{m}$ with FWHM $= 5.5 \pm 0.3\,\mu\text{m}$.

The comparison of the two experiments of the HPPS confirms the periodic wave in the oil-dropping data is indeed caused by the oil droplets. The prototype sensor shows its capability in detecting level changes at least as good as $10\,\mu\text{m}$ in the $5\,\text{mm}$ sensing range.

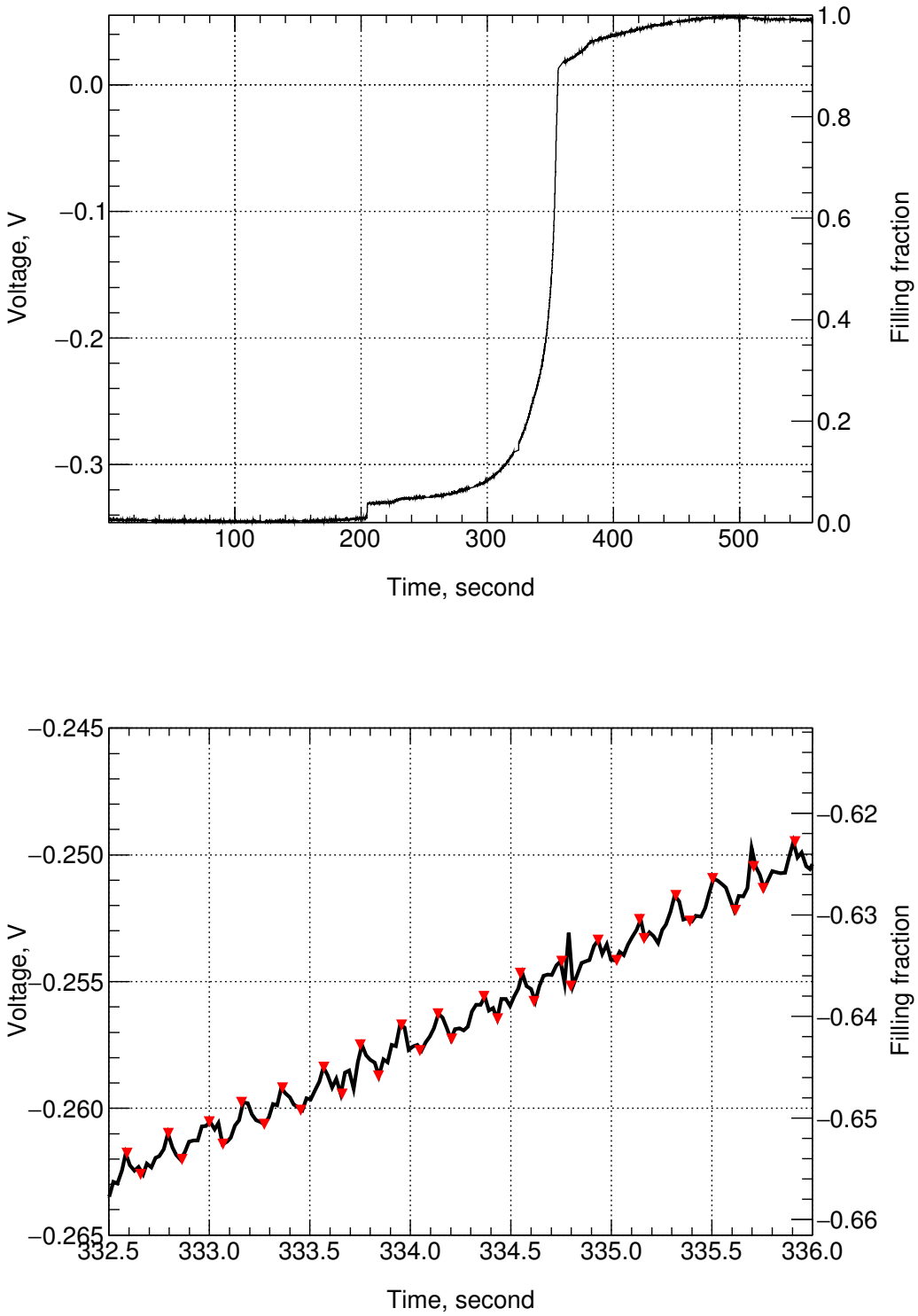


Figure 4.9: (Top): Voltage increases as the beaker is being filled. The drastic level increase at 200 seconds was caused by the adhesion of oil to the surface of the bottom copper plate of the sensor. The effect is thoroughly discussed in section 6.1.1. (Bottom): The periodic change is caused by the impact of oil droplets on the liquid surface. By analysing the crest and trough of the wave, the period, the amplitude, and the increase of voltage level in each drop are calculated.

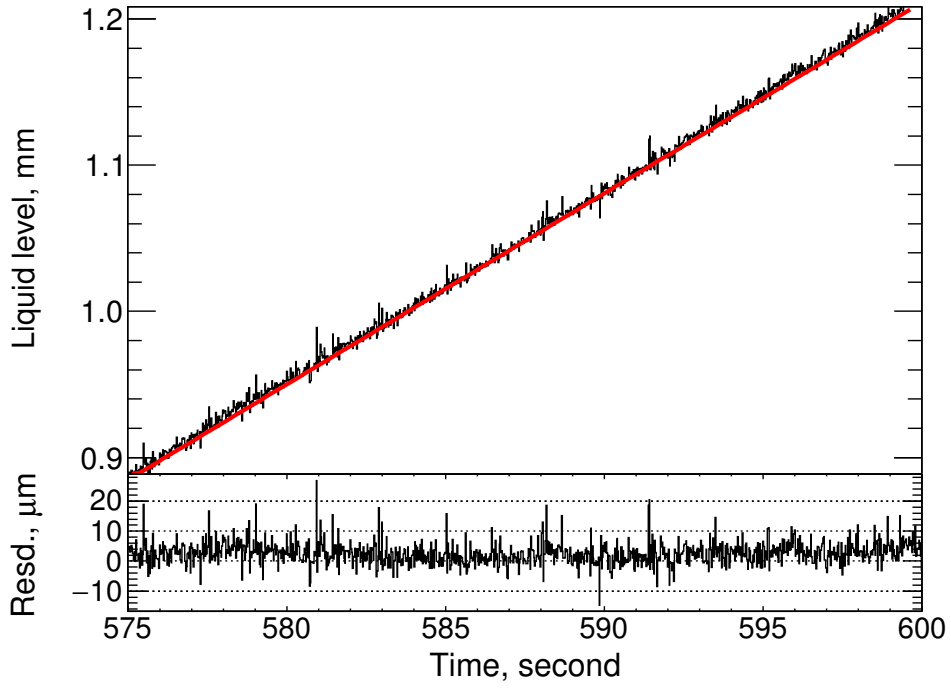


Figure 4.10: A straight line fits result of the HPPS oil-filling experiment in a chosen region. The graph beneath the fitting plot is the residual of the level displacement and the linear fit.

4.7.1.2 Vertical Parallel Rod Sensor (VPRS)

Level sensor with parallel rod geometry (figure 4.7 (Right)) was also tested. The sensor comprises equal length rods fixed by a PEEK structure and surrounded by a shielding box. As the liquid rises in the opening of the PEEK structure, the sensor picked up changes in C_{lvl}.

The experimental setup in figure 4.8 (Bottom Right) for VPRS is the same as that of HPPS. The sensor was fixed upright in a beaker with a nozzle attached to the beaker's wall. The oil within the cup above the beaker flow through the nozzle and gradually fill up the beaker. By comparing the measured liquid level to the measured voltage change, the sensor's performance can be evaluated.

Figure 4.11 (Top) shows the voltage variation due to the C_{lvl} change. A region of the data is selected such that it can be approximated with a straight line (see

figure 4.11(Bottom)). The result of the VPRS shows an 0.8 mm precision spanning a 100 mm detection range. The distribution of the residual gives the FWHM = $373.6 \pm 35.3\,\mu$m.

4.7.1.3 Conclusion on HPPS and VPRS

Both the HPPS and the VPRS have an excellent precision of liquid level measurement and were candidate geometries for the design of LZ level sensors. Comparing the geometry of the two sensors, the HPPS, however, is more favourable than the VPRS. The VPRS functions identically to the vertical version of the HPPS (described in Chapter 4 and 5) but requires a more intricate setup. For example, it was difficult to maintain the parallel wire geometry for C_{ref} and C_{lvl} if the length of the sensor exceeded 20 cm. Also, it is more challenging to model the C_{ref} of the VPRS because the fringe field of its electrodes couple to its guard cage. Such coupling increases the uncertainty in equation 4.13. Therefore, at this point, the R&D effort focuses on studying the design of level sensors with parallel geometry.

4.7.2 Medium Voltage Test

With the sensors at the LZ top-corner being close to the anode and gate, a preliminary test of the HPPS and the electronics under the influence of an applied electric field was carried out to understand their functionality. In principle, the electronics is immune to DC offset which is confirmed in high voltage tests in the LZ system test (discussed in Chapter 5). In the early development of the electronics used for prototype tests, a blocking capacitor C_{BC} was implemented to provide an extra layer of protection for the electronics. The setup of the electronics with

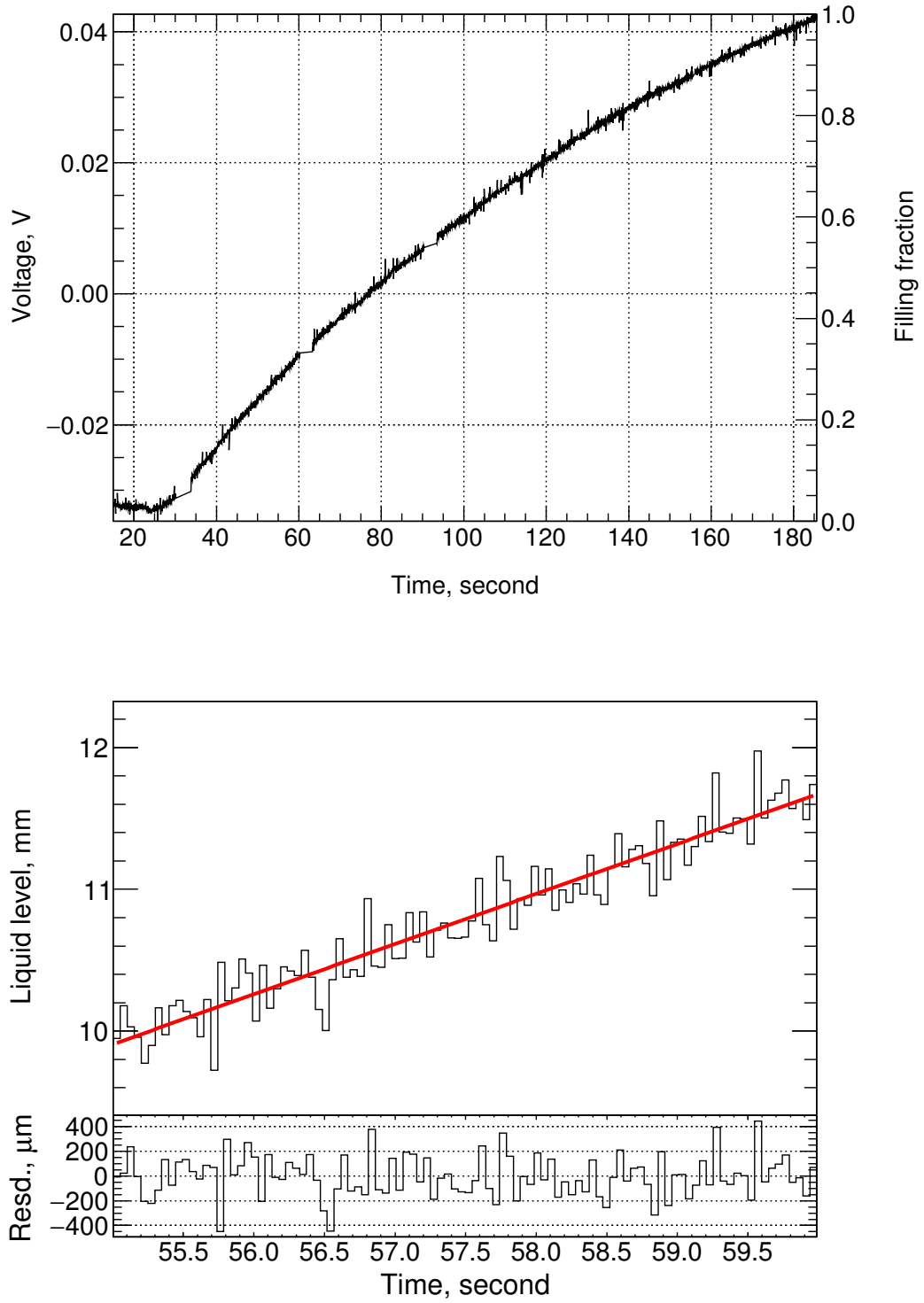


Figure 4.11: (Top): The increase of oil liquid level with time. (Bottom): The red line is a straight line fit to the data. Within this region, the residual difference between the data and the fitting is within $\pm 400\,\mu$m.

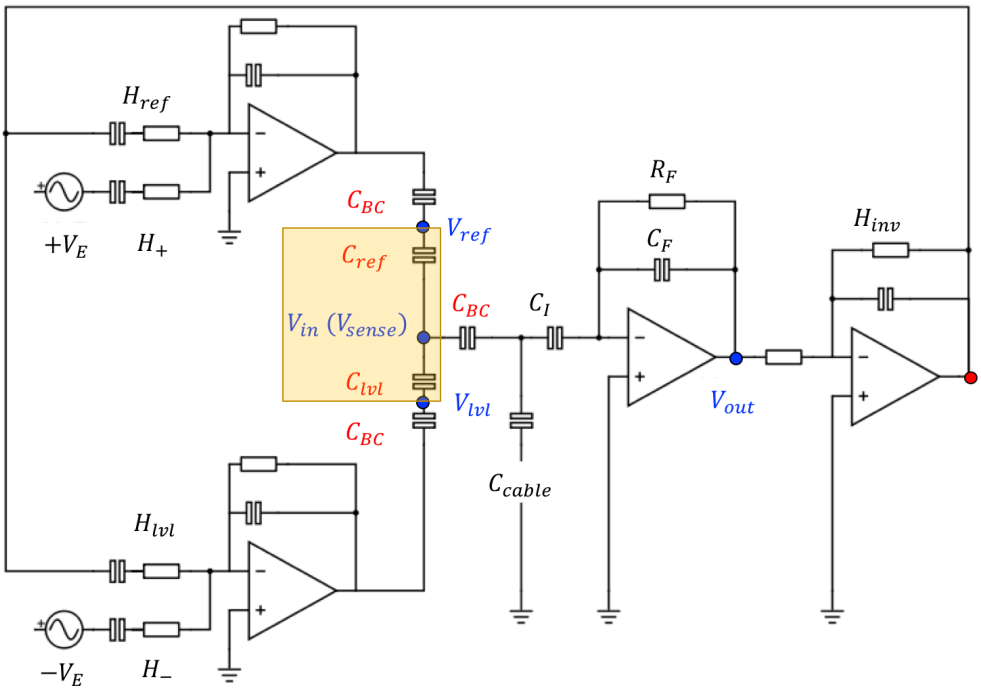


Figure 4.12: The circuit diagram with the implementation of blocking capacitors C_{BC}.

these capacitors is shown in figure 4.12). The C_{lvl} and C_{ref} in equation 4.10 can be rewritten to incorporate C_{BC} as

$$C_{lvl,\ ref+Blocking\ Capacitor} = \frac{C_{lvl,\ ref}}{1 + C_{lvl,\ ref}/C_{BC}}. \tag{4.15}$$

If the blocking capacitor $C_{BC} \sim \mathcal{O}(\text{nF})$, $C_{lvl,\ ref} \sim \mathcal{O}(\text{pF})$, and $C_I \approx 10\ \mu\text{F}$,

$$C_{ref,\ lvl} \approx C_{lvl,\ ref+Blocking\ Capacitor}. \tag{4.16}$$

Thus, the protection scheme will decouple the DC offset from any application of high voltages without introducing an extra term in our final readout in equation 4.10.

Figure 4.13 shows the setup of a HPPS liquid measurement under the presence

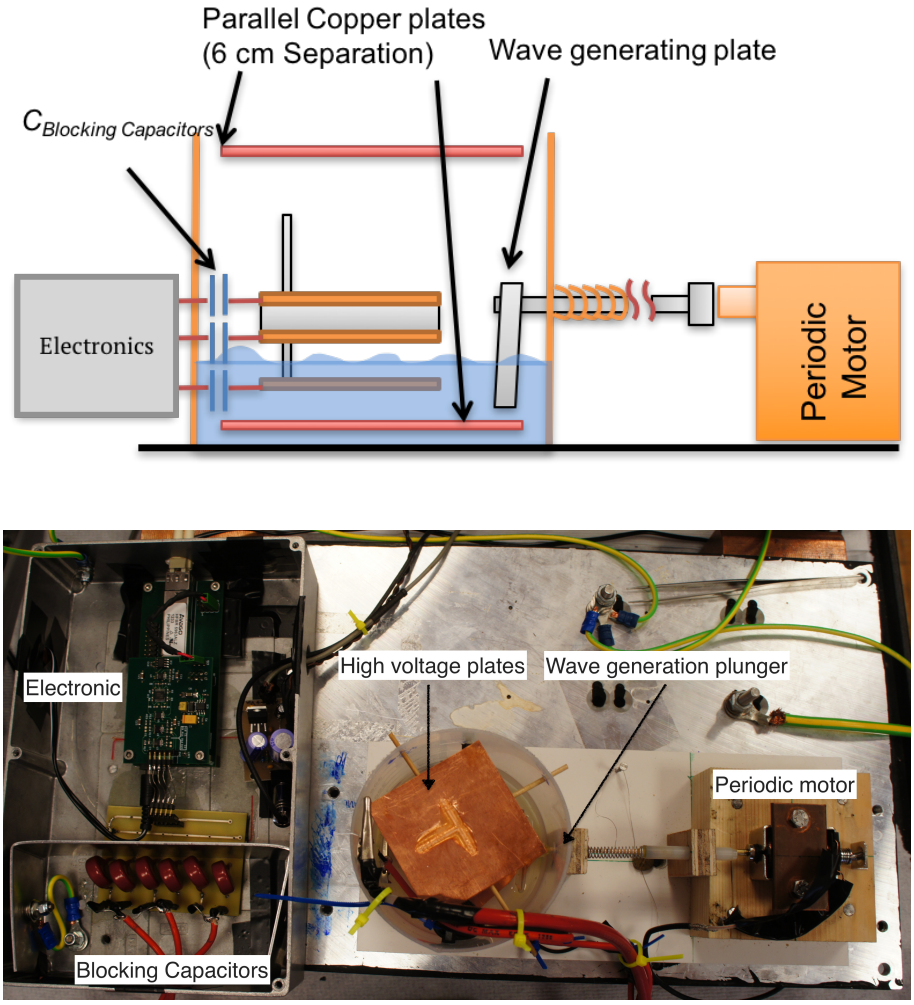


Figure 4.13: Preparation for a high voltage test experiment. (Top): The liquid level half filled the gap of the sensor. The motor, controlled by periodic pulses from a function generator, hit the plunger at 5 Hz to generate surface waves. (Bottom): Blocking capacitors were installed on a bridging PCB and connected to the electronic. Both the electronic and the testing setup were bolted onto a grounding plate and shielded within metal boxes during tests.

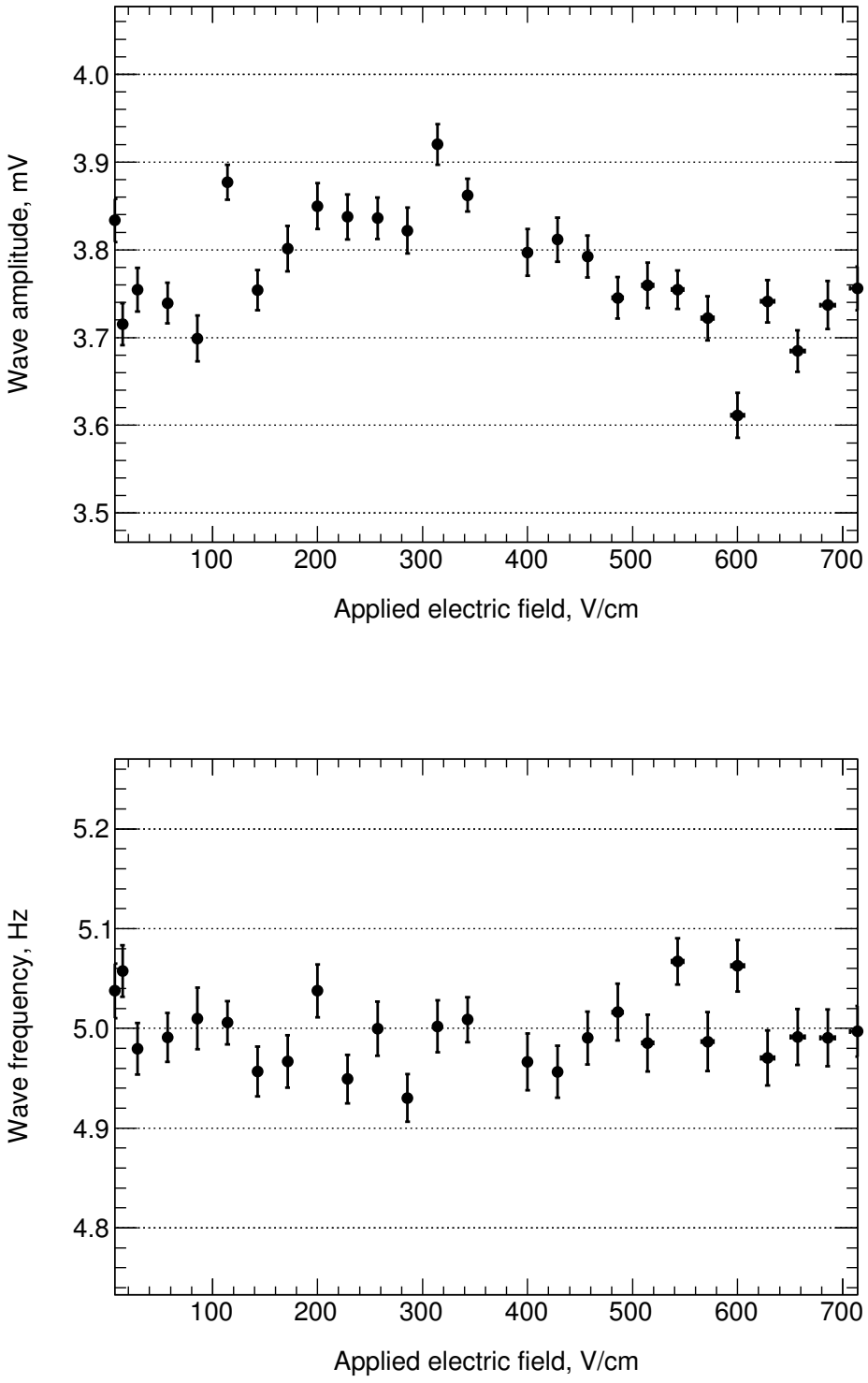


Figure 4.14: Errors of the data points are only statistical. (Top): The voltage amplitude of the periodic wave. (Bottom): The frequency of the detected surface wave while the motor was continuously hitting the rod at 5Hz.

of electric field. The electrodes of the HPPS were exposed to two $50 \times 50\,\mathrm{mm}^2$ copper plates installed above and below the sensor for applying the electric field. The mineral oil filled half of the gap (2.5 mm) of the sensor's C_{lvl}. A periodic motor driven by impulses from a function generator was placed beside the beaker to hit a long rod periodically. A plastic plate at the other end of the rod would vibrate the oil to generate waves. A shielding cage encapsulates the setup to ensure electrical safety.

Before high voltage was applied to the parallel plates, the motor tapped the rod at 5 Hz and generated surface waves in the beaker. The occurrence of periodic waves was confirmed with a high-speed camera. During the tests, while the motor kept tapping the rod at 5 Hz continuously and the sensor kept taking data, the voltage difference between the parallel plates was increased gradually from 0 to 5 kV. The applied voltage effectively means an applied field of $0 - 700\,\mathrm{V/cm}$ on the sensor.

The result of the medium voltage test demonstrates that the capability of a liquid level measurement is largely independent of the applied electric field near the sensor (figure 4.14). In the presence of such applied voltages, the periodic surface wave in the data is still prominent and has the amplitude and frequency of around $3.75 \pm 0.25\,\mathrm{mV}$ and $5.02 \pm 0.07\,\mathrm{Hz}$, respectively. As a result, the preliminary test proves the sensor's capability to work, at least, in an electric field ranging from $0 - 700\,\mathrm{V/cm}$.

4.8 Conclusion of Prototype Sensors

In this chapter, the development of the prototype level sensors for monitoring various parts of the LZ system is discussed. The causes of uncertainties of the S2 signal such as a tilted TPC, liquid surface oscillation, and circulation instability necessitates the installation of level sensors in the detector. The possibility of using the sensors to aid the correction of these uncertainties is also discussed. Furthermore, the techniques of liquid level measurements are summarised. One of the techniques - the capacitive sensor - is shown to satisfy the stringent requirements driven by the science goal of LZ. The requirements are further discussed in detail to illustrate the decision on the choice of material and the design of the sensor.

Next, a dedicated electronic readout scheme is developed. With the interference of cable capacitance at nanofarad level, the scheme allows precision measurement of capacitance changes (due to liquid level variation) at femtofarad level. The electronics also drives one of the general rules in designing level sensors. The design rules, motivated by the need of precision liquid level measurements, are then discussed.

Lastly, two prototype sensors, HPPS and VPRS, were constructed to conduct liquid level measurements in mineral oil. The sensors demonstrate excellent sensitivities at micrometre level ($\pm 10\,\mu$m for HPPS; $\pm 400\,\mu$m for VPRS). Such sensitivity confirms the capability of the electronics in providing a precision measurement. A further test of the HPPS in a medium voltage environment demonstrates that any liquid level measurement with the sensor is independent of the applied electric field. The result also confirms the possibility of operating level sensor around the

LZ top-corner.

Chapter 5

R&D at LZ System Tests

The prototype sensors discussed in Chapter 4 have proved to be a viable technology in precise liquid level measurement for a low dielectric constant medium. Here, the performance of the R&D sensors in monitoring LXe levels and their application in the two-phase TPC is presented. Data for demonstrating the capability and performance of these sensors were taken at Imperial College London (Imperial) and SLAC National Accelerator Laboratory (SLAC). The test systems at Imperial and SLAC are both two phase LXe TPCs. The Imperial chamber allowed a fast turnaround to enable multiple tests within short cycles of ~ 3 weeks. By design, the system did not have an online purification and circulation system to purify and circulate LXe simultaneously during runs. Nevertheless, it is thermodynamically stable during its filling and thus is ideal for studying the sensor's LXe response. As for the SLAC system, it is a scaled down version of the LZ system and tests components such as the circulation system, TPC weir structure, and the wire grids which will be used in LZ. Its online circulation and purification system allows continuous operation of the detector for months. Thus, it is suitable for studying

the application of sensors in an LZ-like system.

In this chapter, we discuss the systems tests at Imperial and SLAC and the systematics of the sensor response obtained from these tests. We first discuss the Imperial system. The design of the system and the level sensor, as well as the operation of the chamber, are described. We then report the study of the sensor's response in LXe and a purity study regarding the suitability of the sensor materials chosen. Next, we discuss the SLAC system. After a discussion on the design and the operation of the system and the sensor, we report the result of the application of the sensor in providing complementary information for stabilising the liquid surface of the TPC as well as for understanding the correlation of the liquid surface and the PMT signal. Lastly, we discuss the major systematic observed in these R&D sensors from both tests which paved the way to the final LZ level sensor described in Chapter 6.

5.1 System Test at Imperial College London

5.1.1 Design of the Imperial System

The chamber at the Imperial was thermodynamically stable during its filling and operation and thus provided a good chance to study the sensor's response to liquid xenon and to verify the choice choice of materials used in sensor construction is acceptable. The system shown in figure 5.1 (Left) was redeveloped from a prototype chamber that preceded ZEPLIN-III to study two-phase operation at high electric fields [118]. The new inner chamber was designed such that the whole cycle of preparation including LXe purification could be performed within

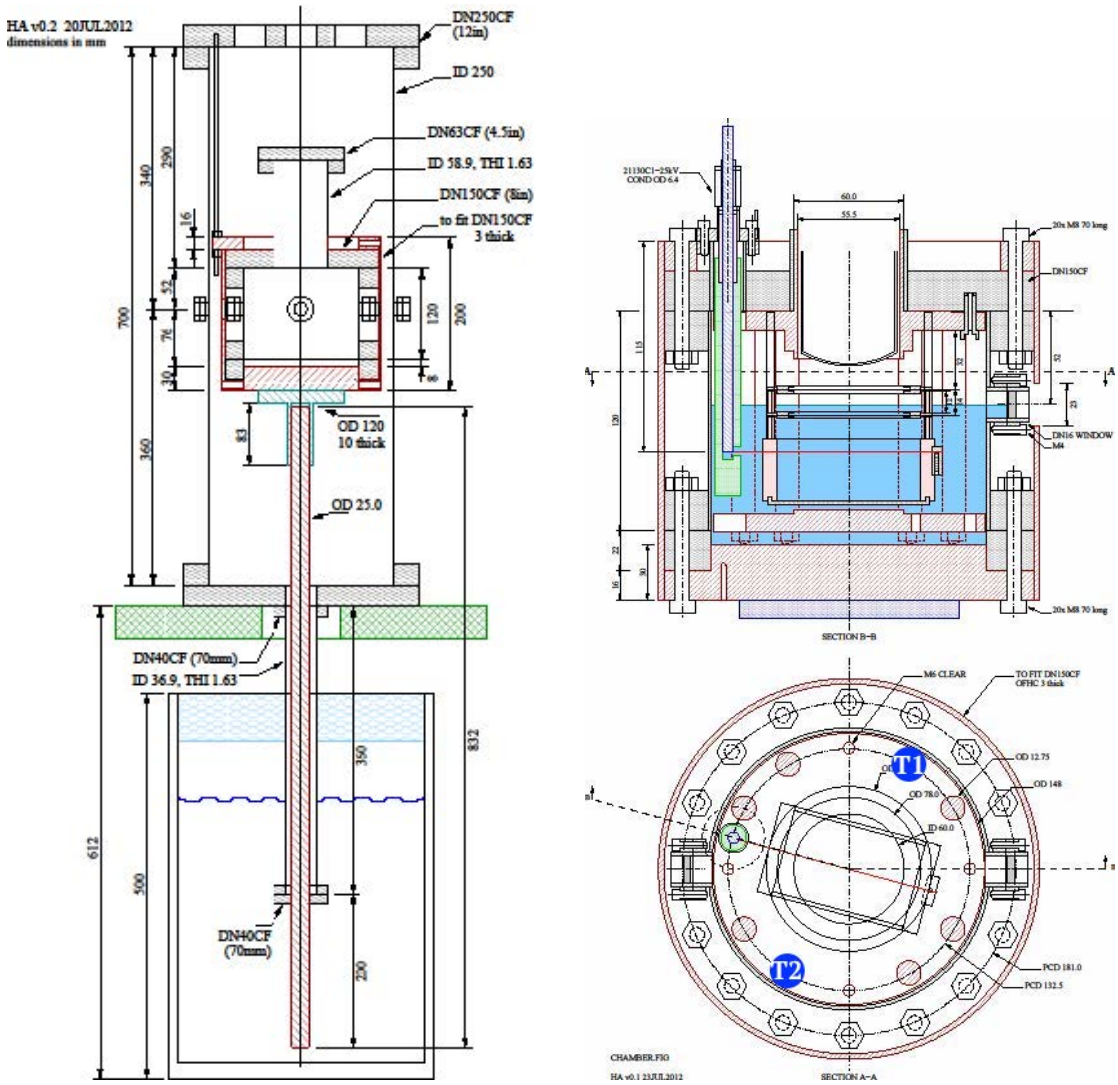


Figure 5.1: Schematic of the two phase chamber at Imperial College. (Left): The full chamber sitting inside a vacuum vessel had a cold finger attached to its bottom. The finger extended out of the vacuum space and was immersed in a LN_2 dewar. (Right): Detail of the chamber. The blue circles were the locations of two towers of sensors. Taken from [110].

2-3 weeks and the actual cool down and test could be performed within two days.

The inner vessel (figure 5.1 (Right)) was a two-phase xenon TPC with 4 kg of LXe, consisting of an anode, a gate, and a cathode for two phase operation. The cathode wire, supported by two mounting poles, sat 16 mm below a fully functioning electroluminescence (EL) region. The EL region, made of wired disks, formed a 12 mm gap between gate and anode. A single PMT installed at the top of the chamber observed scintillation in the chamber to study the emission of electrons on different cathode wires [110].

Various cold fingers in the systems were installed to cool down the chamber for two-phase operation. The main cold finger, which carried the 12 W cooling power, was attached to the base of the chamber and immersed in a LN_2 dewar beneath the vessel shown in figure 5.1 (Left). Another eight internal cold fingers in the chamber were attached to the base and distributed the cooling power uniformly to increase the thermal uniformity of the testing environment. The available cooling power, however, was not sufficient to allow continuous purification of the chamber during liquefaction or testing. The purity of the chamber was achieved by using low outgassing materials and by following thorough cleaning procedures of parts before their installation. This strategy, as shown in Section 5.2.3, maintained the required purity of LXe (electron lifetime $\gtrsim 20\,\mu$s).

The installation locations of the sensors were around the perimeter of the chamber. Ports in figure 5.1 (Right) carried the inlet and outlet of LXe and introduced high voltages to the wires. The blue circles in figure 5.1 (Right), marked T1 and T2, were the ports used for the installation of the sensors. Two towers (described in Section 5.1.2) comprised the level sensors and were inserted

through the ports and mounted onto two DN16 flanges. The towers were separated from the cathode poles and shielded between cold fingers to avoid interfering with the HV ramping tests.

To confirm the choice of materials used in sensor construction as acceptable, an electron lifetime monitor (ELM) from ZEPLIN-III was attached to the gas system. The ELM was partially filled with the LXe used after a run to measure the attenuation of the signal induced by alpha particle ionisation in a small cell. The charges produced in the gas xenon (GXe) within the cell were collected through an applied electric field and amplified by a charge amplifier. By studying the amplified charges, the survival probability of drifted electrons, thus the purity of xenon, was quantified. The purity of the xenon is used to infer the level of cleanliness of the material.

5.1.2 Sensors in Imperial Chamber

Two types of level sensor geometries, one with horizontal, the other with vertical parallel plates, were implemented. Figure 5.2 shows the design of the towers with level sensors in them. The tower consisted of a loop antenna (LA), an Imperial horizontal level sensor (IHLS), and an Imperial vertical level sensor (IVLS). Functions and results of LA are not within the scope of the thesis, and information regarding LA can be found in Ref. [60].

Two towers containing both IHLS and IVLS were installed in the chamber. Tower one (T1) had an LA at the top, an IHLS in the middle, and an IVLS at the bottom. Tower two (T2) had an IVLS at the top, an IHLS in the middle and an LA at the bottom. The measurement ranges of IHLS and IVLS were 5

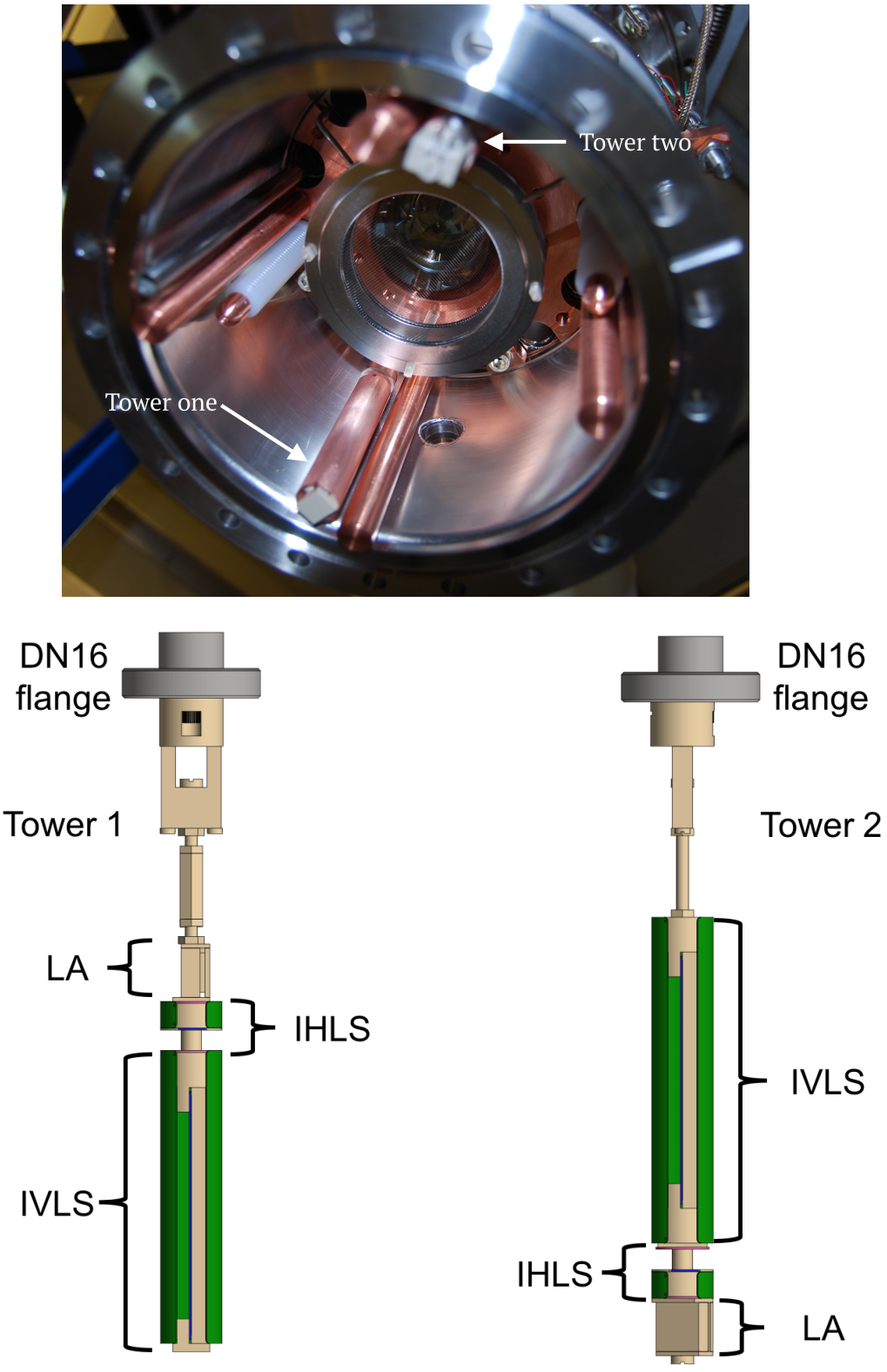


Figure 5.2: Inner look of the Imperial chamber and level sensors on two towers. (Top): The arrows indicate the installation locations of the first and second towers. (Bottom Left): Tower 1 with LA at the top, IHLS in the middle, and IVLS at the bottom. (Bottom Right): Tower 2 with IVLS at the top, IHLS in the middle, and LA at the bottom.

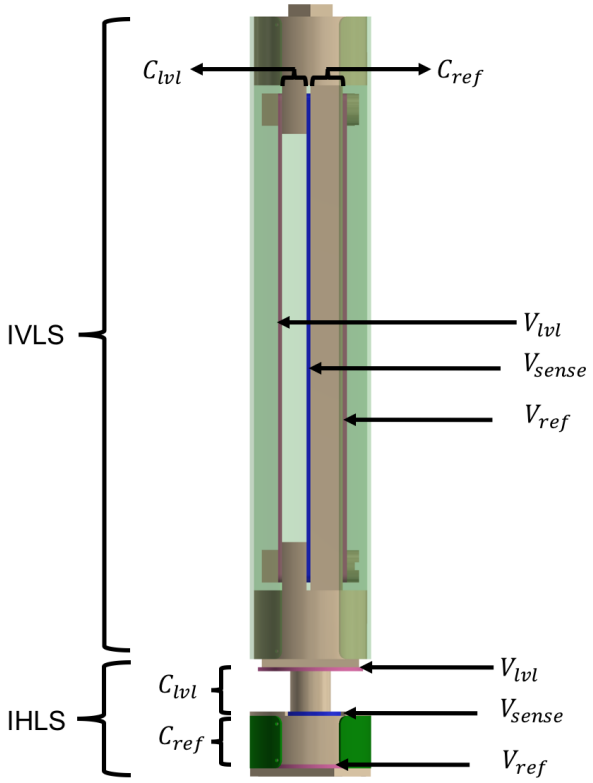


Figure 5.3: CAD drawings of Imperial level sensors. Excitation plates are in pink. Sense plates are in blue. Curved guard tubes are in green. (Top): IVLS. The area of plates is $A_{ref} = A_{lvl} = 429.25\,\mathrm{mm}^2$. The separate distances are $d_{ref} = 4\,\mathrm{mm}$, and $d_{lvl} = 3\,\mathrm{mm}$. (Bottom): IHLS. The area of plates is $A_{ref} = A_{lvl} = 125.5\,\mathrm{mm}^2$. The separate distances are $d_{ref} = 6\,\mathrm{mm}$, and $d_{lvl} = 5\,\mathrm{mm}$.

mm and 50.5 mm respectively. The IHLS and IVLS at the bottom of each tower were fully immersed in LXe as the liquid level reached the gate. T1 IHLS and T2 IVLS were partially filled to understand the liquid level between gate and anode. Therefore, the two towers provided complementary tests of the two types of sensors for understanding their response to LXe.

The high voltage constraint required the installation of sensors such as to avoid scratches on the surface of the inner vessel. The scratches could create sharp edges which could contribute to electron emission background in the wire test [110]. This issue was tackled via inserting the towers directly into the chamber through the DN16 flanges around the perimeter of the vessel. The method allowed the

installation of the towers from the the vacuum space without any operation inside the chamber and thus reduced the risk of scratches. The method, although very effective in reducing the risk of scratching, confined the diameter of the sensors to that of the DN16 port.

Figure 5.3 shows the geometry of the IHLS and IVLS. The optimisation of the sensors followed equation 4.14 to extract parameters to define the sensor's C_{ref} and C_{lvl}. The IHLS comprised three signal plates - sense, positive excitation, and negative excitation. The negative excitation plate and sense plate, separated by a PEEK spacer, formed C_{lvl}. The sense plate and the positive excitation plate, separated by a PEEK disc and shielded by a curved guard plate, formed the C_{ref}. As for the IVLS, the structure of it was identical to that of the IHLS. PEEK spacers and plates filled the gaps between vertical electrodes to form its C_{lvl} and C_{ref}. A grounded curved plate surrounded the plates of the IVLS to provide shielding of the sensor's signal. Due to the space constraint of the DN16 port, the IHLS did not have a guard electrode in place. The IVLS, on the other hand, used the grounded curved plate around it to serve as a guard electrode to decrease stray capacitance.

5.1.3 Imperial System Operation in Run 5

The operation of the Imperial test comprised six stages - chamber cooling, LXe filling, wire emission tests, LXe emptying, chamber warm up, and electron lifetime test with ELM. The first five stages of the operation were within the Imperial chamber. The data of slow control sensors' readings in Run 5 are shown in figure 5.4. We concentrated our data taking of level sensors during the detector cooling

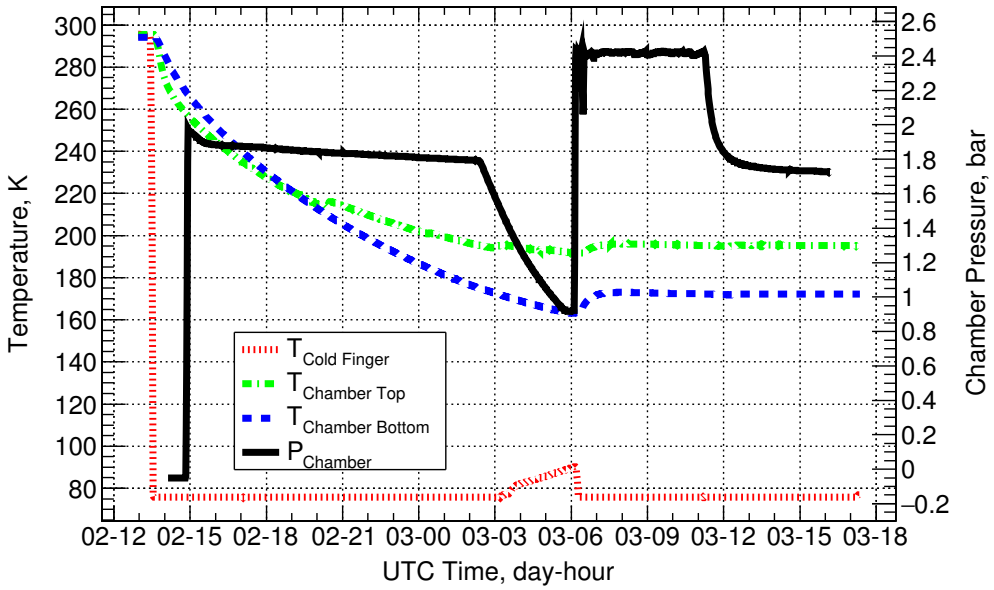


Figure 5.4: Slow control data of the chamber in the Run5 sensor test. Due to the lack of an online purification system, the temperatures of the chamber are taken from thermometers attached to the top and the bottom outside the inner vessel

and filling since these were the most stable stages of the chamber to study sensor responses. The sixth stage, electron lifetime test, was carried out after the run with a small sample of LXe used in Run 5.

The first stage was the detector cooling. The cooling power of the system came from thermal cycling of the long cold finger beneath the chamber with a bucket of LN_2. Around 02-14 day-hour in figure 5.4, the finger was cooled to LN_2 temperature. The temperatures at the top and bottom of the chamber started to drop subsequently. Around 02-15 day-hour, the chamber was filled with xenon gas to a pressure of 2 bar, which helped components in the chamber to exchange heat more efficiently. Between 03-02 day-hour and 03-06 day-hour, the chamber reached thermal equilibrium, and its pressure and temperature were saturated and varied along the xenon vapour equilibrium curve in the phase diagram shown in Figure 3.1. The cold finger started to lose cooling power at 03-03 day-hour

but resumed to provide cooling power around 03-06 day-hour by replenishing the bucket with LN_2.

Next, the filling of the chamber commenced around 03-06 day-hour. The xenon gas pressure of the detector was set to 2.4 bar which drove the chamber to be in liquid xenon condensation phase. The temperature of the chamber rose immediately to reflect the increase of pressure but was prevented from further rises by the cooling from the cold finger. Thus, the chamber was maintained at the condensation phase. Between 03-06 and 03-08 day-hour, the chamber warmed up slightly from 163.5 K to 173.2 K. After then, until the end of the filling at 03-12 day-hour, the temperature and the pressure of the chamber dropped from 173.2K to 172.2K and plateaued at 2.4 bar, respectively. At 03-12 day-hour, we stopped the filling process and set heaters to stabilise the chamber at 173 K. Around 03-14 day-hour, the chamber's pressure had decreased moderately and realigned along the vapour curve of the phase diagram. Then, the wire tests lasted around 4 hours between 03-14 day-hour and 03-18 day-hour. The cathode, gate, and anode were biased at a few kV. After the test, we cooled a xenon storage vessel to LN_2 temperature and retrieved the xenon from the chamber.

During the cooling and filling of the chamber, owing to only one set of a prototype readout electronics[1] available, only one of the two sensors on each tower was taking data. When the chamber was cooling down, T1 IVLS and T2 IHLS were taking data to examine the temperature dependence of the sensors. At the beginning of the filling from 03-07 day-hour, the two sensors kept taking data. Around 03-09 day-hour, since T2 IHLS is filled, we stopped its data taking and

[1]The prototype electronics was analogue and readout capacitances using the equation 4.10. It was used in both system tests at the Imperial and the SLAC.

initiated the data taking of T2 IVLS. LXe covered T1 IVLS around 03-11 day-hour and we subsequently enabled the data taking of T1 IHLS.

5.2 Result of Imperial System Test

5.2.1 Chamber Cool Down

The data of T1 IVLS and T2 IHLS during the cool down helped identify temperature-related issues with the variability of the permittivity of PEEK and contraction of materials when cooling. In general, the temperature effects are more prominent on IHLS than IVLS.

T1 IVLS' data shows around 4 % variation when the sensor was cooled down. In figure 5.5 (Top), the dip between 02-15 day-hour and 02-17 day-hour could be caused by a mix of effects from PEEK shrinkage (CTE of PEEK is 55 ppm/K [104]) and the temperature dependence of PEEK's dielectric constant ε_{PEEK} [119]. Because of the exchange of GXe, the chamber was cooled down rapidly at the beginning of the process. Although the GXe facilitated the cooling, different parts in the chamber were not yet at thermal equilibrium. The shrinkage of parts could be disproportional and increase the C_{lvl} which led in the observed decline after 02-15 day-hour. As for the bounce after 02-16 day-hour, it comes from the moderate temperature dependence of ε_{PEEK} which decreased further as the chamber temperature became lower [2]. The ε_{PEEK} decline caused the reduction of C_{ref} and thus resulted in a fluctuation of the readout signal. After the dip, the two

[2]The dielectric constant of plastics is known to be proportional to temperature changes [119]. Measurement with amorphous PEEK at 1 kHz shows its dielectric constant decrease by$\sim$ 2 % when its temperature reduces from room temperature to 173 K. Between 165 $\sim$ 185 K, the general operation temperature of LXe TPCs, the change of ε_{PEEK} is smaller than 0.4 % [120].

effects could compete with each other between 02-18 day-hour and 03-02 day-hour and fluctuated the readout. When the chamber reached thermal equilibrium after 03-02 day-hour, the effect of ε_{PEEK} was subordinate to the shrinkage effect which contributed to the final decrease of the readout.

As for the T2 IHLS, its readout in figure 5.5 (Bottom) exhibits a clear correlation with changes of chamber temperature. The sensor's reading decreased by 18.7 % when the bottom chamber temperature changed from 285 K to 163 K. The changes mostly come from the shrinkage of PEEK parts in the sensor. If the temperature of the chamber drops by 120 K, the expected changes of C_{lvl} and C_{ref} in the IHLS are 3.3 % and 7.9 %. By considering the error propagation of equation 4.10 of the electronics, the calculated variation with C_{ref} and C_{lvl} is 10.6 %, not far from the observed decrease.

Even though it is difficult to use a qualitative explanation for correcting temperature systematic effects, the effects do not prohibit the use of the sensor to measure the liquid level. Given the temperature gradient of the operation around 170 ± 5 K, the variation of the signal due to the temperature effects is expected at ~ 0.35 % for IVLS and ~ 1.5 % for IHLS. Once the chamber is thermodynamically stable, the signal of a sensor, by design, depends more on the change of a LXe-filled C_{lvl} as shown in Section 5.2.2.

5.2.2 Liquid Xenon Filling

In Run 5, T1 IVLS, T2 IHLS, and T2 IVLS measured the LXe filling the chamber. Their data were evaluated to study the precisions and systematics [3].

[3]Liquid level did not reach T1 IHLS. Thus, it was not used in the evaluation

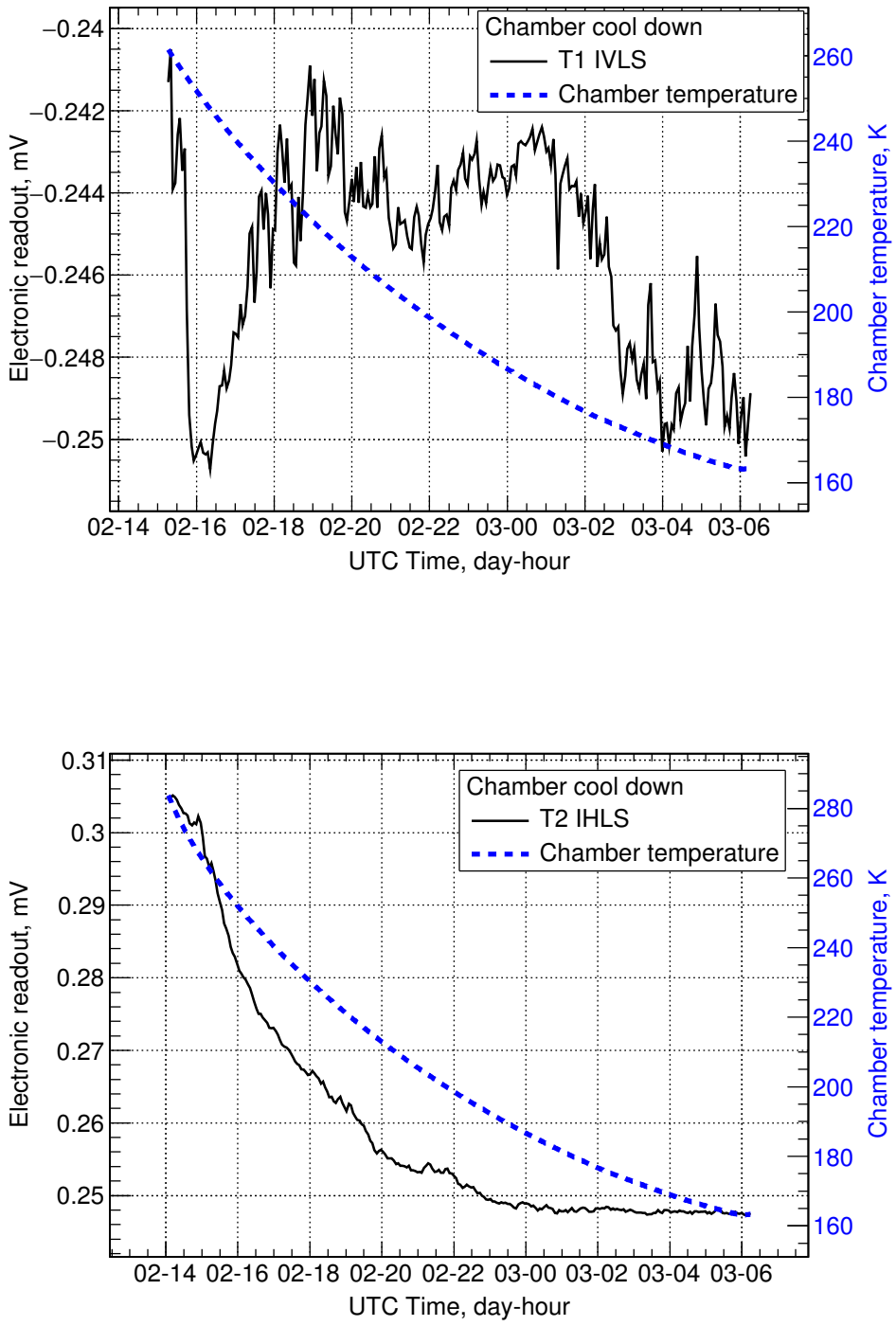


Figure 5.5: Electronic readout of sensors during the cool down process in Run5. (Top): T1 IVLS. (Bottom): T2 IHLS.

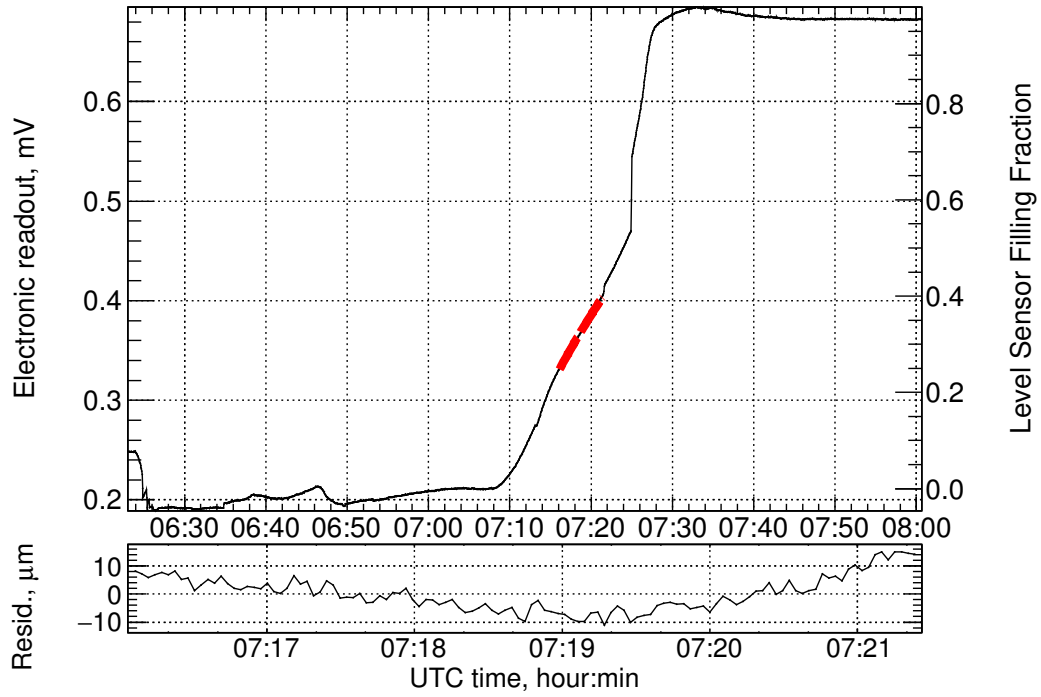


Figure 5.6: Data of the T2 IHLS. The dashed red line is the fitting of equation 5.1. Due to features caused by capillary effects, the fitting range was constrained to a smaller section.

The data of T2 IHLS filling in figure 5.6 shows multiple features due to LXe condensation. The features of the drastic drop before 06:30 hour:min and the bump between 06:30 and 07:00 hour:min in figure 5.6 were due to rapid pressure changes which led to phase changes of xenon. The chamber pressure, at the beginning of the filling, was increased to 2.45 bar within a few minutes. Because the chamber temperature was at 163 K, the pressure increase enabled gas xenon to condense quickly and that resulted in a gentle increase of chamber temperature. The temperature rise vaporised the pre-condensed xenon on the sensor. The vaporisation contributed to the reading drop before 06:30 hour:min. After that, the pressure was stable; the chamber reached its thermal equilibrium state. The stabilised chamber allowed LXe accumulation on sensor plates again. Such accumulation produced the features before 7:00 hour:min. Then, the T2 IHLS began

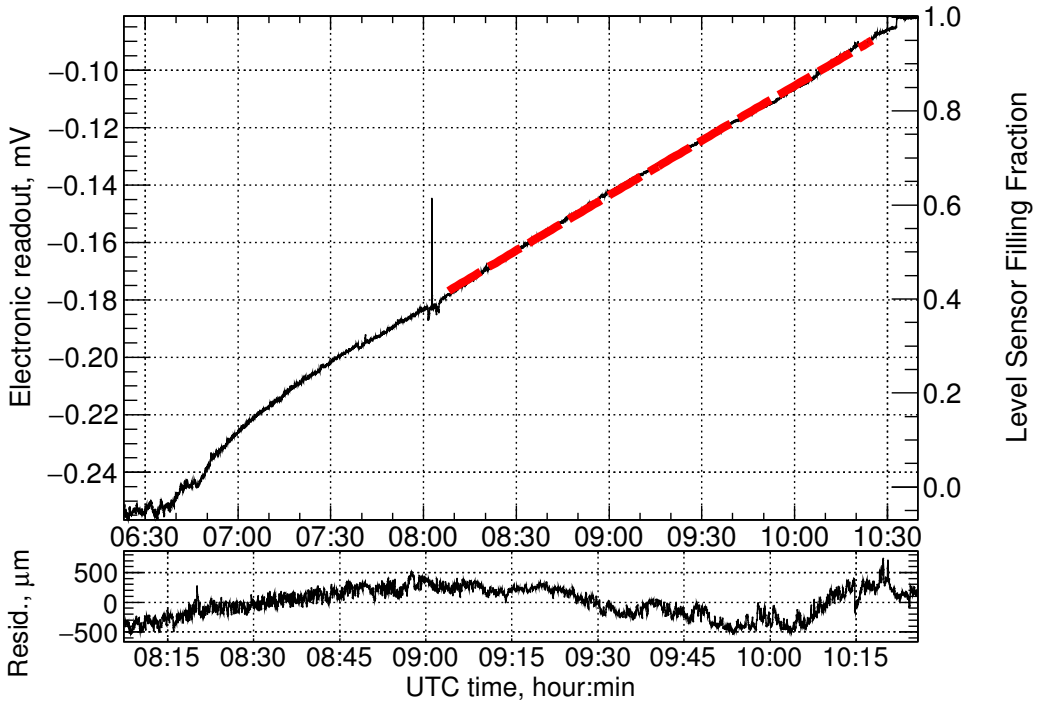


Figure 5.7: Data of T1 IVLS. Because of the non-uniform filling rate at the beginning of the filling process, we chose a range after 09:00 hour:min to perform the fit fit shown as a red dashed line. The spike at 9:00 hour:min was due to an interference from the electronics of T2 IVLS.

to see liquid level around 07:00 hour:min. The sensor exhibited an exponential response between 07:10 and 07:15 hour:min owing to the meniscus effect of LXe. The effect diminished after 07:15 hour:min; the sensor detected a linear increase of liquid level before experiencing a drastic rise of level between 07:25 and 07:35 hour:min. Subsequently, the sensor shows a moderate decrease response due to the fringe field effect which increases the C_{ref} of the sensor.

The filling data of T1 IVLS and T2 IVLS are shown in figure 5.7 and figure 5.8, respectively. Before their filling processes, both sensors experienced precondensation of xenon on their spacers; the condensation contributed to the features of small pedestals. After that, the sensors went through a stable filling period. The T1 IVLS detected a drastic rise of liquid level from the capillary

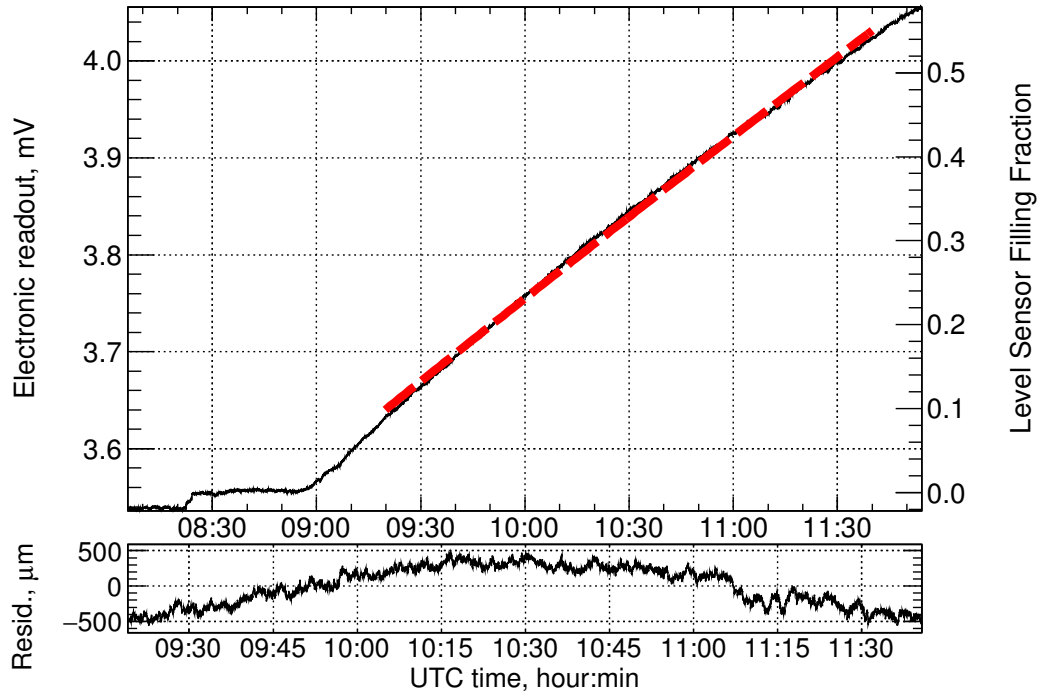


Figure 5.8: Data of T2 IVLS. The stepping feature before 9:00 hour:min was due to pre-condensation of LXe on the spacer of the sensor. The red dashed line is the fit using the equation 5.1.

effect around 10:30 hour:min in figure 5.7 (similar to the feature in T2 IHLS at 07:25 hour:min in figure 5.6). This effect was not observed in the T2 IVLS because the LXe did not completely submerge the sensor.

To extract the sensors' precision and understand the systematics, the data of the sensors were fitted to a modified equation 4.10. The fitting function can be expressed as

$$V_{out}(z) = \frac{C_{lvl}(z) - C_{ref}}{C_{lvl}(z) + C_{ref} + K} \cdot V_{in} + V_0, \tag{5.1}$$

where V_{in} is the electronic excitation, V_0 contains the electronic offset due to electronic component differences, and K includes the contribution from the feedback capacitor and the suppressed cable capacitance. The $C_{lvl}(z)$ term depends on the

geometry of the sensor. For IVLS, the term is

$$C_{lvl}(z) = z \cdot (\frac{\varepsilon_{liq} - 1}{L}) \cdot C_{liq} + C_{lvl}(z = 0), \tag{5.2}$$

where $\varepsilon_{liq} = 1.89$ is the dielectric constant of LXe, $L = 50.5\,\text{mm}$ is the measurement length of the sensor, $C_{liq} = 1.266\,\text{pF}$ is the liquid measurement section in C_{lvl} calculated based on the parallel capacitor equation, and $C_{lvl}(z = 0)$ is the measured capacitance in GXe. As for the IHLS, the $C_{lvl}(z)$ term is

$$C_{lvl}(z) = \frac{z}{(\varepsilon_{liq} \cdot d)/(\varepsilon_{liq} - 1) - z} \cdot C_{liq} + C_{lvl}(z = 0), \tag{5.3}$$

where $C_{liq} = 0.202\,\text{pF}$, and $d = 5\,\text{mm}$ is the measurement gap of the sensor. Assuming the filling rates during the sensors' filling were constant at a short period, the liquid level z in the equation can be rewritten as

$$z = R(t - t_{ref}) + z_{ref}, \tag{5.4}$$

where R is the filling rate, t_{ref} and z_{ref} are reference points of a UTC time and liquid level height. The fitting function constrains the number of unknown variables to two, i.e. R and V_0, by allowing input parameters of L, ε_{liq}, C_{liq}, C_{lvl}, C_{ref}, t_{ref}, and z_{ref} from independent measurements or calculations.

Table 5.1 contains the result of the fitting using capacitance values of C_{ref} and C_{lvl} from table 5.2. The fitting result revealed that the filling of the chamber was slow and stable (at $\mu\text{m}/\text{s}$ level) but affected by the chamber's thermal profile and geometry. In general, because of higher cooling power in the beginning, the filling

	T1 IVLS	T2 IVLS	T2 IHLS
Filling rate$R$, μm$\cdot s^{-1}$	3.058 ± 0.002	1.562 ± 0.001	5.832 ± 0.025
V_0, mV	$-0.072 \pm 1.6\text{E}^{-5}$	$5.406 \pm 2.2\text{E}^{-4}$	$2.058 \pm 6.2\text{E}^{-4}$
K, pF	57.427	1.068	1.068
V_{in}, mV	9.864	9.864	9.864
z_{ref}, mm	48	48	27
t_{ref} in UTC time, second	1438678445	1438678445	1438672085

Table 5.1: Fitting parameters of the sensors. The error are statistical. The filling rate R and the voltage offset V_0 were left unconstrained, the rest of the variables were fixed in the fitting process. The higher cooling power in the beginning of the filling process led to a different filling rates on the sensors.

	T1 IVLS	T2 IVLS	T1 IHLS	T2 IHLS
Measured C_{lvl}, pF	1.90 ± 0.03	-	0.428 ± 0.004	-
Measured C_{ref}, pF	3.54 ± 0.05	-	0.388 ± 0.004	-
Expected C_{lvl}, pF	1.61	1.61	0.263	0.263
Expected C_{ref}, pF	3.42	3.42	0.567	0.567

Table 5.2: The capacitance of the sensors at room temperature without any LXe filling. The errors of the capacitance are statistical only. The expected capacitance was calculated under the assumption that the sensors were ideal parallel plate capacitors. However, the arrangement of guard electrodes increases (decreases) the electric field coupling between the sense plate and the excitation plate which leads to the increase (decrease) of the expected capacitance (see Section 6.2.1.2). The Post-measurements were performed with final LZ electronics which uses equation 4.11 instead of equation 4.10 for measurements. Unfortunately, cables of sensors on T2 were detached after Imperial Run 5. Thus, the fitting for the T2 sensors were performed with capacitance values measured with the T1 sensors.

rate was faster than that near the end of filling. Furthermore, given the stability of the chamber's pressure after 8:00 hour:min, i.e. a steady mass flow rate, the changes of the cross section area of the chamber for LXe could lead to changes in local filling rate which resulted in the features of the residual for IVLS'. For example, in the T1 IVLS result, the residual feature at 10:00 hour:min coincides with the LXe level that reached the cathode delivery pole. The pole caused the decrease of the area and the temporal increase of filling rate.

After all, the result of the chamber filling demonstrates the sensor's capability of measuring LXe level changes. The fitting complementarily proves the filling

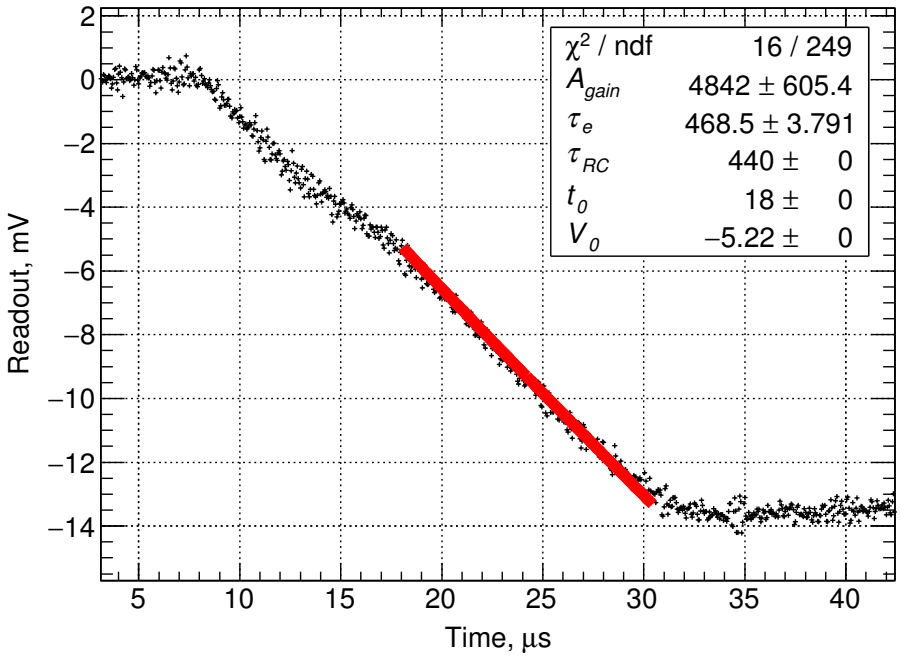


Figure 5.9: Data of the ELM test after the run of the sensors. The feature of slope changes in the pulse was caused by ionisation electrons crossing GXe/LXe interface. The pulse eventually increased back to 0 mV (not shown here) due to the release of charges in a feedback capacitor of the charge amplifier. Data courtesy of Alfredo Thomas.

process was stable. By comparing the data to the fitting curves, the residuals also suggest that the precision of IHLS and IVLS were around $\pm 10\,\mu$m and $\pm 500\,\mu$m over ranges of 5 mm and 50.5 mm, respectively.

5.2.3 Electron Lifetime

Another crucial test of the sensor in the Imperial Chamber is to understand the cleanliness of the sensor's material with ELM. The cleanliness of the LXe depends on the level of impurities from the sensor materials. The impurities are mostly electronegative substances which attract electrons efficiently and thus attenuate the electron lifetime.

The lifetime can be quantified with the waveform data from the ELM test (see

figure 5.9). The data is the development of a pulse caused by ionisation electrons travelling across the GXe/LXe interface in a scintillation cell. The charge is collected by a charge amplifier. If the charges are not attenuated by the electronegative impurities, the waveform will exhibit a straight line feature that suggests a electron lifetime much greater than the maximum allowed drift time in a cell. Any deviation from a straight line behaviour is attributed to a finite electron lifetime τ_e. The lifetime can be extracted with a function,

$$V(t) = A \cdot (\exp(-(t - t_0)/\tau_e) - \exp(-(t - t_0)/\tau_{RC})) + V_0, \tag{5.5}$$

where τ_{RC} is the time constant of the amplifier, A is the amplifier's gain, t_0 is the start time, and V_0 is the offset of readout voltage. Because of different drift velocities in GXe and LXe that resulted in different slopes for times between ~ 7 and $\sim 17\,\mu$s and ~ 17 and $\sim 30\,\mu$s in the waveform, only the section in the data influenced by LXe was fitted. The fit returned a $\tau \sim 468.5\,\mu$s, which was beyond the sensitivity of the instrument ($\tau \sim 100\,\mu$s, the maximum allowed drift time in the cell). By conservatively taking the lifetime of the instrument's sensitivity as that of the run, i.e. $\tau \approx \tau_{Run5} \approx 100\,\mu$s, the survival probability for an electron that is drifted for a time of $15\,\mu$s is $\sim 86\,\%$.

In conclusion, given the result of the electron lifetime test of a sample from the 4 kg LXe used in the chamber for 12 hours, the presence of the sensors (~ 200 grams in total with 90 % PEEK and 10 % copper) is compatible with the detector's ability to extract electrons [4]. The long lifetime indicates that the material and components of the sensor are suitable to be used in LXe.

[4]In LZ, 7 tonnes of LXe will be circulated within 1.8 days and be flowing through 7 level sensors (~ 2000 grams in total with 3 % PEEK and 97 % copper) continuously.

5.3 System Test at SLAC

5.3.1 Design of the SLAC Phase-I System

The SLAC system tested and assessed the performance of the proposed configuration of the LZ detector in terms of the handling of xenon circulation, the design of the reverse field region and drift region, the grids, and the top-corner region [60]. It provided an ideal environment to understand the application of precision level sensors during the normal operation of the proposed LZ extraction region. Figure 5.10 shows the configuration of the test stand consisting of three major units, namely, a purification system, a xenon circulation system, and an LXe TPC; the TPC is shown in figure 5.11 with its top-corner region in detail in 5.12.

The design of the circulation and purification system followed key features of the LZ architecture to prove the capability of handling and purifying $>$ 100 kg LXe. The circulation system consists of a sub-cooler, a weir reservoir, and a two-phase heat exchanger (2PHX). It connects the LXe circulation loop between the TPC vessel to the purification tower. The LXe circulation loop starts at the weir reservoir. The outgoing LXe, collected in the reservoir, is transported to the 2PHX and is vaporised to form cold GXe through exchanging heat with warm GXe. The cold GXe is then moved to the gas heat exchanger and is further heated by the returning hot GXe from the purification system. After the gas exchanger, it enters the purification system and passes through a getter for removing electronegative substances. The returning hot GXe from the getter follows a path opposite to the outgoing LXe. It travels from the purification system, passes along the heat exchangers, and ends up in the sub-cooler. By the time the returning hot GXe

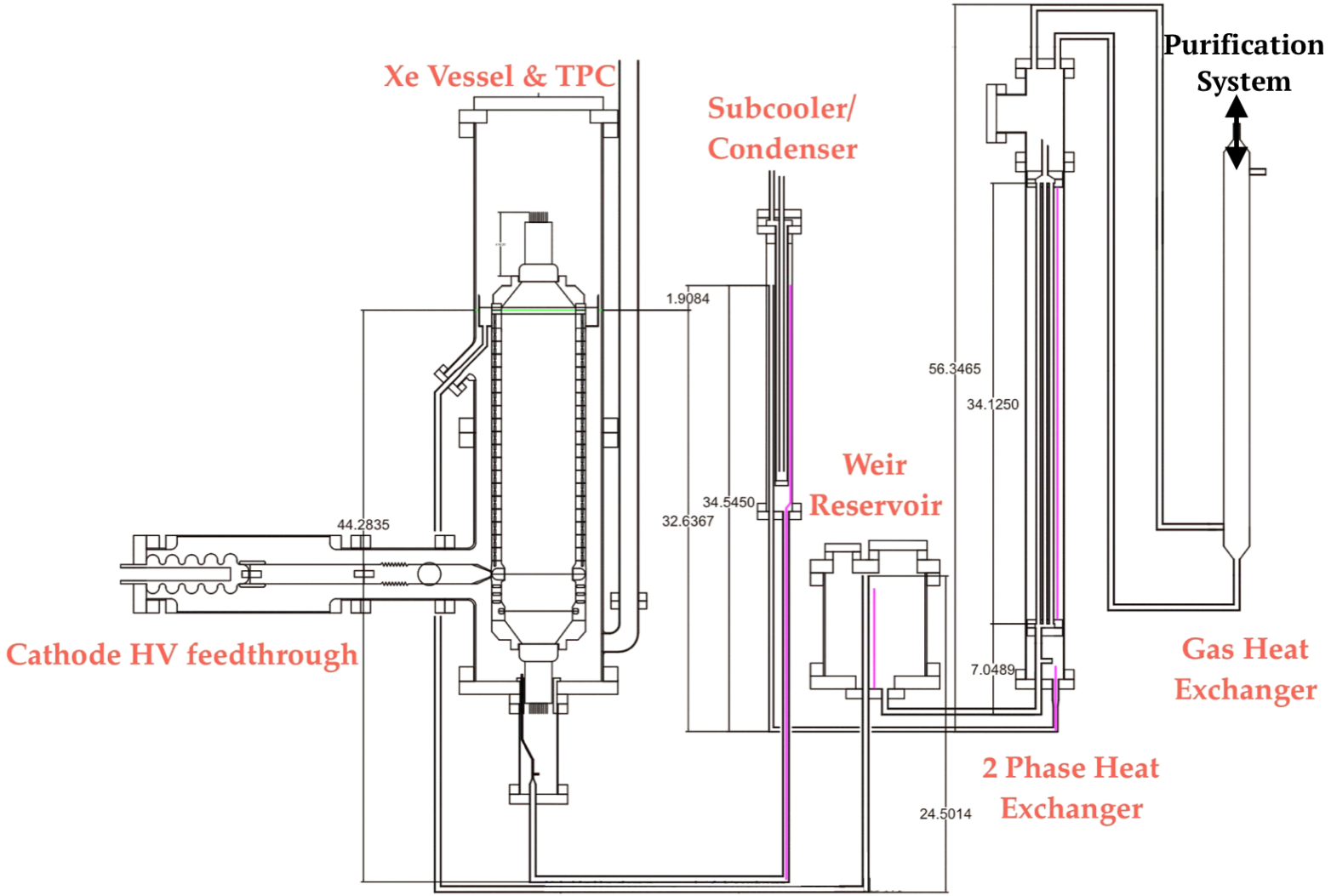


Figure 5.10: Overview of the system test detector system. Reproduced from [121].

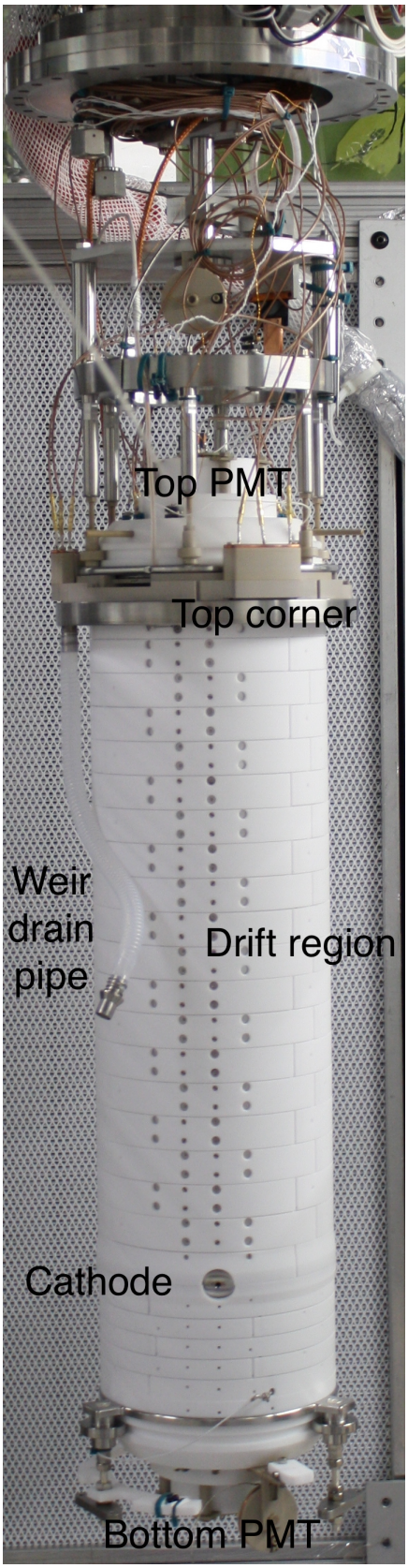


Figure 5.11: SLAC Phase-I system test TPC

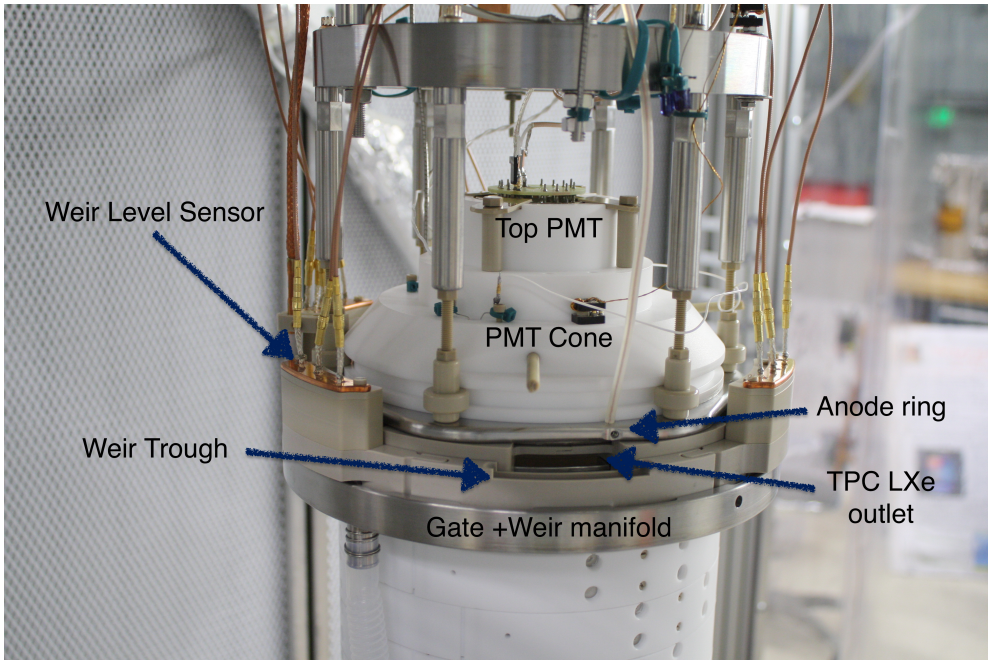


Figure 5.12: SLAC top-corner structure in Run 3-6 of the Phase-I system test. The top-corner structure forms the the extraction region for S2 production. The skin region, following the convention of that in the LZ TPC top-corner, is generally the GXe/LXe region outside the extraction region and drift region of the TPC. The LXe that overspills into the weir trough returns to the circulation and purification system through the weir drain pipe.

enters the sub-cooler, it has become cold GXe. The sub-cooler, powered by the thermal circulation of liquid nitrogen, condenses the cold GXe to LXe. The LXe in the cooler is then transported back to the bottom of the main TPC. As the LXe in the main TPC reaches the weir, it spills over into the weir trough and enters a weir drain pipe (shown in figure 5.12) which connected to the weir reservoir for another circulation and purification cycle.

The SLAC TPC is shown in figure 5.11. Two 3-inch R11410 PMTs is installed at the top and bottom of the TPC to look at the drift region and the extraction region. The drift region, about 1 m tall, resembles the LZ TPC described in Section 3.2.1 and is made of PTFE reflectors, field shaping rings, and a cathode grid, forming the drift region to transport ionisation electrons. The extraction region, formed by the top-corner structure shown in figure 5.12, is beneath the top PMT.

The top-corner structure comprises three main elements: the gate/anode rings to form the extraction region, the weir structure and the gate manifold to facilitate LXe circulation, and precision level sensors. The weir structure, in particular, the weir troughs installed on the gate manifold, is responsible for limiting the height of the liquid level with a given filling rate in the TPC. The weir structure also allows the over-spilled LXe to return to the weir reservoir and enter the circulation system. Level sensors is installed around the perimeter of the top-corner structure to monitor liquid surface activities both inside and outside the weir trough, i.e. the extraction region and the skin region.

The scaled Phase-I TPC had a 6-inch diameter and was built with appropriate scaling to achieve the same surface and bulk fields as LZ with the application of desired cathode, gate, and anode voltages. All the larger, and scaled components of the LZ TPC, in particular, those involving high voltage, were tested in the system [60].

5.3.2 Sensors in the SLAC System

The instrumentation of SLAC level sensors resembled the design of that in the Imperial Chamber, however, with a different implementation of guard plates. Three types of sensors with adaptation from HPPS described in Chapter 4 were designed: SLAC horizontal level sensor (SHLS), SLAC grid level sensor (SGLS) and SLAC vertical level sensor (SVLS).

The sensors' relative locations around the top-corner of the TPC are shown in figure 5.13. Three SHLS were installed at 120 degrees angle relative to each other, facing towards the centre of the TPC to monitor the liquid level near the weir

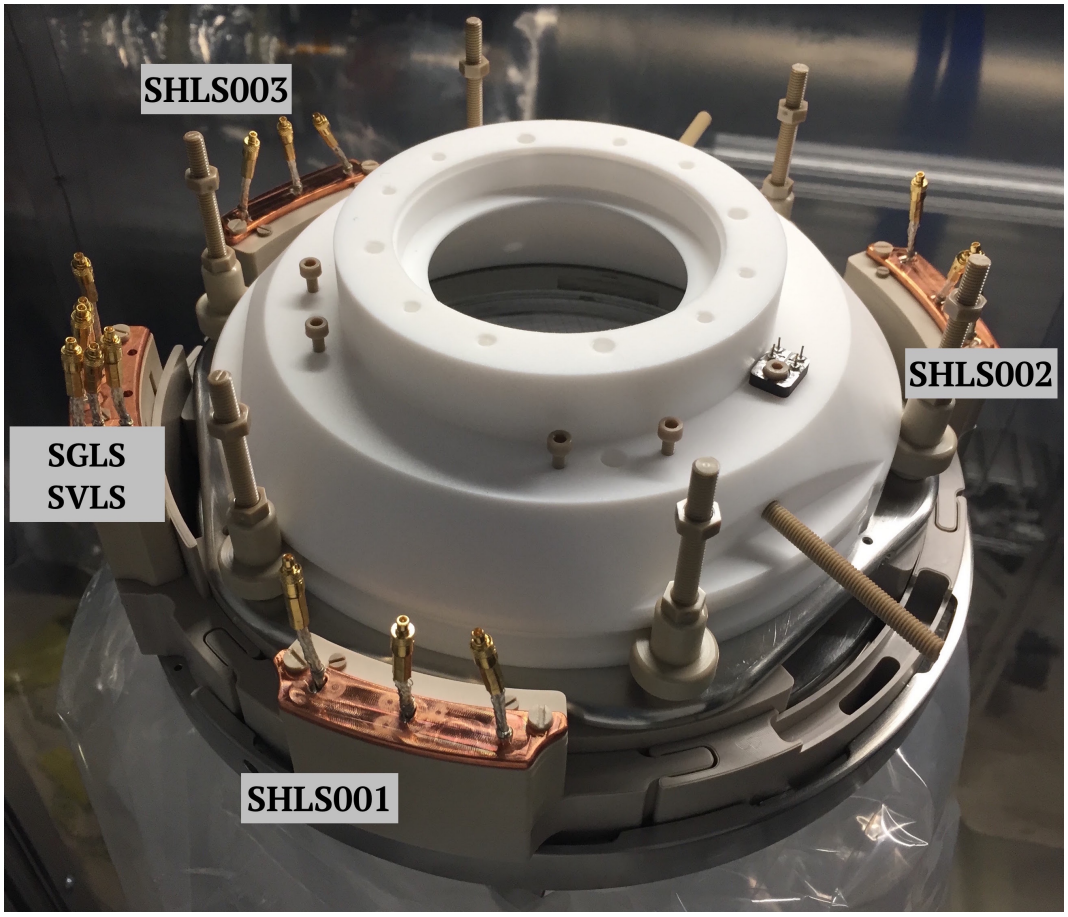


Figure 5.13: Assembly locations of the system test level sensors on the top-corner structure.

trough and possible occurrences of LXe surface waves. The SGLS, an SHLS-like sensor, was installed in the skin region to serve as an indicator as to when the liquid reached the gate and anode grids. The SVLS, installed near the SGLS in the skin region, extended beyond the extraction region grids and monitored liquid level across the entire top corner region. Key design factors of these sensors such as plate distances and areas were again calculated with equation 4.11.

Figure 5.14 shows the CAD drawings and the assembly of the SHLS. Compared with IHLS in the Imperial Chamber, we increased the measurement gap to 9 mm to account for the loss of effective measurement range from liquid artefacts discussed later in Section 6.1.1. The SHLS also had a guard electrode described in Section

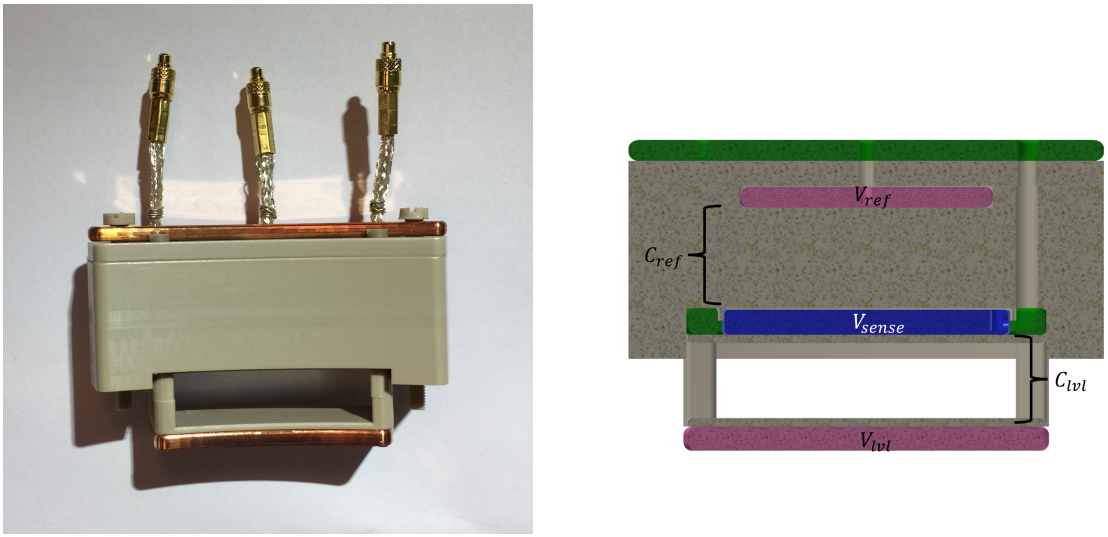


Figure 5.14: SLAC system test level sensors in Runs 3-6. (Left): SLAC horizontal level sensor (SHLS). (Right): CAD cross section of SHLS001-3. We let $A_{ref} = 133\,\mathrm{mm}^2$, $A_{lvl} = 254\,\mathrm{mm}^2$, $d_{ref} = 12.2\,\mathrm{mm}$, $d_{lvl} = 9\,\mathrm{mm}$, and the thickness of PEEK holder for C_{lvl} is 1 mm. Excitation plates are pink, sense plate blue, PEEK parts are light beige, and grounded parts are green.

4.6.2 to reduce its fringe field and increase the field uniformity between plates.

The designs of SGLS and SVLS monitoring the LXe level in the skin region are shown in figure 5.15. The SGLS was a vertically enlarged but horizontally shrank version of SHLS and had an 18 mm measurement range, enough to cover the full EL gap. The SVLS had a shape similar to that of the IVLS except that it had a guard electrode surrounding its sense plate and had a measurement range of 25 mm to detect liquid levels below the gate grid and above the anode grid.

Owing to the installation locations of sensors close to the gate and anode, high voltage concerns had to be addressed and this informed the designs. Preliminary electrostatic simulations were performed to optimise the thickness of metal parts. The goal was to minimise electric fields in GXe space and ensure that fields in LXe space are under 50 kV/cm to avoid sparks. The results shown in figure 5.16 suggested a minimum of 2 mm plate thickness, a radius fillet on all edges, and a distance radially from anode ring and up from weir structure as far as possible.

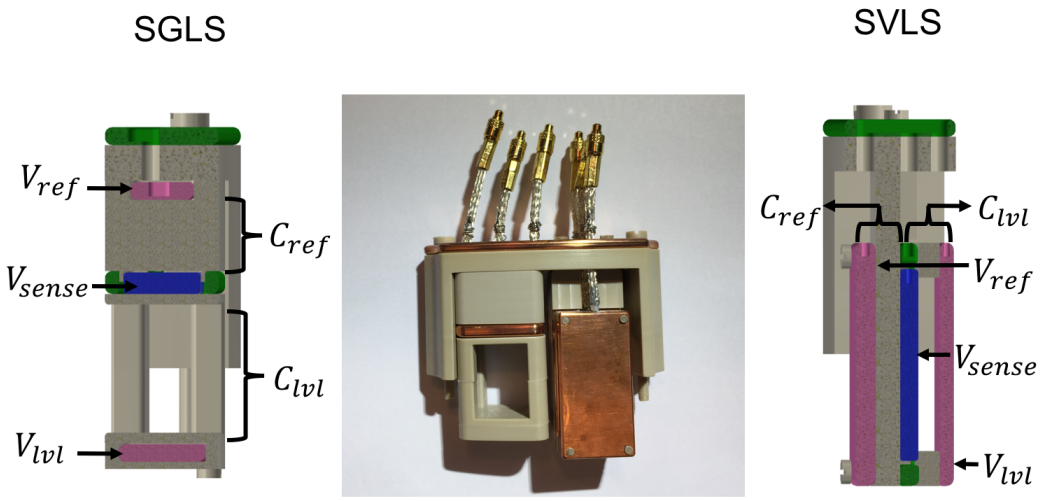


Figure 5.15: SLAC system test level sensors in Runs 3-6. (Left): SGLS CAD drawing, with $A_{ref} = 54\,\text{mm}^2$, $A_{lvl} = 110\,\text{mm}^2$, $d_{ref} = 10.2\,\text{mm}$, $d_{lvl} = 18\,\text{mm}$, and the 1.5 mm thickness of PEEK holder for C_{lvl}. The top surface of the bottom plate was aligned with the gate grid. (Middle): SVLS at right and SGLS at left. (Right): SVLS CAD drawing, with $A_{ref} = 10.6 \times 27.6\,\text{mm}^2$, $A_{lvl} = 10.6 \times 25\,\text{mm}^2$, $d_{ref} = 3.5\,\text{mm}$, $d_{lvl} = 3\,\text{mm}$, and the 3 mm width of PEEK spacer for holding the sense plate.

The simulation, however, was only sufficient to guide the design of sensors. As discussed in Section 5.24, a simulation with final system test geometry in Runs 3-6 demonstrate that the geometry created high field corners for potential HV issues. Such issues were identified in the R&D program (discussed later in the test result) and are resolved thrgouh an improved configuration of electric field at the top-corner region discussed in Section 6.14.

5.3.3 SLAC System Operation in Runs 3-6

The level sensors and the TPC extraction region were fully constructed and assembled for Run 3. In the subsequent Runs, the assembly unchanged. The system was thermodynamically unstable in Runs 3-5 and it was not possible to maintain a steady liquid surface. In the Run 6, the system achieved stable running conditions,

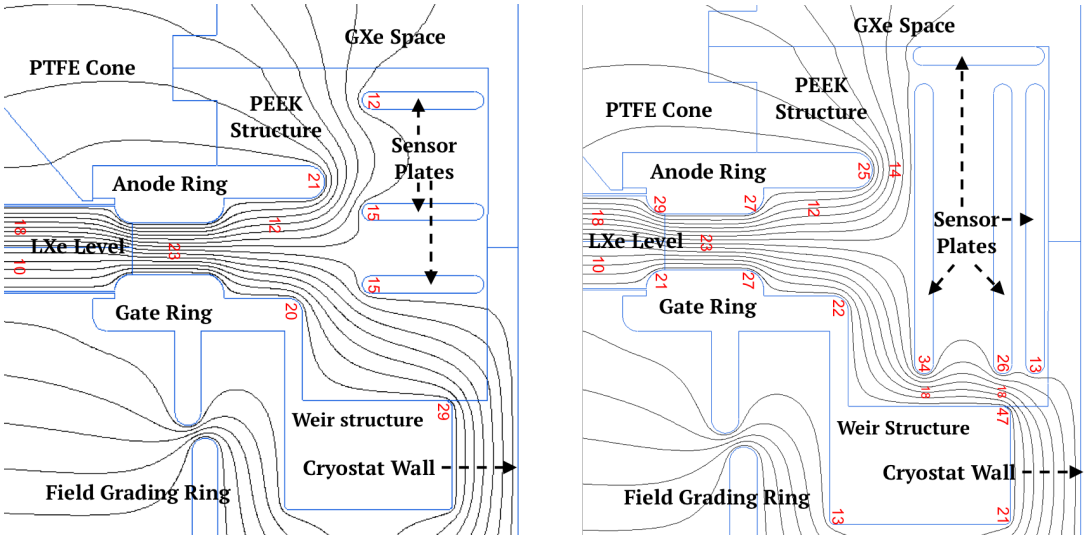


Figure 5.16: High voltage simulation of level sensors at the top-corner with QuickField. The geometries are built with 2D axial symmetry. Red numbers indicate local maximum fields in kV/cm. The settings of dielectric constant of mediums are: $\varepsilon_{PTFE} = 2.1$, $\varepsilon_{PEEK} = 3.3$, $\varepsilon_{GXe} = 1$, and $\varepsilon_{LXe} = 1.84$. The voltages settings of metal parts are: $V_{anode} = 7\,\mathrm{kV}$, $V_{gate} = -7\,\mathrm{kV}$, $V_{grading-rings} = -12\,\mathrm{kV}$, and $V_{sensor} = V_{cryostat} = 0$. (Left): SHLS. (Right): SVLS. Plots were reproduced from [122, 123].

and that allowed probing liquid levels in the extraction region. In the following paragraphs, the conditions of the liquid level and circulation in different Runs are summarised to aid the understanding of level sensor data.

In Run 3, after the TPC was overfilled with LXe (detected by the SVLS), it was found that the top flange thermosypon (TS) had limited cooling power and thus diminished the thermal uniformity of the system. The weir reservoir TS line was also non-operational. Returning LXe from the top corner into the reservoir vaporised immediately and created a large heat load on the top flange TS causing it to shut down. The run was aborted, and an emergency recovery of LXe was carried out.

Run 4 and Run 5 mitigated the problems in Run 3 and achieved LXe circulation during cathode HV testing. In Run 4, however, a vapour lock formed in the weir drain pipe due to a heat load on the line caused by a touch to the room temperature

vacuum jacket. The lock resulted in overfilling the anode for most of the time. The pipe was detached from the vacuum jacket in Run 5 to allow liquid spill over at the weir trough into the weir reservoir. The liquid level at the extraction region had been maintained around the weir for periods of hours, but it occasionally drifted and stayed above the weir for a long period. The trends came from a u-bend at a section of the pipe which led to trapped gas pushing liquid back into the detector.

In Run 6, a stable circulation of LXe in the system was achieved. The detector was able to maintain liquid level around the weir height for a long period ($>$ 5 days). The TPC showed prolonged liquid surface oscillation with periods larger than 10 seconds. Tests with different scenarios such as circulation without condenser cooling, circulation without the heat exchanger, non-circulation, and non-circulation with heat applied to the two-phase exchanger were performed to isolate the cause of these oscillations. Since the liquid surface remained around weir height steadily, extensive high voltage tests of the extraction region were carried out. The gate and anode voltages were ramped up to $-7\,\mathrm{kV}$and $+7\,\mathrm{kV}$ in various combinations such as gate only ramping, anode only ramping, and simultaneous ramping to explore the condition of the grids and the performance of the top-corner region.

5.4 Result from the SLAC system test

5.4.1 Xenon Filling and Recovery of Sensors

The liquid level in Runs 3 and 4 was unstable and rose above the anode several times. The instability allowed multiple LXe filling and recovery processes to calib-

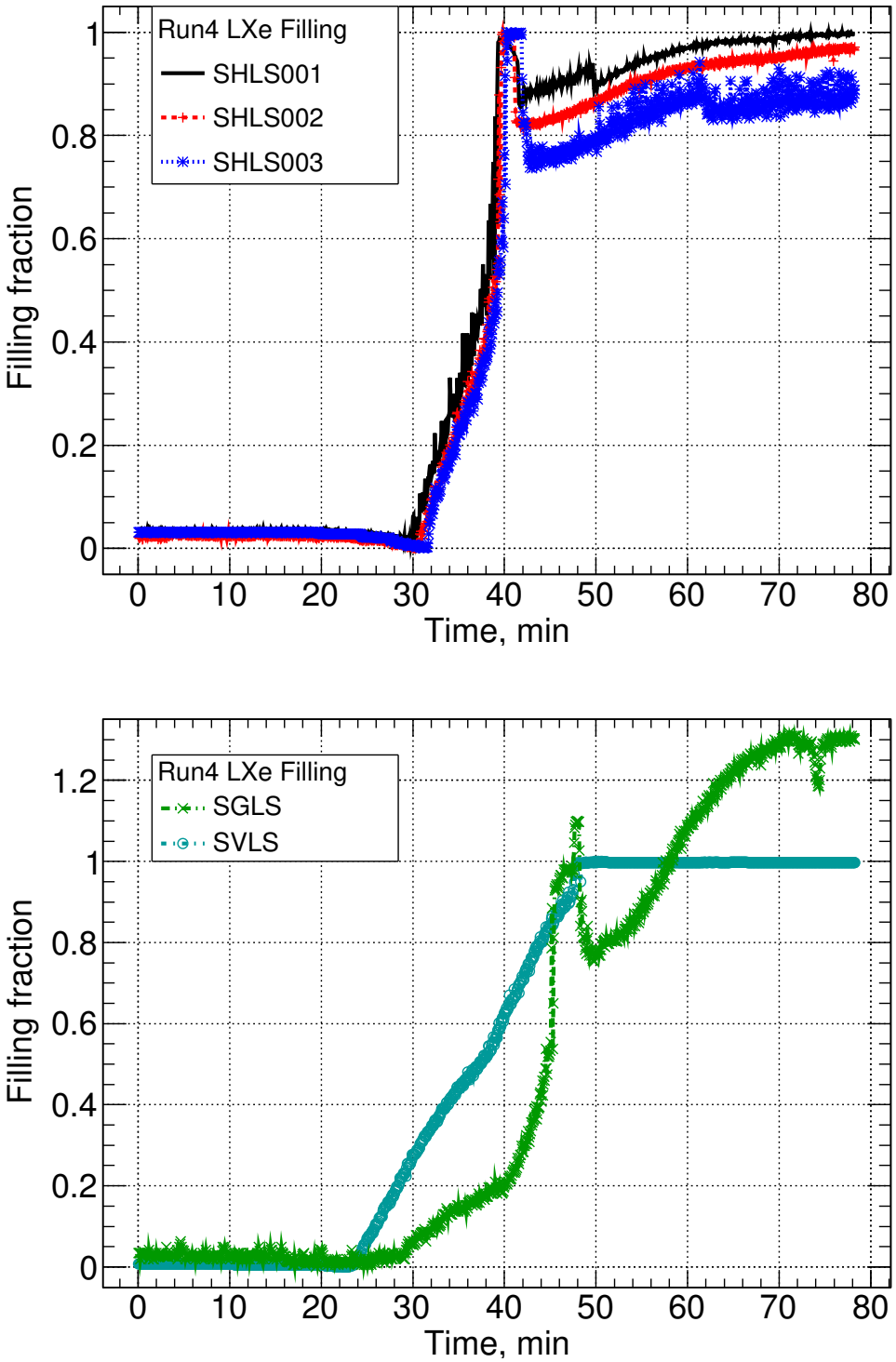


Figure 5.17: LXe filling test of the sensors in Run 4 on 4th May. (Top): Sensors monitoring liquid level at the extraction region, i.e. SHLS001, SHLS002, and SHLS003. The field squeezing effect and differential shrinkage on C_{ref} discussed in Section 5.5 leads to the measured liquid level decrease after 40 min. (Bottom): Sensors monitoring liquid level at the skin region, i.e. SGLS and SVLS. The C_{ref} of the SGLS experience a large influence from the field squeezing effect which leads to the feature of the measured liquid level after 45 min.

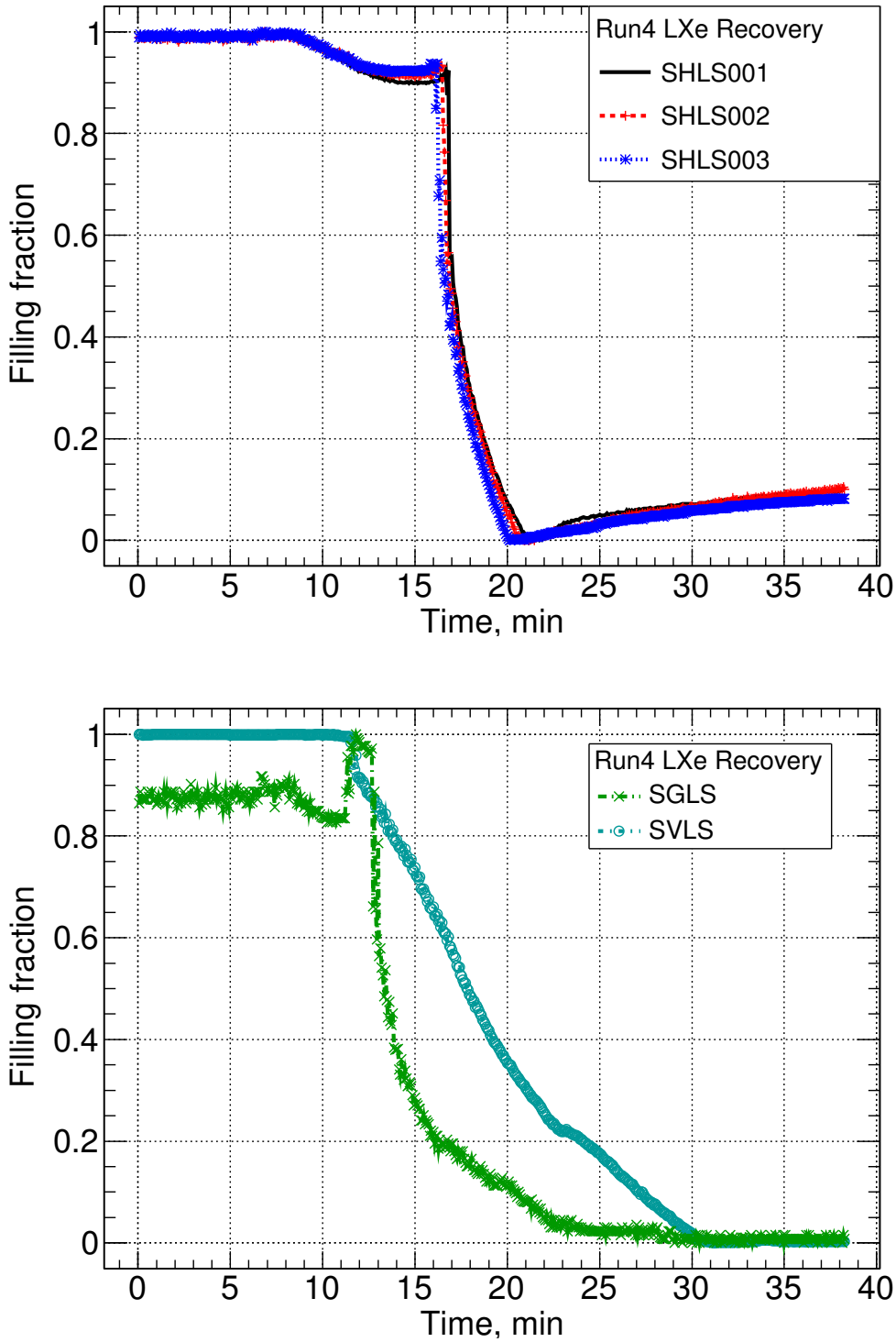


Figure 5.18: LXe recovery test of the sensors in Run 4 on 25th May. (Top): Sensors monitoring liquid level at the extraction region, i.e. SHLS001, SHLS002, and SHLS003. Influence on the measured liquid level due to the differential shrinkage is less prominent but that due to the field squeezing effect persists. (Bottom): Sensors monitoring liquid level at the skin region, i.e. SGLS and SVLS. The The LXe did not fully submerge the SGLS which led to the plateau of SGLS data before 7 min.

rate the sensors. The calibration uses end points of the readout, i.e. an LXe-filled or an emptied sensor. For discussion, we select two examples of data, taken on May 4th and 25th, displayed in figure 5.18 and figure 5.17.

Compared with the SHLS, the SVLS showed a more linear response to liquid level increase and had a larger effective measurement range ($\sim 90\,\%$). The features of response around the filling fraction of $\sim 50\,\%$ in the filling process and $\sim 20\,\%$ in the recovery process were caused by changes to the filling and recovery rates when the liquid level reached the weir trough and gate grids, respectively.

The data from the SHLS indicates an improvement in the measurement range, but systematic features persist. At the beginning and the end of the filling, the data show liquid artefacts similar to those of the IHLS. The data also demonstrates an increase of the SHLS's measurement gap to 9 mm which allowed a larger effective measurement range ($\sim 4.5\,\mathrm{mm}$) compared to that of the IHLS ($\sim 1\,\mathrm{mm}$). As for the features at the end of the filling or the beginning of the emptying, these come from the fringe field of the poorly shielded C_{ref} and the shrinkage of PEEK parts. In the liquid filling process, when the C_{lvl} was submerged, the fringe field between the excitation plate and the guard electrode interacted with nearby LXe causing the C_{ref} to decrease (field squeezing effect, discussed in Section 5.5). The PEEK parts of the sensor, however, were at a different temperature and shrunk differently during the processes which caused C_{ref} to increase (differential shrinkage effect, similar to the effects described in Section 5.2.1). The increase of C_{ref} eventually decreased the readout. In the liquid emptying process, the C_{ref} experienced an opposite change compared to that in the filling process but with less influence from the differential shrinkage effect.

The data from the SGLS demonstrates that careful consideration of the fringe field and the material shrinkage is necessary when designing the sensor. The SGLS data in figure 5.17 (Bottom) presents a dropping feature after the drastic capillary rise around 50 min in the filling process; before the capillary drop in the recovery data of SGLS in figure 5.18 (Bottom), the sensor also shows a sudden rising feature at 10 min. These major features are caused by the known influence from C_{ref} similar to the C_{ref} variation in SHLS. These features do however introduce ambiguity into the data and thus establishing the true liquid level is not possible; they invalidate the sensor's purpose as an indicator to signal the liquid level at gate and anode grids. Therefore, the SGLS was replaced by SVLS and SHLS in Run 3-6.

Because the geometry of SLAC TPC was more complex than that of the Imperial Chamber (see figure 5.12 and figure 5.2 (Top)), the sensors' data cannot be fitted with a simple fit function using equation 5.1 by assuming a constant filling/recovery rate. The precision of the sensors was estimated by comparing the electronic precision with the endpoints at the beginning and the end of the filling and the recovery process. On average, the resolutions for SHLS, SGLS, and SVLS are 6.5 μm, 253.3 μm , and 11.1 μm, respectively. Remarkably, the SVLS exhibits a similar level of precision as the SHLS does and thus is a good replacement for and SHLS sensor in precision measurements. The SVLS is therefore considered to be the early prototype of the final design of the LZ's precision level sensor discussed in Chapter 6.

Process	Filling	Recovery	Recovery	Average
Reference point	Wetting	Capillary drop	Liquid remaining	-
Esti. filling/recovery rate,	0.0162	0.184	0.184	-
SHLS001, z_{diff}, mm	0	0	0	-
SHLS002, z_{diff}, mm	0.62	0.42	0.6	0.54
SHLS003, z_{diff}, mm	1.08	1.02	0.84	0.98

Table 5.3: Estimation of the relative liquid level height. The reference points correspond to the illustration in figure 6.3.

5.4.2 Liquid Surface Map Estimation

Since the installation of the SHLS, we were capable of reconstructing the liquid level map of the system test TPC for detector levelling. The method for correcting tilt in a TPC so far was to assess the uniformity of the detector response to calibration with a source, such as Kr^{83m}. The source allows studies of the S2 width to reconstruct the liquid surface and thus to correct a tilted TPC. The approach, however, is a trial and error method which requires post-analysis of the calibration data [81].

The filling and recovery data of SHLS in Run 4 were studied to achieve the detector tilt correction. Because the capillary features diminish SHLS accuracy, instead of using the sensor's readings, the reconstruction of a tilted TPC was calculated based on timing differences between the occurrences of a feature in different sensors. These features happened at the end of a filling process (wetting), the beginning of the recovery process (capillary drop), and the end of a recovery process (residual remaining) (for a discussion of the features, see Section 6.1.1.2). The timing differences were then converted to liquid level differences with the estimated filling/recovery rates.

Table 5.3 summarises the result of the estimation of the relative heights between sensors using data from Run 4. The primary source of error of the estimation

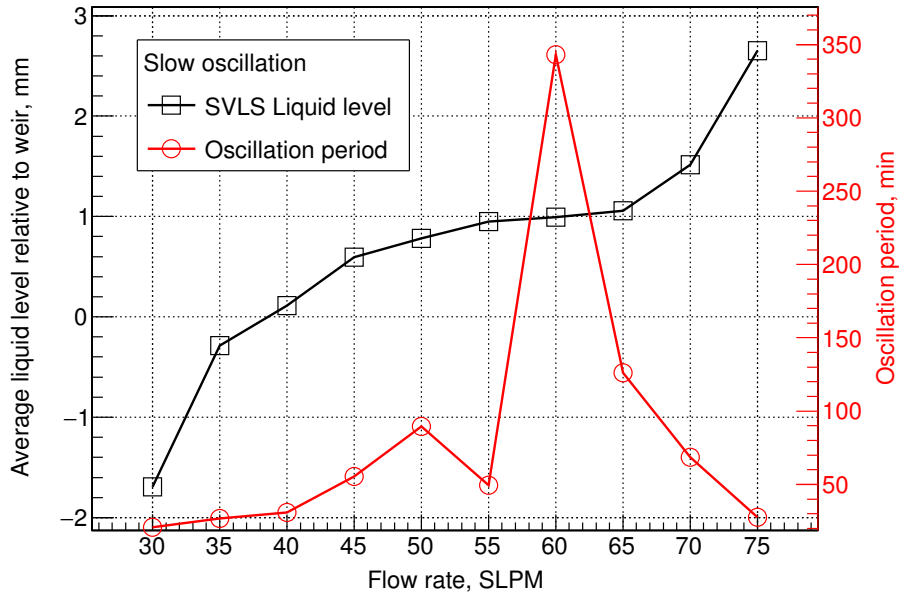


Figure 5.19: Correlations of TPC's liquid level and long-period (> 10 min) oscillations with liquid flow rate.

comes from the filling/recovery rates due to the difficulty in reconstructing local flow rates of the TPC. Nevertheless, the first order estimation of the tilted detector is effective. The tilted TPC was then corrected in Run 5 and Run 6 to obtain a levelled liquid surface (< 0.2 mm height differences).

5.4.3 Continuous Liquid Level Monitoring

The implementation of the level sensors at the top corner actively assisted the identification of issues and complemented the confirmation of the design of the circulation system and the top-corner region. The liquid level in Run 6 was maintained around weir trough level for days allowing tests at the extraction region. The run enabled many studies of liquid level monitoring: the slow and fast oscillation of liquid level during circulation tests, the sensor's continuous measurement during the HV ramping test, and the variation of PMT signals corresponding to level changes.

TPC liquid level and the level's oscillation period (> 10 min) depended on the flow rate of the circulation system (see figure 5.19). When the flow rate was smaller than 45 SLPM, the liquid level was below the weir and oscillated with a period of ~ 50 min. The level plateaued between 45 to 60 SLPM suggesting the rates of liquid inlet and outlet of the TPC reached a balance. The considerable increase of oscillation period to ~ 350 min implied that the balance happens at the flow rate of 60 SLPM. After which, the liquid level and the oscillation period started to increase and decrease, respectively. In general, the liquid height is lower than the expected height ~ 2 mm (flow rate dependent) predicted through the Pifter's equation [124]. The discrepancy could be due to a known leak between the parts of the weir trough and the weir structure. Such leak leads to the liquid level drop below the weir height when the flow rate decreases below 40 SLPM.

Apart from slow oscillations, the sensors also detected oscillation with periods smaller than 60 seconds due to pressure instability in the TPC, e.g. Figure 5.20. The liquid level in the SHLS was higher than that in the SVLS, indicating that the liquid had been pushed out of the extraction region into the skin region (as the flow configuration of internal fluid of LZ TPC discussed in Section 4.3). The levels' anti-correlation also implies that the liquid was sloshing back and forth between the vessels. Furthermore, the liquid level in the sub-cooler oscillated in phase with the level at the extraction region (SHLS). The oscillation was caused by a pressure build-up that acted as a phase separator in trapping liquid between the two-phase heat exchanger and the sub-cooler. The build-up pressure was realeased periodically and led to temporal and micro-level changes in TPC pressure and the flow rate.

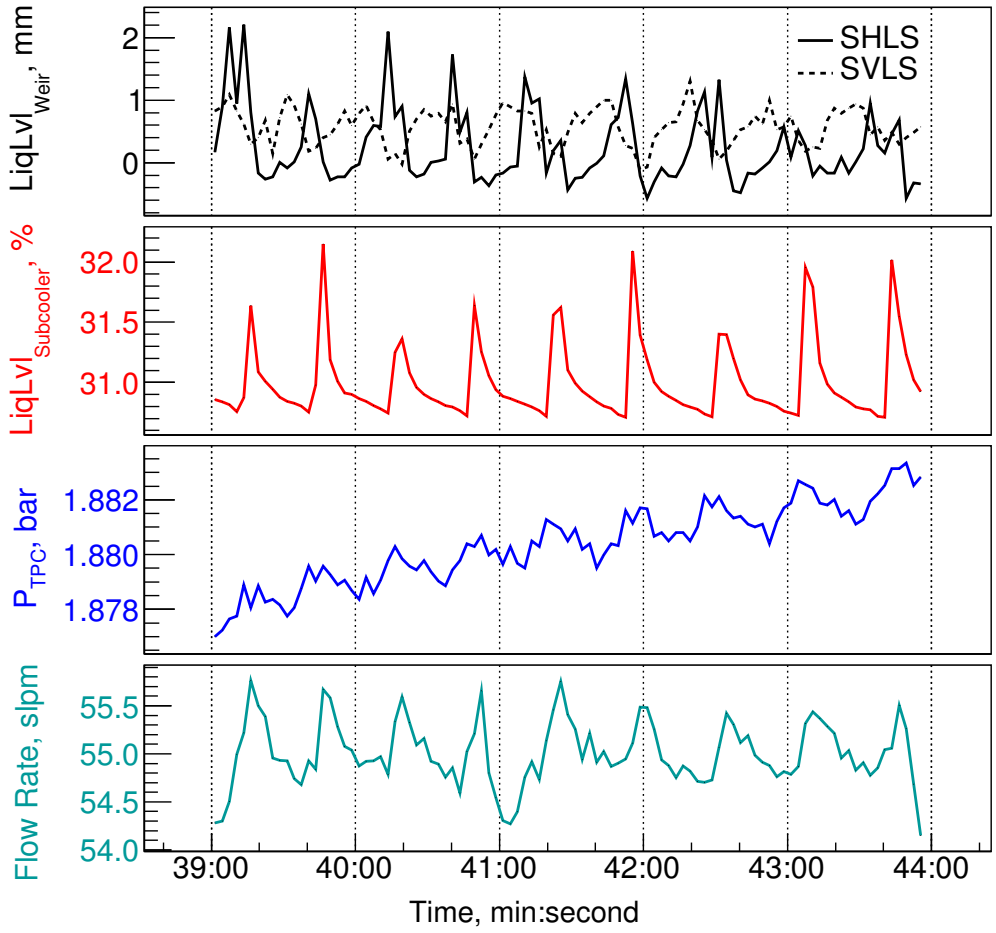


Figure 5.20: Liquid level oscillations with a shorter period (< 60 seconds) due to liquid sloshing, TPC pressure, sub-cooler pressure, and the flow rate.

Other than slow oscillations due to pressure fluctuation or flow rate changes, the sensors had measured fast surface waves. The Fast Fourier Transform (FFT) of the sensors' measurements during a GXe test and a circulation test is plotted in figure 5.21. The FFT results show that the sensors had observed fast surface waves around $1 \sim 10$ Hz. This is consistent with recent measurement of surface wave in LXe by light modulation in the LUX detector (around $1 \sim 4$ Hz and $7 \sim 11$Hz) [125]. Moreover, the SVLS measurement has more frequency peaks from different surface wave modes in the FFT spectrum than the SHLS. This could be caused

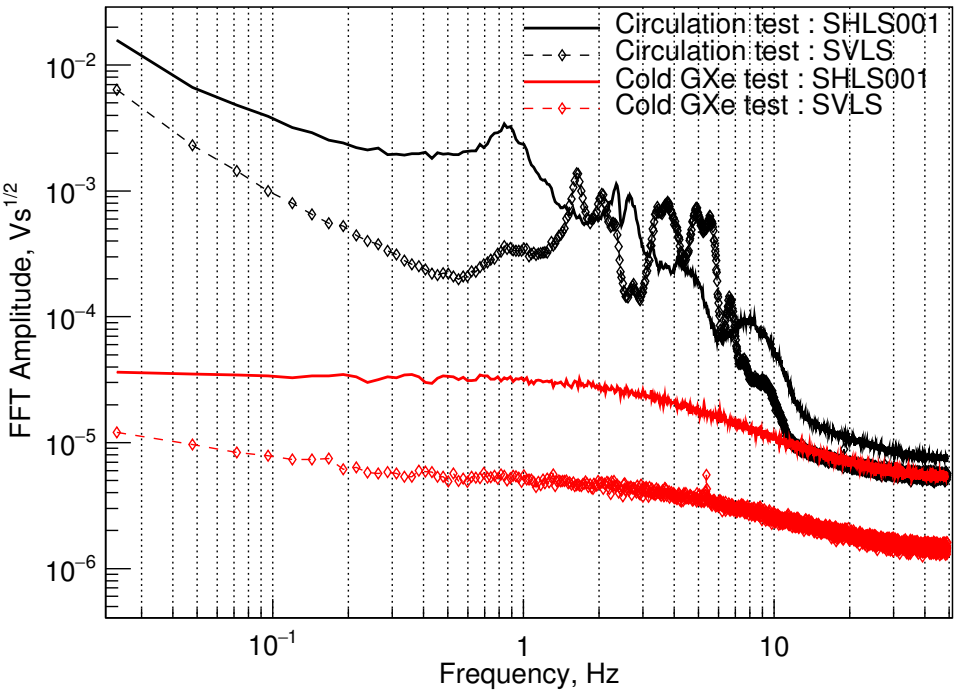


Figure 5.21: Fast Fourier transform the data of SHLS001 and SVLS in a cold GXe test and a circulation test.

by the reflecting wave from the inner vessel. The wave could interact with the outgoing wave from the extraction region to form constructive (destructive) waves which were picked up by the SVLS.

Regarding level measurements during HV ramping, the sensors demonstrated their normal operation in an applied electric field up to $\sim 5.5\,\mathrm{kV/cm}$. Multiple voltage ramping tests of different configurations were performed on the gate and anode with sensors monitoring liquid level simultaneously (an example is shown in figure 5.22). Because the variation of the pressure contributed to temporary liquid filling, the liquid level positively correlated with the TPC pressure as expected. The liquid level, however, shows no correlation with the field indicating that the sensors are capable of monitoring liquid activities continuously during HV operations in LZ.

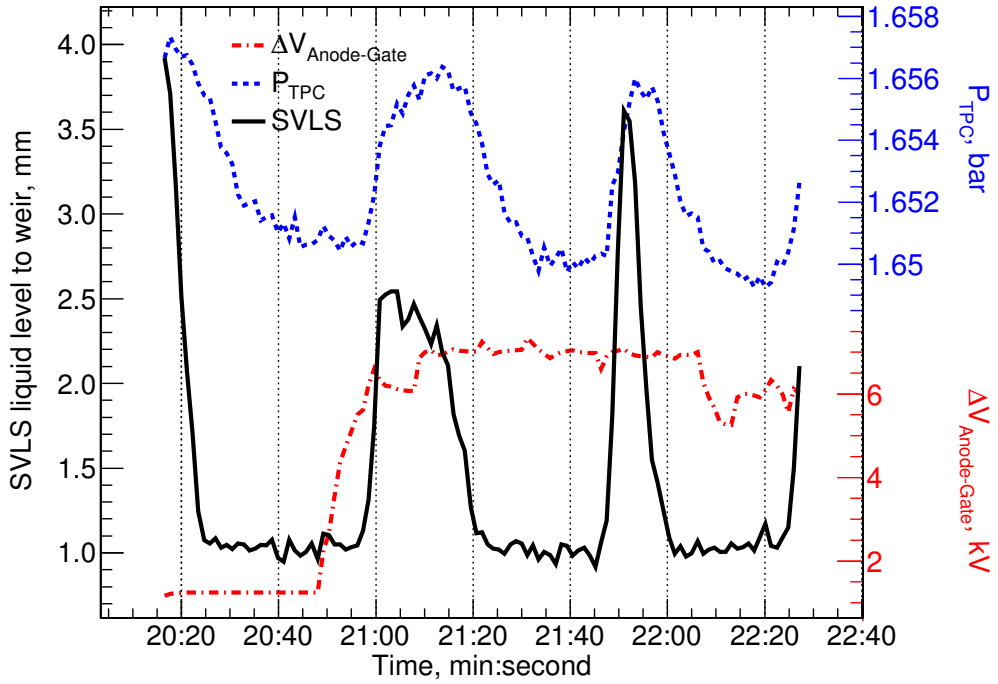


Figure 5.22: Liquid level measurement influenced by the TPC pressure but not the applied electric field.

Lastly, a correlation between the rate of PMT signals and liquid level oscillation was observed. The rate of the top PMT, in figure 5.23 (Top), was proportional to the SHLS level. A further analysis of such correlation of the PMT signal rate with the liquid level was performed to understand its origin. The PMT signals can be preliminarily classified to three major populations - S1, S2, and single photon electron (SPE). An example of the analysis result is shown in figure 5.23 (Bottom). Except for the S1 rate, the S2 and the SPE rates depended on the liquid level variation. Because the production mechanism of S1 does not rely on electron extraction, the S1 signal rate remained independent of the level as expected. The S2 signal rate dropped as the liquid level decreased, owing to the production mechanism based on equation 3.11 and 3.12. When the level was below the gate grid (5 mm below the weir level), the rate plateaued for a short

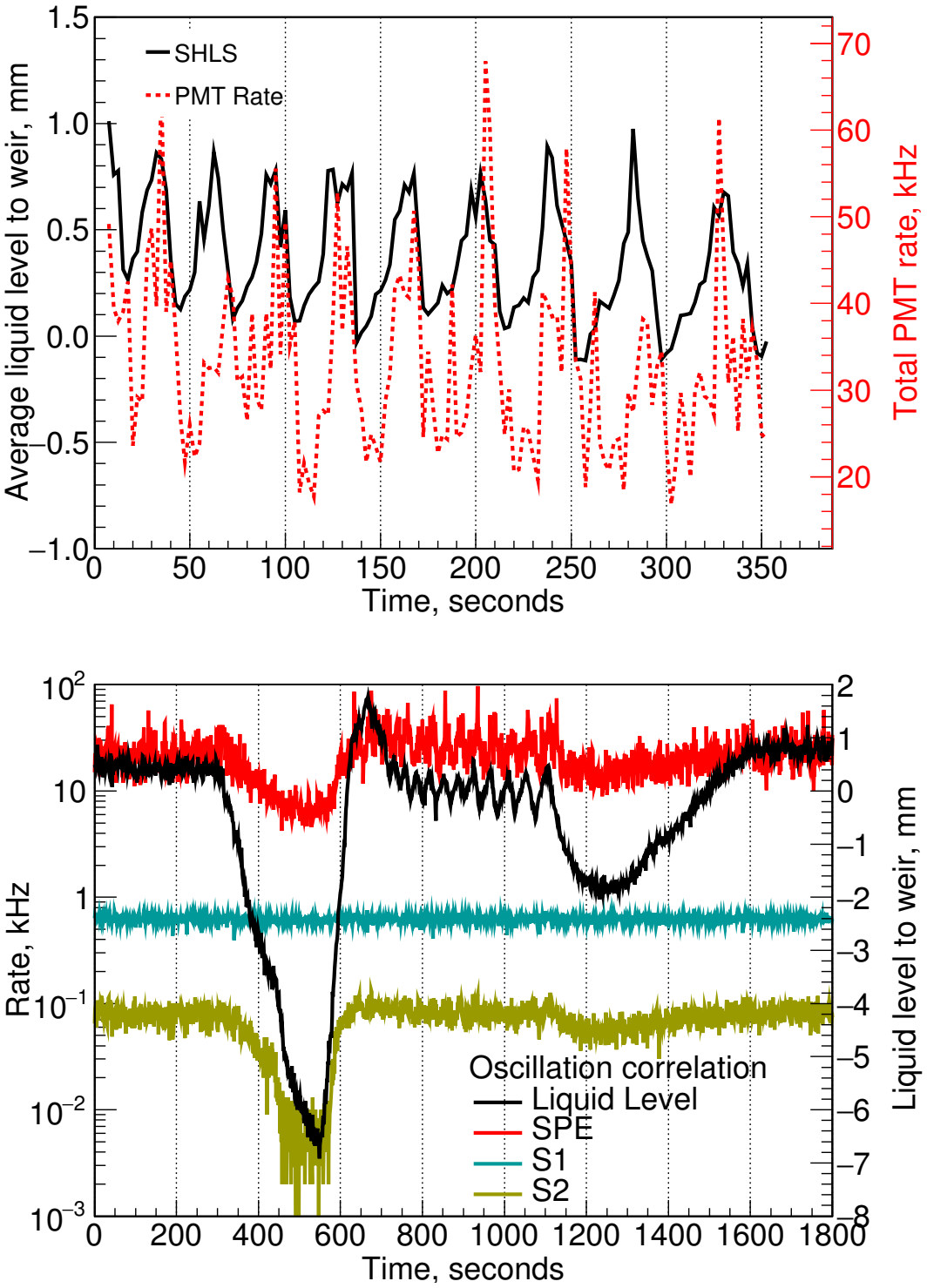


Figure 5.23: Example of correlation between signal and liquid level oscillation on 06/02/2017 in Run 6. (Top): Observation of the correlation between Top PMT rate and the liquid level oscillation. (Bottom): Rates of different populations of signals and the liquid level to weir. Data courtesy of Tomasz Biesiadzinski.

period. Such plateau was caused by the S2 production in a region between the gate and the field shaping rings ($\sim 4\,\mathrm{kV/cm}$ in GXe, around the threshold of EL production). As the liquid level increased back to a level in the extraction region ($\sim 6\,\mathrm{kV/cm}$ of the GXe electric field in the region), an increase of the S2 signal was observed. The SPE rate, which supposedly should primarily depend on the PMT dark count, however, swung with the level fluctuation. The fluctuation could be attributed to the leakage of another population of multi-photons which were likely from EL production outside the extraction region. The electric field simulation at the top-corner in Section 5.4.4 shows that some of the local fields around the skin region and the perimeter of the extraction region were relatively high. The simulation effectively suggests that the electron extraction efficiency there could be between $45 \sim 95\,\%$ (around 45 % in the extraction region, calculated based on liquid level). Thus, some regions with a lower efficiency, which produced photons depending on the liquid level, could contribute to the oscillation of the SPE rate; other regions with higher efficiency, which consistently produced high numbers of photons, could scale with the SPE rate.

5.4.4 High voltage issues

The high SPE rate in Run 6 raised the question about the electric field map of system test's top-corner region. These SPE could leak from another population of time-correlated photons contributed by EL of electrons drifting through a field applied region. The observed population had a lower number of photons per extracted electron and a shorter duration (pulse width) than what is expected for electrons extracted in the EL region. One explanation for the high rate of

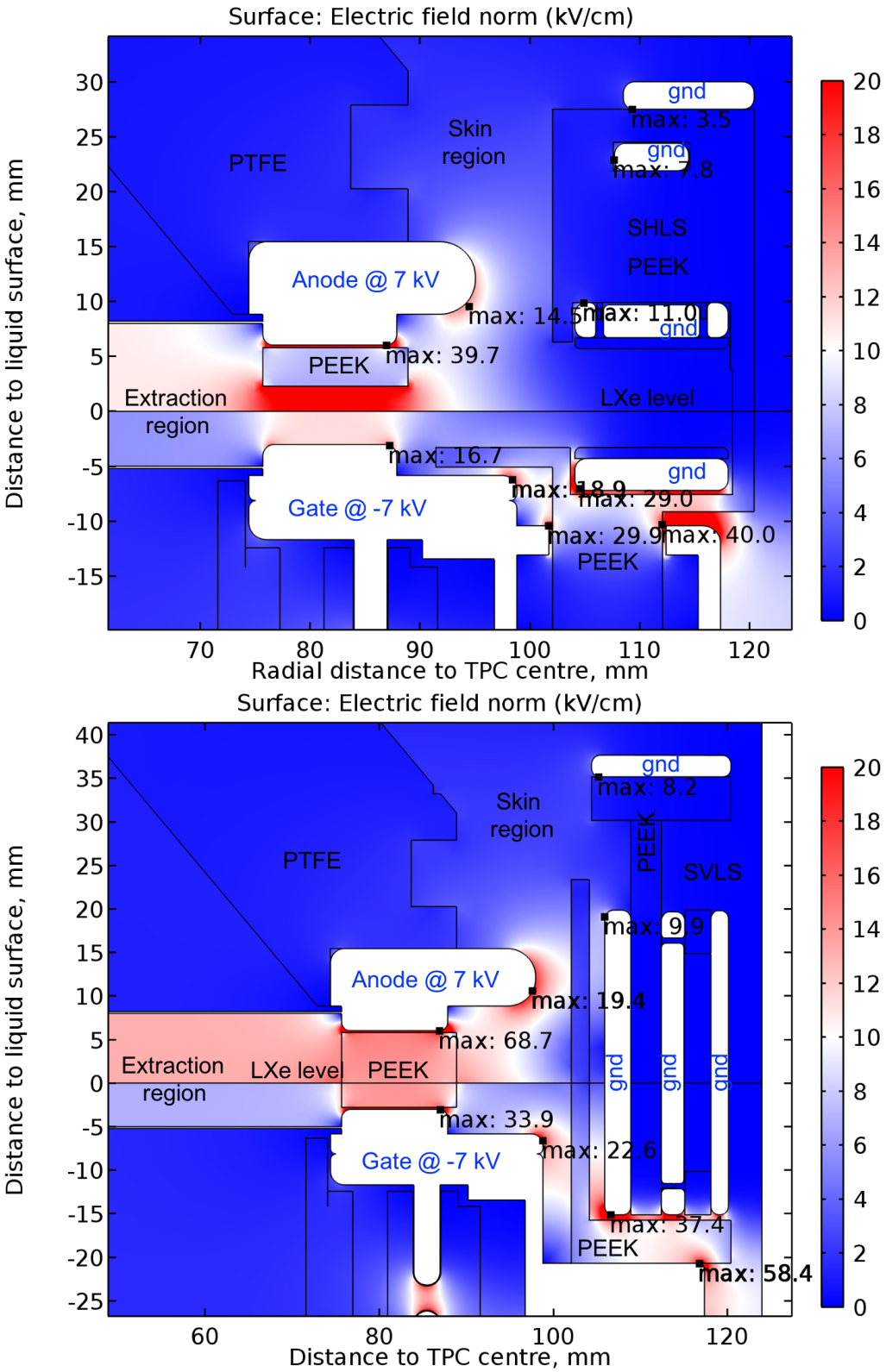


Figure 5.24: High voltage study with COMSOL of system test level sensors. The plates of the sensors were set at ground potential. The anode and gate were set at 7 kV, and −7 kV, respectively. The dielectric constant of PEEK and LXe were set at $\varepsilon_{PEEK} = 3.3$ and $\varepsilon_{LXe} = 1.89$. Dot markers with numbers marked next to them are the maximum field at those local areas. The colour platter is limited within 20 kV/cm. Regions with red colour could have fields higher than 20 kV/cm. (Top): SHLS. (Bottom): SVLS.

SPE from this population could be the leakage of photons that were produced by EL at the skin region and around the perimeter of the extraction region. This suspicion necessitated a further investigation of the electric field map at the TPC top-corner with the final CAD model, especially the complex section of skin region with sensors installed.

An electrostatic simulation with COMSOL Multiphysics was performed to study the electric field map of the SHLS and SVLS. Unlike the preliminary simulation discussed in Section 5.16, the simulation used the final drawings of the system test top-corner in Run 3-6.

The cross-sections of the SHLS and SVLS and the configuration of voltages at the top-corner region are shown in figure 5.24. The result of electric field maps of both sensors show many local high field regions above 20 kV/cm in GXe and LXe regions. In the GXe region, the highest electric fields, which are 39.7 kV/cm for SHLS and 68.7 kV/cm for SVLS, located between the PEEK spacer and the anode structure. Although the field within the spacer is suppressed by its dielectric constant, its presence segments the gas gap and thus decreases the distance between charged surfaces. The segmentation causes a drastic increment of local electric fields. As for regions in LXe, the highest fields, which are around 40 kV/cm for SHLS and 58.4 kV/cm for SVLS, are between the PEEK structure and the weir structure. Even though the fields are suppressed by the LXe dielectric constant, the segmentation still leads to considerable electric field regions.

The simulation result reveals two primary issues. Firstly, although fields around electrodes of sensors in GXe ($\sim$ 10 kV/cm) are not the main contributors for EL production in skin region, the remarkably high fields near the anode

structure allows electrons to be extracted efficiently and creates favourable condition for EL. Secondly, the fields beneath the electrodes of the sensors are close to the threshold for spark generation or potential electrical breakdowns. Fortunately, the possibility of breakdown or trip is suppressed by the presence of LXe. In fact, during a GXe test of the extraction region without LXe in the TPC, a trip near the SVLS was observed. The trip was caused by the proximity between the sensor and the weir structure (the anode and gate were at 8 kV/cm and −6 kV/cm, respectively). All these issues were taken into account when we designed the final LZ level sensors which are discussed in Chapter 6.

5.5 Systematic Effects

We thoroughly explored the application of precision level sensors in the R&D programs and identified three critical systematic effects which influences the accuracy of the sensor. The effects are as follows: liquid artefacts, fringe field and temperature dependence of capacitors, and dielectric constant variation of LXe.

The liquid features described in Section 5.17 and 5.2.2 substantially decreases the accuracy of the level sensors. In general, the artefacts at the beginning and the end of the filling process contributed to ~ 4 mm measurement range loss. Compared with the designed measurement ranges, the effective measurement ranges of IHLS, SHLS, IVLS, and SVLS are 10 %, 55.6 %, 92.1 %, and 84 %, respectively. Moreover, the artefacts also increase the difficulties in defining the active measurement ranges of the sensors quantitatively.

The effects from non-linear temperature dependence and the fringe field are also contributors to the systematic effects of C_{ref} and C_{lvl}. The temperature depend-

	SHLS001	SHLS002	SHLS003	SGLS	SVLS
Meas. C_{lvl}, pF	$0.305^{+0.0\%}_{-1.7\%}$	$0.328^{+0.0\%}_{-0.78\%}$	$0.312^{+0.0\%}_{-1.45\%}$	$0.064^{+0.0\%}_{-1.90\%}$	$1.024^{+0.0\%}_{-1.23\%}$
Meas. C_{ref}, pF	$0.393^{+8.04\%}_{-0.77\%}$	$0.389^{+6.68\%}_{-0.20\%}$	$0.373^{+5.58\%}_{-0.16\%}$	$0.166^{+11.38\%}_{-3.91\%}$	$2.431^{+1.17\%}_{-0.83\%}$
Expected C_{lvl}, pF	0.233	0.233	0.233	0.052	1.034
Expected C_{ref}, pF	0.299	0.299	0.299	0.155	2.294

Table 5.4: Expected and measured capacitance of SLAC level sensors at room temperature. The post-measurements were performed with the final LZ electronics which uses equation 4.11 instead of equation 4.10 for measurements. The error in the capacitance is from systematic effects of the temperature dependence.

ence is mainly caused by shrinkage differences between PEEK parts when parts are at different temperatures (differential shrinkage effect). Such dependence, especially from C_{ref}, affects the true level measurement. Furthermore, examples of fringe field simulations of SHLS in figure 5.25 imply that the presence of dielectric material around the sensors affects their capacitance. When the liquid level reaches the region between the top excitation plate and the sense plate of the SHLS, the fringe field coupling between the excitation plate and the guard electrode squeezes the field lines between the excitation and the sense (field squeezing effect). Such squeezing effect on electric field leads to a decrease of C_{ref}. Nevertheless, the effect is less prominent on the SVLS because its electrodes are comparatively close to each other.

The effect of fringe fields also contributes to the discrepancies between measured and predicted C_{ref} and C_{lvl} at room temperature (Table 5.2 for Imperial sensors and Table 5.4 for SLAC sensors). On the whole, the discrepancies between the designed and measured capacitance of IVLS and SVLS are smaller than that of IHLS, SHLS, and SGLS. The discrepancies are mostly caused by fringe fields

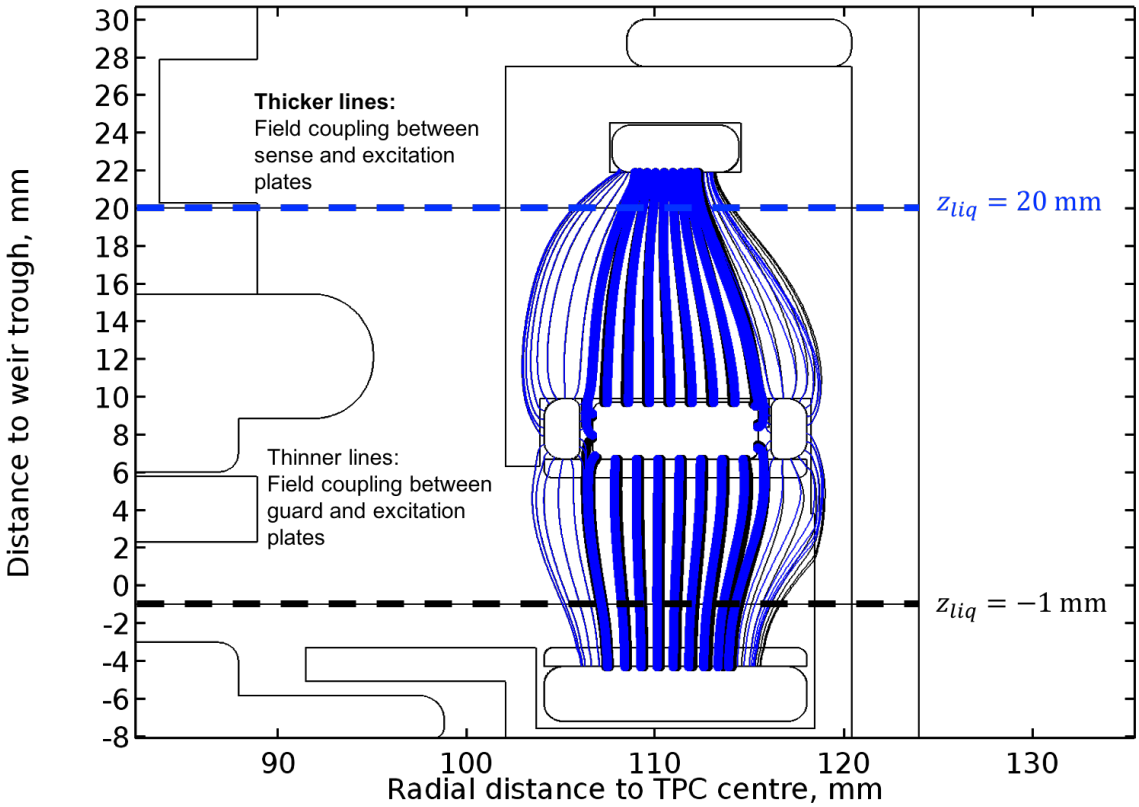


Figure 5.25: Squeezing effect of fringe field that affects the field lines of the C_{ref} and C_{lvl}. Streamlines show filed coupling between the sense and the excitation plates (thicker lines) and between the guard and the excitation plates (thinner lines). Blue field lines correspond to liquid level $z_{liq} = 20\,\text{mm}$; black field lines correspond to liquid level $z_{liq} = -1\,\text{mm}$. The voltage of the excitation plate for C_{ref} and C_{lvl} is 0.7 mV. The sense and guard plates were set at ground potential. Because the gate and anode decoupled from the electronics, they were grounded.

of the non-uniform field lines between the sense and excitation plates which lead to different capacitive coupling with materials. This is understood through how the charged surfaces couples to each other. For example, in the case of C_{ref} in the IHLS, part of the charges on its excitation plate couples to the grounded shield ring, which leads to a smaller C_{ref} than the calculation. In the case of C_{ref} in the SHLS (as shown in figure 5.25), charges on its excitation plate couples to more charges on the sense plate than expected, leading to a higher measured C_{ref}.

The last systematic effect comes from the dielectric constant variation of LXe with temperature. Due to the lack of proper circulation in Run 4 of the SLAC

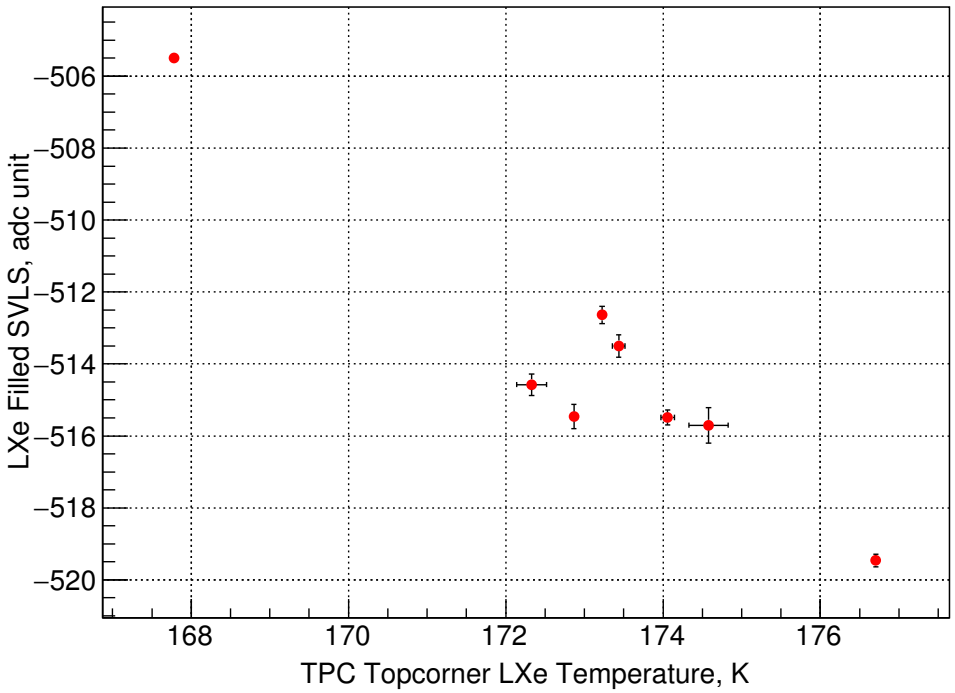


Figure 5.26: Readout dependence of the LX-filled SVLS with liquid temperature in Run4 of the SLAC system test.

system test, the extraction was overfilled to a level above the SVLS for several times. The maximum readout, i.e. the end point, of SVLS shows a correlation with the LXe temperature measured with a nearby thermometer (figure 5.26). The correlation exhibits a variation of 2.7 % in a temperature range of $168 - 178\,\mathrm{K}$. Because the SVLS was overfilled, the variation could come from the change of LXe dielectric constant with temperature. As a result, a misunderstanding of the LXe dielectric constant could lead to an incorrect liquid level measurement and thus the interpretation of the electric field in GXe for electron extraction.

5.6 Conclusion

In this chapter, the tests of sensors at the Imperial Chamber and the SLAC system test were discussed. The sensors made for the Imperial system test proved their

capability in providing precision measurement in LXe at micrometre level which satisfies the LZ requirement. The electron lifetime test of the sensors verifies the cleanliness of the sensor's materials.

As for the practical application of the technology to a two-phase TPC, the SLAC sensors played a crucial role in improving liquid surface stability and in enhancing understanding of the electron extraction in the TPC EL region. The sensor's reading was found to be correlated with various other parameters in the circulation system such as the flow rate, TPC pressure, and sub-cooler liquid level. The correlation complements the studies of an optimal circulation configuration in the SLAC system test which would eventually become the configuration for LZ. Moreover, because of the precision level sensor, liquid surface waves and oscillation were detected. The liquid oscillation was found to be correlated to the PMT rate. The correspondence observed by the sensors, together with the thorough electric field simulation, provides a plausible explanation for the rate and a direction for improving the LZ top-corner design.

Lastly, the tests gave a wealth of data for improving the design of the final LZ sensors. The test results show that liquid artefacts, temperature, fringe field, and xenon dielectric constant affect level sensor's accuracy. It is, therefore, necessary to modify the sensor to diminish the influence of these effects. The effects are tackled by mitigation strategies which are thoroughly discussed in Chapter 6.

Chapter 6

Final Design of LZ Level Sensor

For developing a sensor which achieves a maximum accuracy and a minimum contribution to electric fields in the LZ top-corner region, it is necessary to understand the systematic effects discussed in Chapter 5. In this chapter, we report the solutions to the systematic effects found in earlier R&D designs. A dedicated measurement was carried out to look at the occurrences of liquid artefacts from the capillary rise and meniscus effect. Another measurement with the IVLS in the Imperial chamber was performed to study the systematics of LXe dielectric constant variation with LXe saturated temperature. Next, we discuss the technical issues encountered in designing the final LZ sensor and their mitigation strategies. In particular, we address a solution to the electric field concerns which is based on an electrostatic simulation. Lastly, we introduce the design of the final LZ level sensor, which has taken the mitigation strategies as well as the design methods described in Chapter 4 into account. We then end the chapter with a discussion on the result of liquid nitrogen tests of the sensors which show their significant improvement in accuracy.

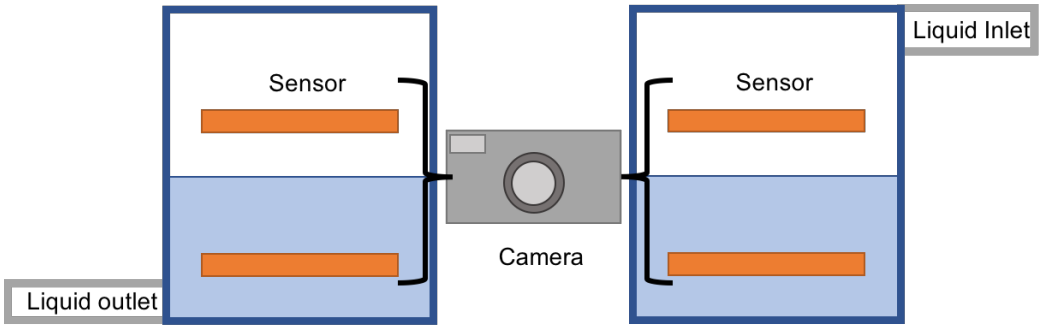


Figure 6.1: Experimental setup of the capillary effect study. The liquid inlet and outlet were installed on different beakers to allow mechanical control of the mineral oil levels.

6.1 Systematic Effects

In this section, we discuss the studies of systematic effects from liquid artefacts, and the correlation of LXe dielectric constant with xenon saturated temperature.

6.1.1 Liquid Artefacts

The features in the LXe filling data described in Section 5.2.2 and 5.4.1 motivated the study of capillary effects in the data. We constructed a test stand to replicate liquid filling/recovery processes with PCB level sensors to understand these effects.

6.1.1.1 Mock-up Test Setup

The test stand used mineral oil to simulate liquid filling and recovery processes. Figure 6.1 shows the setup of the experiment. The setup for the filling followed the same configuration as that of the liquid droplet tests described in Section 4.7.1.1. As for the liquid recovery test, a fluid outlet tube was installed at the bottom of the beaker to control the liquid outlet by Pascal's principle [126]. A camera, taking pictures at a rate of 2 frame/s, was positioned in front of the beaker to allow correlation of liquid features with data taken with the electronics.

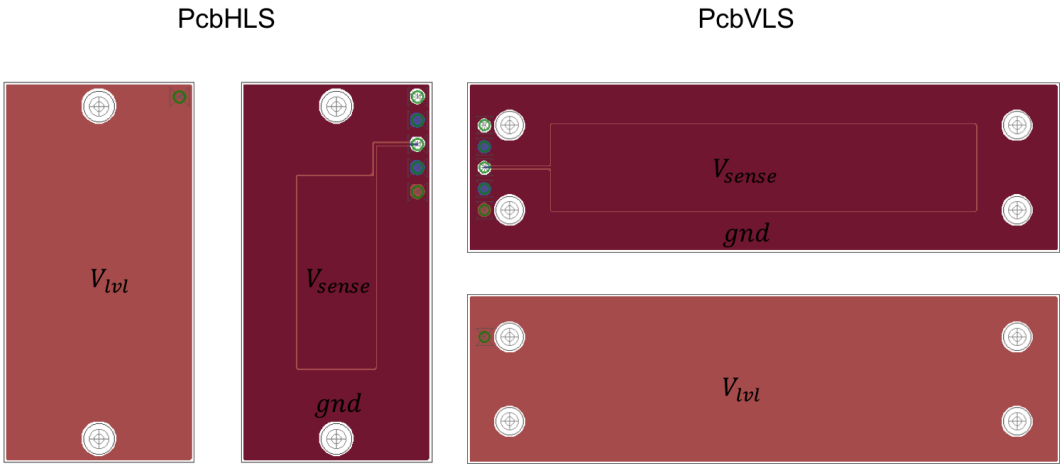


Figure 6.2: PCB drawings of mock-up sensors. (Left): PcbHLS. Two boards were separated 10 mm apart with nylon spacers. The board at the left contains the V_{lvl} excitation pad; the board to the right contains a V_{sense} sense pad and a guard pad on one side and a V_{ref} excitation pad on the other side. (Right): PcbVLS. FR4 spacers separated the boards by 3.2 mm. The board to the top consists of a V_{sense} sense pad and a guard pad on one side and a V_{ref} excitation pad on the other side; the board to the bottom contains another V_{lvl} excitation pad.

Regarding the test sensors, we used sets of PCB sensors to perform the measurements. The CAD drawings of the sensor are shown in figure 6.2. The geometry of the PCB sensors mimicked that of SHLS and SVLS in Run 3 - 6 of the SLAC system test. The PCB versions of SHLS (PcbHLS) and SVLS (PcbVLS), instead of using PEEK spacers to form the capacitors and thicker copper plates as electrodes, used FR4 [127] as the dielectric material and plated copper pads on FR4 boards to form its electrodes. They both had guard pads surrounding sense pads in the centre to decrease the stray capacitance between electrodes. Their reference capacitor C_{ref} were constructed by having another pad at the opposite side of the sense pad on the same PCB board. The level capacitor C_{lvl} was formed by nylon or FR4 spacers between the board with the sense pad and another board with the excitation pad.

6.1.1.2 Result of Mockup Tests

The data taken in the mock-up tests explain the features observed in liquid xenon tests. Figure 6.3 (Top) shows data of PcbHLS in its mineral oil filling process. As the liquid level reached the top surface of the bottom board of the sensor around 50:30 (min:sec) in figure 6.3 (Top), instead of flooding the board immediately, the meniscus effect forced the liquid to creep onto the board gradually and led to the initial filling feature (meniscus flood feature). After a stable filling period between 50:40 and 51:20, a tip of the liquid rise at an edge touched the bottom surface of the top board of the sensor. The adhesion force between the liquid and solid surfaces of the plate triggered a sudden rise in liquid level. Such a sudden rise wetted the bottom surface of the top board and resulted in the drastic increase in the data (wetting feature). After that, the feature which happened around 52:00 was the fringe field effect of the C_{ref} on the sensor (the same effect described in Section 5.5).

The data of PcbHLS in the mineral oil emptying process is shown in figure 6.3 (Bottom) which is similar to that of the filling process. Around 15:30, the liquid level dropped below the top board and perturbed the fringe field, which results in a decrease of C_{ref}, i.e. an increase in the measured signal. At 16:20, the adhesion force of liquid on the bottom surface of the top plate no longer withstood the force of gravity from liquid level reduction, which led to a sharp decline in the signal (capillary drop feature). However, after the decline, the residual of liquid on the top board accumulated to form a droplet which resulted in a temporary rise of the signal. As the weight of the droplet exceeded the adhesion force, it dropped off and created another drastic decline in the measured signal. Lastly, at the end

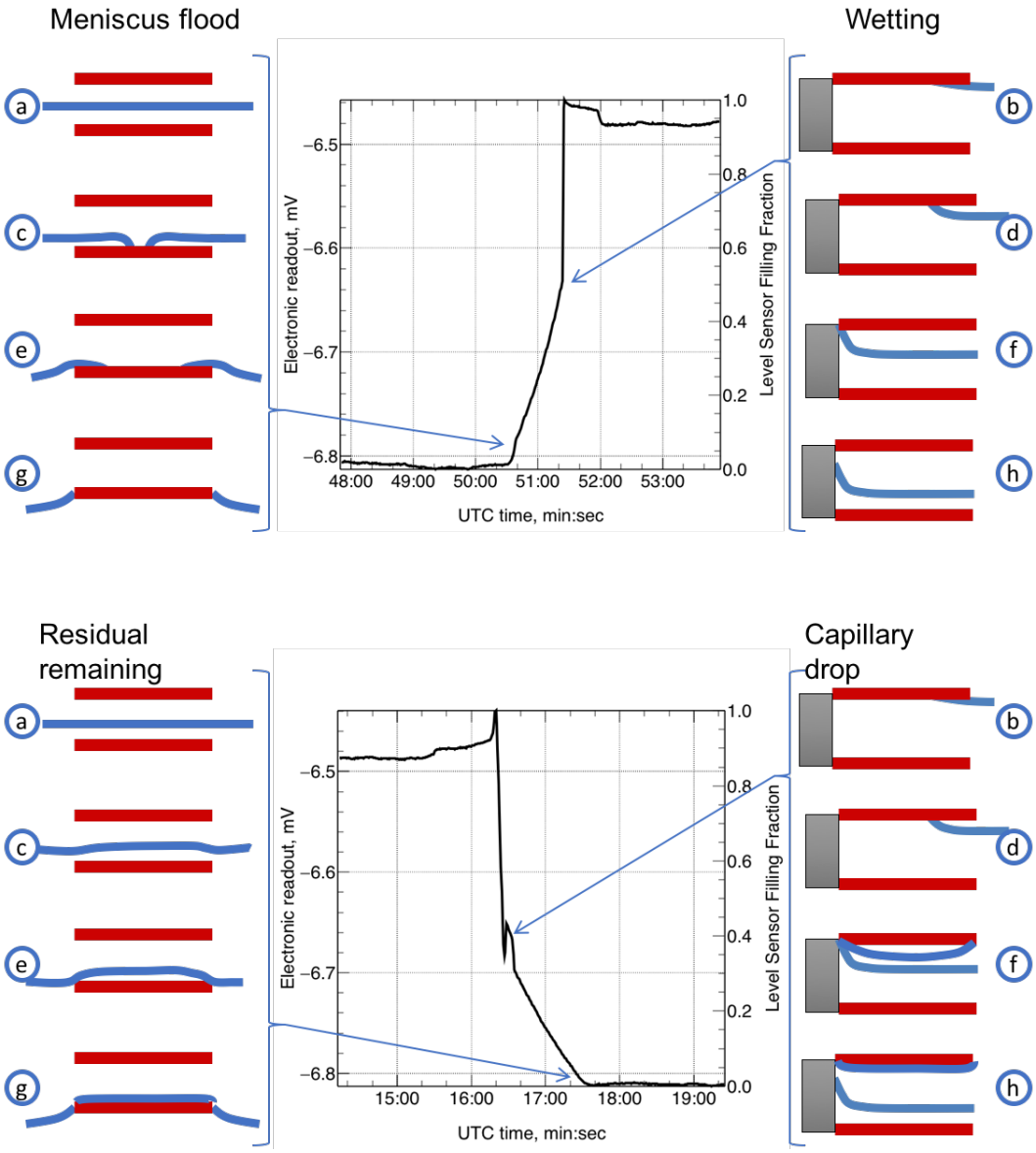
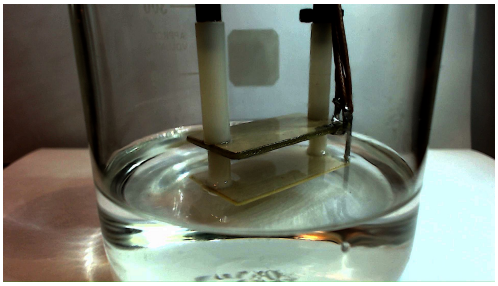
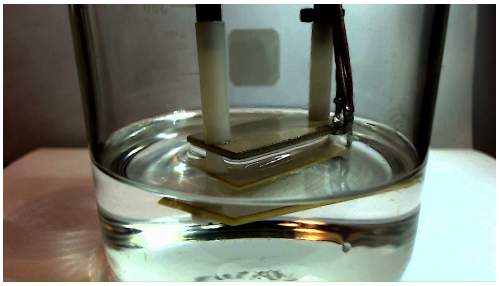


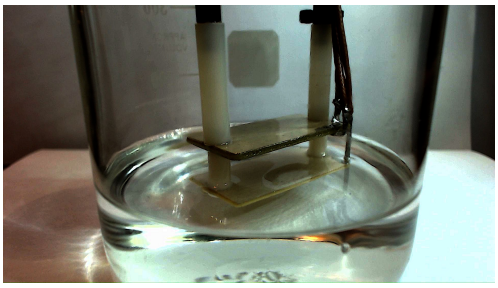
Figure 6.3: Data and illustration cartons show the PcbHLS measurements at the filling and emptying processes. The labels of the cartoons correspond to images in figure 6.4 for the filling process and figure 6.5 for the emptying process. (Top): Liquid filling of PcbHLS. (Bottom): Liquid emptying of PcbHLS.



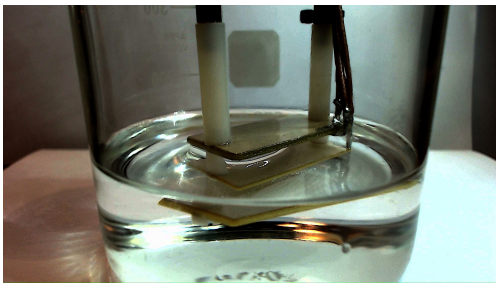
(a) $t_{MeniscusFlood}$ + 10 seconds



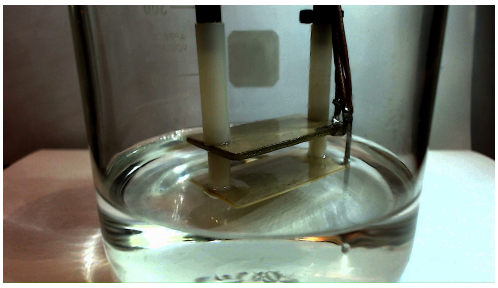
(b) $t_{Wetting}$ + 3 seconds.



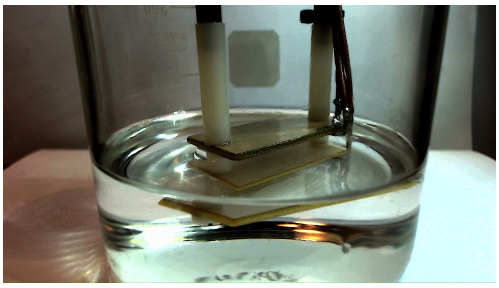
(c) $t_{MeniscusFlood}$ + 8 seconds



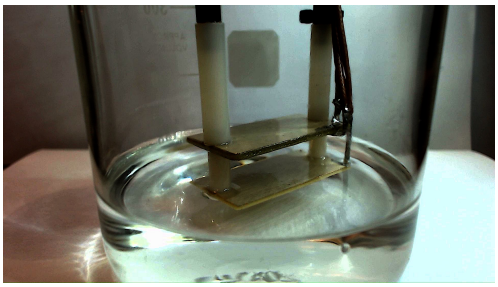
(d) $t_{Wetting}$ + 2 seconds



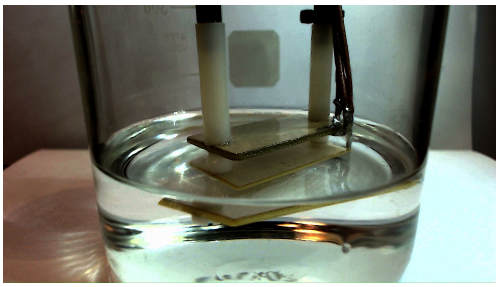
(e) $t_{MeniscusFlood}$ + 4 seconds



(f) $t_{Wetting}$ + 1 second



(g) $t_{MeniscusFlood}$ + 0 second

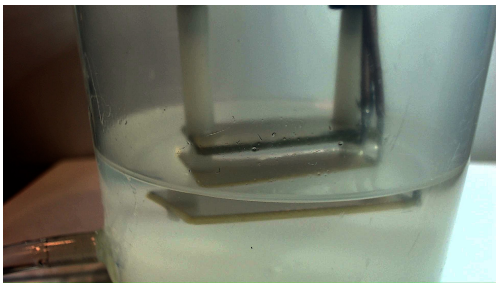


(h) $t_{Wetting}$+ 0 second

Figure 6.4: Images show occurrences of the features during liquid filling. (Left column figures): Sub-figure a, c, e, and g present the process of the gentle meniscus at the start of liquid filling. The timing of the process are reference to a UTC time $t_{MeniscusFlood} = 1441918229$ seconds. (Right column figures): Sub-figure b, d, f, and h show the process of the drastic wetting feature at the end of the filling. The timing of the process are reference to a UTC time $t_{Weting} = 1441918282$ seconds.



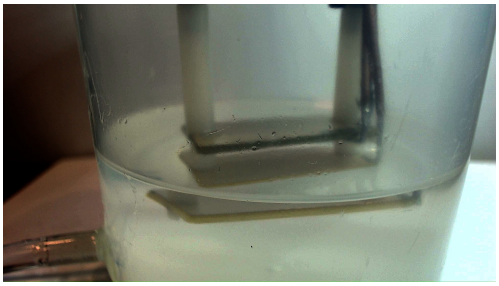
(a) $t_{ResidualRemaining}$ + 0 seconds



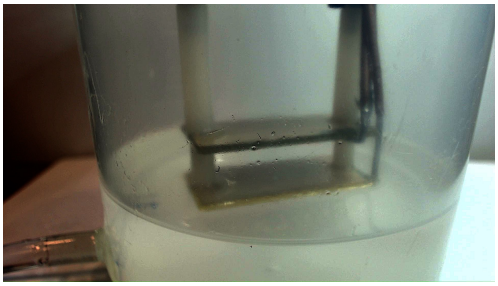
(b) $t_{CapillaryDrop}$+ 0 second



(c) $t_{ResidualRemaining}$+ 4 seconds



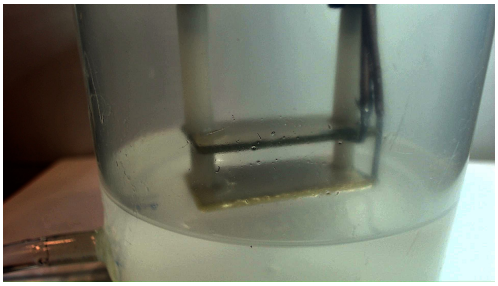
(d) $t_{CapillaryDrop}$ + 4 seconds



(e) $t_{ResidualRemaining}$ + 7 seconds



(f) $t_{CapillaryDrop}$ + 17 seconds



(g) $t_{ResidualRemaining}$ + 10 seconds



(h) $t_{CapillaryDrop}$ + 18 seconds

Figure 6.5: Images show occurrences of the features at emptying. (Right column figures): Sub-figure b, d, f, and h show the process of the liquid drop feature at the beginning of emptying. The timing of the process are reference to a UTC time $t_{CapillaryDrop} = 1441919776$ seconds. (Left column figures): The other four sub-figure. a, c, e, and g illustrate the process of the flat feature at the end of liquid emptying. The timing of the process are reference to a UTC time $t_{ResidualRemaining} = 1441919857$ seconds.

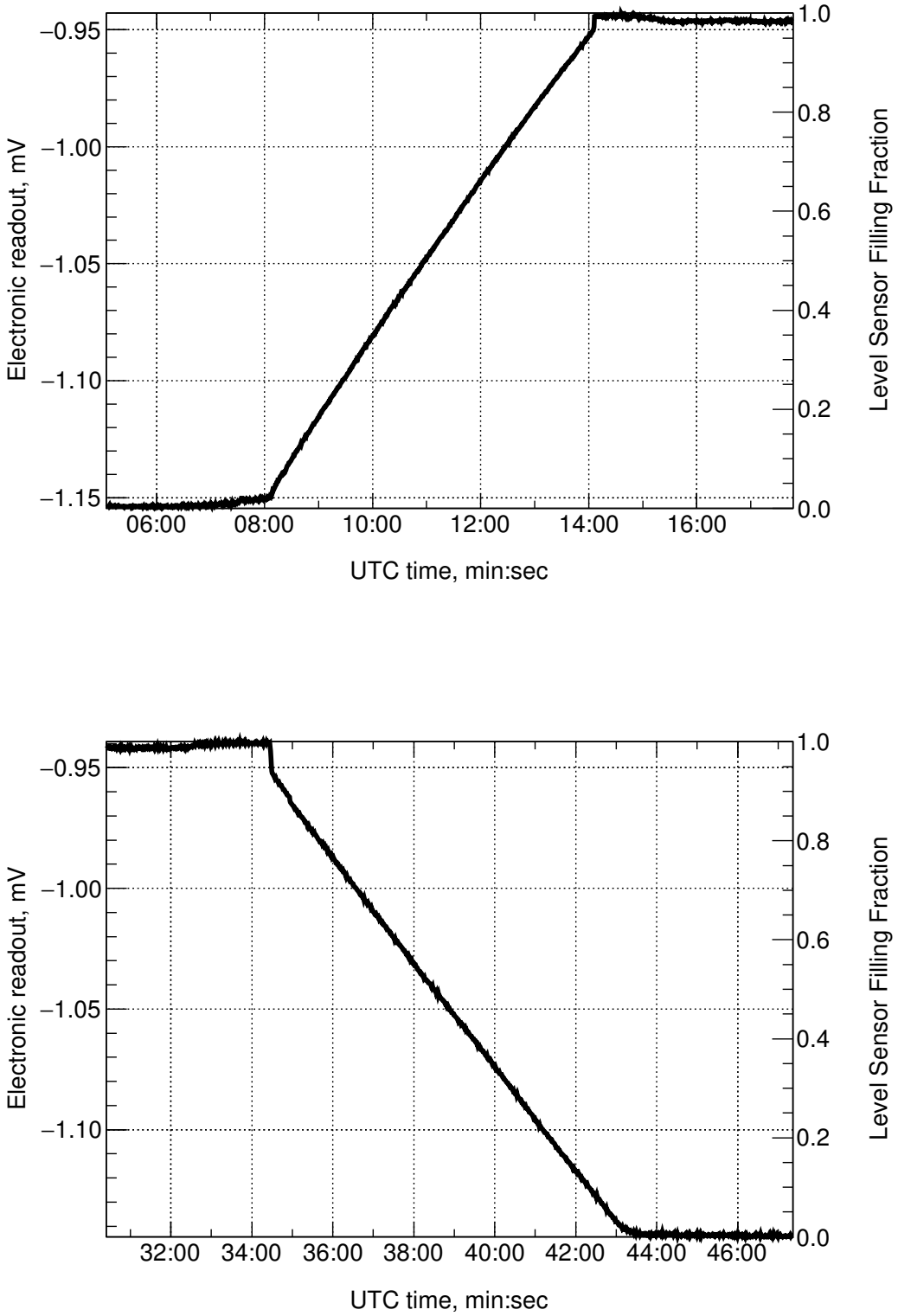


Figure 6.6: Data of PcbVLS mock-up tests. Features seen in PcbHLS are showing in PcbVLS as well. (Top): Liquid filling of PcbVLS. (Bottom): Liquid emptying of PcbVLS.

of the emptying, the residual liquid remaining on the top surface of the bottom board and did not lead to apparent data features like that at the beginning of the filling process (residual remaining feature).

Similar features also happened in PcbVLS mock-up tests. Figure 6.6 (Top) shows the result of PcbVLS in a filling test. Around 8:00, mineral oil crept onto the spacers which separated two boards of PcbVLS and created the meniscus flooding feature. After a period of stable filling, features happening between 13:30 to 14:00 came from the wetting of the spacers. The PcbVLS emptying data shown in figure 6.6 (Bottom) exhibits the typical features from the capillary drop and the residual remaining as that in the PcbHLS emptying. Because the spacing between the boards of PcbVLS was much smaller than that of the PcbHLS, the features from meniscus flood and residual resting on PcbVLS were less prominent.

The correlation of the images and the data confirms that such features are universal in liquid level measurement, both in LXe and in mineral oil. The features are geometry dependent and are either amplified (in the case of PcbHLS) or slightly suppressed (in the case of PcbVLS). The mitigation of the features is further discussed in section 6.2.1.3.

6.1.2 Dielectric Constant Variations

The correlation between the readout value change of an LXe-filled sensor and the LXe temperature discussed in Section 5.5 can be caused by the variation of dielectric constant with liquid temperature. Such variation decreases the accuracy of the level sensor and there is no measurement of the temperature dependence of the constant at frequency that is used for the excitation signals, i.e. $<$ GHz. In this

section, we discuss the theory of the dielectric constant of LXe and its expected dependence on temperature. We also carried out a test in the Imperial Chamber using the SVLS to obtain the dielectric constant variation at an electronic frequency of 200 kHz.

6.1.2.1 Theory of Dielectric Constant for Non-polar Material

The relative permittivity of a linear dielectric material can be expressed by the Clausius-Mossotti equation [101, 128]. If the material consists of atoms or nonpolar molecules, the induced dipole moment of each one is proportional to the electric field. The relationship between the dipole moment per unit atom, $\boldsymbol{p}$, and the dipole moment per unit volume, $\boldsymbol{P}$, due to external field $\boldsymbol{E}_{ext}$ is

$$\boldsymbol{P} = N \cdot \boldsymbol{p} = N\alpha \boldsymbol{E}_{ext}, \tag{6.1}$$

where $N = ((4/3)\pi R^3)^{-1}$ is the number density of atoms, and α is the polarisability of the atom. The average field over the sphere due to the atom itself is

$$\begin{aligned} \boldsymbol{E}_{self} &= -\frac{1}{4\pi\varepsilon_0}\frac{\boldsymbol{p}}{R^3} \\ &= -\frac{1}{4\pi\varepsilon_0}\frac{\alpha \boldsymbol{E}_{ext}}{R^3}. \end{aligned} \tag{6.2}$$

The total macroscopic field in the medium is

$$\begin{aligned} \boldsymbol{E} &= \boldsymbol{E}_{self} + \boldsymbol{E}_{ext} \\ &= (1 - \frac{N\alpha}{3\varepsilon_0})\boldsymbol{E}_{ext}. \end{aligned} \tag{6.3}$$

Thus, the total dipole moment per unit volume due to the total field becomes

$$\boldsymbol{P} = \frac{N\alpha}{(1 - \frac{N\alpha}{3\varepsilon_0})}\boldsymbol{E} = \varepsilon_0 \chi_e \boldsymbol{E}, \tag{6.4}$$

where $\chi_e = \varepsilon_r - 1$ is the electric susceptibility of a medium with a dielectric constant of ε_r. The equation for ε_r then is

$$\frac{\varepsilon_r - 1}{\varepsilon_r - 2} = \frac{N\alpha}{3\varepsilon_0}, \tag{6.5}$$

which can be written with the Avogadro number N_A, the molecular weight M, and the molecular density ρ as

$$\frac{\varepsilon_r - 1}{\varepsilon_r - 2} = \frac{4\pi}{3}\frac{N_A}{M}\alpha\rho. \tag{6.6}$$

At higher densities where interatomic interactions can influence the polarisation of an atom, equation 6.6 could be incorrect. The dependence on the density of the Clausius-Mossotti function is often expressed in a virial form:

$$\frac{n^2(\omega,T) - 1}{n^2(\omega,T) + 2} = \frac{\varepsilon_r(\omega,T) - 1}{\varepsilon_r(\omega,T) + 2} = A_\varepsilon(\omega,T)\rho(T) + B_\varepsilon(\omega,T)\rho(T)^2 + C_\varepsilon(\omega,T)\rho(T)^3 + \dots , \tag{6.7}$$

where the frequency and temperature dependence is explicitly noted and n is the refractive index. The coefficient B_ε and C_ε are from interactions between the neighbouring atoms which would be more prominent in solid than liquid or gas [129].

The validity of the virial form has been confirmed, and its coefficients have been measured to obtain Xe optical properties by many groups. In particular,

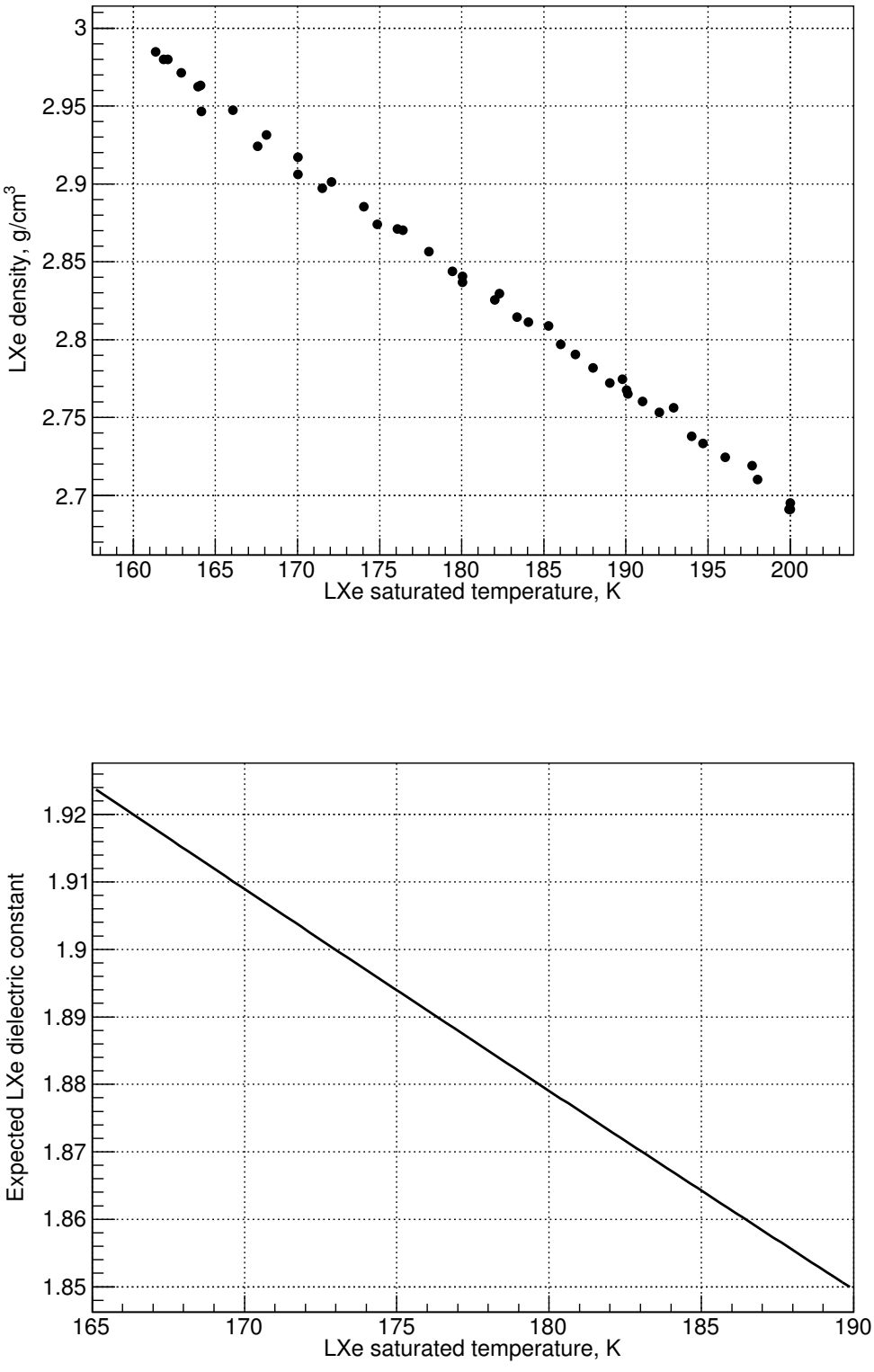


Figure 6.7: (Top): Measured LXe density along the liquid/vapor coexistence line. We used a linear fit to extract the dependence. Data taken from [130–134]. (Bottom): Expected dielectric constant change of LXe with temperature. We use $A_\varepsilon = 10.502 \pm 0.025\,\mathrm{cm^3 mol^{-1}}$, and $M_{Xe} \approx 131.3$ to obtain the correlation.

Sinnock [135, 136] has measured the refractive index with a total refractometer at $\lambda > 546.1\,\text{nm}$ and shows the dependence of the index with LXe saturated temperature in optical frequencies. The author also shows a negligible variation of A_ε in LXe with temperature. Furthermore, Ref. [129, 137] review the contribution of high order coefficients B_ε and C_ε for LXe which are comparatively smaller than A_ε. The suppression of them is from the weak temperature dependence of the spatially averaged interactions among atoms and results in a small effect on the atomic polarisability at the density of the liquid. Therefore, for LXe, equation 6.7 is simplified as

$$\frac{\varepsilon_r(\omega, T) - 1}{\varepsilon_r(\omega, T) + 2} = A_\varepsilon(\omega)\rho(T). \tag{6.8}$$

The typical photon absorption for LXe happens around $\sim 7\,\text{eV}$ (or $2\,\text{PHz}$) [138, 139] and our method of measurement described later in Section 6.1.2.2 was driving the LXe at an electronic frequency with an electromagnetic field of $\sim 200\,\text{kHz}$. Although Ref. [129] suggests a suppression of ω-dependence at lower frequencies for A_ε, the frequency dependence of A_ε is retained since there are no data in the literature to show such a suppression. As a result, the equation for the dielectric constant variation at a given saturated temperature T change is

$$\varepsilon_r(\omega, T) = \frac{2 \cdot A_\varepsilon(\omega)\rho(T) + 1}{1 - A_\varepsilon(\omega)\rho(T)}. \tag{6.9}$$

Figure 6.7 shows the dependence of LXe density with its saturated temperature and its corresponding variations in dielectric constant. We use the A_ε at $\lambda = 643.9\,\text{nm}$ for LXe in Ref. [135] which gives the xenon polarisability $\alpha_{Xe} \approx 4.16 \times 10^{-24}\,\text{cm}^3$. A usual two phase liquid xenon detector, operating at a temperature

between 165 K and 185 K, could see a variation of the LXe dielectric constant of $\sim$ 3.2 %. This is consistent with the observation described in Section 5.5. An improper choice of the xenon dielectric constant could introduce uncertainties for the level sensor and thus increase inaccuracy of the level measurement and the projection of detector's S2 signal and its electron extraction efficiency.

6.1.2.2 ε_{LXe} Measurement Method

To confirm the variation of the LXe dielectric constant at the frequency of the excitation signal produced by the electronics, we performed a measurement test with the level sensor in the Imperial chamber. The T1 IVLS is the most suitable sensor for data taking because it is less affected by fringe fields and can be fully submerged in LXe in the chamber. The data taking was performed with an electronics that obeys equation 4.11 to measure capacitance changes and has a precision of ± 0.42 fF. Instead of using the PEEK part of the sensor's reference capacitor, we installed an external precision capacitor of $C_{ext} = 10.014 \pm 0.002$ pF, calibrated at 100 kHz with an Agilent U1733C Capacitance Meter, outside the xenon space to replace C_{ref}. Such arrangement isolated the effect of T1 IVLS' C_{ref} on its C_{lvl} measurement.

The method of measuring the ε_{LXe} was done by comparing changes of an LXe filled C_{lvl} with its capacitance in GXe. The measured liquid level capacitance in cold GXe at 163 K is

$$\begin{aligned} C_{lvl-GXe} &= C_{liq} + C_{pk} \\ &= 2.0491 \pm 0.0002\,\text{pF}, \end{aligned} \tag{6.10}$$

where C_{liq} is the section of the capacitor used for the ε_{LXe} measurement, C_{pk} is the section with small PEEK spacers. When the LXe filled the C_{lvl}, the equation for its capacitance is

$$\begin{aligned} C_{lvl-LXe}(T) &= C_{liq}\varepsilon_{LXe} + C_{pk} \\ &= C_{lvl-GXe} + C_{liq} \cdot (\varepsilon_{LXe}(T) - 1). \end{aligned} \tag{6.11}$$

By inserting equation 6.11 into equation 4.11, we can obtain

$$\varepsilon_{LXe}(T) = ((\frac{1 + R(T)}{1 - R(T)}) \cdot C_{ext} - C_{lvl-GXe}) \cdot C_{liq}^{-1} + 1, \tag{6.12}$$

where $R = {}^{V_{out}}/_{V_{adc}}$ is the signal ratio from the electronics. We used $C_{liq} = 1.2669\,\text{pF}$, calculated based on the geometry of IVLS, to obtain the changes of $\varepsilon_{LXe}(T)$.

6.1.2.3 ε_{LXe} Result

We followed the same procedure described in Chapter 5 to operate the detector and measured the variation of C_{lvl} with chamber pressure. After we overfilled the sensor, the chamber's liquid reached a favourable level around 11:00 (hour:min). We subsequently stopped the filling, set the heater at 178.5 K, and let the sensor monitor the stabilising period of the chamber as shown in figure 6.8. Because the chamber hadn't reached thermal equilibrium before 12:00, the pressure dropped from 2.44 bar to 2.1 bar, and more xenon was condensed. However, after that, the xenon saturated and the pressure increased slightly from 2.1 bar to 2.35 bar.

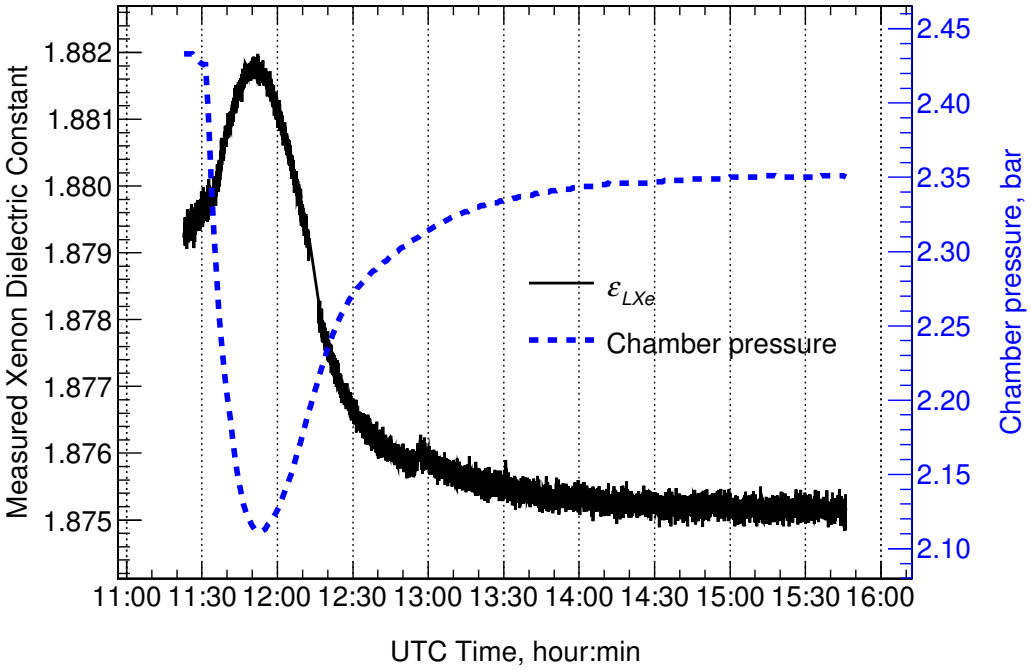


Figure 6.8: Dependence of the LXe-filled C_{lvl} on chamber pressure changes.

The changes of C_{lvl} were apparent during the stabilisation period of the chamber in figure 6.8. The measured C_{lvl} exhibited an inversely proportional relation to chamber's pressure. Since the LXe wasn't saturated before 12:00 due to the condensation, we performed a cut at 12:00 to extract the correlation.

Figure 6.9 shows the observed LXe dielectric constant against the LXe saturated temperature after the cut. The saturated pressure was converted to temperature using the Antoine equation from Ref. [140]; the electronics signal R was translated to ε_{LXe} with equation 6.12.

The measured ε_{LXe} was fitted with with equation 6.9. The fitting gave $A_\varepsilon(200\,\mathrm{kHz}) = 10.436\,\mathrm{cm}^3/\mathrm{mol}$, which is consistent with previous studies from Ref. [135, 136] in optical frequencies and exhibits gentle frequency dependence. By comparing with the data of ε_{LXe} obtained between $643.9 \sim 178\,\mathrm{nm}$ (around $460 \sim 1700\,\mathrm{THz}$) from Ref. [135, 138], the suppression of $A_\varepsilon(\omega)$'s dependence on electronic frequency

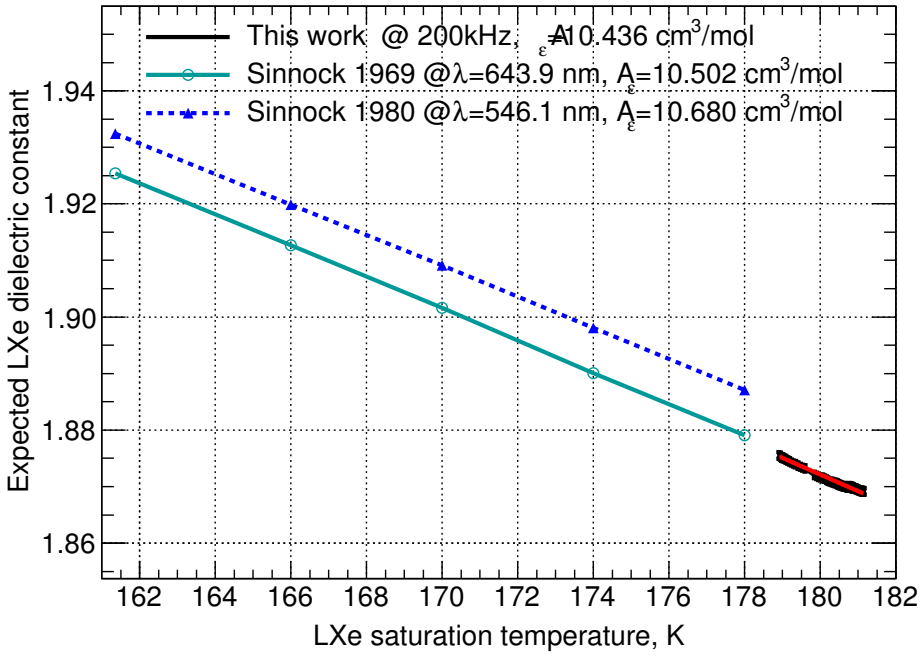


Figure 6.9: Xenon dielectric constant changes with saturated temperature. The black points with error bars about the same size as the marker size are the measurement from this work. The red line is the fitting function using equation 6.9.

($\sim$ 200 kHz), in Ref. [129], is confirmed. The result shown in figure 6.10 suggests a variation of ε_{LXe} by 0.34 % between 200 kHz and 460 THz, indicating a limited frequency dependence. However, as of writing, there is no data in measuring the constant in this frequency range. In conclusion, future work is required to explore the constant at a frequency range of 200 kHz $\sim$ 460 THz and the result of this measurement allows correct interpretations of ε_{LXe} between 165 K and 185 K at an electronic frequency of 200 kHz.

6.2 Design of LZ Level Sensors

The final design of the LZ level sensor, both for the LZ top-corner region and the circulation systems, follows the requirements discussed in Chapter 4 and the

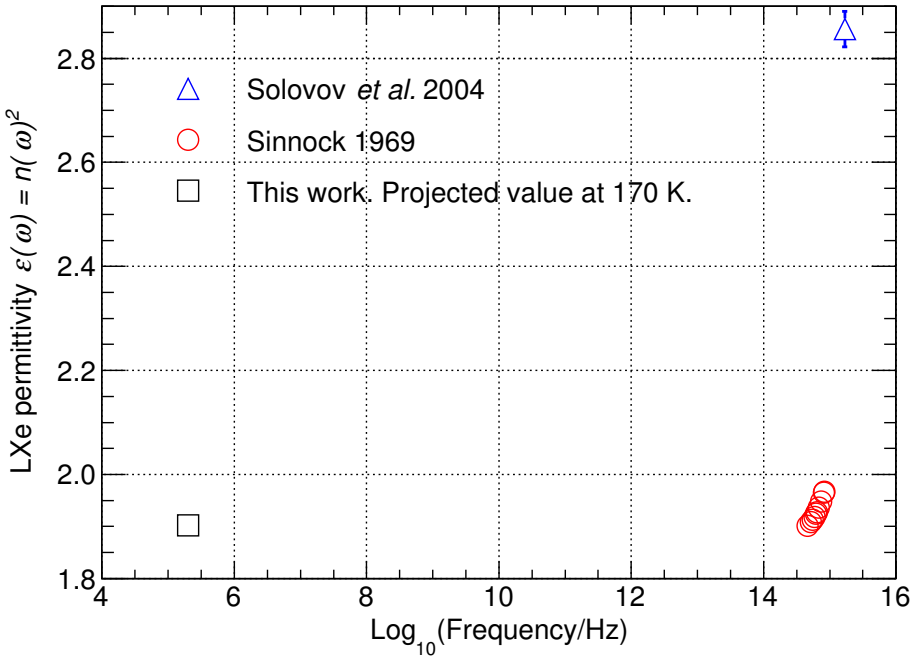


Figure 6.10: Frequency dependence of $\varepsilon_{LXe}(\omega)$ at a 170 K. Our measurement of the constant ranges from 175 K to 185 K. To compare our result with other measurements at 170 K, we project the constant - $\varepsilon_{LXe}(200\,\text{kHz},\ 170\,\text{K})$ at 170 K based on the fitting result of $A_\varepsilon(200\,\text{kHz})$ shown in figure 6.9.

mitigation strategies described later in Section 6.2.1.

Because the level sensors in the circulation system (MLS and LLS) follow similar form factors as that in the top-corner (WPS), we will focus on discussing the design and the result of the WPS in this section (see Appendix A for MLS and LLS in the LZ circulation system). We will start by discussing the mitigation strategies of their technological issues. We will then illustrate the geometrical design incorporating the mitigation strategies and end the section with the result of sensors' performance tests in LN_2.

6.2.1 Technical Issues and Mitigation Strategies

Technical issues such as dielectric constant variation, thermal expansion of materials, capillary effects from the liquid, and electric field issues will diminish the level sensor's accuracy. The issue arising from a material's dielectric constant variation described in Section 6.1.2 has been tackled through experimental measurements with the use of the Clausius-Mossotti equation. However, the thermal expansion of materials, the fringe field interference, liquid artefacts, and high voltage issues cannot be corrected for as is possible for the other effect. They have to be solved through the optimisation of geometric design. Their mitigation strategies are discussed in this section.

6.2.1.1 Material Expansion and its Mitigation

The effects from material expansion on sensors led to shrinkage differences between parts, described in section 5.2.1 and 5.4.1. The shrinkage mostly impact the stability of the reference capacitors. As a result, a minimal number of PEEK parts should be used to construct the sensor's C_{ref}, preferably only a PEEK spacer between the sense and the excitation plates. This would leave the shrinkage of PEEK to a single part and relax the complexity in interpreting systematic effects from material shrinkage of the capacitor. Furthermore, instead of using PEEK to construct most of the sensor's part, a material with high thermal conductivity and lower CTE, e.g. copper, should be used to form the bulk part of the sensor (see table 4.3.2). Because of the high thermal conductivity of copper ($\sim 401\,\mathrm{W}\cdot\mathrm{m}^{-1}\cdot\mathrm{K}^{-1}$), the sensor's temperature profile would be more uniform when it is is partly submerged in LXe. Such an approach would also ensure the

PEEK plate of C_{ref} thermally couples to copper parts efficiently, and thus decrease the variation of the reference capacitor (discussed in section 6.2.3).

6.2.1.2 Fringe Field Interference and its Mitigation

The fringe field at the edges of capacitor plates introduces unwanted capacitance variations during liquid level measurements by the field squeezing effect discussed in section 5.5. The solution to the effect would be breaking such capacitive coupling with better implementation of the guard parts and the excitation electrodes. For the C_{ref}, this would be shielding the sense and excitation plates in a grounded guard cage. The cage isolates the capacitor from external common mode interferences and any potential capacitive couplings to the sense plate. As for the C_{lvl}, the sense plate can be sandwiched between excitation plates and surrounded by guard electrodes. The sandwiching arrangement will establish uniform electric field couplings to the excitation plates and thus minimise the squeezing effects at either side of the sense plate (implemented in WPS and discussed in 6.2.2).

6.2.1.3 Liquid Artefacts and their Mitigation

The liquid artefacts discussed in section 6.1.1 are irreducible systematics. The presence of such effects decreases the effective measurement range and the accuracy of sensors. For instance, the liquid level in a typical filling or emptying process can be calculated by comparing data of a liquid-filled and liquid-emptied sensor. However, the residual liquid remaining on sensor plates and that within structures between the sense and excitation plates in the liquid-emptied data can contribute to measurement uncertainty. This means that a solution of the artefacts would be decreasing the possibility of liquid residue remaining on the sensor and require

a modification of the geometry of C_{lvl}. A horizontal geometry, e.g. a SHLS-like sensor, fundamentally cannot accommodate changes to alleviate the problems from meniscus rise, wetting, capillary drop and residual resting. However, using a SVLS-like geometry for the LZ level sensors can be the solution. By removing or extending the PEEK spacers of such SVLS-like sensor outside its effective measurement range, despite the fundamental presence of the liquid artefacts, it can achieve an artefact-free liquid level measurement. Moreover, as we have proved the precision of SHLS at $\sim 7\,\mu$m and SVLS at $\sim 11\,\mu$m, although the SVLS-like sensor may not have a precision equivalent to that of the SHLS-like sensor, it should still be sufficient to perform surface level measurement and achieve the LZ requirement, i.e. $< 20\,\mu$m.

6.2.1.4 High Voltage and Mitigation

The high voltage concerns in the skin region around the perimeter of the top-corner structure are non-trivial. The issues discussed in section 5.4.4 of the SLAC TPC suggest corners with high EL production and potential breakdown points near the level sensors. A solution to the HV issues for the LZ top-corner region would be identifying an optimal location for the sensor through electrostatic simulations. Such a location should lead to minimum fields outside the S2 production region in both LXe and GXe. Thus, a detailed field simulation with COMSOL Multiphysics was carried out to quantify and identify such a location for the LZ level sensors.

Figure 6.11 shows the drawing of the LZ top-corner geometry in 2 dimensions. Because the geometry of LZ TPC is cylindrically symmetric, a cross-section slice of the top-corner can represent the rest of the region to first order. A rectangular box

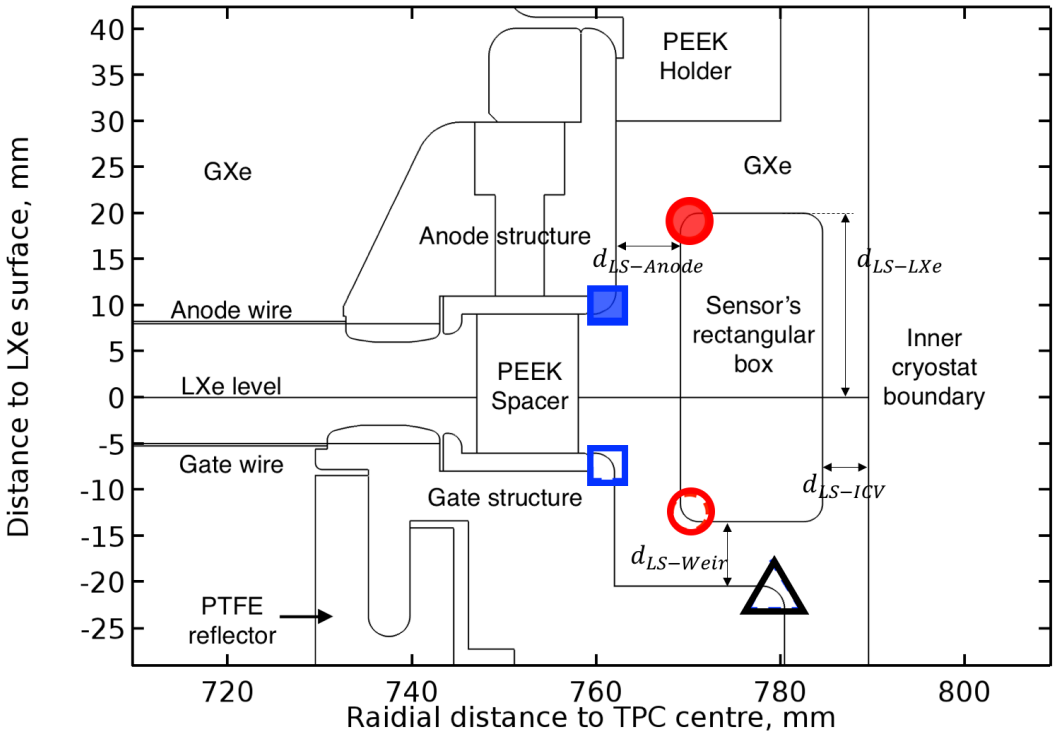


Figure 6.11: Drawing of the LZ top-corner design. The rectangular box represents a dummy sensor situated in the TPC skin region. The markers are the locations of local high fields in LXe or GXe. In LXe: the blue solid square is the edge of anode structure; the red solid circle is the top edge of sensor's box. In GXe: the blue empty square is the edge of anode structure; the red empty circle is the bottom edge of sensor's box; the black empty triangle is the edge of the weir structure.

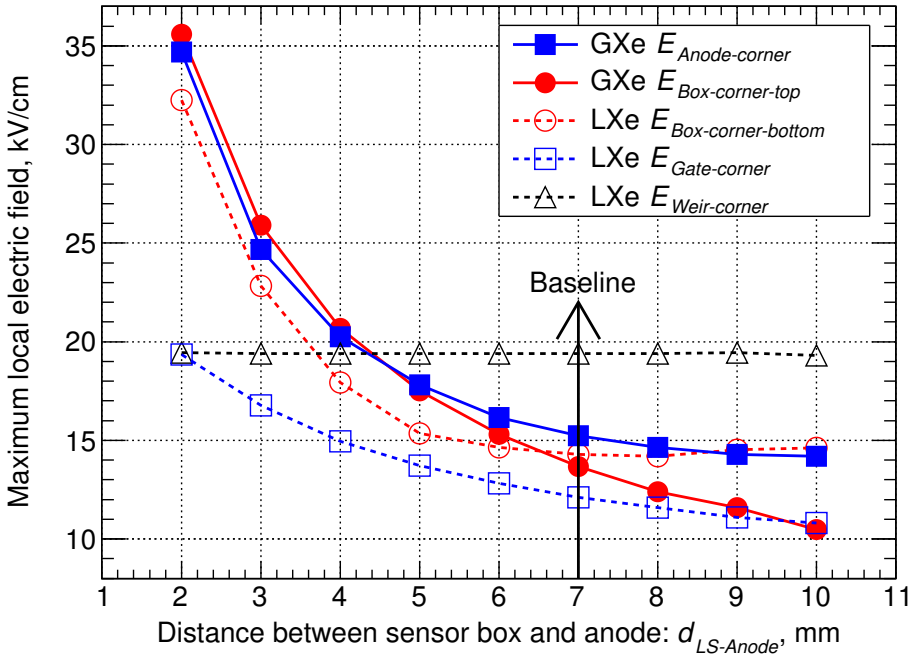


Figure 6.12: Field simulation of various $d_{LS-Anode}$ with fixed $d_{LS-Weir} = 5\,\text{mm}$, $d_{LS-ICV} = 5\,\text{mm}$, and $d_{LS-LXe} = 20\,\text{mm}$. Data points with different marker styles correspond to the locations with same marker style shown in figure 6.11. Solid lines represent fields in GXe; dashed lines indicate fields in LXe.

was placed near the top-corner to represent the placement of a level sensor. This approach assumed that the shape of the sensor is curved so that the radial distance of the box to the centre of the TPC does not change with the choice of a cross-section slice. By moving the box around the region to look for minimal electric fields on components, an optimal placement and size of it can be determined.

The distances between the box and different surfaces at the top-corner region were first parameterised. The distance between the box and the inner cryostat wall d_{LS-ICV} and the height of the sensor above the LXe level at the weir trough d_{LS-LXe} were fixed at 5 mm and 20 mm, respectively. Then, distances between the box and a corner of the anode ($d_{LS-Anode}$) and a surface of the weir structure ($d_{LS-Weir}$) were varied to study different field situations.

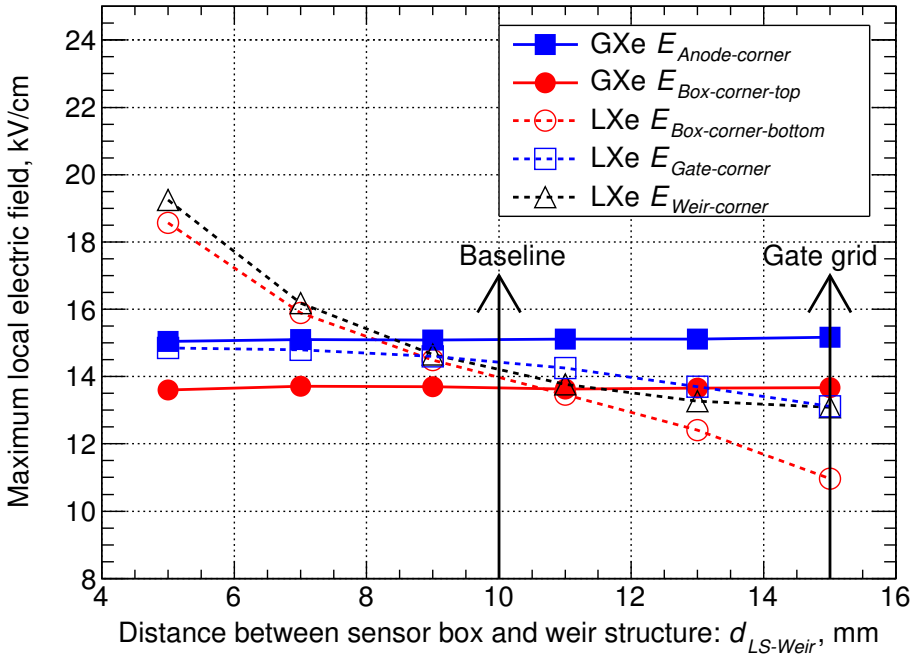


Figure 6.13: Field simulation of various $d_{LS-Weir}$ with fixed $d_{LS-Anode} = 7\,\text{mm}$, $d_{LS-ICV} = 5\,\text{mm}$, and $d_{LS-LXe} = 20\,\text{mm}$. Data points with different marker styles correspond to the locations with same marker style shown in figure 6.11. Solid lines represent fields in GXe; dashed lines indicate fields in LXe.

Before studying different scenarios of the box's placement, the result of the electric field map of the top-corner region without the implementation of the box is shown in figure 6.14 (Top). The map shows that the maximum field in the skin GXe region happens at a corner on the anode ($\sim 14\,\text{kV/cm}$) and that in the skin LXe region happens at a corner of the weir structure ($\sim 12\,\text{kV/cm}$). The values are much lower than the maximum field in the extraction ($\sim 21\,\text{kV/cm}$) or the $50\,\text{kV/cm}$ surface field baseline in LXe. The result, compared with that in SLAC system test, exhibits a remarkable reduction of fields at the skin region in the top-corner region. Next, we looked at how the implementation of the box would affect these fields.

When the $d_{LS-Anode}$ was decreased gradually, the result of fields at various

locations in the skin region changed accordingly and this is shown in figure 6.12. The simulations show that the field was more intense in the GXe than that in the LXe because the dielectric constant of LXe contributed to the field suppression. In general, fields coupling to the weir structure, i.e. the empty square and triangle, were less affected by the distance change; the closer the sensor to the anode, the higher the maximum fields in skin GXe/LXe regions was. The strongest fields in the skin region were at the corner of the anode structure ($E_{Anode-corner}$, solid square) in GXe and the bottom corner of the box ($E_{Box-corner-bottom}$, empty circle) in LXe. Both fields were very high when the box was close to the anode. They, however, plateaued around 15 kV/cm as the $d_{LS-Anode} > 7$ mm. Such a trend suggests that the field coupling between the gate and anode dominated the field distribution nearby them at larger $d_{LS-Anode}$. Moreover, another corner with a large electric field was at a top-corner of the box ($E_{Box-corner-top}$, solid circle). The field followed the same trend as the $E_{Anode-corner}$ and $E_{Box-corner-bottom}$ but decreased below them as $d_{LS-Anode} > 6$ mm. This suggests that the field in the skin GXe region is dominated by $E_{Anode-corner}$ when $d_{LS-Anode} > 6$ mm. Therefore, the baseline limit of $d_{LS-Anode} = 7$ mm is decided. The upper limit of the distance is set at 9 mm because a further increase of the distance would increase the difficulty in building a smaller sensor with full implementation of the mitigation strategies discussed in previous sections.

Next, the search for the optimal distance between the box and the weir structure $d_{LS-Weir}$ followed the same optimisation process as that of $d_{LS-Anode}$. The constraints of d_{LS-ICV} and d_{LS-LXe} remained the same; $d_{LS-Anode}$ was fixed at 7 mm; $d_{LS-Weir}$ was varied between 5 mm to 15 mm. The result is shown in figure

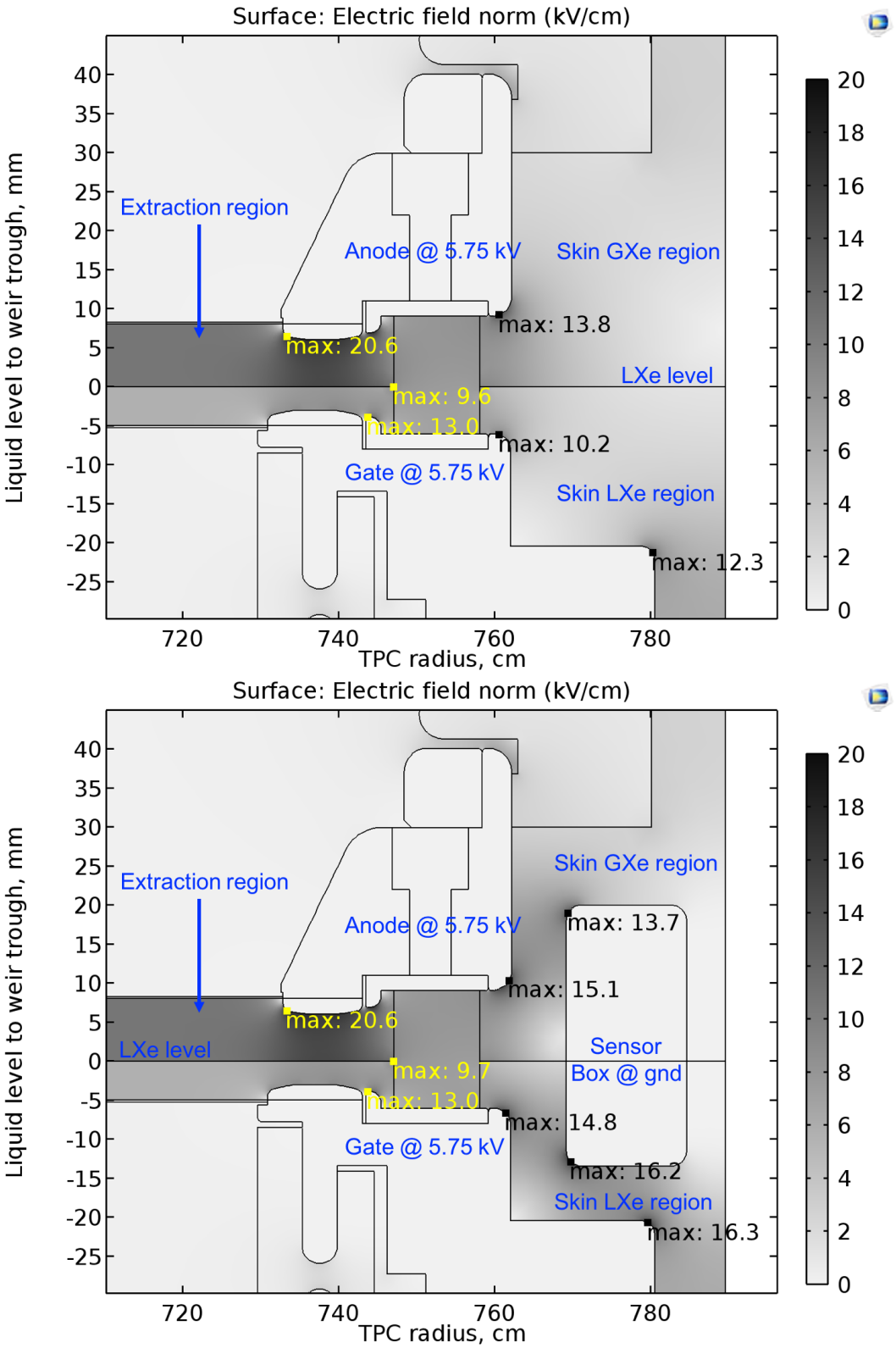


Figure 6.14: The result of electric field maps at the top corner region. The grid voltages - V_{gate} and V_{anode} were set at $-5.75\,\mathrm{kV}$ and $+5.75\,\mathrm{kV}$, respectively. Dot markers with numbers marked next to them are the maximum field in those local areas. Field values inside the extraction region are yellow; field values in the skin region are black. (Top): Field map without the sensor's box. (Bottom): Field map with the presence of the box using $d_{LS-Anode} = 8\,\mathrm{mm}$, $d_{LS-Weir} = 10\,\mathrm{mm}$, $d_{LS-ICV} = 5\,\mathrm{mm}$, and $d_{LS-LXe} = 20\,\mathrm{mm}$.

6.13. In general, fields such as $E_{Anode-corner}$, $E_{Box-corner-top}$, and $E_{Gate-corner}$ at their corresponding local regions did not change as the $d_{LS-Weir}$ increased; the larger the $d_{LS-Weir}$ was, the lower the fields - $E_{Box-corner-bottom}$ and $E_{Weir-corner}$ - were. The former case was due to the stronger field coupling between the anode and gate structure; the latter case was purely from the inverse-square law of the electric field. Interestingly, fields in the later case decreased below that in the first instance when $d_{LS-Weir} > 10\,\text{mm}$. Thus, a baseline value of $d_{LS-Weir}$ was chosen at 10 mm. This value also conveniently allows measurements of the liquid level at the gate grid which would aid the filling process of the LZ extraction region.

Figure 6.14 shows the comparison of the top-corner field maps before and after the implementation of the sensor box at its optimal location. The result demonstrates a gentle rise of the maximum field in skin LXe to 16 kV/cm but still far below the 50 kV/cm limit ($3-4$ times lower than that of the result of SHLS and SVLS in figure 5.24). The GXe field on the anode structure's corner slightly increases to 15 kV/cm. The field is larger than that on the sensor ($\sim 14\,\text{kV/cm}$) but smaller than that in the extraction region ($\sim 21\,\text{kV/cm}$). After all, it is shown that the presence of the sensor at the top-corner region does not increase fields considerably. The simulation result provides a mitigation solution which suppresses the HV fields at the LZ top-corner region considerably and concludes an optimal location for level sensors to monitor the LXe surface activities.

6.2.2 Final Design of a Forest-like Geometry

Here, we present the final design of the LZ top-corner level sensor, i.e. the weir precision sensor (WPS), with a forest-like geometry that will be tested in Run 7 of

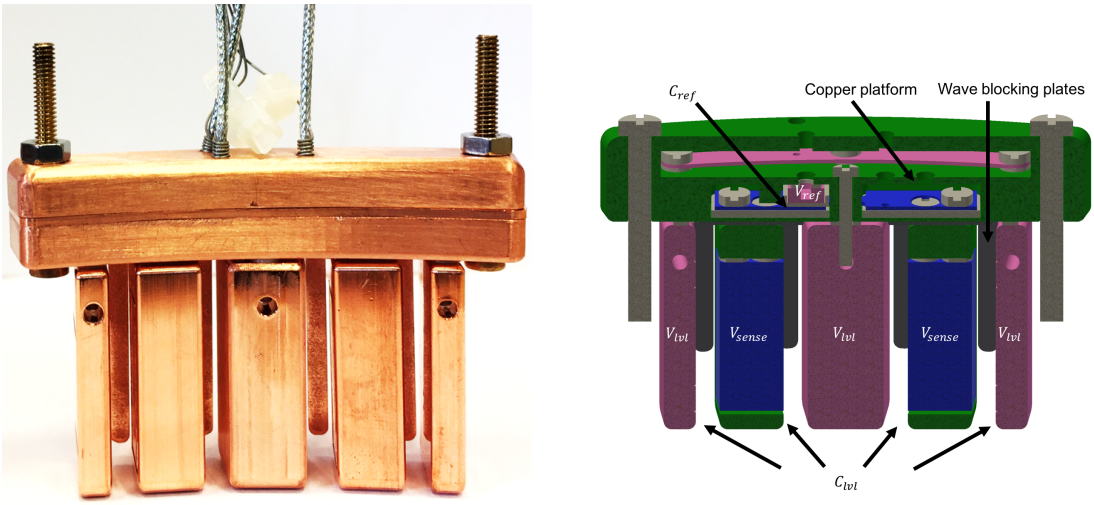


Figure 6.15: The level sensor with a set of vertically parallel plates. (Left): Level Sensor with a forest-like geometry. The vertical plates forms the C_{lvl} section; the C_{ref} section is sealed inside the horizontal cage. (Right): Cross-section view of the WPS, with $d_{lvl} = 3\,\text{mm}$, $W_{lvl} = 7\,\text{mm}$, $L_{lvl} = 20\,\text{mm}$, $d_{ref} = 0.5\,\text{mm}$ and $A_{ref} = 40\,\text{mm}^2$. Pink: excitation joint plate and electrodes; blue: sense joint plate and electrodes; light beige: PEEK screws, spacers, and washers; green: guard cage and electrodes; grey: grounded wave blocking plates to reduce reflecting waves from the cryostat vessel.

the SLAC system test. The design of WPS follows the measurement method and requirements described in Chapter 3. Most importantly, it has been integrated with the mitigation strategies of liquid artefacts, material expansion, fringe fields, and HV issues.

The drawing and the assembly of the sensor are shown in figure 6.15. The WPS has an IVLS/SVLS like arrangement for the C_{lvl}. The capacitor's sense plates together with its guard plates are hung below a horizontal copper platform. This vertical geometry minimises the amount residual liquid on the sense plates. Also, the guard plates do not have spacers between them at the bottom of the sensor as that in SVLS and extend the sense plate away from the platform. Hence, this design effectively eliminates the artefacts of meniscus-flood/residual-remaining and restricts the occurrence of the expected wetting/capillary-drop features to the

bottom surface of the platform. Therefore, the geometrical arrangement highly suppresses the liquid artefacts within the sensor's designed measurement range.

The material expansion issue is tackled by maximising (minimising) the number of copper (PEEK) parts. The variation of C_{lvl} is controlled by the copper platform at the top of the sensor, which confines the shrinkage of gaps between plates in one direction. As for the C_{ref}, it is moved to the top of the sensor and shielded within the platform. The platform not only provides shielding for the capacitor but also aids the thermal conduction of the capacitor's PEEK spacer, which improves its stability during the liquid level measurement.

The fringe field issues are resolved through better implementation of guard electrodes. The mitigation strategies for the fringe field discussed in section 6.2.1.2 are the result of electrostatic simulations. The result for both C_{lvl} and C_{ref} of the WPS is shown in figure 6.16. The excitation plates of the C_{lvl} with a forest-like the geometry hides and sandwiches the sense electrodes to establish smooth field lines between plates. As for the C_{ref}, its excitation electrode is surrounded by the structure of the copper platform which effectively serves as a guard cage. The cage reduces the possibility of the field squeezing effect (described in section 5.5) and increases the uniformity of field lines between C_{ref}'s sense and excitation electrodes within PEEK spacer. These designs based on the simulation reduces the fringe field issues considerably.

Lastly, the implementation of the HV mitigation strategies described in section 6.2.1.4 is achieved in two ways. Firstly, the copper structure of the sensor is open to LXe/GXe. This open structure avoids creating multiple local areas with high fields as that in the case which buries electrodes in PEEK. The curved sensor shape

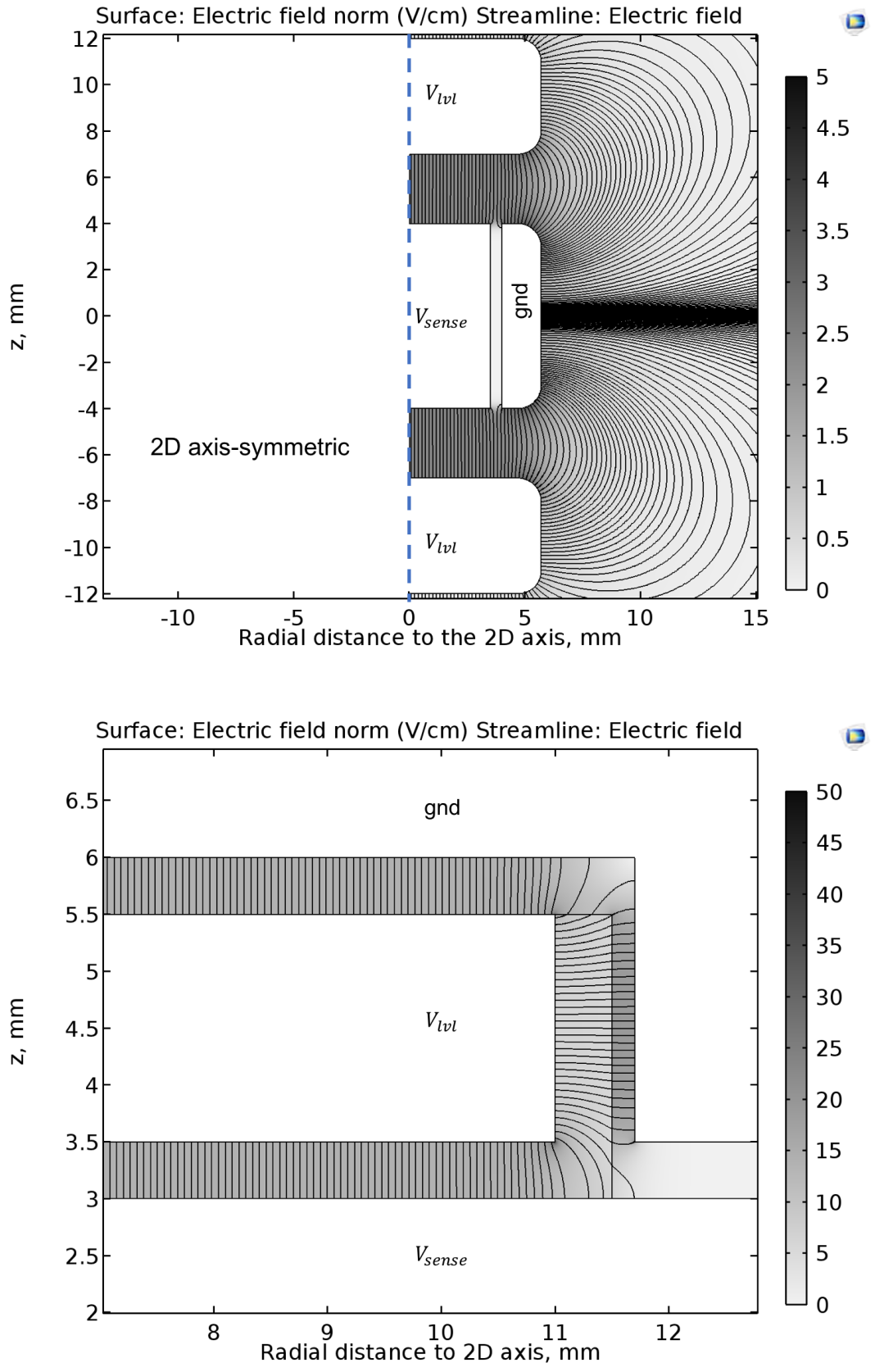


Figure 6.16: COMSOL Simulation of fringe field of sensor's C_{ref} and C_{lvl}. $V_{lvl} = V_{ref} = 0.7\,\mathrm{V}$. Because the electronics adjusts the excitation signals such that the sense plate is at ground potential, $V_{sense} = 0$. (Top): WPS' C_{lvl} in GXe. (Bottom): WPS' C_{ref} in GXe. The region between the V_{lvl} and V_{sense} is the PEEK spacer.

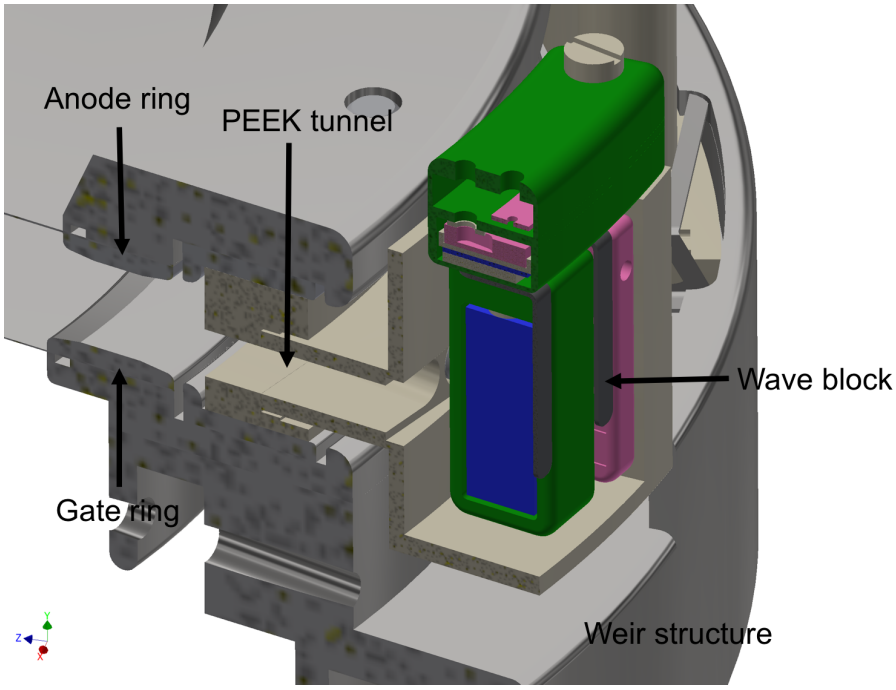


Figure 6.17: CAD drawing of the interface of the WPS with the top-corner region through a PEEK tunnel in Run 7 of the SLAC system test. The test will examine the final design of the LZ top-corner region.

allows equal distances between the sensor and the anode so that the simulation result shown in Figure 6.14 can be realised. Next, a further reduction of light production at the LZ top-corner region is achieved through implementing a PEEK tunnel (shown in figure 6.17). The tunnel part not only delivers the LXe surface wave from the extraction region to the sensor but also prohibits a large amount of space in the skin region for local electroluminescence production.

6.2.3 Performance of the Sensor

A set of calibration tests for verifying the final design of the C_{lvl} and C_{ref} of the sensor were performed with three WPS' produced for Run 7 of the SLAC system test [1]. The sensor's capacitors were first characterised separately at room

[1]The top-corner structure in the Run 7 is designed based on the electrostatic simulation shown in figure 6.14. The run will confirm the performance of the final design of the top-corner structure which will eventually become the LZ top-corner structure.

	WPS001	WPS002	WPS003
Measured C_{lvl}, pF	$1.758^{+0.04\ \%}_{-0.73\ \%}$	$1.752^{+0.04\ \%}_{-0.53\ \%}$	$1.702^{+0.02\ \%}_{-0.46\ \%}$
Measured C_{ref}, pF	$2.799^{+0.58\ \%}_{-1.86\ \%}$	$2.616^{+0.63\ \%}_{-1.41\ \%}$	$2.647^{+0.50\ \%}_{-2.80\ \%}$
Expected C_{lvl}, pF	1.65	1.65	1.65
Expected C_{ref}, pF	2.27	2.27	2.27
Used C_{aux}, pF	10.030 ± 0.004	9.912 ± 0.003	10.067 ± 0.002

Table 6.1: The measured and expected capacitance of the level sensors. We use the Agilent U1733C in 100 kHz mode to measure C_{aux}. Systematic errors were estimated based on results of liquid nitrogen evaporation tests shown in figure 6.18.

temperature. Their C_{lvl} and C_{ref} were measured independently with the final LZ electronics [2] which has sets of 10 pF auxiliary capacitors (C_{aux}) installed as the reference capacitors. Then, three different LN_2 evaporation tests were performed, namely a C_{lvl}-only test, a C_{ref}-only test, and a combination test of both C_{lvl} and C_{ref}. The tests were meant to simulate the liquid level decrease and temperature variation to confirm the reduction of liquid artefacts and the effect of material expansion on the sensors. At the beginning of each test, all three sensors were placed in a polystyrene bucket filled with LN_2 and were shielded within an aluminium vessel. As the LN_2 evaporates, the sensors' electronics measured the changes of capacitance from 77 K to room temperature. Although the temperature of the sensors was not measured because thermometers could not be attached, each test lasted at least 12 hours to ensure the temperature of the sensors returned to room temperature.

The result of measurements of sensors' capacitance in room temperature (table 6.1) shows some discrepancies with their expected capacitance. The discrepancies of the capacitance are mostly from the mechanical tolerances. A tolerance of 0.1

[2]The final LZ electronics uses equation 4.11 for capacitance measurements. This is different from the electronics used in the system tests which performed measurements based on equation 4.11.

mm in machining will contribute $\sim 3.3\,\%$ uncertainty to C_{lvl} and $\sim 20\%$ uncertainty to C_{ref}. The larger uncertainty on C_{ref} is due to its smaller plate thickness $d_{ref} = 0.5\,\text{mm}$(in contrast to $d_{lvl} = 3$ mm on C_{lvl}). Because the geometrical tolerance is fixed once the sensors are produced, such uncertainties are mitigated through calibrating the capacitance before operating the sensor.

The data of the C_{lvl}-only tests in figure 6.18 show a considerable reduction of the liquid artefacts. Compared with the sensors' data in Imperial and SLAC systems, the response of C_{lvl} of WPS was smooth and artefacts-free. Such suppression suggests the validity of using the full range of the C_{lvl} for liquid level measurement. Moreover, although C_{lvl} exhibited a moderate temperature dependence between 77 K and room temperature (around $0.4 \sim 0.7\,\%$), the dependence can be attributed to the thermal expansion of the copper. It is expected that the expansion contributes $\sim 0.37\,\%$ to the change of C_{lvl} capacitance under a 220 K temperature variation. Nevertheless, because the expansion effect was moderate and the targeted temperature range of operation in LZ is between 165 K and 185 K, the expected variation of C_{lvl} is $\sim 0.04\,\%$ and can, therefore, be neglected.

The capacitors, in C_{ref}-only test, showed a more drastic but understandable correlation with LN_2 evaporation and its temperature changes (see figure 6.18 (Bottom)). At the beginning of the test, LN_2 filled the space that forms the C_{ref} and caused the plateau in the data. As the LN_2 evaporated out of the space, capacitive interference from the liquid decreased. After that, when the LN_2 continued to vaporise out of the gaps in C_{lvl}, the C_{ref} experienced a stable period (cyan box in figure 6.18 (Bottom)). The period within the cyan box indicates the thermal uniformity of the C_{ref} when the C_{lvl} was picking up liquid level changes. Fur-

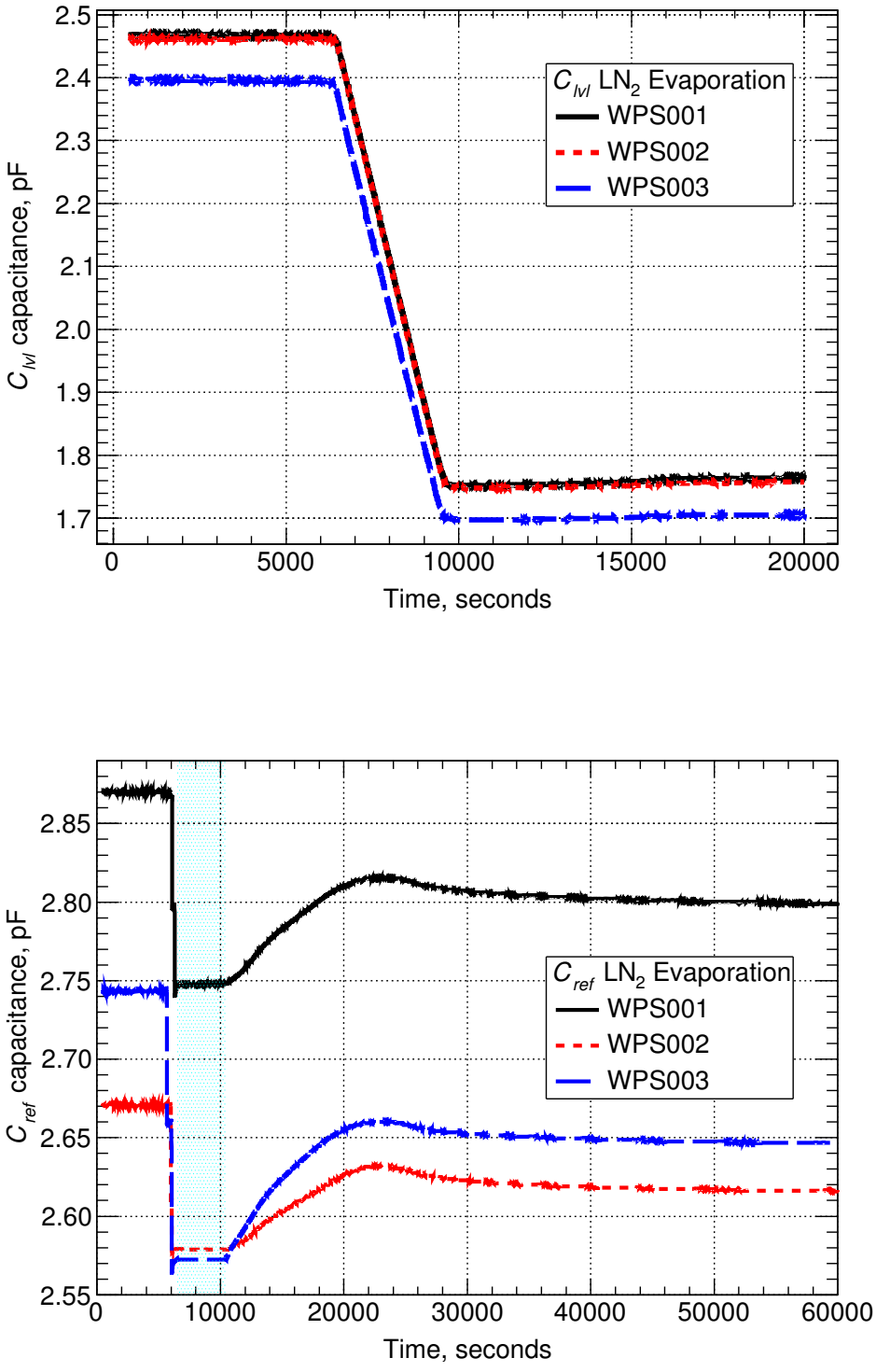


Figure 6.18: Separate tests of C_{lvl} and C_{ref} of all three WPS'. (Top): C_{lvl}-only measurement. The response of WPS001 almost overlaps with that of WPS002. (Bottom): C_{ref}-only measurement. The filled cyan colour box represents the period which the liquid was vaporising in C_{lvl} in all three sensors.

thermore, once the LN_2 entirely vaporised, the C_{ref} value rose and then dropped. The C_{ref} variation, between 77 K and room temperature, could be attributed to the PEEK dielectric constant change ($\sim 2\,\%$) and thermal expansion of geometry ($\sim 1.21\,\%$). On average, the C_{ref} experienced a $\sim 2.5\,\%$ capacitance changes when it warmed up from 77 K. As for the drop after 25000 seconds, the C_{ref} could have icing or water condensation on it, which evaporated near the end of the test and affected it. Such feature from potential water icing/condensation were not observed in the Run7 of SLAC system test because of the implementation of the cryogenic system. Even though C_{ref} varied by $\sim 2.5\,\%$ for a 220 K temperature change, the variation decreases to less than $0.3\,\%$ under the LZ operation temperature range.

The responses of WPS001's C_{ref}, WPS002's C_{lvl}, and WPS003 (using both C_{ref} and C_{lvl}) in the combination test are shown in figure 6.19. The test allowed observation of the influence of individual capacitors to the final measurement. Importantly, the response proves that the C_{ref} was indeed stable when LN_2 was evaporating through the sensors' C_{lvl} (see the cyan box in figure 6.19 (Top)). Moreover, by comparing the response of WPS003 with that of a reconstructed curve using WPS001's C_{ref} and WPS002's C_{lvl}, different stages of the effects, from the liquid evaporation and the temperature variation, on the sensor's capacitors can be studied independently. The result is shown in figure 6.19 (Bottom). The C_{ref}, filled with LN_2 at the beginning of the test, caused the stepping feature when C_{lvl} remained uninterrupted. The C_{lvl}, owing to the liquid level decrease to the sensor's effective measurement range, resulted in the slope feature as the C_{ref} remained steady. The C_{ref}, affected more by the warm up after LN_2 vaporisation, dominated the feature of the moderate decrease while the C_{lvl} suffered less from

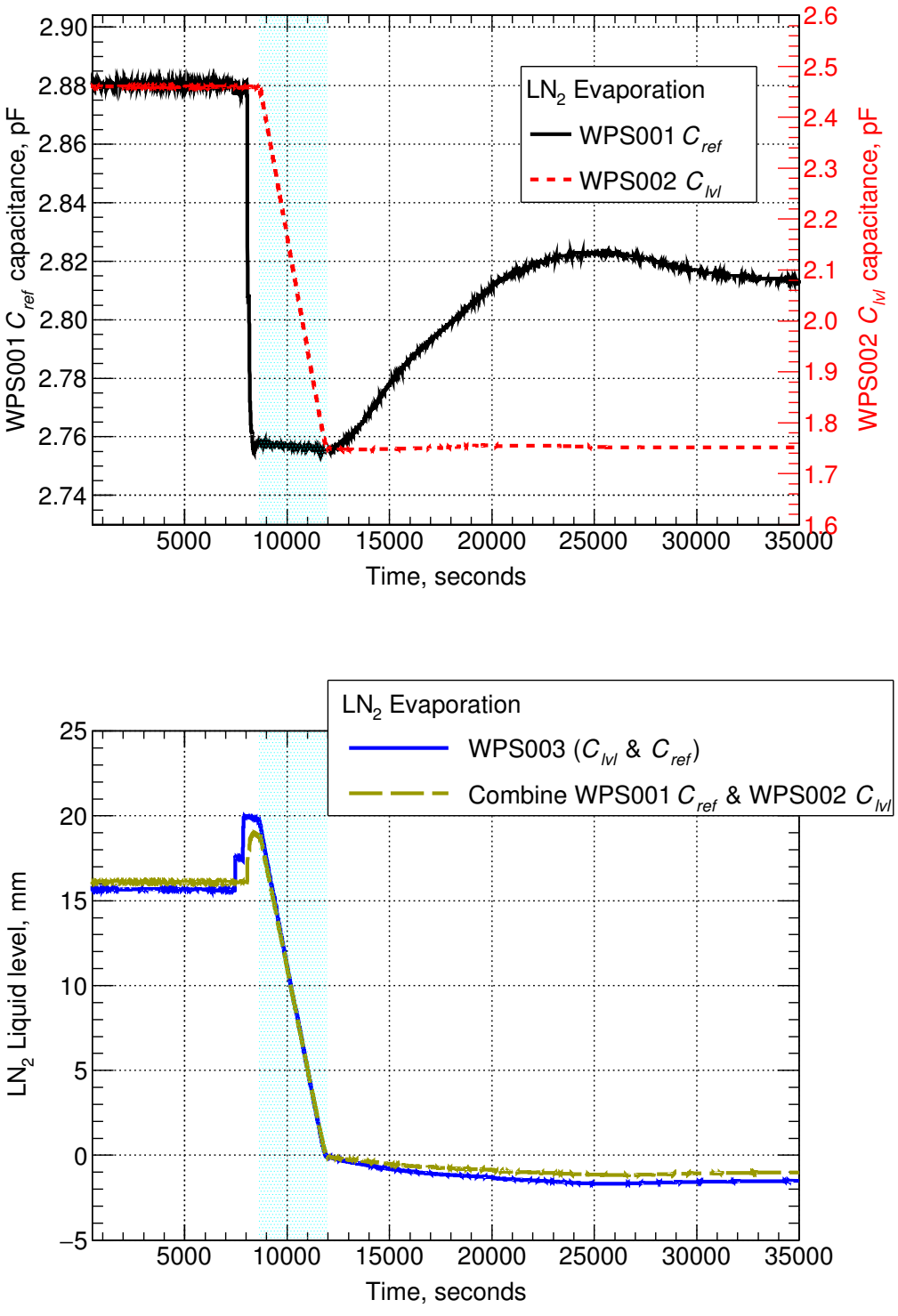


Figure 6.19: The result of the combination test. (Top): Measurements of WPS001's C_{ref}, and WPS002's C_{lvl} with the use of their corresponding C_{aux}. The filled cyan colour box represents the period which the liquid was vaporizing in C_{lvl} of both WPS001 and WPS002. (Bottom): Measurement of WPS003 using both of its C_{lvl} and C_{ref}. The dashed curve was reconstructed with data from WPS001's C_{ref} and WPS002's C_{lvl}. The liquid levels were calculated with equation 6.13.

thermal expansion. Lastly, the response of the sensors was translated to the liquid level shown in figure 6.19 (Bottom). The level was obtained by rewriting equation 4.11 as

$$\begin{aligned} C_{lvl}(T,z) &= \frac{1+R}{1-R}\cdot C_{ref}(T) \\ &= C_{lvl}(T,0)\cdot(1+\frac{\varepsilon_{liq}(T)-1}{L}\cdot z), \end{aligned} \tag{6.13}$$

where $R = {}^{V_{out}}/_{V_{adc}}$, ε_{liq} is the dielectric constant of a given liquid, L is the length of the active measurement range, T is the temperature of capacitors, and z is the height of liquid level. The relation between readout signal change and the liquid level then is

$$z = (\frac{L}{\varepsilon_{liq}(T)-1})\cdot(\frac{1+R}{1-R}\cdot\frac{C_{ref}(T)}{C_{lvl}(T,0)}-1). \tag{6.14}$$

Thus, for a given temperature of the sensor, the equation gives the liquid level simply by swapping the correct $\varepsilon_{liq}(T)$, $C_{ref}(T)$, and $C_{lvl}(T,0)$, which can be pre-determined before a liquid level measurement.

In conclusion, compared with previous prototype sensors, WPS shows considerable improvement in systematic error reduction. Its C_{lvl} exhibits substantial suppression of the liquid artefacts and has minor systematic effect at sub-percentage level due to thermal expansions; its C_{ref} demonstrates the stability during the liquid level measurement. Although C_{ref} contributes more features to the response in the measurement using both capacitors, it can be corrected by performing an in-situ calibration test as the C_{ref} only and C_{lvl} only tests. Furthermore, the preliminary tests with LN_2 show that on average the sensor has a precision of $12\,\mu$m

under a measurement range of 20 mm. Thus, the expected precision of the WPS in LXe level measurement would be $\sim 9\,\mu$m.

6.3 Conclusion

In this chapter, the systematic effects of the level sensor have been investigated. Liquid artefacts are shown to be the systematics which considerably reduces sensor's effective measurement range. The artefacts are generic and can also be observed in other liquid level measurements [102, 141]. The systematic from LXe dielectric constant's correlation with temperature was measured with the level sensor installed in the Imperial chamber. The measurement demonstrates a strong correlation between the constant and the LXe saturated temperature. The correlation is independent of the applied electromagnetic field at the frequency of the excitation signals (200 kHz) and can be used to predict the constant in LZ operation temperature, i.e. 175.8 K.

Apart from the systematics, electric field simulations were performed to aid the design of the level sensor and the LZ top-corner geometry. The simulation result alleviates the field in TPC skin region and predicts an optimal location for the sensor to monitor liquid level. The result has also been adopted in designing the LZ top-corner. The performance of a scaled-down version of the LZ top-corner will be tested with the final LZ level sensor in the Run 7 of the SLAC system test.

The final LZ level sensor has been designed and tested in liquid nitrogen. The design is based on the measurement methods described in Chapter 3 and 4 and the mitigation strategies which are driven by past tests in Run 5 of the Imperial Chamber and Run 3-6 of the SLAC system test. The result of the LZ sensor's

LN_2 test exhibits an excellent linear liquid response. The response, if not features free, does not show much influence from liquid artefacts.

Chapter 7

Conclusions

The construction of the LZ detector systems is ongoing; the first science run to look for a potential WIMP signal will start in 2020. The liquid level monitoring system for the secondary scintillation (S2) of the TPC will be tested and installed in 2018/2019 and is expected to play an important role in aiding the correction and stabilisation of the S2 signal.

The development of the monitoring system of the S2 signal described in this thesis resulted in the designs of radiopure level sensors - weir precision sensor (WPS), medium level sensor (MLS), and long level sensor (LLS). The sensors can precisely and accurately measure the liquid level of a two-phase xenon TPC in a rare event experiment. The electronics of the sensor described in Chapter 4 have shown to provide a precise capacitance measurement. This eventually leads to the precision liquid level measurement of the WPS discussed in Chapter 6 at $\sim 10\,\mu$m (or $< 1/1600$) level. Next, the studies of the application of sensors to the two-phase TPCs, discussed in Chapter 5 and 6, contributed to the improvement of designs of the LZ top-corner region and circulation system. This includes a better

electric field configuration at the top-corner region to reduce electroluminescence outside the S2 production region and a better pressure control between subsystems in the xenon circulation loop to decrease TPC liquid surface oscillation. Finally, the studies regarding the systematic effects of such sensors in Chapter 6 contribute to the final design of the LZ level sensors. The study with mock-up tests showed that solving the intrinsic systematics from the meniscus and capillary effects can increase the effective measurement range and the accuracy of the level sensor. The study of xenon dielectric constant variation with xenon saturated temperature provides a correct choice of the constant at a given LXe temperature for interpreting liquid level data.

The develpment of the LZ level sensors has been completed within this thesis. The final design of the WPS together with the final design of the LZ top-corner structure will be verified in the Run 7 of the SLAC system test. The MLS and the LLS have been produced for construction and assembly with the LZ subsystems.

Future applications of the LZ level sensor in the WIMP search experiments includes indentification of potentially mistaken S2 signal, affected by LXe droplets or the optimisation of the S2 signal for low-mass WIMP search ($1 \sim 10\,\mathrm{GeV/c^2}$) with S2-only analysis [142]. In the former case, if LXe droplets formed on the top PMT array drop into the TPC extraction region and affect the expected S2 signal, the surface wave due to the droplets can be pick up by WPS and be used to correlate the sensor signal with such type of event population. In the latter case, the determination of z-position of an interaction site for establishing the fiducial volume depends on the diffusion of drifted electrons. The information of the longitudinal diffusion will affect the S2 width. To ensure the S2 width

is dominantly affected by the diffusion instead of the gas gap of the extraction region, a precision measurement of the liquid surface level will allow a fine-tuning of the S2 width to achieve this. Furthermore, the S2-only study requires the understanding of electron emission background which could reduce the sensitivity of the analysis [87, 142]. The background could be affected by the liquid surface perturbation which effectively heats up electrons at the surface [143]. Modelling such a background requires a correct understanding of the electron extraction efficiency of a TPC [86, 87] which also depends on the liquid level to first order and is in tension with a recent measurement [144]. As a result, it is expected that the level sensors would complement the studies of these analyses such that LZ can confidently distinguish a potential WIMP signal from its detector background.

Appendix A

Level Sensors in the LZ Circulation System

In this appendix, the designs of a medium level sensor (MLS) and a long level sensor (LLS) are described. They are some of the final LZ level sensors which will be installed in the circulation system. Their motivation and location in the LZ system are described in Chapter 4.

A.1 Design of the Sensors

Both the MLS and LLS are shown in figure A.1 share similar form factors. They are both vertical parallel plate sensors similar to the weir precision sensor (WPS). Their sense electrodes are long plates, with V_{lvl} excitation plates and V_{ref} excitation plates installed near the bottom and the top of the structure, forming the C_{lvl} and C_{ref}. The copper spacers at the bottom and the top of the V_{lvl} excitation plates function as the guard electrodes for the C_{lvl}. They also help to suppress the occurrences of liquid artefacts described in Section 6.1.1 within the effective

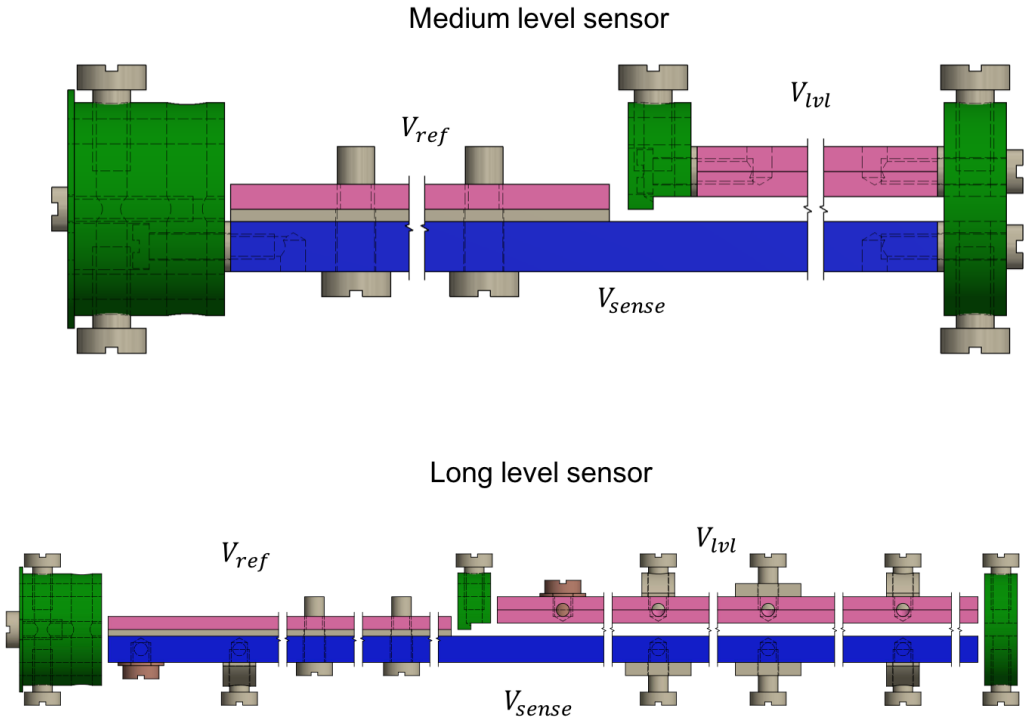


Figure A.1: CAD drawings of MLS and LLS. The sensors are shielded inside a grounded guard tube (not shown here). Green: grounded supporting structures. Blue: V_{sense} plate. Pink: excitation plates of V_{ref} and V_{lvl}. Light beige: PEEK supporting structure. The parameters as follows correspond to the parameters in equation 4.5. (Top): Medium level sensor, with $L_{lvl} = 200\,\text{mm}$, $L_{ref} = 43\,\text{mm}$, $d_{lvl} = 2\,\text{mm}$, $d_{ref} = 1\,\text{mm}$, and $W_{lvl} = W_{ref} = 13\,\text{mm}$. (Bottom): Long level sensor, with $L_{lvl} = 800\,\text{mm}$, $L_{ref} = 175\,\text{mm}$, $d_{lvl} = 2\,\text{mm}$, $d_{ref} = 1\,\text{mm}$, and $W_{lvl} = W_{ref} = 13\,\text{mm}$.

measurement range, i.e. the region where the V_{lvl} excitation plates are. As for the C_{ref}, PEEK plates are sandwiched between the sense and V_{ref} excitation plates at the top of the sensors. The sensors are shielded within 20 mm diameter copper tubes which decouple the sensors from external interferences at given installation locations.

	MLS	LLS
Measured C_{lvl}, pF	$15.967^{+1.02\ \%}_{-2.92\ \%}$	$40.494^{+1.2\ \%}_{-3.25\ \%}$
Measured C_{ref}, pF	$14.356^{+3.78\ \%}_{-1.03\ \%}$	$57.415^{+1.84\ \%}_{-4.97\ \%}$
Expected C_{lvl}, pF	10.973	42.499
Expected C_{ref}, pF	14.607	58.427
Used C_{aux}, pF	10.030 ± 0.004	9.912 ± 0.003

Table A.1: The measured and expected capacitance of the level sensors. We use the Agilent U1733C in 100 kHz mode to measure C_{aux}. Systematic errors were estimated based on results of liquid nitrogen evaporation tests shown in figure A.3 and A.2. The measured C_{lvl} of MLS is much higher than its expected value, owing to a closer distance between the sense plate and the excitation plate (the tolerance of the distance between plates is ± 0.5 mm).

A.2 Performance Tests

The performance tests of the MLS and LLS consist of a C_{lvl}-only test and a C_{ref}-only test in liquid nitrogen. For the C_{lvl}-only test, the sensors were tested in different buckets. As for the C_{ref}-only test, the sensors were tested in the same bucket; LLS was placed upside down with MLS attached next to it. The C_{ref} section of the LLS overlapped with that of the MLS. As the liquid nitrogen evaporation happened, the capacitance changes in the tests were recorded by the electronics.

The result of the C_{lvl}-only test is shown in figure A.2. The C_{lvl} response of the MLS is linear and similar to that of WPS. The C_{lvl} response of LLS is less linear owing to a slightly bent sense electrode. Also, after the liquid nitrogen evaporation, the reading of the LLS's C_{lvl} was increasing. This is caused by icing and water condensation on the sense plate due to a lack of a sealed vacuum vessel to prevent such effect. As for the result of the C_{ref}-only test, this is given in figure A.3. The C_{ref} response of the MLS is similar to that of the WPS discussed in Chapter 6. The capacitor was stable when the liquid nitrogen was evaporating through the C_{lvl} section of the sensor (cyan box). After that, the features in the response were due

to warm-up of the sensor's parts and the water-condensation/evaporation. The C_{ref} response of the LLS is shown in figure A.3 (Bottom). After an initial decrease due to the liquid evaporation out of the sensor's C_{ref}, features during the warm-up (from the red box onward) can also be caused by icing/water-condensation/water-evaporation on the capacitor.

Finally, the comparison between the expected and the measured capacitance of the sensors is shown in table A.1. In general, the measured capacitances are consistent with the expected capacitances with less than 5 % discrepancy. The only exception is the C_{lvl} of MLS, which is caused by a closer alignment of the sense and the excitation plates.

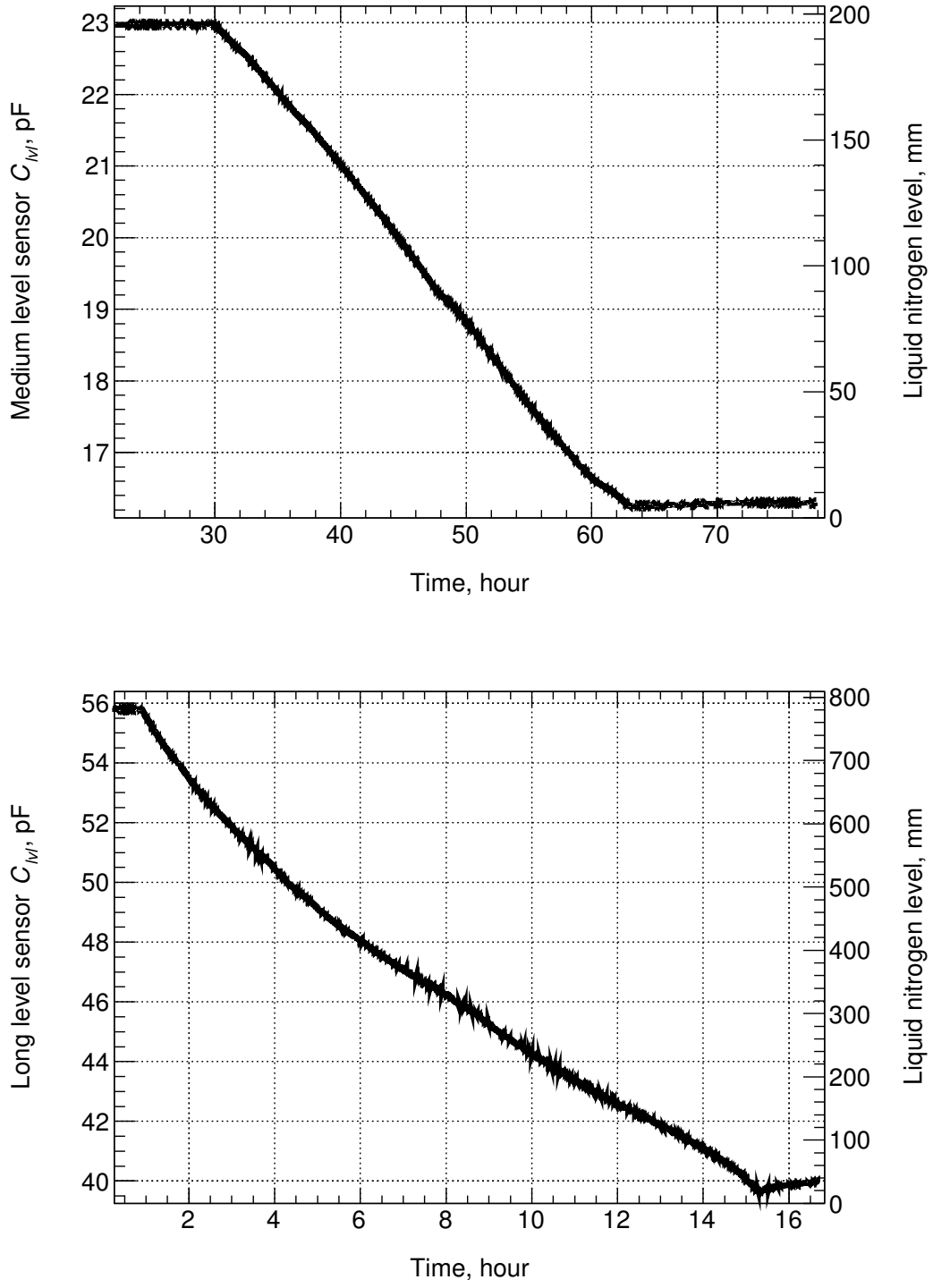


Figure A.2: C_{lvl}-only test result for MLS and LLS. The sensors were tested in two different buckets of liquid nitrogen. (Top): MLS. (Bottom): LLS. The rising of the reading of the liquid nitrogen evaporation is due to icing and water condensation on the warmer part of the electrodes of the sensor.

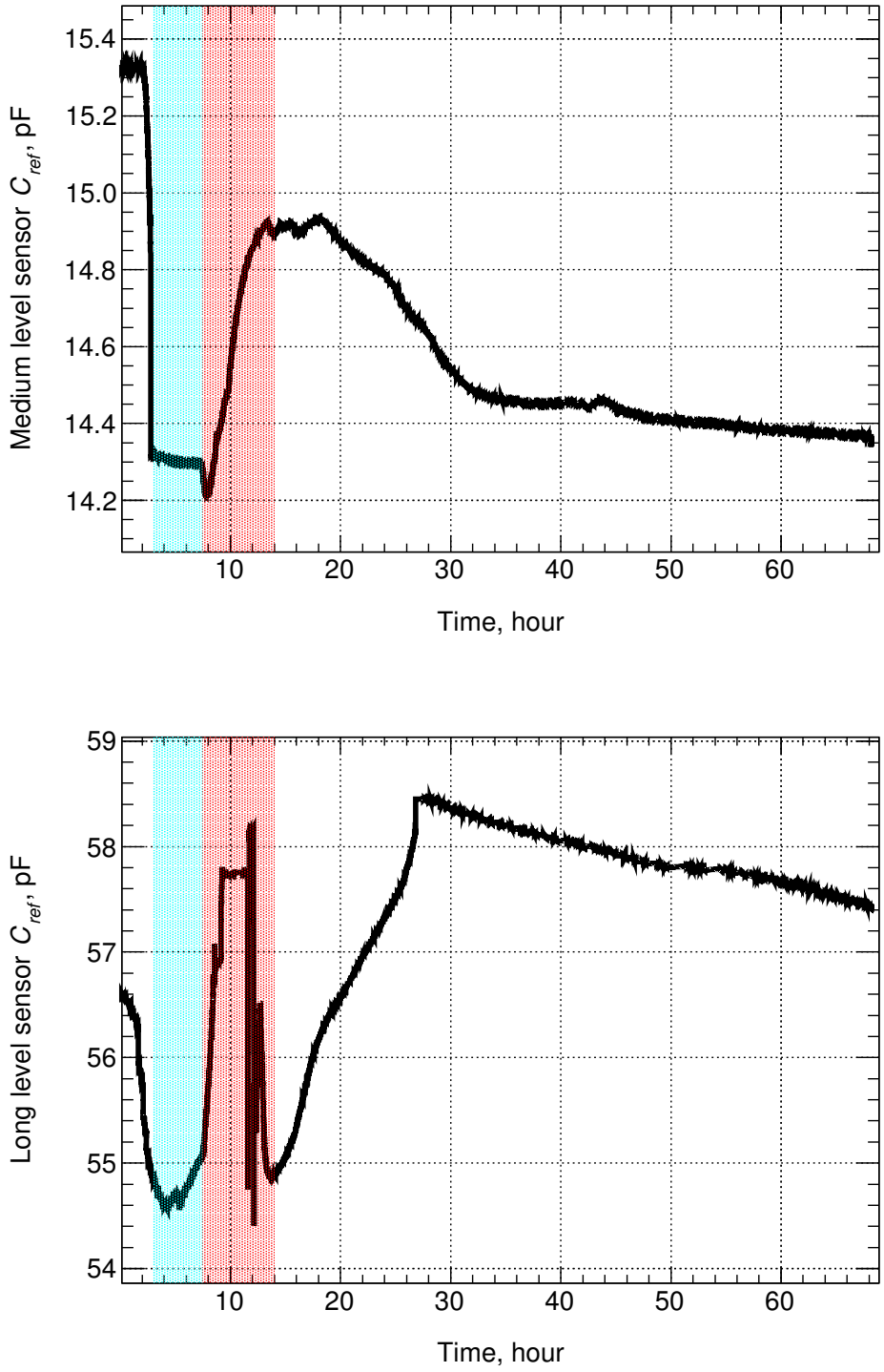


Figure A.3: C_{ref}-only test result for MLS and LLS. The sensors were tested with the same bucket of liquid nitrogen. The LLS was installed upside down with MLS attached to its end. The cyan box in the data represents the period when liquid nitrogen was evaporating pass the C_{lvl} of MLS; the red box represents the time when effects of icing and water-condensation on the sensors were dominant. (Top): MLS. The reading decreasing after the red box is due to water-evaporation and sensor warm-up. (Bottom): LLS. The rise of the reading after the red box was due to sensor warm-up. The reading decreasing after 30 hours is due to a continuous evaporation of the water on the sensor.

References

[1] DES Collaboration, T. M. C. Abbott, F. B. Abdalla, *et al.*, (2017), arXiv:1708.01530 .

[2] V. C. Rubin, N. Thonnard, and J. Ford, W. K., Astrophys. J. **238**, 471 (1980).

[3] D. Clowe, M. Bradač, A. H. Gonzalez, *et al.*, Astrophys. J. **648**, L109 (2006), arXiv:0608407 [astro-ph] .

[4] P. A. R. Ade, N. Aghanim, M. Arnaud, *et al.*, Astron. Astrophys. **594**, A13 (2016).

[5] S. Dodelson, *Modern Cosmology* (Academic Press).

[6] J. A. Peacock, *Cosmological Physics* (Cambridge University Press).

[7] D. Baumann, (2009), arXiv:0907.5424 .

[8] L. L. Bergström and A. Goobar, *Cosmology and Particle Astrophysics*, Springer Praxis Books (Springer Berlin Heidelberg, 2004).

[9] N. Suzuki, D. Rubin, C. Lidman, *et al.*, Astrophys. J. **746**, 85 (2012).

[10] W. J. Percival, B. A. Reid, D. J. Eisenstein, *et al.*, Mon. Not. R. Astron. Soc. **401**, 2148 (2010).

[11] G. Bertone and D. Hooper, (2016), arXiv:1605.04909 .

[12] F. Zwicky, Astrophys. J. **86**, 217 (1937).

[13] S. Smith, Astrophys. J. **83**, 23 (1936).

[14] A. B. Newman, T. Treu, R. S. Ellis, *et al.*, Astrophys. J. **765**, 24 (2013).

[15] K. G. Begeman, A. H. Broeils, and R. H. Sanders, Mon. Not. R. Astron. Soc. **249**, 523 (1991).

[16] V. C. Rubin and J. Ford, W. Kent, Astrophys. J. **159**, 379 (1970).

[17] M. Persic, P. Salucci, and F. Stel, (1995), 10.1093/mnras/281.1.27, arXiv:9506004 [astro-ph] .

[18] M. Markevitch, (2005), arXiv:0511345 [astro-ph] .

[19] D. Clowe, A. Gonzalez, and M. Markevitch, Astrophys. J. **604**, 596 (2004), arXiv:0312273 [astro-ph] .

[20] A. Einstein, Ann. Phys. **354**, 769 (1916).

[21] F. W. Dyson, A. S. Eddington, and C. Davidson, Philos. Trans. R. Soc. A Math. Phys. Eng. Sci. **220**, 291 (1920).

[22] I. Kovner, Nature **327**, 193 (1987).

[23] Y. Mellier, Annu. Rev. Astron. Astrophys. **37**, 127 (1999).

[24] D. M. Wittman, J. A. Tyson, D. Kirkman, I. Dell'Antonio, and G. Bernstein, Nature **405**, 143 (2000).

[25] K.-H. Chae, Mon. Not. R. Astron. Soc. **346**, 746 (2003).

[26] V. Springel, C. S. Frenk, and S. D. M. White, Nature **440**, 1137 (2006).

[27] S. D. M. White, C. S. Frenk, and M. Davis, Astrophys. J. **274**, L1 (1983).

[28] S. Dodelson, (2011), 10.1142/S0218271811020561, arXiv:1112.1320 .

[29] B. P. Abbott, R. Abbott, T. D. Abbott, *et al.*, Astrophys. J. **848**, L13 (2017).

[30] M. Battaglieri, A. Belloni, A. Chou, *et al.*, (2017), arXiv:1707.04591 .

[31] J. L. Feng, Annu. Rev. Astron. Astrophys. **48**, 495 (2010).

[32] R. D. Peccei and H. R. Quinn, Phys. Rev. Lett. **38**, 1440 (1977).

[33] L. Abbott and P. Sikivie, Phys. Lett. B **120**, 133 (1983).

[34] M. Dine and W. Fischler, Phys. Lett. B **120**, 137 (1983).

[35] J. Preskill, M. B. Wise, and F. Wilczek, Phys. Lett. B **120**, 127 (1983).

[36] P. Sikivie, Phys. Rev. Lett. **51**, 1415 (1983).

[37] The ADMX Collaboration, S. J. Asztalos, G. Carosi, *et al.*, (2009), 10.1103/PhysRevLett.104.041301, arXiv:0910.5914 .

[38] J. Hoskins, J. Hwang, C. Martin, *et al.*, Phys. Rev. D **84**, 121302 (2011).

[39] G. Jungman, M. Kamionkowski, and K. Griest, Phys. Rep. **267**, 195 (1996).

[40] J. Lewin and P. Smith, Astropart. Phys. **6**, 87 (1996).

[41] T. M. Undagoitia and L. Rauch, (2015), 10.1088/0954-3899/43/1/013001, arXiv:1509.08767 .

[42] C. McCabe, Phys. Rev. D **82**, 023530 (2010).

[43] R. Catena and P. Ullio, J. Cosmol. Astropart. Phys. **2010**, 004 (2010).

[44] M. Pato, O. Agertz, G. Bertone, B. Moore, and R. Teyssier, Phys. Rev. D **82**, 023531 (2010).

[45] C. Savage, K. Freese, and P. Gondolo, Phys. Rev. D **74**, 043531 (2006).

[46] P. Klos, J. Menéndez, D. Gazit, and A. Schwenk, (2013), 10.1103/PhysRevD.88.083516, arXiv:1304.7684 .

[47] C. Amole, M. Ardid, I. J. Arnquist, *et al.*, Phys. Rev. Lett. **118**, 251301 (2017), arXiv:1702.07666 .

[48] D. S. Akerib, S. Alsum, H. M. Araújo, *et al.*, Phys. Rev. Lett. **118**, 251302 (2017).

[49] R. Bernabei, P. Belli, F. Cappella, *et al.*, (2008), 10.1140/epjc/s10052-008-0662-y, arXiv:0804.2741 .

[50] The XENON collaboration, E. Aprile, J. Aalbers, *et al.*, (2017), 10.1103/PhysRevLett.118.101101, arXiv:1701.00769 .

[51] XMASS Collaboration, K. Abe, K. Hiraide, *et al.*, (2015), arXiv:1511.04807 .

[52] C. E. Aalseth, P. S. Barbeau, J. Colaresi, *et al.*, (2012), 10.1103/PhysRevD.88.012002, arXiv:1208.5737 .

[53] Q. Yue, W. Zhao, K. J. Kang, *et al.*, (2014), 10.1103/PhysRevD.90.091701, arXiv:1404.4946 .

[54] R. Agnese, A. J. Anderson, M. Asai, *et al.*, (2014), 10.1103/PhysRevLett.112.241302, arXiv:1402.7137 .

[55] EDELWEISS Collaboration, L. Hehn, E. Armengaud, *et al.*, (2016), 10.1140/epjc/s10052-016-4388-y, arXiv:1607.03367 .

[56] The CRESST Collaboration, G. Angloher, A. Bento, *et al.*, (2015), 10.1140/epjc/s10052-016-3877-3, arXiv:1509.01515 .

[57] D. S. Akerib, S. Alsum, H. M. Araújo, *et al.*, Phys. Rev. Lett. **118**, 021303 (2017).

[58] E. Aprile, J. Aalbers, F. Agostini, *et al.*, (2017), arXiv:1705.06655 .

[59] P.-I. Collaboration, :, X. Cui, *et al.*, (2017), 1708.06917, arXiv:1708.06917 .

[60] B. J. Mount, S. Hans, R. Rosero, *et al.*, (2017), arXiv:1703.09144 .

[61] J. Aalbers, F. Agostini, M. Alfonsi, *et al.*, (2016), 10.1088/1475-7516/2016/11/017, arXiv:1606.07001 .

[62] J. L. Feng, S. Ritz, J. J. Beatty, *et al.*, (2014), arXiv:1401.6085 .

[63] M. Chadwick, M. Herman, P. Obložinský, *et al.*, Nucl. Data Sheets **112**, 2887 (2011).

[64] M. Berger, J. Hubbell, S. Seltzer, *et al.*, *XCOM: Photon Cross Sections Database*, Tech. Rep. (NIST, PML, Radiation Physics Division, 2010).

[65] E. Dahl, *The physics of background discrimination in liquid xenon, and first results from Xenon10 in the hunt for WIMP dark matter*, Ph.D. thesis, Princeton University (2009).

[66] T. Takahashi, S. Konno, T. Hamada, *et al.*, Phys. Rev. A **12**, 1771 (1975).

[67] T. Doke, A. Hitachi, S. Kubota, A. Nakamoto, and T. Takahashi, Nucl. Instruments Methods **134**, 353 (1976).

[68] D. S. Akerib, S. Alsum, H. M. Araújo, *et al.*, (2016), 10.1103/PhysRevD.95.012008, arXiv:1610.02076 .

[69] Q. Lin, J. Fei, F. Gao, *et al.*, Phys. Rev. D **92**, 032005 (2015).

[70] P. Sorensen and C. E. Dahl, Phys. Rev. D **83**, 063501 (2011).

[71] J. Lindhard, V. Nielsen, M. Scharff, and P. Thomsen, Medd. Dan. Vid. Selsk **10** (1963).

[72] LUX Collaboration, D. S. Akerib, S. Alsum, *et al.*, (2016), arXiv:1608.05381 .

[73] H. Cao, T. Alexander, A. Aprahamian, *et al.*, Phys. Rev. D **91**, 092007 (2015).

[74] A. Manzur, A. Curioni, L. Kastens, *et al.*, Phys. Rev. C **81**, 025808 (2010).

[75] D. S. Akerib, H. M. Araújo, X. Bai, *et al.*, Phys. Rev. Lett. **112**, 091303 (2014).

[76] V. N. Lebedenko, H. M. Araújo, E. J. Barnes, *et al.*, Phys. Rev. D **80**, 052010 (2009).

[77] LUX Collaboration, D. S. Akerib, H. M. Araújo, *et al.*, (2015), 10.1103/PhysRevD.93.072009, arXiv:1512.03133 .

[78] J. Jortner, L. Meyer, S. A. Rice, and E. G. Wilson, J. Chem. Phys. **42**, 4250 (1965).

[79] A. Hitachi, T. Takahashi, N. Funayama, *et al.*, Phys. Rev. B **27**, 5279 (1983).

[80] A. Hitachi, T. Takahashi, N. Funayama, *et al.*, Phys. Rev. B **27**, 5279 (1983).

[81] Carlos Faham, *Prototype, Surface Commissioning and Photomultiplier Tube Characterization for the Large Underground Xenon (LUX) Direct Dark Matter Search Experiment*, Ph.D. thesis, Brown University (2013).

[82] W. T. Chen, H. Carduner, J. P. Cussonneau, *et al.*, Defect Diffus. Forum **326-328**, 567 (2012).

[83] P. Sorensen, Nucl. Instruments Methods Phys. Res. Sect. A Accel. Spectrometers, Detect. Assoc. Equip. **635**, 41 (2011).

[84] D. Akerib, X. Bai, E. Bernard, *et al.*, Astropart. Phys. **45**, 34 (2013).

[85] J. Mock, *A Search for Dark Matter with the Large Underground Xenon Detector*, Ph.D. thesis, University of California, Davis (2014).

[86] E. Gushchin, A. Kruglov, and I. Obodovskii, J. Exp. Theor. Phys. **55**, 860 (1982).

[87] P. Sorensen, (2017), arXiv:1702.04805 .

[88] A. Bolozdynya, Nucl. Instruments Methods Phys. Res. Sect. A Accel. Spectrometers, Detect. Assoc. Equip. **422**, 314 (1999).

[89] G. W. HUTCHINSON, Nature **162**, 610 (1948).

[90] V. Chepel and H. Araújo, J. Instrum. **8**, R04001 (2013).

[91] T. Takahashi, S. Himi, M. Suzuki, J.-z. Ruan(Gen), and S. Kubota, Nucl. Instruments Methods Phys. Res. **205**, 591 (1983).

[92] F. P. Santos, T. H. V. T. Dias, A. D. Stauffer, and C. A. N. Conde, J. Phys. D. Appl. Phys. **27**, 42 (1994).

[93] D. S. Akerib, C. W. Akerlof, D. Y. Akimov, *et al.*, (2017), arXiv:1702.02646 .

[94] F. Neves, A. Lindote, A. Morozov, *et al.*, J. Instrum. **12**, P01017 (2017).

[95] P. Barrow, L. Baudis, D. Cichon, *et al.*, (2016), 10.1088/1748-0221/12/01/P01024, arXiv:1609.01654 .

[96] J. Kwong, *The development of two-phase xenon dark matter detectors*, Ph.D. thesis, Princeton University (2009).

[97] D. Akerib, X. Bai, S. Bedikian, *et al.*, Nucl. Instruments Methods Phys. Res. Sect. A Accel. Spectrometers, Detect. Assoc. Equip. **709**, 29 (2013).

[98] The LZ Collaboration, D. S. Akerib, C. W. Akerlof, *et al.*, (2015), arXiv:1509.02910 .

[99] J. Loach, J. Cooley, G. Cox, *et al.*, Nucl. Instruments Methods Phys. Res. Sect. A Accel. Spectrometers, Detect. Assoc. Equip. **839**, 6 (2016).

[100] D. Akerib, X. Bai, S. Bedikian, *et al.*, Nucl. Instruments Methods Phys. Res. Sect. A Accel. Spectrometers, Detect. Assoc. Equip. **704**, 111 (2013).

[101] J. D. Jackson, *Classical Electrodynamics*, three ed. (Wiley, 1999).

[102] J. Hu, H.-W. Gong, Q. Lin, *et al.*, Chinese Phys. C **38**, 056002 (2014).

[103] Larry K. Baxter, *Capacitive Sensors: Design and Applications* (Wiley-IEEE Press, 1996) p. 320.

[104] Victrex, *VICTREX PEEK 450G Datasheet*, Tech. Rep.

[105] Atena Plastics Corp., *DuPont Teflon PTFE Specifications*, Tech. Rep.

[106] DuPont, *DELRIN Datasheet*, Tech. Rep.

[107] Wrought Materials, *Oxygen-Free Copper Datasheet*, Tech. Rep.

[108] "ESA Material Outgassing Database," .

[109] C. T. W. Hall and A. Tomas, "Private Communication: Component Compatibility," .

[110] A. Tomas, H. Araújo, L. Adam, Bailey (Imperial Coll., and T. J. Sumner, *D300.2 - Study of High Field Processes on the Surface of Cathode Wire in Liquid Xenon*, Tech. Rep. (Imperial College, London, 2015).

[111] T. Shutt, "Private communication: Spark Gerneration in LXe," .

[112] K. Boast, *A System of Position Sensors for the LUX-ZEPLIN Experiment*, Ph.D. thesis, University of Oxford (2017).

[113] R. L. Amey and R. H. Cole, J. Chem. Phys. **40**, 146 (1964).

[114] A. D. Sen, V. G. Anicich, and T. Arakelian, J. Phys. D. Appl. Phys. **25**, 516 (1992).

[115] "NIST Chemistry Database," .

[116] A. A. Carey, *The Dielectric Constant of Lubrication Oils*, Tech. Rep. (COMPUTATIONAL SYSTEMS INC KNOXVILLE TN, 1998).

[117] Suwarno and I. S. Darma, in *2008 Int. Symp. Electr. Insul. Mater. (ISEIM 2008)* (IEEE, 2008) pp. 514–517.

[118] A. S. Howard, Phys. At. Nucl. **67**, 2032 (2004).

[119] K. D. Timmerhaus and R. P. Reed, eds., *Cryogenic Engineering*, Interna-

tional Cryogenics Monograph Series (Springer New York, New York, NY, 2007).

[120] A. G. Al Lafi, Polym. Bull. **68**, 2269 (2012).

[121] K. Palladino, T. P. Biesiadzinski, A. Fan, *et al.*, *LZ Internal Note: Phase-I System Test Summary*, Tech. Rep. (2016).

[122] W. L. Waldron, *LZ Internal Note: Long Level Sensor Electrostatic*, Tech. Rep. (LBNL, 2015).

[123] W. L. Waldron, *LZ Internal Note: Weir Precision Sensor Electrostatic*, Tech. Rep. (LBNL, 2015).

[124] M. Pfister, E. Battisacco, G. De Cesare, and A. Schleiss, in *Proc. 2nd Int. Work. Labyrinth Piano Key Weirs - PKW 2013* (2013) pp. 73–82.

[125] C. Flexman, *Detection of Liquid Xenon Surface Waves by Light Modulation in the LUX Dark Matter Experiment*, Ph.D. thesis, Brown University (2016).

[126] D. Halliday, R. Resnick, and J. Walker, *Fundamentals of physics*, 10th ed. (Wiley, 2014).

[127] Ventec, "VT-481 Datasheet," .

[128] L. D. Landau, E. M. Lifshitz, and A. L. King, Am. J. Phys. **29**, 647 (1961).

[129] A. Baldini, C. Bemporad, F. Cei, *et al.*, IEEE Trans. Dielectr. Electr. Insul. **13**, 547 (2006).

[130] A. J. Leadbetter and H. E. Thomas, Trans. Faraday Soc. **61**, 10 (1965).

[131] R. C. Reid, AIChE J. **21**, 1235 (1975).

[132] W. Streett, L. Sagan, and L. Staveley, J. Chem. Thermodyn. **5**, 633 (1973).

[133] M. Terry, J. Lynch, M. Bunclark, K. Mansell, and L. Staveley, J. Chem. Thermodyn. **1**, 413 (1969).

[134] F. Theeuwes and R. J. Bearman, J. Chem. Thermodyn. **2**, 507 (1970).

[135] A. C. Sinnock and B. L. Smith, Phys. Rev. **181**, 1297 (1969).

[136] A. C. Sinnock, J. Phys. C Solid State Phys. **13**, 2375 (1980).

[137] G. Seidel, R. Lanou, and W. Yao, Nucl. Instruments Methods Phys. Res. Sect. A Accel. Spectrometers, Detect. Assoc. Equip. **489**, 189 (2002).

[138] V. Solovov, V. Chepel, M. Lopes, *et al.*, Nucl. Instruments Methods Phys. Res. Sect. A Accel. Spectrometers, Detect. Assoc. Equip. **516**, 462 (2004).

[139] J. L. Subtil, P. Laporte, R. Reininger, and V. Saile, Phys. status solidi **143**, 783 (1987).

[140] A. Michels and T. Wassenaar, Physica **16**, 253 (1950).

[141] T. Shutt, "LUX Level Meter Response (Private communication)," (2016).

[142] E. Aprile, J. Aalbers, F. Agostini, *et al.*, Phys. Rev. D **95**, 059901 (2017).

[143] J. Xu, *LZ Internal Meeting: Electron background in LUX and implications for LZ*, Tech. Rep. (LLNL, 2017).

[144] B. N. V. Edwards, E. Bernard, E. M. Boulton, *et al.*, (2017), arXiv:1710.11032 .